EFFECTIVE INTERACTIONS IN SOFT CONDENSED MATTER PHYSICS

Christos N. LIKOS

Institut für Theoretische Physik II. Heinrich-Heine-Universität Düsseldorf, Universitätsstraße 1,
D-40225 Düsseldorf, Germany

ELSEVIER

AMSTERDAM – LONDON – NEW YORK – OXFORD – PARIS – SHANNON – TOKYO

ELSEVIER

Physics Reports 348 (2001) 267–439

PHYSICS REPORTS

www.elsevier.com/locate/physrep

Effective interactions in soft condensed matter physics

Christos N. Likos*

Institut für Theoretische Physik II, Heinrich-Heine-Universität Düsseldorf, Universitätsstraße 1, D-40225 Düsseldorf, Germany

Received September 2000; editor: M.L. Klein

Contents

---

* Tel.: + 49-211-811-3699; fax: + 49-211-811-2262.
E-mail address: likos@thphy.uni-duesseldorf.de (C. N. Likos).

PII: S0370-1573(00)00141-1

Abstract

In this work, we present a review of recently achieved progress in the field of soft condensed matter physics, and in particular on the study of the static properties of solutions or suspensions of colloidal particles. The latter are macromolecular entities with typical sizes ranging from 1 nm to 1 μm and their suspension typically contain, in addition to the solvent, smaller components such as salt ions or free polymer chains. The theoretical tool introduced is the effective Hamiltonian which formally results by a canonical trace over the smaller degrees of freedom for a fixed, "frozen" configuration of the large ones. After presenting the formal definitions of this effective Hamiltonian, we proceed with the applications to some common soft matter systems having a variable softness and ranging from free polymer chains to hard colloidal particles. We begin from the extreme case of nondiverging effective interactions between ultrasoft polymer chains and derive an exact criterion to determine the topology of the phase diagrams of such systems. We use star polymers with a variable arm number f as a hybrid system in order to interpolate between these two extremes. By deriving an effective interaction between stars we can monitor the change in the phase behavior of a system as the steepness of the repulsion between its constituent particles increases. We also review recent results on the nature and the effects of short-range attractions on the phase diagrams of spherical, nonoverlapping colloidal particles.

PACS: 82.70.Dd; 61.25.Hq; 61.20. − p; 64.70.Dv

Keywords: Soft matter; Colloids; Polymers; Liquid structure

---

1. Introduction

A common state of soft matter systems in room temperature and pressure is the liquid one and a great deal of this work deals with liquids. Even when solids are examined, the liquid state of matter is somehow always present, as in the modern approaches solids are considered as spatially inhomogeneous (periodically modulated) fluids. Hence, a theoretical understanding the structure and properties of fluids is of great importance in soft matter physics. Among the three states of matter, the liquid state was the last to be quantitatively analyzed and understood by the tools of modern physics. The nature of the gaseous phase has already been examined since the 19th century and the progress in understanding the physics of crystalline solids has experienced an explosion since the middle of the 20th century, facilitated by the advances in quantum mechanics and the applications of symmetry principles arising from lattice periodicity. On the contrary, the liquid phase is a peculiar state of matter, whereupon the system is on the one hand translationally invariant, in close similarity to the gases, but on the other hand the typically high densities encountered in this phase give rise to nontrivial short- and sometimes long-range correlations between the constituent particles which are very difficult to handle analytically. To paraphrase Victor Weisskopf [1]: if the world's most brilliant theoretical physicists were gathered in a desert island, equipped with the laws of physics but otherwise isolated from the external world and were asked to guess the forms of matter, then they would pretty soon come up with predicting the existence of atoms, molecules and a bit later of the ideal gases. After some time they would realize that atoms can also self-organize in periodic arrangements, thus discovering the crystalline solids. But they would probably never come up with the liquids – although in their island they would be surrounded by a large mass of the most abundant liquid in our planet!

What is it that makes liquids so difficult to study? For one thing, the theories of statistical mechanics are readily applicable to any system, including translationally invariant systems at high densities, such as liquids. Yet, the large densities involved make any kind of perturbative approach, based on the noninteracting gas as a reference system, hopeless. Only nonperturbative approaches are viable and, in this way, one ends up with hierarchies of integral equations involving the correlation functions of the system, which are analytically intractable. This has sometimes led to rather exaggerated statements regarding the level of our understanding of classical fluids, such as '*... neither statistical mechanics nor chemical physics understands the liquid state ...*' [2]. Though somewhat extreme in its formulation, the above comment is in line with the belief that '*the classical fluid is not everyone's cup of tea*' [3].

Nowadays, the theory of the liquid state is a well-established branch of condensed matter physics. The many standard textbooks on the subject [4–9] are a testimony that the theories of classical fluids have gained widespread acceptance and that the field of liquids rests on solid foundations (no pun intended). The rapid development of liquid-state physics started with the arrival of powerful computers in the 1960s which had a doubly positive effect: on the one hand, they made the solution of approximate integral equations tractable, thus yielding information about the structure of the liquids and providing impetus for the development of new, more sophisticated theories. On the other hand, they made possible the development of computer simulations which provide, in principle, an exact solution to the statistical–mechanical problem [10,11]. In this way, it became possible to approach the problem of understanding liquid structure from three different angles, namely

(i) Performing real experiments (such as X-ray, electron or neutron scattering) in liquids.
(ii) Developing theoretical models for the interactions between the particles in the liquid and determining the structure by solving some variety of integral equation theories.
(iii) Performing simulations to test the validity of the theoretical model and the accuracy of the approximate theories.

The first liquids to be so analyzed were the so-called simple, atomic liquids [4]. Here, "simple" means that we are dealing with one-component systems, whose constituent particles are spherical in shape and interact by means of some radially symmetric, pairwise additive potential $V(r)$. "Atomic" means that the constituent particles are simple atoms, mostly the noble gases, which are generally accepted to interact by means of the Lennard-Jones potential. In other words, in atomic liquids the typical length scales of the particles involved are of the order of a few Ångstroms. On the other hand, a very large class of liquids we encounter in our everyday lives, which have great biological importance and vast industrial applications, are of a different kind: they are solutions or suspensions of solid particles of considerably larger than atomic size, containing additional constituents such as salt or polymeric coils. When the typical size of the dissolved particles ranges between 1 and 10^3 nm, one speaks about a colloidal suspension. In view of the richness and variety of the constituent particles, one calls such systems "complex fluids". It has been mainly during the last 20 years that the field of colloidal science has experienced a revival owing to the development of physical theories applicable to such systems which now play a complementary role to the more traditional approaches to these problems [12], the ones that come under the conventional characterization of "physical chemistry".

The above-mentioned progress was made mainly possible by the realization that, though complicated at first sight, complex liquids admit great simplification if one achieves to "trace out" the degrees of freedom associated with the smaller particles in the solution, to be left with an effective Hamiltonian that describes the interactions between the large particles as some kind of pseudo-one-component system. In this way, one can take advantage of the experience and the techniques accumulated from the theory of simple liquids, to examine the properties of their complex counterparts. As far as *static* properties of the system are concerned, one can then make predictions about the structure of the liquid, the influence of changing its chemistry and/or composition on its behavior and, finally, the possibility of phase transitions and the location of the associated phase boundaries as functions of some externally controlled thermodynamic parameters.

The purpose of this work is to offer a review on certain classes of complex liquids, where the program of constructing effective Hamiltonians has been carried out with success and also present the way in which one goes from these effective Hamiltonians to phase diagrams. We shall limit ourselves to suspensions of spherical particles only. The rest of this work is organized as follows: in Section 2 we present a more quantitative description of the field known as "soft matter", which is the topic of this paper, and a summary of the basic techniques which facilitate the quantitative analysis of soft matter systems from the point of view of a theoretical physicist. In the subsequent sections we proceed with a review of recent results on some typical soft matter systems: in Section 3 we discuss the properties of free polymer chains and the possibility to describe their behavior in terms of effective interactions. In Section 4 we turn to colloidal suspensions and present a range of recently developed notions and associated phenomena in such systems, stemming from the depletion interaction and the possibility of novel, isostructural transitions in the solid phase. In Section 5 we turn our attention to a hybrid system between polymer chains and colloidal suspensions, namely star-shaped polymers of uncharged chains and discuss their properties in terms of a recently developed effective Hamiltonian. In Section 6 we discuss current and future work on problems of increased complexity, including star polymer–colloid mixtures, star-shaped polyelectrolytes (the counterpart of star polymers when the constituent chains are charged) and columnar assemblies of DNA molecules. We summarize and conclude in Section 7.

2. Soft matter

In this section we present a general introduction to soft matter systems. At first, we describe the defining characteristics of such systems, set by the typical length scales of the constituent particles involved and then we give specific examples of soft matter mixtures from everyday life. We then proceed to justify the term "soft" by estimating typical shear moduli for such systems and comparing them with those of atomic compounds. We discuss the issue of stabilization of colloidal suspensions against coagulation and present the main mechanisms in which this stabilization is achieved. Subsequently, we give a precise, statistical–mechanical definition of the notion of the effective Hamiltonian for complex fluids and then we sketch the ways in which such an effective Hamiltonian can be used to derive information on the structural and thermodynamic properties of the system.

2.1. What is soft matter

The term *soft matter* describes a very large class of materials whose common characteristic is that they are composed of *mesoscopic* particles, i.e., particles with typical sizes 1 nm–1 μm, dispersed into a solvent whose molecules are much smaller in size (typically of atomic dimensions). In addition, soft matter systems may contain other, smaller unities such as short polymeric chains, salt dissociated into ions, etc. Other terms that are used as synonyms are *complex fluids* (though soft matter is not necessarily fluid) as well as *colloidal suspensions* or *colloidal dispersions*.[1] The term "colloid" derives from the Greek words *κόλλα* (glue) and *εΐδος* (kind). Its original meaning, "sticky stuff", coined in the 1860s by Thomas Graham, a pioneer in the field [12], reflects the fact that almost all of the compounds used as glues are indeed colloids.

Colloids are abundant in everyday experience. From mayonnaise to blood and from ink to smoke, soft matter is what we are made of and what we use in countless industrial applications in the chemical, pharmaceutical and food industries. Microemulsions as well as self-organized micelles of soap molecules in aqueous solutions also belong to the same category and are

---

[1] According to the definition of the International Union of Pure and Applied Chemistry, the term "colloid" describes supramolecular entities whose extension in *at least* one spatial direction lies between 1 nm and 1 μm. Hence, not only spherical but also ellipsoidal particles in solution, as well as platelets and rods in suspension can be classified as colloidal systems.

Table 1
The various types of colloidal dispersions with some common examples (Taken from Ref. [12].)

Disperse phase	Dispersion medium	Notation	Technical name	Examples
Solid	Gas	S/G	Aerosol	Smoke
Liquid	Gas	L/G	Aerosol	Hairspray, mist, fog
Solid	Liquid	S/L	Sol or dispersion	Printing ink, paint
Liquid	Liquid	L/L	Emulsion	Milk, mayonnaise
Gas	Liquid	G/L	Foam	Fire-extinguisher foam
Solid	Solid	S/S	Solid dispersion	Ruby glass; some alloys
Liquid	Solid	L/S	Solid emulsion	Road paving; ice cream
Gas	Solid	G/S	Solid foam	Insulating foam

sometimes referred to as *association colloids*. The macromolecules form the disperse phase and the solvent the dispersion medium. Both can be in any of the three states of matter, thus giving rise to a large variety of colloidal dispersions, see Table 1.

To offer a comprehensive review of the properties of this enormous variety of systems is well beyond the scope of this work and for such purposes we refer the reader to the literature [12–14]. We rather focus our attention on a particular type of soft matter systems, namely on solutions of spherical mesoscopic particles in liquid solvents and we review the progress that has been done in the understanding of their static structure and thermodynamics using the tools of statistical mechanics. The dispersed particles can be either solid particles, such as, e.g., polystyrene, polymethylmethacrylate (PMMA) or silica spheres, or "fractal" objects, such as polymer chains or stars. The spherical shape of the dissolved entities, even in an average sense, simplifies their study in terms of effective interactions, as symmetry dictates that these interactions must depend solely on the distance between the particles.[2]

The mesoscopic size of the constituent particles is the key in understanding the fact that such systems are indeed soft, i.e., they have a rigidity against mechanical deformations which is many orders of magnitude smaller than that of their atomic counterparts. To illustrate this point, let us consider a perfect crystal having lattice constant a, as shown in Fig. 1(a). This crystal is sheared by an external force with the result that every lattice plane is displaced parallel to itself by an amount x, with respect to the plane immediately below it, as shown in Fig. 1(b). Associated with this deformation is an energy per unit area $u(x)$ which, for small values of x, is a quadratic function of the deformation, as $x = 0$ is an equilibrium position. In a crystal, this energy depends on the direction of the applied shear and it is given in general by a relation of the form

$$u(x) = \frac{1}{2}\left(\frac{x}{a}\right)^2 G \, , \tag{2.1}$$

---

[2] We are assuming that the particles do not carry any additional, "internal" degrees of freedom, such as electric or magnetic moments.

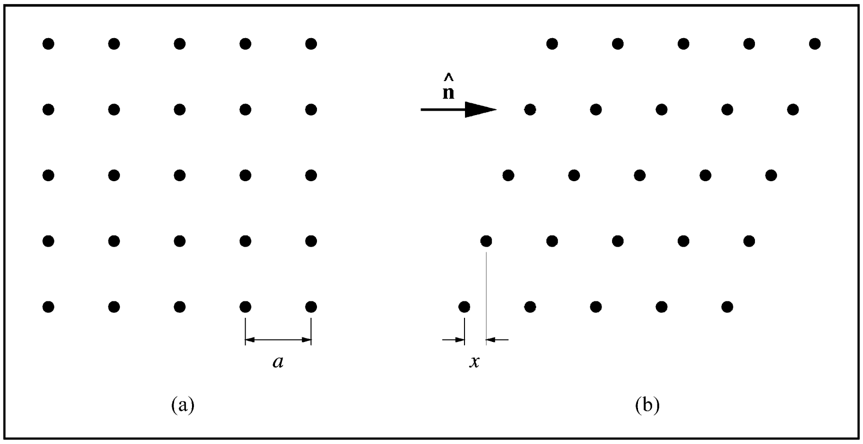

Fig. 1. Deformation of a crystal under shear: (a) undeformed crystal, (b) deformed crystal under a shear applied in the direction $\hat{\boldsymbol{n}}$.

where G stands for any one of the several elastic constants of the solid [15]. The shear stress σ is defined as the force per unit area of plane and per plane necessary to maintain such a deformation x. With Ω denoting the volume of the crystal, N the number of lattice planes and taking a cubic crystal for simplicity, this quantity will be given by

$$\sigma(x) = \frac{1}{NA}\frac{\mathrm{d}}{\mathrm{d}x}(\Omega u) = a\left(\frac{\mathrm{d}u}{\mathrm{d}x}\right) . \tag{2.2}$$

To roughly estimate the critical value σ_{c} of shear stress which is necessary to make a lattice plane slip, we set the maximum displacement x equal to $a/4$.[3] Then, Eqs. (2.1) and (2.2) give the result

$$\sigma_{\mathrm{c}} \approx \frac{\mathrm{d}}{\mathrm{d}x}\frac{1}{2}G\frac{x^2}{a}\bigg|_{x=a/4} = \frac{1}{4}G . \tag{2.3}$$

The elastic constants can be calculated within the framework of the theory of the harmonic crystal [15] and the expression giving these constants in terms of the microscopic interactions and the crystal structure is rather involved and we leave it for Appendix A. Assuming that the pairwise, spherically symmetric interaction between the particles is given by $\phi(r)$ and that only nearest-neighbor interactions are relevant, we show in Appendix A that in a simple cubic crystal the elastic constant c_{xxxx}, taken as representative for G, is given through the expression

$$c_{xxxx} = G = \frac{1}{v}a^2\phi''(r = a) , \tag{2.4}$$

where $v = a^3$ is the volume of the elementary unit cell and the double primes denote the second derivative. The length scale a is set by the interaction, so one can mimic a large class of interparticle

---

[3] Though, physically, the plane slips when $x = a/2$, for such large displacements the assumption that $\sigma(x)$ is a linear function of x breaks down and we have to limit this analysis to smaller x-values.

potentials for both atomic and colloidal systems by employing a parameter-dependent family of functions $\tilde{\phi}(x;\{\boldsymbol{p}\})$ with the set of parameters $\{\boldsymbol{p}\}$ as follows:

$$\phi(r) = \varepsilon\tilde{\phi}(r/a;\{\boldsymbol{p}\}) , \tag{2.5}$$

where ε is an energy scale of the order of the cohesive energy per particle. The values of the parameters $\{\boldsymbol{p}\}$ determine, e.g., the range of the potential or the relative extent of its repulsive and attractive parts. Typical values of these parameters for atomic and colloidal systems can be found in Ref. [16]. Eqs. (2.4) and (2.5) finally yield for the elastic constant the expression

$$G = \frac{1}{v}\varepsilon\tilde{\phi}''(1,\{\boldsymbol{p}\}) . \tag{2.6}$$

The energy scale ε for atomic systems, ranges from 10^{-1} eV for the noble gases to 10 eV for the alkali halides and the metals [15]. For typical colloidal crystals, ε ranges between $k_B T$ and $100k_B T$, where k_B is Boltzmann's constant and T is the absolute temperature. As $k_B T \cong 1/40\,\mathrm{eV}$ at room temperature, we conclude that the energy scales for atomic and colloidal systems are about the same. The family of functions $\tilde{\phi}(x,\{\boldsymbol{p}\})$ is rather insensitive to the set of parameters $\{\boldsymbol{p}\}$, hence a similar conclusion holds for the term $\tilde{\phi}''(1,\{\boldsymbol{p}\})$: for colloidal systems it can be only up to two orders of magnitude higher than for atomic systems [16]. Therefore, the major difference in the values of the elastic constants comes from the denominator in Eq. (2.6). As the typical length scales involved in colloidal crystals exceed those of their atomic counterparts by three to four orders of magnitude, the ratio between the elastic constants of colloidal and atomic systems is extremely small:

$$\frac{G_{\mathrm{colloidal}}}{G_{\mathrm{atomic}}} \approx 10^{-12}\text{–}10^{-9} . \tag{2.7}$$

Eqs. (2.3) and (2.7) show that there is an enormous difference in the critical stress required to cleave an atomic and a colloidal crystal. One can shear the latter by moving one's little finger but one needs to apply extreme shear stresses of the order of 10^{11} dyn/cm^2 in order to shear the former.[4]

The calculation above demonstrates the softness of colloidal solids, i.e., of a state of matter where the mesoscopic particles form a crystalline arrangement. There exist, of course, other states in which a soft matter system can be and in those cases the softness can be understood in terms of the very low densities of the colloidal particles or of the network-forming configuration of the supporting polymeric chains that hold the system mechanically together [17].

Colloidal suspensions have both experimental and theoretical advantages in comparison to their atomic counterparts. In atomic systems, the (effective) interactions between the particles are determined by their electronic structure and therefore cannot be influenced externally. As we will see in what follows, the situation for colloidal suspensions is different: a change in the quality of the solvent, in the temperature, in the salt concentration or in the chemistry of the mixture can bring

---

[4] This estimate of the critical shear stress of an atomic crystal is based on the assumption of a perfect lattice. In fact, lattice defects cause a reduction of this number by as much as four orders of magnitude [15] but the extreme difference between atomic and colloidal critical shears remains.

about spectacular changes in the effective interactions between the macromolecular aggregates, thus rendering these systems into a playground for statistical mechanics and phase transitions [18–20].

From the experimental point of view, the size of the colloidal particles, which is of the same order of magnitude as the wavelength of visible light, opens up the possibility of performing light scattering experiments to probe the static and dynamical behavior of colloidal suspensions, a technique which is much cheaper to perform than the traditional neutron scattering approaches. Moreover, direct observation of the particle motion in real space (video microscopy) is also possible, as a complementary approach to scattering, which works in wavevector space [21–24]. This is achieved usually by labeling the particles with an appropriate photosensitive dye [25,26]. Two common associated techniques are forced Rayleigh scattering (FRS) and fluorescence recovery after photobleaching (FRAP) [27]. In performing neutron scattering experiments, one can take advantage of the possibility of selectively substituting hydrogen atoms with deuterium ones in the particles and/or in the solvent, a technique known as deuteration [28]. As hydrogen and deuterium have identical electronic structures, and hence chemical properties, such a substitution does not alter the behavior of the system. However, neutrons and protons scatter neutrons differently and by selective substitution it is possible to match the scattering length density of a fraction of the particles with that of the solvent, which acts as a uniform background. In this way, only the selected fraction of the particles in the sea of the remaining ones is visible in a scattering experiment. This *labeling* technique has been successfully applied for many decades in polymer physics [28,29].

On the other hand, colloidal systems also have a disadvantage with respect to atomic ones: since they are usually man-made, one cannot avoid polydispersity in sizes [22] and/or charges [30], in the case when the particles carry a charge. The theoretical investigations of polydisperse systems are technically more complicated than those of monodisperse ones and are typically based on the assumption of a prescribed size distribution $p(R)$ or $p(Z)$, where R is the radius and Z the charge of the particles, respectively. A useful measure σ of the polydispersity is given by the relative root mean square of the radius [22]:

$$\sigma = \frac{\sqrt{\langle R^2 \rangle - \langle R \rangle^2}}{\langle R \rangle}\,, \tag{2.8}$$

where

$$\langle R^n \rangle = \int R^n p(R)\,\mathrm{d}R\,. \tag{2.9}$$

The minimum value of σ with the present technical capabilities is about 1% and in those cases it is reasonable to treat the system theoretically as monodisperse. The general effect of the polydispersity is to destroy order, i.e., to suppress crystallization of a putative monodisperse system at the same average density and temperature as the polydisperse one [22,31–33].

2.2. Stabilization of colloidal suspensions

Colloidal particles dispersed in a medium undergo constant Brownian motion due to their random collisions with the solvent molecules and have thermal (kinetic) energies of the order $k_B T$.

In the process of this motion, the particles may approach each other and then a mechanism should be in place to prevent them from forming lumps: a colloidal suspension should be stable against aggregation. The issue of stabilization is particularly important as there always exists an attractive force between the particles, which tends to bring them together, namely the van der Waals attraction. The latter (also called *dispersion* force) stems from the fact that a spontaneously forming electric dipole on one molecule induces on a neighboring molecule another dipole which tends to align itself with the former [34].

The van der Waals attraction between microscopic dipoles, separated by a distance r, scales as $-r^{-6}$ for intermediate and $-r^{-7}$ for large distances, due to retardation effects. If we consider two large spheres, each of radius R, separated by a center-to-center distance r, then the nonretarded van der Waals interaction energy between them is given by the expression [14,22]

$$V_{\mathrm{vdW}}(r) = -\frac{1}{6}A\left[\frac{2R^2}{r^2-4R^2} + \frac{2R^2}{r^2} + \ln\left(\frac{r^2-4R^2}{r^2}\right)\right], \tag{2.10}$$

where the *Hamaker constant* A accounts for material properties and depends on the polarizabilities of *both* the colloidal particles and the surrounding solvent. Typical values of this constant for substances immersed in water range from 30×10^{-20} J for metals to 3×10^{-20} J for oxides and halides to 0.3×10^{-20} J for hydrocarbons. The detailed calculation of Hamaker constants is a challenging task and for details we refer the reader to the literature [12,14]. However, for many practical purposes, the following crude estimate by Israelachvili [35] is sufficient:

$$A = \frac{3h\nu(n_1+n_2)^2(n_1-n_2)^2}{16\sqrt{2}(n_1^2+n_2^2)^{3/2}}, \tag{2.11}$$

where h is Planck's constant, ν is a characteristic frequency and n_1, n_2 are the optical refractive indices of the colloids and the solvent, respectively. By *index matching* the two materials, i.e., by choosing a solvent with $n_2 = n_1$ one can strongly suppress the van der Waals attraction. For unmatched materials, Eq. (2.10) shows that at close approaches, $r \approx 2R$, the van der Waals interaction diverges negatively as $-(r-2R)^{-1}$ and thus would inevitably lead to particle coagulation.[5] Overlaps between the colloids are forbidden by the Born repulsion and this is usually modeled as a hard sphere potential for separations $r < 2R$. One needs a stabilization mechanism to provide an additional repulsion which dominates over the dispersion force and keeps the particles apart. Index matching is, obviously, a rather restrictive (and not always possible) stabilization technique. The two common mechanisms are *charge stabilization* and *steric stabilization*.

2.2.1. Charge stabilization

The field of charge-stabilized colloidal suspensions and the associated "theory of electric double layers" [12] have a long history. We are going to present only a short description of the physics of electric double layers here, referring the reader to the article of Hansen and Löwen [36] for details and a review of recent developments.

---

[5] In reality, the strong Born repulsions between electrons as well as solvation forces associated with the finite size of the solvent molecules make the value of the van der Waals potential finite at contact but this is still many times larger than the thermal energy $k_{\mathrm{B}}T$, thus leading in general to *irreversible* aggregation.

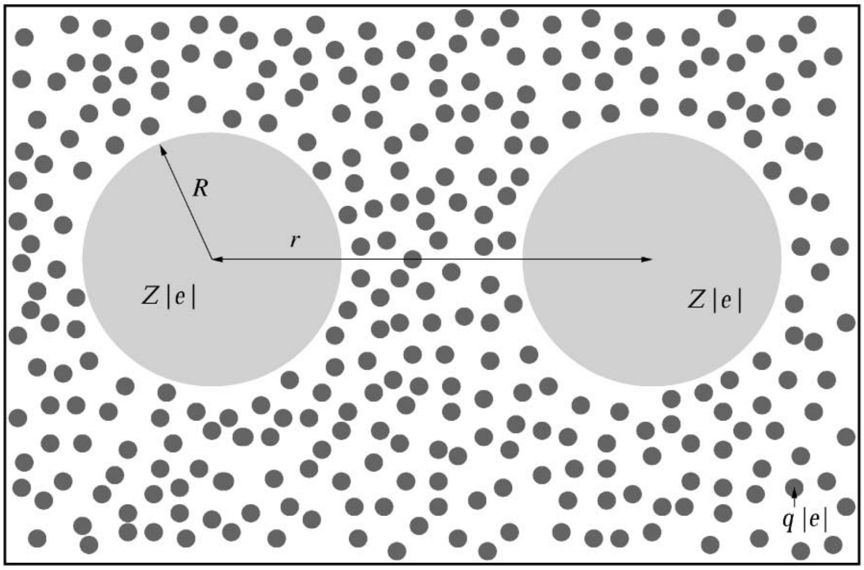

Fig. 2. Two large colloidal particles, each carrying a bare charge $Z|e|$ and having radius R, separated by a distance r in a charge-stabilized suspension. The small circles denote the counterions, each carrying a charge $q|e|$ of opposite sign. The molecules of the solvent are not shown because the latter is treated as a continuous medium.

We assume that each of the colloidal particles carries a *bare charge* $Z|e|$, where e denotes the electron charge. Then the Coulomb interaction between the polyions acts as a repulsive barrier against the dispersion attraction. Charging of the colloids takes place by charge dissociation on the surface of the particles which releases counterions into a polar solvent (such as water), each carrying a charge $q|e|$. Typically, $|Z|$ ranges between 100 and 10 000 and $|q| = 1$ or 2. In Fig. 2 we show a sketch of a charge-stabilized suspension with two colloidal particles, each of radius R and the free-moving counterions. Usually, the granular nature of the solvent is not manifestly taken into account; the solvent enters as a continuous medium having dielectric constant ε. Simulations taking explicitly into consideration the solvent granularity have been carried out recently by Allahyarov and Löwen [37], shedding light into a new host of interesting phenomena, such as hydration and depletion-like forces (see Section 4) between the polyions. However, we will not discuss these effects here, limiting ourselves to the basic "traditional" results instead.

The strong electric field generated by the bare charge of the colloidal particles attracts the free counterions, a fraction of which get absorbed or remain tightly bound to the surface of the colloids, forming a so-called Stern layer of condensed counterions. It is customary to treat the bound and free counterions separately. The effect of the bound counterions is to renormalize the charge of the colloids from its bare value Z into a new value Z^*, with $Z^* < Z$. The determination of Z^* as a function of Z and the thermodynamic parameters is a challenging theoretical task. The phenomenological approach is to consider Z^* as a free parameter adjusted to experimental data, such as scattering profiles determined by light scattering [38–41]. Early theoretical attempts to determine the renormalized charge Z^* were based on considering a single polyion within the cell model [42,43], whereas the effects of counterion correlations on Z^* have been studied by density functional methods and Monte-Carlo simulations [43,44]. The general trend is that $Z^* \to Z$ for low polyion charges, increases with Z but it *saturates* for high values of the bare charge, as a result of counterion condensation.

The remaining, free counterions in the solution screen the bare Coulomb repulsion between the charged colloids and reduce its range. A commonly used expression for the screened Coulomb repulsion is the Derjaguin–Landau–Verwey–Overbeek (DLVO) expression [45,46]:

$$V_{\mathrm{C}}(r) = \frac{(\tilde{Z}e)^2 \exp(-\kappa r)}{\varepsilon r}, \tag{2.12}$$

where $\tilde{Z}$ is a charge incorporating finite-size polyion effects and is given by

$$\tilde{Z} = Z^* \frac{\exp(\kappa R)}{1 + \kappa R} \tag{2.13}$$

and κ is the inverse Debye screening length:

$$\kappa = \sqrt{\frac{4\pi\rho_{\mathrm{c}}(qe)^2}{\varepsilon k_{\mathrm{B}} T}}, \tag{2.14}$$

where ρ_{c} denotes the density of the free counterions and q their valence. Due to charge neutrality, the density ρ of the colloidal particles is related to ρ_{c} via

$$Z^*\rho + q\rho_{\mathrm{c}} = 0. \tag{2.15}$$

Eqs. (2.14) and (2.15) above, hold for the case where the suspension contains no added salt.

The derivation of the screened potential, Eq. (2.12) above, is based on the Poisson–Boltzmann equation for the electrostatic potential [12] and depicts the charge of the macroions as screened by the surrounding counterion cloud. Its validity is limited to weakly screened suspensions, i.e., to dilute solutions. For condensed suspensions, many-body forces on the macroions, induced by the counterions, are expected to become relevant [47,48]. The modern derivations of the charge-stabilizing interactions between macroions include the application of liquid integral-equation theories [49–51], density-functional theory [48,52,53] and linear-response theory [54]. An important result of these modern approaches is that in some theories the inverse Debye screening length κ has to be redefined with respect to the value given by Eq. (2.14). In particular, Denton [54] showed that as the volume taken by the macroions is not accessible to the counterions, the parameter κ should be replaced in Eq. (2.12) by a new parameter, κ' defined as

$$\kappa' = \sqrt{\frac{4\pi\rho_{\mathrm{c}}(qe)^2}{(1-\eta)\varepsilon k_{\mathrm{B}} T}}, \tag{2.16}$$

where η is the fraction of the total volume occupied by the macroions.

In the presence of added salt, where additional counterions and coions form spontaneously into the mixture, the general expression (2.12) for the electrostatic potential between two charged colloids remains valid at low concentrations. However, the screening due to the additional ions has to be taken into account, resulting into an inverse Debye screening length which is enhanced.

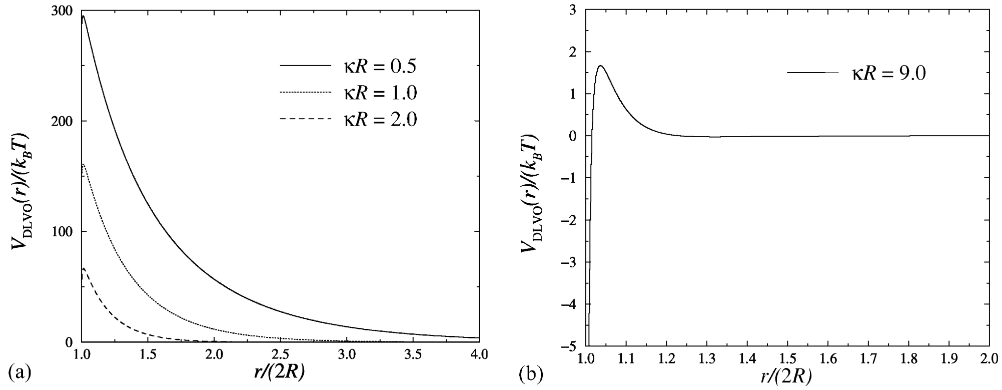

Fig. 3. The sum of the van der Waals potential of Eq. (2.10) and the screened Coulomb repulsion of Eq. (2.12) for realistic values of the parameters and for various degrees of screening. For the plots, we have chosen $A = 10^{-20}$ J; $\varepsilon = 80$; $R = 1$ μm; $Z^* = 1000$; $T = 300$ K. In (a) we show typical results for weak screening, where the electrostatic repulsion completely dominates the van der Waals attraction. In (b) the potential barrier is barely capable of keeping the particles apart. Notice also the very shallow secondary minimum of the potential at about $r/(2R) = 1.3$. The hard-sphere repulsion for $r < 2R$ is not shown.

Denoting by $q_{\pm}$ and $\rho_{\pm}$ the valences and densities of the two kinds of salt ions, we have [cf. Eq. (2.14)]

$$\kappa = \sqrt{\frac{4\pi}{\varepsilon k_B T}[\rho_c(qe)^2 + \rho_+(q_+e)^2 + \rho_-(q_-e)^2]}\ . \tag{2.17}$$

The electroneutrality condition now reads as [cf. Eq. (2.15)]

$$Z^*\rho + q\rho_c + q_+\rho_+ + q_-\rho_- = 0\ . \tag{2.18}$$

The screened Coulombic repulsion decays at the characteristic Debye length $\lambda_D = \kappa^{-1}$. The total interaction between charged colloids is the sum of the hard repulsion for $r < 2R$, the van der Waals attraction given by Eq. (2.10) and the repulsion given by Eq. (2.12) and is commonly known as the DLVO-potential:

$$V_{DLVO}(r) = \begin{cases} \infty & \text{if } r < 2R\ , \\ V_{vdW}(r) + V_C(r) & \text{if } r \geq 2R\ . \end{cases} \tag{2.19}$$

In Fig. 3(a) we show the DLVO potential for some typical values of the parameters at weak screening, where the Coulomb repulsion dominates over the van der Waals attraction and stabilizes the suspension. In Fig. 3(b) we show a marginal case, where the screening is strong and the height of the barrier against coagulation is less than $2k_BT$, barely preventing the particles from aggregating onto each other.

The DLVO interaction between colloids in charge-stabilized suspensions can be modified externally. The ways in which this can be achieved are listed below:

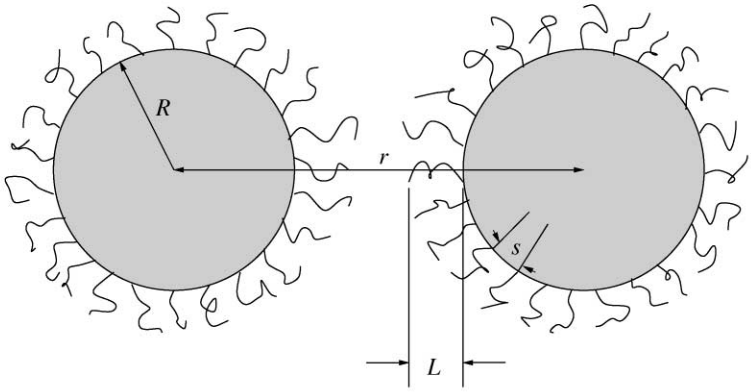

Fig. 4. Two sterically stabilized colloidal particles, each being covered with a polymeric brush whose height is L. The distance between neighboring anchored chains is denoted by s.

1. The solvent influence comes through its dielectric constant which affects both the dispersion term through the Hamaker constant and the electrostatic term. In this way, the strength of the attractive dispersion force can be tuned.
2. As shown in Fig. 3, by increasing the salt concentration one can decrease the range of the electrostatic term and make the interaction less repulsive. In fact, increasing the salt concentration can lead to a complete collapse of the stabilizing barrier thus causing irreversible aggregation [55]. The same effect is achieved by increasing the counterion valence.
3. Thermodynamic quantities, such as density and temperature also affect the interaction as they explicitly enter into the definition of the screening constant κ.

2.2.2. Steric stabilization

Another technique used to suppress the dispersion forces is steric stabilization. In this approach, every particle is covered with a brush of flexible polymers, as shown in Fig. 4. The chains can be either adsorbed on the surface or chemically attached to it. In a good solvent, the polymers are *self-avoiding*, i.e., there exists an excluded volume interaction between the monomers which prevents them from coming arbitrarily close to each other. It is this self-avoidance which brings about a repulsion between the coated spheres, as explained below.

Let us assume that the spatial extent of each brush is L when the spheres are isolated. When the center-to-center separation r between the coated spheres is larger than $2(R + L)$, the brushes do not overlap. However, as soon as the distance becomes smaller, the volume available to the chains of one particle is limited by the presence of the chains of the other: the self-avoidance acts as a mechanism which restricts the total volume available for the chains to fluctuate, as compared with the volume available when the two spheres are far apart. This is a typical example of *entropic* or *steric* repulsion which in this case acts as a barrier against the ubiquitous van der Waals attraction.

Although no general expression analogous to Eq. (2.12) exists for the steric repulsion, the latter has the following general characteristics which immediately point out to the ways in which it can be externally tuned. Some of these follow from the solubility properties of polymers, which will be discussed in more detail in Section 3.

1. The repulsion sets in for separations $r \leq 2L$. Hence, by changing the length of the chains (through, e.g., their degree of polymerization) one can externally adjust its range.
2. The strength of the repulsion grows with increasing grafting density, i.e., with decreasing distance s between neighboring anchored chains on the surface of the colloidal particles (see Fig. 4).
3. The effect of self-avoidance gets more pronounced as the solubility of polymer into the solvent improves. Hence, also the strength of the repulsion grows with increasing solvent quality. Given that for many polymers the quality of the solvent increases with increasing temperature, one can tune the height of the repulsive barrier by controlling the latter. In fact, by *reducing* the temperature one can turn the entropic repulsion into an attraction. This attraction, in turn, leads to aggregation of particles which, when it is caused by worsening of the solvent quality of the polymeric brush, is technically known under the name *critical flocculation* [12]. Measurements of the temperature at which critical flocculation occurs, for a number of sterically stabilized colloidal suspensions [56–59], reveal that the latter practically coincides with the characteristic Θ-temperature, which marks the border between a good- and a poor-quality solvent for the coating polymer (see Section 3).

Finally, it should be mentioned that combined mechanisms of charge and steric stabilization are also possible, such as, e.g., covering of the balls with flexible chains which carry a net charge, such as gelatin [60] or polyelectrolytes [61]. This opens up even more possibilities for external control of the interactions, as the amount of charge on the polyelectrolytes or polyampholytes is dependent on pH and ionic strength. Though the stabilizing effect of such a process is intuitively obvious, a theory of the effective interactions for these cases is still not fully developed. Sometimes it is possible to describe the stabilizing effect by a simple superposition of the electrostatic and steric forces [62], see also Section 6.3.

2.3. *The effective Hamiltonian*

In the examples mentioned in Section 2.2, a drastic simplification of the picture of a complex fluid was presented: instead of treating the full, many-component system, we talked about a one-component fluid involving the colloidal particles only. We introduced (albeit in a sketchy way) *effective interactions* between colloidal particles, which include not only the direct interactions between the colloids but the indirect effects of solvent, counterions, salt and grafted chains as well. The motivation for such a simplified or “effective” treatment of a complex fluid is twofold: it allows direct contact with experiments on the one hand and simplifies the theoretical approaches on the other.

In performing experiments with colloidal suspensions, one usually focuses attention on the static and dynamical properties of the large particles only. This can be achieved by matching the refractive indices or the neutron scattering length densities of the smaller entities and the solvent, so that only the large particles are visible. In other words, one looks at the system at length scales where *only* the large particles are visible and the rest plays the role of a background. The ensuing scattering profiles have to be then interpreted by means of an effective interaction between the colloids, which indirectly includes all the effects of the remaining constituents. As far as dynamics is concerned, the enormous discrepancy in sizes between the colloidal and the remaining entities causes a corresponding mismatch of the characteristic time scales for the motion of the components: the colloidal particles are much slower and one typically observes the system at time scales in which the rapid motion of the small degrees of freedom has been averaged out [23].

From the theoretical point of view, the large number and the large asymmetries between the species comprising the complex fluid, render a full theoretical treatment of the statistical–mechanical system as a mixture practically impossible. It is again desirable to devise an approximate effective Hamiltonian between the colloids and treat the remaining system as a one-component fluid. In what follows, we will define the notion of effective Hamiltonians precisely, using the tools of statistical mechanics.

2.3.1. Formal definitions

We start with the full description of a multicomponent system and reduce it to a one-component system by tracing out all the degrees of freedom but the ones we are interested in. In order to keep the discussion as simple as possible, we are going to assume that all components of the system are classical. The ideas to be presented below are also applicable if one or more components are quantal, only the corresponding statistics has to be modified. In charge-stabilized colloids, for example, both the polyions and the counterions can be treated as classical, whereas in deriving effective potentials between the ions in liquid metals a full, quantum-mechanical treatment of the electronic degrees of freedom is necessary [7,63].

Classical statistical mechanics in a ν-component system is applicable to component α ($\alpha = 1, 2, \ldots, \nu$) when the thermal de Broglie wavelength Λ_α associated with it is much smaller than the typical interparticle distances a in the many body system. Λ_α is defined as

$$\Lambda_\alpha = \sqrt{\frac{h^2}{2\pi m_\alpha k_B T}}\,, \tag{2.20}$$

where h is Planck's constant, m_α stands for the mass of a particle of the component α. Having in mind a colloidal dispersion at room temperature, containing mesoscopic particles and some smaller component such as counterions, for example, one can verify that the condition $\Lambda_\alpha \ll a$ is easily satisfied for both components and classical statistical mechanics applies.

Without loss of generality, we are now focusing on two types of particles only, $\alpha = 1, 2$. In what follows, we think of the first type of particles as the "large" and the second as the "small" and the goal is to eliminate the small ones from the picture. Let us assume that the system contains N_1 particles of component 1 and N_2 particles of component 2, enclosed in a macroscopic volume Ω and being at temperature T. The partial number densities of the two components are $\rho_{1,2} = N_{1,2}/\Omega$. The sets $\{\boldsymbol{R}_i\}$, $i = 1, 2, \ldots, N_1$ and $\{\boldsymbol{r}_j\}$, $j = 1, 2, \ldots, N_2$ denote the coordinates of the large and small particles, respectively, and the sets $\{\boldsymbol{P}_i\}$, $i = 1, 2, \ldots, N_1$ and $\{\boldsymbol{p}_j\}$, $j = 1, 2, \ldots, N_2$ their momenta. The starting point is the full, two-component Hamiltonian $\mathscr{H}$ of the system

$$\mathscr{H} = \mathscr{H}_{11} + \mathscr{H}_{22} + \mathscr{H}_{12}\,, \tag{2.21}$$

where $\mathscr{H}_{\alpha\beta}$ contains the interactions between species α and species β only. Assuming that all interactions are pairwise additive and radially symmetric, the three terms in Eq. (2.21) read as

$$\mathscr{H}_{11} = \sum_{i=1}^{N_1} \frac{\boldsymbol{P}_i^2}{2M} + \sum_{i=1}^{N_1} \sum_{j=i+1}^{N_1} v_{11}(|\boldsymbol{R}_i - \boldsymbol{R}_j|) , \tag{2.22}$$

$$\mathscr{H}_{22} = \sum_{i=1}^{N_2} \frac{\boldsymbol{p}_i^2}{2m} + \sum_{i=1}^{N_2} \sum_{j=i+1}^{N_2} v_{22}(|\boldsymbol{r}_i - \boldsymbol{r}_j|) \tag{2.23}$$

and

$$\mathscr{H}_{12} = \sum_{i=1}^{N_1} \sum_{j=1}^{N_2} v_{12}(|\boldsymbol{R}_i - \boldsymbol{r}_j|) . \tag{2.24}$$

In Eqs. (2.22)–(2.24) above, M and m stand for the masses of the large and small particles, respectively, and $v_{\alpha\beta}(r)$ denotes the potential energy between two particles of species α and β at center-to-center separation r. To facilitate the presentation, we also introduce the shorthand notation

$$V_{11}(\{\boldsymbol{R}\}) = \sum_{i=1}^{N_1} \sum_{j=i+1}^{N_1} v_{11}(|\boldsymbol{R}_i - \boldsymbol{R}_j|) , \tag{2.25}$$

$$V_{22}(\{\boldsymbol{r}\}) = \sum_{i=1}^{N_2} \sum_{j=i+1}^{N_2} v_{22}(|\boldsymbol{r}_i - \boldsymbol{r}_j|) \tag{2.26}$$

and

$$V_{12}(\{\boldsymbol{R}\},\{\boldsymbol{r}\}) = \sum_{i=1}^{N_1} \sum_{j=1}^{N_2} v_{12}(|\boldsymbol{R}_i - \boldsymbol{r}_j|) , \tag{2.27}$$

where $\{\boldsymbol{R}\}$ and $\{\boldsymbol{r}\}$ are shorthands for $\boldsymbol{R}_1, \boldsymbol{R}_2, \ldots, \boldsymbol{R}_{N_1}$ and $\boldsymbol{r}_1, \boldsymbol{r}_2, \ldots, \boldsymbol{r}_{N_2}$, respectively.

We work in the canonical ensemble.[6] The double trace over any quantity $\mathscr{O}$ that depends on all coordinates and momenta, is defined in this ensemble through the relation

$$\mathrm{Tr}_1\, \mathrm{Tr}_2[\mathscr{O}] = \frac{h^{-3N_1}}{N_1!} \frac{h^{-3N_2}}{N_2!} \int \mathrm{d}\boldsymbol{P}^{N_1} \int \mathrm{d}\boldsymbol{p}^{N_2} \int \mathrm{d}\boldsymbol{R}^{N_1} \int \mathrm{d}\boldsymbol{r}^{N_2}\, \mathscr{O}(\{\boldsymbol{P}\},\{\boldsymbol{p}\},\{\boldsymbol{R}\},\{\boldsymbol{r}\}) , \tag{2.28}$$

where Tr_i denotes the multiple integral over the positions and momenta of all degrees of freedom of the particles of species i ($i = 1,2$), the prefactor $h^{-3N_i}/N_i!$ being included. The canonical partition function $Q(N_1, N_2, \Omega, T)$ is the double trace of the Boltzmann factor $\exp(-\beta\mathscr{H}) = \exp[-\beta(\mathscr{H}_{11} + \mathscr{H}_{22} + \mathscr{H}_{12})]$:

$$\begin{aligned} Q(N_1, N_2, \Omega, T) &= \frac{h^{-3N_1}}{N_1!} \frac{h^{-3N_2}}{N_2!} \int \mathrm{d}\boldsymbol{P}^{N_1} \int \mathrm{d}\boldsymbol{p}^{N_2} \int \mathrm{d}\boldsymbol{R}^{N_1} \int \mathrm{d}\boldsymbol{r}^{N_2}\, \mathrm{e}^{-\beta(\mathscr{H}_{11} + \mathscr{H}_{22} + \mathscr{H}_{12})} \\ &= \frac{(\Omega\Lambda_1^{-3})^{N_1}}{N_1!} \frac{(\Omega\Lambda_2^{-3})^{N_2}}{N_2!} Z(N_1, N_2, \Omega, T) , \end{aligned} \tag{2.29}$$

---

[6] Sometimes it is useful to work in other ensembles, such as the semigrand ensemble, where the number of particles of the one component and the chemical potential of the other are fixed but this does not change any of the results as all ensembles are equivalent in the thermodynamic limit.

where $\beta = (k_B T)^{-1}$ is the inverse temperature. In Eq. (2.28), we have used the shorthand $\int \mathrm{d}\boldsymbol{R}^{N_1}$ to denote $\int\int \ldots \int \mathrm{d}\boldsymbol{R}_1\,\mathrm{d}\boldsymbol{R}_2 \ldots \mathrm{d}\boldsymbol{R}_{N_1}$ and similarly for the $\{\boldsymbol{r}\}$-coordinates and the momenta. The integrals over the coordinates are carried over the macroscopic volume Ω of the system. In the second line of Eq. (2.29) we have carried out the trivial integrations over the canonical momenta and we have defined the *configurational part* of the partition function, $Z(N_1, N_2, \Omega, T)$, which reads as

$$Z(N_1, N_2, \Omega, T) = \frac{1}{\Omega^{N_1}} \int \mathrm{d}\boldsymbol{R}^{N_1}\, \mathrm{e}^{-\beta V_{11}(\{\boldsymbol{R}\})} \frac{1}{\Omega^{N_2}} \int \mathrm{d}\boldsymbol{r}^{N_2}\, \mathrm{e}^{-\beta[V_{22}(\{\boldsymbol{r}\}) + V_{12}(\{\boldsymbol{R}\},\{\boldsymbol{r}\})]} \,. \tag{2.30}$$

For brevity, we drop the dependence of quantities on N_1, N_2, Ω and T from the argument list from now on. In taking the double trace of the Boltzmann factor, the order of tracing is immaterial. Hence, we can integrate out the small degrees of freedom first, keeping the coordinates of the large particles fixed at positions $(\boldsymbol{R}_1, \boldsymbol{R}_2, \ldots, \boldsymbol{R}_{N_1})$, thus obtaining a partial partition function $Q_2(\{\boldsymbol{R}\})$ as follows:

$$Q_2(\{\boldsymbol{R}\}) = \frac{(\Omega \Lambda_2^{-3})^{N_2}}{N_2!} \frac{1}{\Omega^{N_2}} \int \mathrm{d}\boldsymbol{r}^{N_2}\, \mathrm{e}^{-\beta[V_{22}(\{\boldsymbol{r}\}) + V_{12}(\{\boldsymbol{R}\},\{\boldsymbol{r}\})]} = \frac{(\Omega \Lambda_2^{-3})^{N_2}}{N_2!} Z_2(\{\boldsymbol{R}\}) \tag{2.31}$$

with the partial configurational part $Z_2(\{\boldsymbol{R}\})$. The physical meaning of the quantity $Q_2(\{\boldsymbol{R}\})$ is clear: it represents the partition function of the small particles in an external field generated by the large particles, whose positions are held fixed at $(\boldsymbol{R}_1, \boldsymbol{R}_2, \ldots, \boldsymbol{R}_{N_1})$. A comparison between Eqs. (2.29) and (2.31) shows that the partition function of the system can also be expressed as

$$Q = \mathrm{Tr}_1[\mathrm{e}^{-\beta \mathscr{H}_{11}} Q_2(\{\boldsymbol{R}\})] \,. \tag{2.32}$$

We now define the following *effective Hamiltonian*, $\mathscr{H}_{\mathrm{eff}}$ which depends on coordinates and momenta of the large particles only, as follows:

$$\mathscr{H}_{\mathrm{eff}} = \mathscr{H}_{11} - k_B T \ln Q_2(\{\boldsymbol{R}\}) \,. \tag{2.33}$$

It can be easily seen that an equivalent definition is

$$\exp(-\beta \mathscr{H}_{\mathrm{eff}}) = \mathrm{Tr}_2[\exp(-\beta \mathscr{H})] \,, \tag{2.34}$$

which brings forward the fact that $\mathscr{H}_{\mathrm{eff}}$ is a mixture between a pure Hamiltonian and a free energy of the small particles in the instantaneous environment of the large ones. By its construction, $\mathscr{H}_{\mathrm{eff}}$ guarantees that the partition function of the original, two-component system, coincides with the partition function of the new, effective one-component system, when the latter is expressed as $\mathrm{Tr}_1[\exp(-\beta \mathscr{H}_{\mathrm{eff}})]$. We have formally succeeded in reducing the original problem to a simpler one.

Apart from preserving the partition function (and hence the thermodynamics) of the system, the reduction to an effective Hamiltonian also preserves the expectation value $\langle \mathcal{O} \rangle$ of any operator $\mathcal{O}(\{\boldsymbol{P}\}, \{\boldsymbol{R}\})$ whose value depends on the momenta and coordinates of large particles only. To verify this property, we start from the definition of $\langle \mathcal{O} \rangle$ in the original system, carry out the trace over subsystem 2 first and end up with the expression of the average in the effective system, namely

$$\begin{aligned}\langle \mathcal{O} \rangle &= \frac{\mathrm{Tr}_1\, \mathrm{Tr}_2[\mathcal{O}(\{\boldsymbol{P}\}, \{\boldsymbol{R}\}) \exp(-\beta\mathcal{H})]}{\mathrm{Tr}_1\, \mathrm{Tr}_2[\exp(-\beta\mathcal{H})]} \\ &= \frac{\mathrm{Tr}_1[\mathcal{O}(\{\boldsymbol{P}\}, \{\boldsymbol{R}\}) \mathrm{Tr}_2[\exp(-\beta\mathcal{H})]]}{\mathrm{Tr}_1[\mathrm{Tr}_2[\exp(-\beta\mathcal{H})]]} \\ &= \frac{\mathrm{Tr}_1[\mathcal{O}(\{\boldsymbol{P}\}, \{\boldsymbol{R}\}) \exp(-\beta\mathcal{H}_{\mathrm{eff}})]}{\mathrm{Tr}_1[\exp(-\beta\mathcal{H}_{\mathrm{eff}})]} \,. \end{aligned} \tag{2.35}$$

In the second line above, we have used the fact that $\mathcal{O}$ does not depend on coordinates or momenta of the small particles and the third line follows from Eq. (2.34). As far as the properties of particles of type 1 are concerned, the description in terms of the effective Hamiltonian is completely equivalent to the original one and no information has been lost. The correlation functions involving only particles of species 1 are the same in both descriptions.

2.3.2. *Structure of the effective Hamiltonian*

The definition of the effective Hamiltonian given in Eq. (2.33) is exact; if the process of carrying out the partial trace over the small degrees of freedom could be carried out exactly, then the resulting $\mathcal{H}_{\mathrm{eff}}$ would contain no approximations. In practice, this is possible only in some special cases and one has to resort to approximate schemes to come up with a reasonable and manageable expression for this quantity. It is worth, therefore, looking into some of the characteristic properties of $\mathcal{H}_{\mathrm{eff}}$ in order to realize what problems we are faced with.

Starting with Eq. (2.33) and using Eq. (2.22) we see that the effective Hamiltonian reads as

$$\begin{aligned}\mathcal{H}_{\mathrm{eff}} &= \sum_{i=1}^{N_1} \frac{\boldsymbol{P}_i^2}{2M} + \sum_{i=1}^{N_1} \sum_{j=i+1}^{N_1} v_{11}(|\boldsymbol{R}_i - \boldsymbol{R}_j|) \\ &\quad + \tilde{V}(\{\boldsymbol{R}\}; N_1, N_2, \Omega, T) + k_{\mathrm{B}} T \Omega [\rho_2 \ln(\rho_2 \Lambda_2^3) - \rho_2] \end{aligned} \tag{2.36}$$

with

$$\begin{aligned}\tilde{V}(\{\boldsymbol{R}\}; N_1, N_2, \Omega, T) &= -k_{\mathrm{B}} T \ln\left\{\frac{1}{\Omega^{N_2}} \int \mathrm{d}\boldsymbol{r}^{N_2}\, \mathrm{e}^{-\beta[V_{22}(\{\boldsymbol{r}\}) + V_{12}(\{\boldsymbol{R}\}, \{\boldsymbol{r}\})]}\right\} \\ &= -k_{\mathrm{B}} T \ln Z_2(\{\boldsymbol{R}\}) \,. \end{aligned} \tag{2.37}$$

The last term in Eq. (2.36) above is the ideal gas contribution from the kinetic degrees of freedom of the second component, $F_{\mathrm{id}}^{(2)}$. The term $\tilde{V}$ includes all the nontrivial contributions arising from the interactions.

A formal diagrammatic expansion of the term $\ln Z_2(\{\boldsymbol{R}\})$, involving the Mayer bonds $f_{12}(|\boldsymbol{R}_i - \boldsymbol{r}_j|) = \exp[-\beta v_{12}(|\boldsymbol{R}_i - \boldsymbol{r}_j|)] - 1$ and $f_{22}(|\boldsymbol{r}_k - \boldsymbol{r}_l|) = \exp[-\beta v_{22}(|\boldsymbol{r}_k - \boldsymbol{r}_l|)] - 1$, has been recently developed by Dijkstra et al. [64–67]. The authors have shown that this expansion has the following structure: there is a term involving no coordinates of the large particles, and then a whole hierarchy of sums of terms, each term in the sum involving single coordinates, pairs, triplets and so on. In mathematical terms, the expansion has the form

$$-k_B T \ln Z_2(\{\boldsymbol{R}\}) = \tilde{V}_0 + \tilde{V}_1 + \tilde{V}_2 + \tilde{V}_3 + \cdots \,, \tag{2.38}$$

where

$$\tilde{V}_0 = \Omega \tilde{v}_0(\rho_1, \rho_2, T) \,, \tag{2.39}$$

$$\tilde{V}_1 = \sum_{i=1}^{N_1} \tilde{v}_1(\boldsymbol{R}_i;\, \rho_1,\, \rho_2, T) \,, \tag{2.40}$$

$$\tilde{V}_2 = \sum_{i=1}^{N_1} \sum_{j=i+1}^{N_1} \tilde{v}_2(|\boldsymbol{R}_i - \boldsymbol{R}_j|;\, \rho_1,\, \rho_2, T) \,, \tag{2.41}$$

$$\tilde{V}_3 = \sum_{i=1}^{N_1} \sum_{j=i+1}^{N_1} \sum_{k=j+1}^{N_1} \tilde{v}_3(|\boldsymbol{R}_i - \boldsymbol{R}_j|,\, |\boldsymbol{R}_j - \boldsymbol{R}_k|,\, |\boldsymbol{R}_k - \boldsymbol{R}_i|;\, \rho_1,\, \rho_2, T) \tag{2.42}$$

and so on. The functions $\tilde{v}_m$ represent m-body effective interactions between the particles. Note that, as all terms are a result of a canonical trace, they depend, in general, not only on the coordinates but on thermodynamic variables (densities and temperature) as well. It is precisely this dependence that allows us to "tune" the effective interactions by controlling some external parameter.

The extensitivity of the term $\tilde{V}_0$ follows from the requirement of extensitivity of the total free energy. Moreover, the term $\tilde{V}_1$ represents a sum of one-body potentials. However, the original problem has full translational symmetry which cannot be violated by the operation of taking a partial trace over the second component. As this term manifestly violates this symmetry, we conclude that it has to vanish:

$$\tilde{V}_1 = 0 \,. \tag{2.43}$$

The remaining terms are sums of pair-, triplet- and higher-order interactions. The terms $\tilde{V}_0$ and the kinetic contribution of the second component in Eq. (2.36) constitute the so-called *volume terms* F_0 of the effective Hamiltonian, with the terminology arising from their extensitivity:

$$\begin{aligned} F_0 &= k_B T \Omega[\rho_2 \ln(\rho_2 \Lambda_2^3) - \rho_2] + \Omega \tilde{v}_0(\rho_1,\, \rho_2, T) \\ &= \Omega f_0(\rho_1,\, \rho_2, T) \end{aligned} \tag{2.44}$$

with some function $f_0(\rho_1,\, \rho_2, T)$. The series of the remaining terms, $\tilde{V}_i$, $i = 2, 3, \ldots$ is usually truncated at second order, thus yielding a system interacting effectively in terms of pair potentials only. This constitutes the *pair-potential approximation.* There is very little evidence of a breakdown of the pair-potential approximation [22], though many-order effects may be "hidden" in parameters of the effective potential [68]. In general, problems with the pair-potential picture are to be expected at very high concentrations of macroparticles only.

The choice to trace out the small particles in favor of the large ones could have been reversed: nothing in the formalism prevents us from tracing out the large ones and ending up with an effective Hamiltonian for the small ones. However, as one has always to resort to approximations, it should be physically clear that the pair-potential approximation is a very poor one for the small particles in the presence of the large ones, whereas it can be remarkably accurate for the reverse case. This asymmetry, as well as need to make the connection with experiments where attention is focused on the statics and dynamics of the colloids, are the reasons for the usual practice to always attempt to trace out the small particles in favor of the big ones, not the other way around.

Gathering now the results for Eqs. (2.36)–(2.44) we find that *in the pair-potential approximation* the effective Hamiltonian reads as

$$\mathscr{H}_{\mathrm{eff}} = \sum_{i=1}^{N_1} \frac{\boldsymbol{P}_i^2}{2M} + \sum_{i=1}^{N_1} \sum_{j=i+1}^{N_1} V_{\mathrm{eff}}(|\boldsymbol{R}_i - \boldsymbol{R}_j|;\, \rho_1, \rho_2, T) + \Omega f_0(\rho_1, \rho_2, T)\,, \tag{2.45}$$

where the *effective interaction potential* V_{eff} is given by

$$V_{\mathrm{eff}}(r;\, \rho_1, \rho_2, T) = v_{11}(r) + \tilde{v}_2(r;\, \rho_1, \rho_2, T)\,, \tag{2.46}$$

i.e., it is a sum of direct interactions and those mediated by the small particles. It is precisely such an interaction that we have introduced in the preceding section in the form, e.g., of the DLVO potential, Eq. (2.19). We emphasize that, as manifestly seen in Eq. (2.45) above, the effective Hamiltonian, even in the pair potential approximation, is *not* just the sum of kinetic energy plus the effective interaction but it also includes the volume term $\Omega f_0(\rho_1, \rho_2, T)$.

2.3.3. Measuring the effective Hamiltonian

Up to this point, we have introduced the effective Hamiltonian as a theoretical concept which facilitates the analysis of a complex fluid, as it reduces the original, many-component problem to an effective single-component one. It is the task of the theorist to come up with reasonable approximations for the effective potential. The validity of such approximations has to be tested before they can be used to calculate the structure and thermodynamics of the effective one-component system. It is then important to know how the effective interactions can be measured, so that they can be compared with the theoretical results.

One possibility is to perform experiments in real systems. One usual experimental method is to measure the *force* between two colloidal particles using a surface force apparatus (SFA) [62,69,70] or atomic force microscopy (AFM) [71]. A different technique used is total internal reflection microscopy (TIRM) [72–75]. TIRM allows for the direct measurement of the probability $P(r)$ of finding two colloidal particles at distance r. As the latter is proportional to the Boltzmann factor $\mathrm{e}^{-\beta V_{\mathrm{eff}}(r)}$, TIRM offers a possibility to measure the effective interaction directly [76]. Nevertheless, neither force measurements nor TIRM offer a possibility to measure the volume term $\Omega f_0(\rho_1, \rho_2, T)$ in Eq. (2.45) above. Rather, they provide information on the effective potential $V_{\mathrm{eff}}(r)$ *only* [77].

A different approach is to perform standard Monte-Carlo (MC) or molecular dynamics (MD) simulations on model systems [10,11]. As is clear from its definition, Eq. (2.33), the effective Hamiltonian is the sum of the direct Hamiltonian $\mathscr{H}_{11}$ and the free energy of the small degrees of freedom in the external field generated by the large particles. It is a well-known fact that in a standard simulation only averages of operators can be calculated [11]; the calculation of a partition function, such as $Q_2(\{\boldsymbol{R}\})$, requires the use of special techniques, such as thermodynamic integration [77]. Hence, a straightforward simulation cannot yield the effective Hamiltonian directly. Instead, one resorts to the calculation of the force $\boldsymbol{F}_i$ acting on the macroparticle i, which is given by [77]

$$\boldsymbol{F}_i = -\nabla_{\boldsymbol{R}_i} \mathscr{H}_{\mathrm{eff}}(\{\boldsymbol{R}\})\,. \tag{2.47}$$

Using Eqs. (2.36) and (2.37) we find

$$\begin{aligned}\boldsymbol{F}_i &= \sum_{j\neq i}[-\nabla_{\boldsymbol{R}_i} v_{11}(|\boldsymbol{R}_j-\boldsymbol{R}_i|)]\\ &\quad+\frac{1}{Z_2(\{\boldsymbol{R}\})}\int \mathrm{d}\boldsymbol{r}^{N_2}[-\nabla_{\boldsymbol{R}_i} V_{12}(\{\boldsymbol{R}\},\{\boldsymbol{r}\})]\mathrm{e}^{-\beta[V_{22}(\{\boldsymbol{r}\})+V_{12}(\{\boldsymbol{R}\},\{\boldsymbol{r}\})]}\\ &= \sum_{j\neq i}[-\nabla_{\boldsymbol{R}_i} v_{11}(|\boldsymbol{R}_j-\boldsymbol{R}_i|)] + \langle -\nabla_{\boldsymbol{R}_i} V_{12}(\{\boldsymbol{R}\},\{\boldsymbol{r}\})\rangle_2\ ,\end{aligned} \tag{2.48}$$

which shows that the effective force is the sum of the direct force and the average over the small degrees of freedom of the forces exerted from the small particles to the large one, denoted by $\langle \dots \rangle_2$. This method has been applied recently by Jusufi et al. [77,78] for the calculation of the effective forces between star polymers (see Section 5). As simulations are suitable for calculations of statistical averages, the force can be measured in a straightforward way. We see that, once more, the volume terms cannot be measured in this way; their gradient with respect to any coordinate vanishes identically. Despite of the difficulties in calculating them, the volume terms cannot be ignored because they are important in the investigations of phase transitions, as we demonstrate in Section 2.5.

2.4. Structure and thermodynamics of one-component systems

In what follows, we present a summary of the quantities of interest that we wish to calculate with the help of the effective Hamiltonian given by Eq. (2.45). As we are now dealing with a single-component system, in what follows, we drop the superfluous subscript 1. The structural and thermodynamic properties of the effective one-component system follow by using the standard tools of statistical mechanics. We already introduced in Section 2.3 the canonical partition function Q of the system

$$Q = \mathrm{Tr}[\exp(-\beta\mathscr{H}_{\mathrm{eff}})]\ , \tag{2.49}$$

yielding the Helmholtz free energy F as

$$F = -k_{\mathrm{B}}T\ln Q\ . \tag{2.50}$$

The structure of the system is described by the expectation values of suitably defined operators, taken in a canonical way according to Eq. (2.35). Of particular importance are the one- and two-particle densities $\rho^{(1)}(\boldsymbol{r}) = \langle\hat{\rho}^{(1)}(\boldsymbol{r})\rangle$ and $\rho^{(2)}(\boldsymbol{r},\boldsymbol{r}') = \langle\hat{\rho}^{(2)}(\boldsymbol{r},\boldsymbol{r}')\rangle$, where the operators $\hat{\rho}^{(1)}(\boldsymbol{r})$ and $\hat{\rho}^{(2)}(\boldsymbol{r},\boldsymbol{r}')$ are defined as [79]

$$\hat{\rho}^{(1)}(\boldsymbol{r}) = \sum_{i=1}^{N}\delta(\boldsymbol{r}-\boldsymbol{R}_i) \tag{2.51}$$

and

$$\hat{\rho}^{(2)}(\boldsymbol{r},\boldsymbol{r}') = \sum_{i=1}^{N}\sum_{j=1}^{N}\delta(\boldsymbol{r}-\boldsymbol{R}_i)\delta(\boldsymbol{r}'-\boldsymbol{R}_j) - \sum_{i=1}^{N}\delta(\boldsymbol{r}-\boldsymbol{R}_i)\delta(\boldsymbol{r}'-\boldsymbol{R}_i)\ . \tag{2.52}$$

2.4.1. The fluid state

The translational invariance of $\mathscr{H}_{\mathrm{eff}}$ implies that the one-particle density of the system is a position-independent constant which is simply equal to the average particle density. In the absence of spontaneous symmetry breaking, the physical state of the system is also translationally invariant and we are dealing with a uniform fluid of density ρ:

$$\rho^{(1)}(\boldsymbol{r}) = \rho = \frac{N}{\Omega} \; . \tag{2.53}$$

Accordingly, in a fluid, the two-particle density depends only on the magnitude of the difference of its arguments:

$$\rho^{(2)}(\boldsymbol{r},\boldsymbol{r}') = \rho^{(2)}(|\boldsymbol{r}-\boldsymbol{r}'|) \; . \tag{2.54}$$

In the theory of classical fluids, a quantity of central importance for the investigation of the pair structure of the system is the radial distribution function $g(|\boldsymbol{r}-\boldsymbol{r}'|)$ defined through

$$\rho^{(2)}(|\boldsymbol{r}-\boldsymbol{r}'|) = \rho^2 g(|\boldsymbol{r}-\boldsymbol{r}'|) \; . \tag{2.55}$$

Physically, the quantity $\rho g(|\boldsymbol{r}-\boldsymbol{r}'|)$ is proportional to the conditional probability density of finding a particle at position $\boldsymbol{r}'$ given that another particle is located at position $\boldsymbol{r}$. The typical shape of $g(r)$ for a dense liquid is shown in Fig. 5(a).

Another important quantity is the structure factor $S(Q)$ of a fluid defined as a three-dimensional Fourier transform of the total correlation function $h(r) = g(r) - 1$:

$$S(Q) = 1 + \rho \int \mathrm{d}\boldsymbol{r}\, h(r) \mathrm{e}^{-\mathrm{i}\boldsymbol{Q}\cdot\boldsymbol{r}} \; , \tag{2.56}$$

which depends only on the magnitude Q of the wavevector $\boldsymbol{Q}$ since $h(r)$ is a radially symmetric function. A typical structure factor for a dense liquid is shown in Fig. 5(b). It can be shown [4] that the scattering intensity from a liquid sample at momentum transfer $\boldsymbol{Q}$ is proportional to $S(Q)$. This

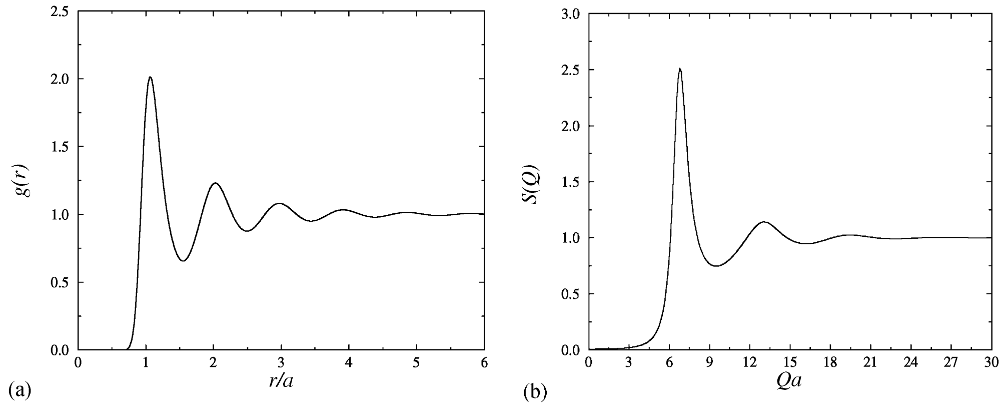

Fig. 5. Typical shapes of (a) the radial distribution function $g(r)$ and (b) the structure factor $S(Q)$ of a dense, classical liquid. The length scale a is set by the density, $a = \rho^{-1/3}$. Notice the successive coordination shells in real space (represented by the maxima of the radial distribution function), reflecting the short-range order of the fluid state.

makes the structure factor an important diagnostic tool for testing the accuracy of liquid-state theories, in which this quantity is usually calculated by means of some approximation.[7] Moreover, the quantity $S(Q)$ offers a path to thermodynamics, as its $Q = 0$ value is proportional to the isothermal compressibility χ_T of the system [4]:

$$S(0) = \rho k_{\mathrm{B}} T \chi_T \ . \tag{2.57}$$

For the theoretical approaches to the determination of the pair structure in the fluid state, one important function is the direct correlation function $c(r)$ connected to $h(r)$ through the *Ornstein–Zernike relation* which has the form

$$h(r) = c(r) + \rho \int \mathrm{d}\boldsymbol{r}'\, c(|\boldsymbol{r} - \boldsymbol{r}'|)h(r') \ . \tag{2.58}$$

The Ornstein–Zernike relation is exact. As it connects two unknown functions, one more relation or *closure* is needed in order to determine $g(r)$ and $c(r)$. Closures are approximate relations which arise from exact diagrammatic expansions of $g(r)$ in terms of $c(r)$ but with certain classes of diagrams ignored. The exact relation between $g(r)$ and $c(r)$ reads as [4]

$$g(r) = \exp[-\beta v(r) + g(r) - 1 - c(r) + B(r)] \ , \tag{2.59}$$

where $v(r)$ is the pair potential and $B(r)$ is the so-called *bridge function*, consisting of the sum of all elementary diagrams that are not nodal. The bridge function is of short range and rather insensitive to the detailed form of the pair potential [80]. All known closures can be thought of as approximate relations for the form of $B(r)$. Common closures are the Percus–Yevick (PY) and hypernetted chain (HNC) approximations [4]. In the PY closure, the approximation for $B(r)$ reads as

$$B_{\mathrm{PY}}(r) = -[g(r) - c(r)] + 1 + \ln[g(r) - c(r)] \quad (\mathrm{PY}) \ , \tag{2.60}$$

whereas in the HNC the approximation is made that the bridge function vanishes:

$$B_{\mathrm{HNC}}(r) = 0 \quad (\mathrm{HNC}) \ . \tag{2.61}$$

Eqs. (2.60) and (2.61) together with the exact relation (2.59) yield the common forms of the PY and HNC closures as

$$c(r) = g(r)[1 - \mathrm{e}^{\beta v(r)}] \quad (\mathrm{PY}) \tag{2.62}$$

and

$$g(r) = \mathrm{e}^{-\beta v(r) + h(r) - c(r)} \quad (\mathrm{HNC}) \ . \tag{2.63}$$

The Ornstein–Zernike relation, supplied with a closure, leads to the determination of the quantities $c(r)$, $g(r)$ and $S(Q)$ for a given interaction potential $v(r)$ and at given thermodynamic conditions, e.g.,

---

[7] The scattering intensity is directly proportional to $S(Q)$ only when we consider scattering from point particles. When we deal with large particles, such as colloids, then the form factor $P(Q)$ of the particle has to be taken into account and the scattering intensity is proportional to the *product* $P(Q)S(Q)$ [28], see also Section 5.

density and temperature. Various other quantities of interest, such as the pressure P or the energy U can be calculated as integrals involving the radial distribution function:

$$P = k_B T\rho - \frac{2\pi\rho^2}{3}\int_0^\infty r^3 v'(r) g(r)\,\mathrm{d}r \tag{2.64}$$

and

$$\frac{U}{N} = \frac{3k_B T}{2} + 2\pi\rho\int_0^\infty r^2 v(r) g(r)\,\mathrm{d}r\ , \tag{2.65}$$

where $v'(r) = \mathrm{d}v(r)/\mathrm{d}r$. The free energy F can then be determined by thermodynamic integration of P (the *pressure route*) or of U (the *energy route*) as given in Eqs. (2.64) and (2.65) above. A third possibility is to use Eq. (2.57) and the thermodynamic definition of the isothermal compressibility, $\chi_T = (\Omega\partial^2 F/\partial\Omega^2)^{-1}$. This constitutes the *compressibility route*. If the *exact* radial distribution function $g(r)$ were known, then all three routes would yield identical results for the free energy. Due to the approximations in constructing a closure, however, this is not the case: every route yields a different free energy curve. This is the problem of *thermodynamic inconsistency* of the closure [4].

The procedure to obtain the structure and thermodynamics of translationally invariant systems (liquids and gases) described above, is known under the name *integral equation theories* (IETs). For every possible closure, one has to solve two coupled integral equations. There is by now a large variety of closures in the literature and the accuracy of a given closure depends sometimes on the characteristics of the interaction potential. For example, the PY closure is known to yield very accurate results for short-range, hard interactions, whereas the HNC is accurate for long-range, soft potentials [81].

The problem of thermodynamic inconsistency mentioned above is usually addressed by modifying the integral equation through the inclusion in the closure of a function which contains one or more additional parameters [80–84]. These parameters are then tuned until thermodynamic consistency is achieved, obtaining in this way not only the thermodynamics but also the pair structure with high accuracy. A particularly simple closure which yields excellent results for purely repulsive potentials was introduced by Rogers and Young (RY) [81] and reads as

$$g(r) = \exp[-\beta v(r)]\left[1 + \frac{\exp[\gamma(r) f(r)] - 1}{f(r)}\right], \tag{2.66}$$

where

$$\gamma(r) = h(r) - c(r) \tag{2.67}$$

and the function $f(r)$ is chosen to have the form

$$f(r) = 1 - \exp(-\alpha r)\ . \tag{2.68}$$

Thermodynamic consistency is achieved by varying the parameter α. A comparison between Eqs. (2.66), (2.68) and (2.62), (2.63) shows that the RY closure reduces to the PY when $\alpha = 0$ and to the HNC when $\alpha = \infty$. We are going to make extensive use of the RY closure in the sections that follow, and in particular in Section 5.

2.4.2. The solid state

Translationally invariant phases are not the only possible states in many-body systems. Crystalline solids and the associated freezing transition are one of the oldest problems in condensed matter physics. In a solid, the one-particle density is not any more a position-independent constant ρ but a space-varying field $\rho(\boldsymbol{r})$, possessing the periodicity of the underlying crystal lattice. The broken-symmetry states do not arise spontaneously in a translationally invariant Hamiltonian; one has to either brake the symmetry by hand and calculate the free energy of various prescribed candidate crystal structures or, formally, apply an infinitesimal symmetry-breaking field and send its strength to zero *after* the thermodynamic limit has been taken.

In the early approaches to the fluid–solid transition, the latter was regarded upon as a *melting transition*, i.e., from the crystal as a reference point. The central idea is that the atoms sitting on the lattice sites of a crystal perform small oscillations around their equilibrium positions, with the amplitude of these oscillations growing as the melting line is approached. In 1910, Lindemann formulated his celebrated criterion [85], which states that a crystal melts when the ratio of the root-mean-square displacement of an atom around its equilibrium position to the nearest-neighbor distance reaches a quasi-universal value of about 10%. With the development of a microscopic understanding of the crystalline state and the associated theory of phonons, it became possible to calculate the free energy of a harmonic solid by means of a simple Einstein model [16] or more sophisticated, self-consistent phonon theories [86] which are capable of incorporating anharmonic effects.

The presumption behind this description is that the physical characteristics of the interparticle interaction enable a harmonic expansion of the local potential experienced by every particle in the lattice. This is feasible when the interaction is soft. The important exception is the hard-sphere interaction, which allows for no such expansion [87]. For such systems, a useful approach is to employ the so-called cell model [88–91], which exploits the picture of a particle in a solid as being confined in cells (cages) formed by the neighboring ones, from which it cannot escape. As the interaction is purely entropic in origin, the calculation of the free energy of a hard-sphere solid amounts then simply to the calculation of the free volume available to each particle in its own cage. Hence, theories of this kind are also known under the name "free volume theories".

The main criticism traditional theories of melting have received, is that they employ different approximations for the two associated phases (liquid and solid) and hence the errors done in the two are completely uncorrelated and can lead to serious inaccuracies in the determination of phase boundaries. A more satisfactory approach is one in which the fluid and the solid are treated on equal footing by means of a unified, underlying theory which views the solid as a spatially inhomogeneous fluid, possessing the periodically modulated density $\rho(\boldsymbol{r})$. In the last 20 years, spectacular progress has been made in understanding the freezing transition by the development of density functional theory (DFT) [79]. The basic theorem of DFT asserts that the free energy F of a spatially inhomogeneous system is a *unique functional* of the one-particle density, $F = F[\rho(\boldsymbol{r})]$. This approach uses the fluid as the state of reference and hence it can be seen as a theory of *freezing* of a liquid, rather than as a theory of melting of a solid. Under the conditions of fixed temperature, volume and number of particles, the equilibrium density of the system is given by the profile $\rho_0(\boldsymbol{r})$ which minimizes this functional, i.e.

$$\left.\frac{\delta F[\rho(\boldsymbol{r})]}{\delta\rho(\boldsymbol{r})}\right|_{\rho(\boldsymbol{r})=\rho_0(\boldsymbol{r})} = \mu\ , \tag{2.69}$$

where $\delta/\delta\rho(\boldsymbol{r})$ denotes a functional derivative with respect to the density and μ is the chemical potential, entering the formalism as a Lagrange multiplier in order to satisfy the constraint $\int \mathrm{d}\boldsymbol{r}\rho(\boldsymbol{r}) = N$. The functional $F = F[\rho(\boldsymbol{r})]$ splits into two terms, the ideal, entropic term $F_{\mathrm{id}}[\rho(\boldsymbol{r})]$, which is known exactly, and the excess term $F_{\mathrm{ex}}[\rho(\boldsymbol{r})]$, which arises from the interactions between the particles and whose form is not known:

$$\begin{aligned} F[\rho(\boldsymbol{r})] &= F_{\mathrm{id}}[\rho(\boldsymbol{r})] + F_{\mathrm{ex}}[\rho(\boldsymbol{r})] \\ &= k_{\mathrm{B}}T \int \mathrm{d}\boldsymbol{r}\rho(\boldsymbol{r})[\ln[\rho(\boldsymbol{r})\Lambda^3] - 1] + F_{\mathrm{ex}}[\rho(\boldsymbol{r})] \, . \end{aligned} \tag{2.70}$$

The challenge is to construct an accurate yet manageable approximation for the unknown functional $F_{\mathrm{ex}}[\rho(\boldsymbol{r})]$. Since the pioneering work of Ramakrishnan and Yussouff [92], enormous progress has been made in constructing such functionals, leading to quantitative predictions on freezing of a large variety of systems, ranging from the short-range hard-sphere liquid [93] to the long-range one-component plasma [94]. For recent reviews of the various schemes developed, we refer the reader to Refs. [18,95–97]. A major contribution in the field has also been the development and refinement in the last few years of the fundamental measure functional of Rosenfeld et al. [98,99], whose geometrical foundation allows for a broad range of applications in bulk and constrained systems, as well as in different spatial dimensions [98–101]. A pivotal idea in this approach is to fix the correct behavior of the approximate density functional in zero spatial dimensions, which is the limiting case for a particle confined in a cell of a densely packed solid. Similar considerations play an important role in the recent, generalized density functional theory of Khein and Ashcroft [102,103].

Density functional theory is particularly well suited for the study of freezing, as one can parametrize various different profiles, each possessing the symmetry of a chosen crystal structure, and minimize the functional $F[\rho(\boldsymbol{r})]$. The minimum value $F[\rho_0(\boldsymbol{r})]$ is then the free energy of the system possessing the symmetries dictated by the form of $\rho_0(\boldsymbol{r})$. Comparison of these minima among themselves and also with the free energy of the fluid yields the equilibrium configuration of the many-body system. In general, the free energy density $f(\rho) = F/\Omega$ is constructed as a function of the average density ρ for any phase, fluid or solid, and for the nonconvex segments of the curve the common-tangent construction [104] ensures the convexity of the reconstructed free energy and determines the coexistence densities across phase transitions.

2.5. The importance of the volume terms

The sum of the two volume terms, $F_{\mathrm{id}}^{(2)} = k_{\mathrm{B}}T\Omega[\rho_2 \ln(\rho_2\Lambda_2^3) - \rho_2]$ and $\tilde{V}_0 = \Omega\tilde{v}_0(\rho,\rho_2,T)$ in Eq. (2.44), enters the effective Hamiltonian in Eq. (2.45) in the form of an extensive contribution which is independent of the coordinates or momenta of the degrees of freedom. Though the term $F_{\mathrm{id}}^{(2)}$ is readily available, the calculation of the contribution $\tilde{V}_0$ is in general a challenging task. Dijkstra et al. have explicitly calculated this term for the case of hard-sphere mixtures [64,66] and for a model colloid–polymer mixture [67], by making use of the diagrammatic expansion mentioned in Section 2.3. For the case of charge-stabilized colloidal suspensions, $\tilde{V}_0$ has been evaluated within the framework of density functional theory by van Roij et al. [52,53] and within the linear-response approximation by Denton [54,105]. Graf and Löwen [106] have applied density functional perturbation theory to estimate the volume terms for model soft matter systems, including charge-stabilized colloidal suspensions with and without added salt and a bead-spring model for supramolecular aggregates.

The importance of these terms has been first discussed in general terms by Rowlinson [107] and their relevance in the context of charge colloids by Grimson et al. [108,109]. Barker et al. [110] have derived an approximation for these terms for mixtures of colloids and free, nonadsorbing polymers when the polymeric degrees of freedom are traced out, finding that they represent essentially the free energy of the homogeneous polymer solution. Ashcroft and Stroud [111] have pointed out the importance of the volume terms in the context of liquid metals. The lack of dependence of the volume terms on the coordinates and momenta of the large particles implies that the expectation value of any operator $\mathcal{O}$ depending on these coordinates is unaffected by their presence, as is clear from Eq. (2.35): the contributions from the volume terms cancel from the numerator and the denominator of the right-hand side. Yet, the volume terms do *not* represent an unimportant constant in the Hamiltonian, because they have a nonvanishing, density-dependent contribution to the total free energy of the system.

To illustrate this point, let us consider a reduced effective Hamiltonian, $\hat{\mathcal{H}}_{\text{eff}}$, featuring the same interactions as $\mathcal{H}_{\text{eff}}$ but lacking the volume terms, i.e.

$$\hat{\mathcal{H}}_{\text{eff}} = \mathcal{H}_{\text{eff}} - \Omega f_0(\rho, \rho_2, T) . \tag{2.71}$$

With $\hat{F}$ denoting the reduced Helmholtz free energy of the Hamiltonian $\hat{\mathcal{H}}_{\text{eff}}$, it follows from Eq. (2.71) that

$$F = \hat{F} + \Omega f_0(\rho, \rho_2, T) . \tag{2.72}$$

The contribution of the second term in Eq. (2.72) above is important in constructing phase boundaries between coexisting phases. The quantity of interest in this case is the free energy density $f = F/\Omega$ at fixed temperature, considered as a function of ρ. With $\hat{f} = \hat{F}/\Omega$, Eqs. (2.44) and (2.72) imply that

$$\begin{aligned} f(\rho) &= \hat{f}(\rho) + f_0(\rho, \rho_2, T) \\ &= \hat{f}(\rho) + k_B T[\rho_2 \ln(\rho_2 \Lambda_2^3) - \rho_2] + \tilde{v}_0(\rho, \rho_2, T) . \end{aligned} \tag{2.73}$$

The common tangent construction for the determination of the coexisting densities ρ_A and ρ_B between phases A and B amounts to equating the pressures and chemical potentials between the two phases, i.e., solving the coupled equations

$$\rho_A f'(\rho_A) - f(\rho_A) = \rho_B f'(\rho_B) - f(\rho_B) \tag{2.74}$$

and

$$f'(\rho_A) = f'(\rho_B) , \tag{2.75}$$

where the prime denotes the derivative with respect to density.

Ignoring the volume terms is equivalent to performing the common tangent construction not on the curves $f(\rho)$ but on the curves $\hat{f}(\rho)$, i.e., solving the above equations with $\hat{f}$ replacing f.

Before we proceed to a discussion of the consequences of such a substitution, let us distinguish two cases:

I. The partial densities ρ and ρ_2 are independent quantities. This is the case, for example, when one deals with mixtures of two neutral species. Then, the "kinetic" term $k_B T[\rho_2 \ln(\rho_2 \Lambda_2^3) - \rho_2]$ in Eq. (2.73) is irrelevant for the common tangent construction and only the "interaction" term $\tilde{v}_0(\rho, \rho_2, T)$ affects the phase boundaries, through its ρ-dependence. However, for this case, it has been shown [64–67] that $\tilde{v}_0(\rho, \rho_2, T)$ is a linear function of ρ, therefore it has no effect on the location of phase transitions, as is clear from Eqs. (2.73)–(2.75) above and only the total pressure of the mixture and the partial chemical potentials are shifted by constants.

II. The partial densities ρ and ρ_2 are coupled to each other by some kind of "conservation law". Such is, for example, the total electroneutrality condition in charge-stabilized suspensions, Eq. (2.15), with ρ_c playing the role of ρ_2. Then, this dependence of ρ_2 on ρ has to be taken explicitly into account in both the kinetic and the interaction terms in Eq. (2.73).

There are two famous cases in which the volume terms are a linear function of ρ: additive hard-sphere mixtures [64–66] and a nonadditive colloid–polymer mixture in which the polymers are modeled as spheres that do not interact among themselves but have a hard-sphere interaction with the colloids [67], see also Section 4. In dealing with case II above, there are no reasons to expect this linear dependence and hence the effects of the volume terms must be investigated.

We work at constant temperature, so we drop the explicit dependence of f_0 on T. Moreover, if we are dealing with case I, ρ_2 is irrelevant and we can also drop it. If we are dealing with case II, then we substitute explicitly the expression for ρ_2 in terms of ρ in the form of the function $f_0(\rho, \rho_2, T)$. In either case, we end up with a new function of a single variable, which we still call $f_0(\rho)$ for the sake of parsimony in notation. $f_0(\rho)$ includes all the effects of the volume terms and we have

$$f(\rho) = \hat{f}(\rho) + f_0(\rho) . \tag{2.76}$$

The quantities of interest are the second density derivatives $f''(\rho)$, $\hat{f}''(\rho)$ and $f_0''(\rho)$. We examine below in some detail the various effects the term $f_0(\rho)$ can have on the determination of phase boundaries, distinguishing between phases of the same or different symmetries.

(I) *Phases A and B have the same symmetry*: This case corresponds, for example, to the liquid–gas coexistence. A "van der Waals loop", i.e., a region where the quantity $f''(\rho)$ is negative signals an instability and therefore a phase transition. On the contrary, if $f''(\rho) > 0$ there is only one stable phase. A calculation of the reduced free energy density $\hat{f}(\rho)$ alone, without consideration of the volume terms, could lead to the *erroneous conclusion* that there are no phase transitions whereas in reality there are. This situation is depicted in Fig. 6(a). It occurs when $\hat{f}''(\rho) > 0$ but $f_0''(\rho) < 0$ in some region and at the same time $|f_0''(\rho)| > \hat{f}''(\rho)$, so that for their sum it holds $f''(\rho) < 0$ in some region. Thus, even if the effective potential is purely repulsive, leading to a convex reduced free energy density $\hat{f}(\rho)$, this does *not* exclude the possibility of liquid–gas coexistence. The volume terms may bring about a van der Waals loop. In fact, it was shown by van Roij et al. [52,53] that it is precisely the volume terms which can bring about a liquid–gas coexistence in charge-stabilized colloidal suspensions, although the effective, DLVO-interaction between the colloids is purely repulsive.

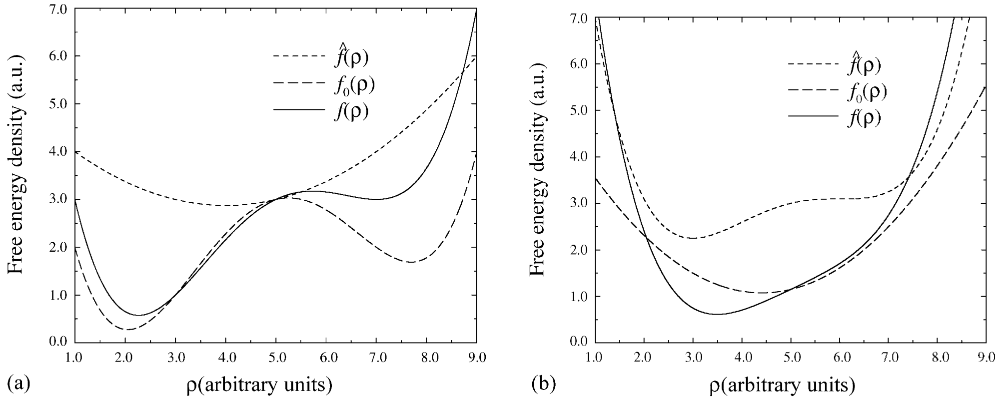

Fig. 6. The effect of the volume terms on the possibility of phase transitions between phases of the same symmetry. In (a), the volume terms act to bring about a phase transition, by inducing a region of negative curvature on the total free energy density curve, whereas the free energy density $\hat{f}(\rho)$ is a convex function of the density. In (b) the opposite happens.

The opposite situation is also possible, though we are not aware to-date of any physical system for which it materializes: we may have $\hat{f}''(\rho) < 0$ but $f_0''(\rho) > 0$ with $f_0''(\rho) > |\hat{f}''(\rho)|$, so that $f''(\rho) > 0$ everywhere. In this case, depicted in Fig. 6(b), the volume term acts to *extinguish* a pseudo-phase transition which occurs for the system interacting by means of $\hat{\mathscr{H}}_{\text{eff}}$. If both $\hat{f}''(\rho)$ and $f_0''(\rho)$ are positive, then no phase transitions are created or suppressed by the volume terms, although of course the values of thermodynamic quantities, such as pressure, chemical potential, energy, etc., are affected by their presence. If, finally, $\hat{f}''(\rho) < 0$ and $f_0''(\rho) < 0$ in some region, then the volume terms alter the coexistence densities of a phase transition already predicted on the basis of $\hat{f}(\rho)$ alone.

(II) *Phases A and B have different symmetries*: This is the relevant case for a liquid–solid transition or for structural phase transitions between crystals with different lattices. Let us consider again the reduced free energy density $\hat{f}(\rho)$, ignoring the volume terms for the moment, and let us also suppose that, on the basis of $\hat{f}(\rho)$ alone, a phase transition is taking place. In contrast to the previous case, the free energy density $\hat{f}(\rho)$ is not given by the same function for the two different phases. Rather, one has two different functions or branches for the free energy of each phase, $\hat{f}_{\text{l}}(\rho)$ for the liquid and $\hat{f}_{\text{s}}(\rho)$ for the solid, taking now the freezing transition as a concrete example. Freezing does not take place because a single free energy curve develops a van der Waals loop; both the liquid and the solid branch are convex functions of the density themselves. It rather occurs because the branches cross at some density $\hat{\rho}_*$, thus giving rise to the possibility of lowering of the total free energy through a phase separation into a liquid with density $\hat{\rho}_{\text{l}}$ and a solid with density $\hat{\rho}_{\text{s}}$, as shown in Fig. 7(a).

The volume term $f_0(\rho)$ is state-independent. The difference with the case of phases with same symmetry is that the volume term cannot extinguish a phase transition that is predicted on the basis of the system interacting by $\hat{\mathscr{H}}_{\text{eff}}$, even when $f_0''(\rho) > 0$. The total free energies $f_{\text{l}}(\rho)$ and $f_{\text{s}}(\rho)$ will still cross at the density $\rho_* = \hat{\rho}_*$, because the same term, $f_0(\rho)$, is added to both $\hat{f}_{\text{l}}(\rho)$ and $\hat{f}_{\text{s}}(\rho)$. However, as demonstrated in Fig. 7(b), the effect of the volume term now is to shrink the extent of the coexistence region, i.e., to make the difference $\rho_{\text{s}} - \rho_{\text{l}}$ smaller than $\hat{\rho}_{\text{s}} - \hat{\rho}_{\text{l}}$. This effect has been

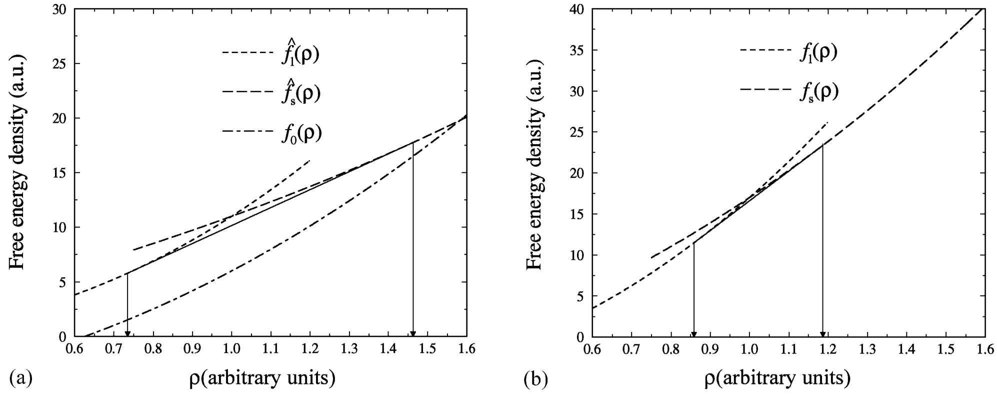

Fig. 7. The effect of the volume term on a phase transition between two phases of different symmetry. Here, we consider the case where a phase transition is predicted when the volume term is ignored and the latter has a positive curvature, $f_0''(\rho) > 0$. In (a), the thin solid line denotes the common tangent between the curves $\hat{f}_l(\rho)$ and $\hat{f}_s(\rho)$, yielding the coexistence densities $\hat{\rho}_l$ and $\hat{\rho}_s$ marked with the arrows. In (b), the volume term has been added and the common tangent construction (thin sold curve) has been performed on the curves $f_l(\rho)$ and $f_s(\rho)$. The coexistence region has shrunk with respect to the situation displayed in (a). In both cases, the free energy curves cross at the density $\hat{\rho}_* = \rho_* = 1.0$.

analyzed quantitatively for model systems by Graf and Löwen [106], in the framework of density functional perturbation theory. The opposite effect, i.e., an expansion of the coexistence region, is to be expected when $f_0''(\rho) < 0$.

Another interesting effect of the volume terms is the possibility to transform a thermodynamically metastable phase, nested between two stable states, into a stable one, by lowering its free energy appropriately. Denton and Löwen [112] have demonstrated that this mechanism is partly responsible for the stability of quasi-crystals in charge-stabilized colloidal mixtures containing additional salt as well as polymer coils.

2.6. Concluding remarks

The notion of the effective Hamiltonian, which we have presented in some detail in this section, is a commonly used tool in condensed matter physics [113]. Faced with the enormous complexity of real systems, which renders a truly microscopic treatment unmanageable, one usually has to resort to approaches in which the system is looked upon only above a certain length scale and all the degrees of freedom with typical length below this cutoff value drop out of sight. This reduction of degrees of freedom can be performed in a variety of ways. In the majority of cases, however, the functional form of an effective Hamiltonian involving the relevant degrees of freedom is simply *postulated* on symmetry grounds and the effect of the microscopic degrees of freedom is hidden in a small number of coupling constants [114]. A characteristic example of this procedure are the effective Hamiltonians usually employed in the study of ternary mixtures of oil, water and amphiphilic surfactants [115]. The enormous variety of phenomenology and degrees of self-organization of these systems makes, at present, a microscopic investigation of their properties impossible. Instead, one usually looks at coarse-grained quantities, such as the local density contrast between water and oil, constructing in this way Landau–Ginzburg-type theories for the fluctuating fields [115]. Alternatively, the fluctuating amphiphilic membrane separating oil- from water-rich regions can be considered as the relevant degree of freedom, thus leading to the introduction of geometrically based, Helfrich-type Hamiltonians [116,117]. Either way, the coupling constants appearing in the effective Hamiltonian are purely phenomenological in nature and the contact with the microscopic parameters of the constituting molecules is lost.

Though the effective Hamiltonian we have introduced in the context of colloidal suspensions is not a concept whose validity is limited to these, it differs from the phenomenological, effective Hamiltonians commonly encountered in condensed matter physics precisely in that the contact with the microscopic degrees of freedom is not completely broken. In some cases, in fact, it remains fully intact. In this way, we have the possibility to go all the way from microscopic interactions to macroscopic phase behavior and understand how the microscopic parameters of the system must be adjusted in order to influence the phase behavior of the system in a particular way. We will examine some characteristic cases in detail in the sections that follow.

3. Polymer chains

In this section we discuss the properties of solutions of polymer chains. We start with the scaling properties of a single chain and introduce the notion of quality of the solvent by considering the effective monomer–monomer interactions which formally result when the solvent degrees of freedom are traced out. Going from isolated chains to polymer solutions, we review the results from the Flory–Huggins and scaling theories, regarding the concentration dependence of thermodynamic quantities of polymer solutions. We then present an alternative way to look at solutions of free chains, in the spirit of the methods discussed in the preceding section. By tracing out the degrees of freedom of the constituent monomers, we end up with an effective interaction between the centers of mass of the chains, which has a Gaussian form. We discuss the structural and phase properties of this Gaussian core model as they are predicted from integral equation theories for the liquid and harmonic theory for the solid state.

3.1. Conformations of single chains

In Section 2 we mentioned that a common mechanism for the stabilization of colloidal suspensions is steric stabilization, whereupon every colloidal particle is covered with a polymeric brush. Moreover, in Sections 4 and 5 that follow, we are going to consider mixtures of colloids and polymers as well as solutions star-shaped polymeric entities, respectively, and examine their structural and phase behavior. It is, therefore, of major importance to become familiar with the properties of polymeric chains and their solutions, with the effects of solvent quality and with the concentration dependence of such systems. The purpose of this section is twofold: on the one hand, to introduce some basic concepts in polymer science and to summarize useful results concerning isolated polymers and polymer solutions, which will be used in later considerations. On the other, to present new ways to look at polymer solutions, in the spirit of introducing an effective Hamiltonian between the chains and employing subsequently the techniques described in Section 2.4.

Polymer chains are macromolecular entities, consisting of segments (monomers) attached sequentially to each other. The number of monomers in a chain, also called *degree of polymerization* will be denoted in this section by N. Though the chemistry of polymers does depend on the details of the electronic structure and bonding between the monomers, a wealth of other properties does not. One can look at the polymer chain at a variety of length scales. Below the monomer length or bond length a, which is typically of the order of a few Ångstroms, the details of the chemical structure of the polymer are indeed relevant. However, as the chain is looked upon at larger and larger length scales, a new picture emerges. Then, all polymers look like flexible strings, having an enormous number of possible conformations. This flexibility has its microscopic origin at the existence of various choices every monomer has to orient itself with respect to the preceding one in the chain sequence. Though these possible orientations are not all equally favorable energetically, thermal fluctuations constantly change the instantaneous orientations of successive monomers, thus giving rise to the flexibility of the chain.

The consequence is that, with increasing length scale upon which the chain is probed, and also with increasing degree of polymerization, all chains behave in the same way, i.e., a certain *universality* appears. A typical quantity which shows this universal behavior is, for example, the expectation value of the distance R between the two ends of the chain, and in particular its dependence on the degree of polymerization N. As we will see in what follows, this quantity scales as a power law of N, $R \sim N^{\nu}$, with the exponent ν being independent of the microscopic details of the chain.

When faced with phenomena exhibiting universality, we usually construct simple models to make a caricature of the system, which on the one hand capture the essential physics and on the other they hide as many of the irrelevant details as possible. To begin with, we can neglect all the details about the atoms forming the backbone of the chain and simply model them as point particles. $N + 1$ atoms are needed to construct a chain of N segments and their instantaneous configuration can be described by the array of position vectors $(\boldsymbol{r}_0, \boldsymbol{r}_1, \dots, \boldsymbol{r}_N)$, where $\boldsymbol{r}_i$ is the position vector of the ith atom in the sequence. From this array one can construct the array of bond vectors $(\boldsymbol{l}_1, \boldsymbol{l}_2, \dots, \boldsymbol{l}_N)$, where $\boldsymbol{l}_i = \boldsymbol{r}_{i+1} - \boldsymbol{r}_i$, as shown in Fig. 8. The end-to-end vector $\boldsymbol{R}$ is given by the relation

$$\boldsymbol{R} = \boldsymbol{r}_N - \boldsymbol{r}_0 = \sum_{i=1}^{N} \boldsymbol{l}_i \ . \tag{3.1}$$

The magnitude of the end-to-end vector $\boldsymbol{R}$ is one possible measure of the spatial extent of the chain; another quantity, which is also frequently used due to its direct connection with experimental results is the radius of gyration R_g. With $\boldsymbol{s}_i$ being the vector connecting the center of mass of the chain with particle i, the radius of gyration is defined as

$$R_g = \left[\frac{1}{N+1}\sum_{i=0}^{N} s_i^2\right]^{1/2} . \tag{3.2}$$

Defining the vector connecting atom i with atom j by $\boldsymbol{R}_{ij}$, taking into account that $\boldsymbol{R}_{ij} = \boldsymbol{s}_j - \boldsymbol{s}_i$ and using Lagrange's theorem, it follows that R_g can also be expressed as

$$R_g = \left[\frac{1}{(N+1)^2}\sum_{i=0}^{N}\sum_{j=i+1}^{N} R_{ij}^2\right]^{1/2} . \tag{3.3}$$

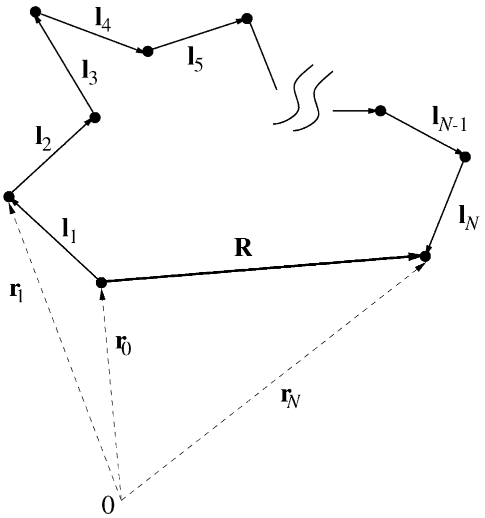

Fig. 8. A simple picture for the description of the conformations of a polymer chain. The filled circles denote the atoms, whose position vectors are $\boldsymbol{r}_i$. The bond vectors are $\boldsymbol{l}_i = \boldsymbol{r}_{i+1} - \boldsymbol{r}_i$ and $\boldsymbol{R}$ is the end-to-end vector.

The measured spatial extension of an isolated chain and its dependence on N is given by the theory as the expectation value over all possible conformations of the chain of the magnitude of the end-to-end distance or the radius of gyration. If we assume that all bond vectors have equal length a, then Eq. (3.1) implies

$$\langle R^2 \rangle = Na^2 + 2\sum_{i=1}^{N} \sum_{j=i+1}^{N} \langle \boldsymbol{l}_i \cdot \boldsymbol{l}_j \rangle \,, \tag{3.4}$$

where $\langle \dots \rangle$ denotes a statistical average.

The simplest picture of a flexible chain is provided by the random walk (RW). Here, one assumes that every bond vector $\boldsymbol{l}_i$ is uncorrelated in its motion with all other bond vectors. In this way, the inner product $\boldsymbol{l}_i \cdot \boldsymbol{l}_j$ in Eq. (3.4) above is uniformly distributed in the interval $[-a^2, a^2]$ and its expectation value vanishes. Hence, the expectation value of the magnitude of the end-to-end vector scales with the square root of N, i.e.

$$R_0 \equiv \sqrt{\langle R^2 \rangle} = aN^{1/2} \,. \tag{3.5}$$

The above result corresponds to the so-called *ideal* or *Gaussian* chain. The term "ideal" stems from the fact that real chains do not follow this rule; they are more extended that Eq. (3.5) predicts, i.e., the exponent ν of N has a value which is larger than 1/2. The value $\nu_G = 1/2$ for the N-exponent is likewise known as the Gaussian value.

It is possible to define a free energy associated with ideal chains, by making use of the central limit theorem. The end-to-end vector $\boldsymbol{R}$ is a sum of a very large number of random variables, hence it must follow a normal distribution, since the bond vectors are, for an ideal chain, independent.

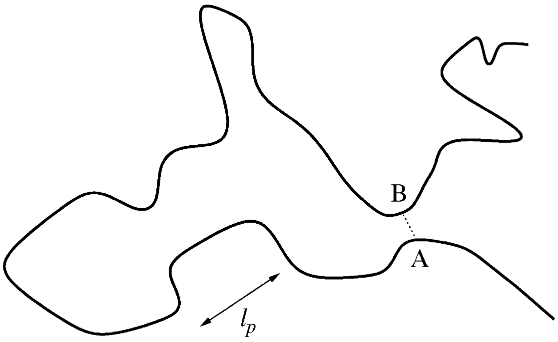

Fig. 9. An instantaneous conformation of a self-avoiding chain. The two monomers located at positions A and B experience a steric repulsion, denoted by the dotted line, and hence develop a correlation in their positions, although their separation along the chain is many times larger than the persistence length l_p.

This implies that the quantity $W_0(R)$, where $W_0(R)\,dR$ denotes the total number of ideal chains with end-to-end distances lying between R and $R + dR$, has the form [118]

$$W_0(R) \propto R^2 \exp\left(-\frac{3R^2}{2Na^2}\right). \tag{3.6}$$

The prefactor R^2 on the right-hand side of Eq. (3.6) above arises from geometry; the exponent can be identified with a Boltzmann factor, thus giving rise to an elastic free energy $F_0(R)$ of the ideal chain, which is entropic in nature and reads as [29]

$$F_{el}(R) = F(0) + \frac{3k_B T}{2}\frac{R^2}{Na^2}, \tag{3.7}$$

where $F(0)$ is an unimportant constant. The last equation allows for the interpretation of the ideal chain as an elastic spring with spring constant $k = 3k_B T/Na^2$.

The physical reason for the fact that the measured exponent ν in real polymers deviates from the Gaussian value $\nu_G = 1/2$ is that the RW-model (and all its refinements) fail to capture the fact that the chain cannot intersect itself, it is *self-avoiding*. The microscopic origin of the self-avoidance lies in the steric repulsions between the monomers which prohibit them from approaching arbitrarily close to one another. Though the steric forces are short-range in nature, they have a long-range effect along the chain, irrespective of the persistence length l_p.[8] No matter how far away from each other two monomers lie in the polymer sequence, once they approach each other the steric interactions enforce a correlation in their positions, as shown in Fig. 9. The excluded volume interaction between monomers, $v_{mm}(\boldsymbol{r}_n,\boldsymbol{r}_m)$ is usually approximated by a delta-function repulsion [120–122]:

$$v_{mm}(\boldsymbol{r}_n, \boldsymbol{r}_m) = v_0 k_B T \delta(\boldsymbol{r}_n - \boldsymbol{r}_m), \tag{3.8}$$

---

[8] The persistence length l_p is defined as the length along the chain in which orientational correlations among the monomers are lost [119].

where $\boldsymbol{r}_n$ denotes the position vector of the nth monomer along the chain and v_0 is the so-called *excluded volume parameter*.

A quantitative analysis of the excluded volume effects was first proposed by Flory [123,124]. The free energy of a self-avoiding polymer chain is taken to be given by the sum of the elastic free energy of Eq. (3.7) and an interaction free energy $F_{\mathrm{int}}(R)$ due to the excluded volume effects. Assuming a uniform distribution of monomers within the coil of radius R and neglecting correlations, the latter is estimated from Eq. (3.8) as [29,120]

$$F_{\mathrm{int}}(R) \cong v_0 k_{\mathrm{B}} T \frac{N^2}{2R^3} . \tag{3.9}$$

Adding the elastic and interaction free energies from Eqs. (3.7) and (3.9) and minimizing with respect to R, the size R_* of the chain is obtained as

$$R_* = (v_0 a^2)^{1/5} N^{3/5} \sim N^{3/5} , \tag{3.10}$$

yielding the Flory exponent $\nu_{\mathrm{F}} = 3/5$. A more detailed calculation can be performed on a lattice [118], yielding the quantity $W(R)$, which is the analog for the self-avoiding chain of the quantity $W_0(R)$ introduced above for the ideal chain. The result reads as [118]

$$\begin{aligned} W(R) &\propto R^2 \exp\left[-\left(\frac{3R^2}{2Na^2} + \frac{N^2 v_0}{2R^3} \right) \right] \\ &= R^2 \exp\left\{ -\frac{1}{k_{\mathrm{B}} T} [F_{\mathrm{el}}(R) + F_{\mathrm{int}}(R)] \right\} . \end{aligned} \tag{3.11}$$

Maximizing the exponent with respect to R is evidently equivalent with the previously mentioned minimization of $F_{\mathrm{el}}(R) + F_{\mathrm{int}}(R)$ and yields once more the result

$$R_* \sim N^{3/5} . \tag{3.12}$$

The last expression is the celebrated Flory result and demonstrates that the self-avoiding chain is indeed swollen with respect to the ideal one. The above argument can be generalized to d-dimensions and reads as

$$R_*^{d+2} \propto v_0 a^2 N^3 \tag{3.13}$$

with the corresponding Flory exponent $\nu_{\mathrm{F}}(d)$:

$$\nu_{\mathrm{F}}(d) = \frac{3}{d+2} . \tag{3.14}$$

Though simple in its formulation, the Flory theory captures the essential physics of the problem and yields quantitative results which are in excellent agreement with reality. Eq. (3.14) predicts the exact value $\nu_{\mathrm{F}} = 1$ for $d = 1$ and the value $\nu_{\mathrm{F}} = 3/5$ for $d = 3$ is in excellent agreement with the "exact" value 0.588 calculated through renormalization-group methods [125] and simulations [126]. Moreover, at $d = 4$ it returns the ideal value $\nu_{\mathrm{F}} = 1/2 = \nu_{\mathrm{G}}$, signaling the fact that above $d = 4$ the effects of self-avoidance are irrelevant and all chains become ideal, a result confirmed by using modern, renormalization-group techniques [127]. We will return to Flory theory in Section 5 in order to derive scaling laws for the size of star-shaped polymers.

In both the ideal and the self-avoiding chain the number of monomers N and the size R of the chain are connected by a power law of the form $N(R) \propto (R/a)^D$, where $D = D_G = 2$ for the Gaussian chain and $D = D_F = 5/3$ for the self-avoiding chain. This allows us to think of polymer chains as *fractal objects* whose fractal dimension is D [128]. The highest value D can take is the dimension d of the ambient space and this case corresponds to a compact object; the fact that $D_G > D_F$ means that the Gaussian chain is a "more compact" fractal object than the self-avoiding one, in agreement with the intuitive understanding that self-avoidance swells the chain. Finally, we remark that these scaling laws remain valid when the end-to-end distance of the chain is replaced by some other characteristic length which measures the macroscopic size of the chain, such as the radius of gyration R_g [see Eq. (3.3)]. As long as $R \gg a$, $R_g \gg a$ or, equivalently, $N \gg 1$, we obtain $N(R_g) \propto (R_g/a)^D$ with the *same* exponent D but with a different constant of proportionality. The fractal dimension of an object can also be measured in scattering experiments; it can be shown that at high values of the scattering vector Q, the scattering intensity $I(Q)$ from an object with fractal dimension D scales as [28,113]

$$I(Q) \sim Q^{-D} . \tag{3.15}$$

3.2. The effects of the solvent

Polymeric chains are always found in solution. However, in the preceding section, we considered the chain exclusively and the solvent was not taken into consideration. In what follows, we present a suitable modification of the previously introduced lattice model, to account for the solvent effects and introduce the notion of solvent quality [118].

The model is depicted in Fig. 10. Every lattice site can be occupied by a single molecule only, be it a monomer (black circles) or solvent molecule (white circles). In addition to the hard-core exclusion, there exist nearest-neighbor attractions, having the values $-\varepsilon_{mm}$, $-\varepsilon_{ms}$ and $-\varepsilon_{ss}$ between monomer–monomer, monomer–solvent and solvent–solvent molecules, respectively.[9]

Let $\tilde{W}(R)$ be the analog of $W(R)$ in the presence of interactions between solvent and monomer molecules. A mean-field calculation of this quantity is carried out in Ref. [118]. Here we only cite the final result which reads as

$$\begin{aligned}\tilde{W}(R) &\propto R^2 \exp\left[-\frac{3R^2}{2Na^2} - \frac{N^2 v_0}{2R^3}\left(1 - \frac{2z\Delta\varepsilon}{k_B T}\right)\right] \\ &= R^2 \exp\left[-\frac{3R^2}{2Na^2} - \frac{N^2 v_0}{2R^3}(1 - 2\chi)\right] ,\end{aligned} \tag{3.16}$$

where the parameter χ is defined as

$$\chi \equiv \frac{z\Delta\varepsilon}{k_B T} \tag{3.17}$$

---

[9] The parameters ε_{mm}, ε_{ms}, and ε_{ss} are all positive. The physical reason is that these interactions arise from the attractive dispersion force between the molecules.

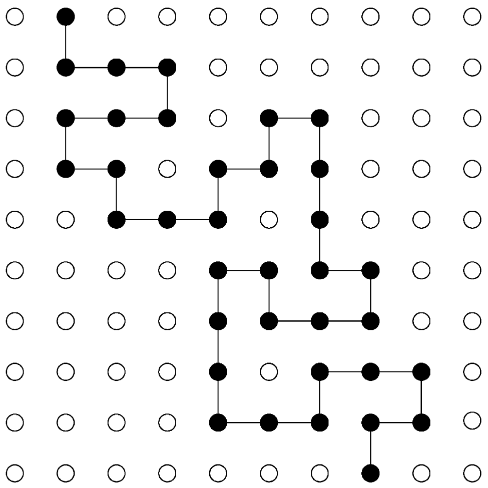

Fig. 10. A lattice model of a chain in a solvent. The monomers are denoted by the black circles and the solvent molecules by the white ones. For the sake of simplicity, these two species are taken to have the same size.

with z being the coordination number of the lattice and $\Delta\varepsilon$ being given by

$$\Delta\varepsilon = (\varepsilon_{\mathrm{mm}} + \varepsilon_{\mathrm{ss}})/2 - \varepsilon_{\mathrm{ms}} \; . \tag{3.18}$$

The ideas employed in the derivation of Eq. (3.16) above are the same with those presented in Section 2 in deriving an effective Hamiltonian: the degrees of freedom of one type of particles (the solvent molecules) are traced out and an effective Hamiltonian for the remaining ones (the monomers) is obtained, with coupling constants depending on some external parameters. A comparison between Eqs. (3.11) and (3.16) shows that the effect of the solvent is to bring about a renormalized, temperature-dependent excluded-volume parameter, $v(T)$, which replaces the bare parameter v_0:

$$v_0 \to v(T) = v_0(1 - 2\chi) \; . \tag{3.19}$$

The origin of the nearest-neighbor attractions modeled by the parameters $\varepsilon_{\mu\nu}$ ($\mu, \nu = \mathrm{m}, \mathrm{s}$), is usually the dispersion force between the molecules, hence these parameters are proportional to products of the atomic polarizabilities α_μ, α_ν, i.e., $\varepsilon_{\mathrm{mm}} = k\alpha_{\mathrm{p}}^2$, $\varepsilon_{\mathrm{ss}} = k\alpha_{\mathrm{s}}^2$ and $\varepsilon_{\mathrm{ms}} = k\alpha_{\mathrm{p}}\alpha_{\mathrm{s}}$, with some positive proportionality constant k. Substituting these expressions into the definition of the quantity $\Delta\varepsilon$, Eq. (3.18), we obtain

$$\Delta\varepsilon = \frac{k}{2}(\alpha_{\mathrm{p}} - \alpha_{\mathrm{s}})^2 > 0 \; , \tag{3.20}$$

which implies, through Eq. (3.17), that $\chi > 0$ as well. The effect of the solvent is, in general, to decrease the bare excluded volume parameter and to tend to bring the segments closer to each other. Whether this only effects the constant of proportionality in the Flory scaling law $R_* \sim N^{3/5}$

or changes the exponent itself, depends on the magnitude of χ. The latter can be externally controlled by changing the temperature. We examine the three distinct cases below:

1. *Good solvent*: This corresponds to the case $(1 - 2\chi) > 0$ or $\chi < 1/2$ and occurs physically for high temperatures. According to Eq. (3.19), in this case the renormalized excluded volume parameter $v(T)$ remains positive and the analysis of Section 3.1 carries over to the present case. The size of the chain still scales according to the law $R_* \sim N^{3/5}$. In the high-temperature regime, $k_B T \gg \Delta\varepsilon$, the solvent effects are in fact completely suppressed, the temperature plays no role and the solvent is called *athermal*.
2. *Poor solvent*: At sufficiently low temperature T, we reach the regime $(1 - 2\chi) < 0$ or $\chi > 1/2$. The excluded volume parameter becomes negative and the chain collapses into a compact coil, thus following the scaling law $R_* \sim N^{1/3}$. The monomers dislike the solvent molecules and try to stay as close as possible to each other, minimizing at the same time the interface with the solvent.
3. *Θ-solvent*: This is the intermediate case where $\chi = 1/2$ and the effective excluded volume interaction vanishes. The chain behaves macroscopically as ideal, following the scaling law $R_* \sim N^{1/2}$. The particular value of the temperature when this occurs is called the Θ-temperature T_Θ and is given, according to Eq. (3.17), by the expression

$$T_\Theta = \frac{2z\Delta\varepsilon}{k_B} . \tag{3.21}$$

In raising the temperature from values corresponding to a poor solvent to those corresponding to a good solvent, the chain undergoes swelling, changing its scaling behavior from $R_* \sim N^{1/3}$ at low T to $R_* \sim N^{3/5}$ at high T.[10] This is the so-called coil-to-globule transition, which has been observed experimentally [129]. For degrees of polymerization $N \sim 10^6$, a change of a few degrees in temperature can bring about a dramatic swelling in the size of the chain by almost two orders of magnitude.

The discussion presented above was formulated within the picture of a lattice model. In a good solvent, the net effect is that the excluded volume parameter gets renormalized but otherwise the scaling behavior of the chain remains intact: the scaling exponent of a chain is that of a self-avoiding random walk (SARW), which is $0.588 \approx 3/5$ in three dimensions. This universality is captured in a continuum version of the Hamiltonian which describes the conformation of a single chain, and is widely believed to be the correct starting point for the description of the excluded volume chain. The discrete nature of the segments is lost when the polymer looked upon at length scales $l > a$ and the self-avoidance is expressed by means of delta-like exclusions at contact between the chain segments [121,122]. Explicitly, the continuum Hamiltonian has the form [120,124]

$$\beta\mathscr{H}[\boldsymbol{r}_n] = \frac{3}{2a^2}\int_0^N \mathrm{d}n\left(\frac{\partial \boldsymbol{r}_n}{\partial n}\right)^2 + \frac{v(T)}{2}\int_0^N\int_0^N \mathrm{d}n\,\mathrm{d}m\,\delta(\boldsymbol{r}_n - \boldsymbol{r}_m) , \tag{3.22}$$

---

[10] The scaling $R_* \sim N^{1/3}$ in a poor solvent results into a fractal dimension $D = d = 3$ for the chain which, according to the discussion in Section 3.1, means that chains in poor solvents are compact.

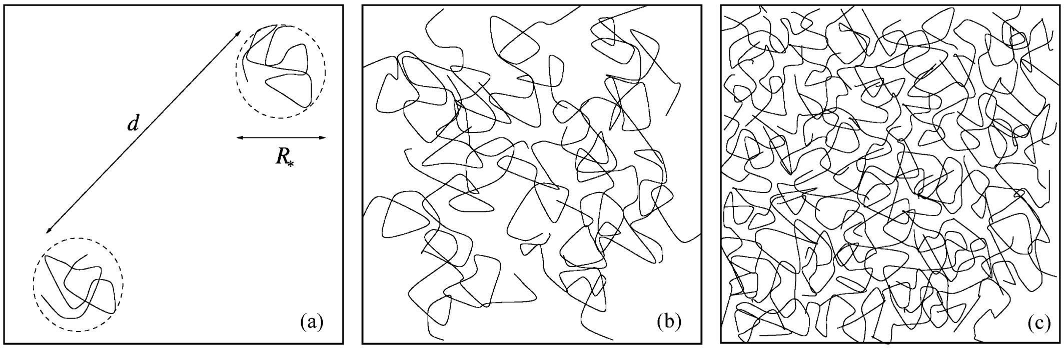

Fig. 11. The three concentration regimes for polymer solutions: (a) dilute, where the average separation d between the coils is much larger than the typical size R_* of the coil; (b) semidilute, above the overlap concentration c_*; (c) concentrated solution, above the concentration c_{**}.

where $\boldsymbol{r}_n$ denotes the position vector of the nth monomer in the chain and the index n is treated as a continuous variable. The first term in this Hamiltonian is the elastic contribution associated with the ideal chain alone and the second term encapsulates the excluded-volume interactions. In this formulation, the partition function Q of the chain is given by a functional integral of the Boltzmann factor over all possible conformations of the elastic string:

$$Q = \int \mathscr{D}\boldsymbol{r}_n \exp\{-\beta\mathscr{H}[\boldsymbol{r}_n]\}\ . \tag{3.23}$$

It has been shown [29] that this partition function scales with the degree of polymerization N for large N as

$$Q \propto \tau^N N^{\gamma-1}\ , \tag{3.24}$$

where $\gamma = 7/6$ is another universal exponent, whereas τ is a parameter whose value depends on the microscopic details of the chain. We will employ the continuum Hamiltonian in Section 3.4 in order to derive an effective interaction between polymer chains.

3.3. *Polymer solutions*

Up to this point, the discussion has been limited to the conformations of a single chain. We now introduce the notion of a polymer solution, containing many interacting chains. In dealing with polymer solutions, one usually distinguishes three concentration regimes, sketched in Fig. 11.

1. *Dilute solutions*: In this case, shown in Fig. 11(a), the average distance between chains is much larger than the spatial extension of a single chain.
2. *Semidilute solutions*: Here, the chains start overlapping thus giving rise to a picture similar to the one depicted in Fig. 11(b). The crossover between the dilute and semidilute regimes occurs at the *overlap concentration* of monomers c_*.

3. *Concentrated solutions*: Here, the chains form a dense intertwining net in which the individual character of every chain is lost, as shown in Fig. 11(c). The crossover between the semidilute and concentrated regimes occurs at the monomer concentration c_{**}.

In the dilute and semidilute regimes, there exist strong density fluctuations around the average values and hence strong correlations between the monomers. In the concentrated regime, the fluctuations are suppressed. The overlap monomer concentration c_* is estimated by setting the volume fraction occupied by the chains equal to unity. As the chain concentration is equal to c_*/N and the volume of each chain scales as $R_*^3 \cong a^3 N^{9/5}$, we obtain

$$c_* \cong a^{-3} N^{-4/5} , \tag{3.25}$$

which shows that for high degrees of polymerization c_* can be very low. For polystyrene of molecular weight 10^6, for example, c_* is already reached at a polymer weight fraction of 0.5%. The concentration c_{**} will be determined in Section 3.3.2. We now proceed with a review of the main results that have been established, regarding the structural and thermodynamic properties of polymer solutions.

3.3.1. Flory–Huggins theory

The lattice model presented in Section 3.2, regarding the conformations of a single chain in a solvent, can be generalized to the case of polymer solutions, giving rise to the so-called *Flory–Huggins theory* of solutions [124,130–132]. The Flory–Huggins theory is a mean-field-type theory which neglects correlations between neighboring segments and thus also carries the name *random phase approximation*. As in the dilute and semidilute regimes there exist strong density fluctuations, the Flory–Huggins theory does not yield quantitatively correct results there. However, it gives a correct prediction of the trends and qualitative characteristics of polymer solutions and, as many mean-field-type theories, can be a very useful tool in understanding the behavior of the system, due to its simplicity and transparency. Here, we only present a summary of the results of the Flory–Huggins theory; for the details of the derivation we refer the reader to Ref. [118].

The quantity of central interest is the mixing free energy per lattice site, f_{mix}, defined as the difference between the total free energy and the sum of the free energies of the pure solvent plus the that of the pure polymer melt. In the Flory–Huggins theory, f_{mix} reads as [118]

$$\beta f_{\mathrm{mix}}(\phi) = \chi\phi(1-\phi) + (1-\phi)\ln(1-\phi) + \frac{\phi}{N}\ln\phi , \tag{3.26}$$

where ϕ denotes the monomer volume fraction.

The various thermodynamic quantities of interest now follow from Eq. (3.26) above. Of particular importance is the osmotic pressure Π of the solution, i.e., the pressure difference which develops across a semipermeable membrane that allows the passage of solvent molecules but not polymers and which separates a solution from pure solvent. It can be shown [118] that Π is given by the relation

$$\Pi(\phi) = \frac{k_B T}{v_0}\left[\phi\frac{\partial f_{\text{mix}}(\phi)}{\partial\phi} - f_{\text{mix}}(\phi)\right] = \frac{k_B T}{v_0}\left[\frac{\phi}{N} - \ln(1-\phi) - \phi - \chi\phi^2\right], \tag{3.27}$$

where v_0 is the volume of the elementary cell of the lattice and can be identified with the bare excluded volume parameter. By expanding the logarithm, a virial expansion of the osmotic pressure in powers of the monomer concentration ϕ can be obtained, which reads as

$$\Pi(\phi) = \frac{k_B T}{v_0}\left[\frac{\phi}{N} + \left(\frac{1}{2} - \chi\right)\phi^2 + \frac{1}{3}\phi^3 + \cdots\right], \tag{3.28}$$

equivalently

$$\Pi(c) = k_B T\left(\frac{c}{N} + \frac{1}{2}vc^2 + \frac{1}{3}v_0^2 c^3 + \cdots\right), \tag{3.29}$$

where we have introduced the monomer concentration $c = \phi/v_0$ and also made use of Eq. (3.19) to replace χ by $v \equiv v(T)$. For very dilute solutions, Eq. (3.28) becomes

$$\Pi(c) \simeq k_B T\frac{c}{N}, \tag{3.30}$$

which represents van't Hoff's law for a dilute solution of *chains*, whose concentration is c/N. This expression for an "ideal osmotic pressure" holds at very low concentrations only; in comparing with the second term in the virial expansion, we find that c has to satisfy the relation

$$c \ll \frac{1}{vN}, \tag{3.31}$$

and the right-hand side becomes very small with increasing degree of polymerization. Another important consequence of Eq. (3.28) is that at the Θ-temperature, where $\chi = 1/2$ or $v = 0$, the quadratic term in the expansion of the osmotic pressure vanishes. Hence, we can identify the Θ-temperature with the temperature at which the second virial coefficient of the effective monomer–monomer interaction vanishes. This definition is used in experiments for the determination of the Θ-temperature of a polymer in a particular solvent.

In a good solvent, where $\chi < 1/2$, all terms in the virial expansion of the osmotic pressure have positive coefficients. However, in a poor solvent, where $\chi > 1/2$, the quadratic term in Eq. (3.28) has a negative coefficient and this is signaling a phase separation between polymer-rich and polymer-poor phases. This terminates at the critical point (ϕ_c, χ_c), whose coordinates are determined by the conditions

$$\left.\frac{\partial^2 f_{\text{mix}}}{\partial\phi^2}\right|_{(\phi_c,\chi_c)} = \left.\frac{\partial^3 f_{\text{mix}}}{\partial\phi^3}\right|_{(\phi_c,\chi_c)} = 0\,. \tag{3.32}$$

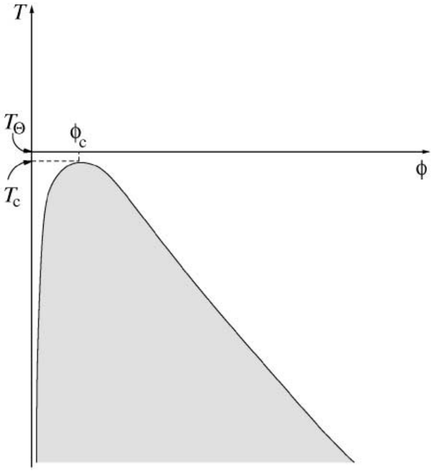

Fig. 12. Schematic phase diagram for a polymer solution. The shaded region denotes the region of two-phase coexistence.

At low temperatures, $\chi > \chi_c$, energy wins and we expect the solution to phase separate, whereas at high temperatures the entropy dominates and we are in a one-phase region. Combining conditions (3.32) with the Flory–Huggins expression (3.26), we obtain the critical parameters as

$$\phi_c = \frac{1}{1+\sqrt{N}}, \qquad \chi_c = \frac{1}{2}\left(1+\frac{1}{\sqrt{N}}\right)^2 . \tag{3.33}$$

Eqs. (3.33) above show that with increasing degree of polymerization, the critical concentration becomes smaller, approaching zero, and the critical temperature indexcritical(!) temperature approaches the Θ-temperature T_Θ from below. The phase diagram of a polymer solution is sketched in Fig. 12. Though the Flory–Huggins theory fails to capture the quantitative effects of concentration fluctuations, its predictions on the trends of ϕ_c and χ_c and their dependence on N are correct and have been experimentally confirmed [133].

3.3.2. Concentrated solutions

In concentrated solutions, three regimes can be distinguished in the structure of the segments:

(a) On the local scale, properties are nonuniversal as the detailed bonding chemistry matters.
(b) At intermediate distances, intrachain correlations dominate and the chain statistics is that of a self-avoiding chain.
(c) On a larger scale, a drastic simplification takes place because in concentrated solutions the density fluctuations are suppressed. Every macromolecule experiences the influence of a very large number of neighboring molecules in the solution and in this way inhomogeneities in the local concentration are smoothed out. Intra- and interchain correlations are equally important and the statistics of the chain becomes approximately Gaussian. This in turn means that mean-field theory becomes in this limit quantitatively correct.

The length scale at which a crossover between regimes (b) and (c) takes place is called the *density screening length* ξ. In very concentrated solutions or melts, ξ becomes microscopic (of the order of the segment length) and the random-phase approximation becomes useful in describing the solution in a wide range of length scales. Accordingly, significant progress can be achieved by employing the chain Hamiltonian of Eq. (3.22), generalizing it to a many-chain system and performing a perturbation expansion around a system of noninteracting chains. Though such an expansion does not converge for the case of an isolated chain, it turns out to be perfectly convergent for a concentrated solution. Here, we only present the basic results and refer the reader to Ref. [120] for details.

A first significant result is that the osmotic pressure Π of a solution, regarded as a function of the monomer concentration c is modified with respect to the simple virial expansion given by Eq. (3.28) into [134]

$$\Pi(c) = k_B T\left(\frac{c}{N} + \frac{1}{2}vc^2 - \frac{\sqrt{3}}{\pi}\frac{(vc)^{3/2}}{a^3}\right). \tag{3.34}$$

The last term represents a correction to the virial expansion and stems from chain connectivity. Intramolecular excluded volume does not contribute to the osmotic pressure and its contribution has to be taken away. Eq. (3.34) above allows us to estimate the concentration c_{**} at which the crossover between semidilute and concentrated domains occurs. The osmotic compressibility, $\partial\Pi/\partial c$, cannot be negative and this immediately implies that for the result to hold, we must have

$$vc \gtrsim \frac{v^{3/2}c^{1/2}}{a^3}, \quad \text{i.e.} \quad c_{**} \cong \frac{v}{a^6}\ . \tag{3.35}$$

In contrast with the overlap concentration c_* [cf. Eq. (3.25)], the concentration c_{**} does not depend on the degree of polymerization.

Another important effect of high polymer concentrations is that, in a good solvent, the chains are less extended than in low concentrations. In fact, at concentrated solutions, the size of the chains is given by a scaling law very similar to the ideal law, Eq. (3.5), namely

$$R_* \sim \xi^{1-1/2\nu} N^{1/2} \tag{3.36}$$

and not by the Flory result, Eq. (3.12). This was first put forward as a conjecture by Flory [123,124], a precise theoretical calculation deriving this result was later developed by Edwards [135,136] and the general aspect of this theoretical prediction was confirmed by neutron scattering experiments of labeled polymers [137]. The physical idea behind this fact is simple: the swelling of the chain with respect to its ideal size is caused by excluded volume interactions which tend to lower the local monomer concentration. However, in a concentrated solution, swelling is not an effective mechanism any more. The whole volume is saturated with polymer and if an individual chain spreads out it will meet there the segments of the neighboring chains. This mechanism is called *screening* of the excluded volume interactions by the concentration. In Section 5 we will present experimental evidence for the shrinking of polymeric entities above the overlap concentration in the context of star polymer solutions.

3.3.3. Scaling theory

In the preceding sections, we have already encountered the problems and limitations of the conventional, mean-field-type theories. They yield qualitatively correct results but they fail to take into account anomalous dimensions, connectivity effects, etc. Moreover, we have seen that the chains have fundamentally different behavior in dilute and in concentrated solutions, hence a unified picture which would smoothly bridge between these two extremes is of great use. Finally, we note that the correct concentration scaling of thermodynamic quantities of a polymer solution, such as the osmotic pressure, is very important in deriving quantitatively reliable results for effective interactions between star polymers, as will be demonstrated in Section 5.

An elegant framework, which unifies the results and leads to new, powerful predictions about the behavior of polymer solutions is provided by *scaling theory* which owes its development to de Gennes [29]. Scaling theory is a combination of dimensional analysis, known facts about different scaling regimes and pure physical argumentation [134]. In what follows, we present two of the major results of scaling theory, regarding the concentration dependence of the osmotic pressure and the size of a polymer chain, always in a good solvent.

The basic idea of scaling theory goes back to the fact that, for long chains, there is some arbitrariness in choosing what we consider as a "monomer segment". By grouping segments together and redefining a new monomer length in a suitable way, many properties of the chain remain invariant. If we group λ monomers together, forming a chain with $N' = N/\lambda$ segments and at the same time rescale the monomer length by a factor λ^{ν}, so that the new monomer length is $a' = \lambda^{\nu} a$, then Eqs. (3.5) and (3.12) show that the sizes of the ideal and self-avoiding chain remain invariant with the choices $\nu = \nu_G = 1/2$ for the ideal and $\nu = \nu_F = 3/5$ for the self-avoiding chain, respectively. Expressing this in mathematical terms, first we introduce the transformations

$$N \to \lambda^{-1} N \quad \text{and} \quad a \to \lambda^{\nu} a \tag{3.37}$$

and then require that certain physical quantities, mathematically expressed through the function $\mathscr{F}$ below, must remain invariant under transformation (3.37) above, satisfying thus the equation

$$\mathscr{F}(N, a; \{\boldsymbol{p}\}) = \mathscr{F}(\lambda^{-1} N, \lambda^{\nu} a; \{\boldsymbol{p}'\}) . \tag{3.38}$$

Here $\mathscr{F}$ is some function and $\{\boldsymbol{p}\}$ is a set of additional parameters on which the physical quantity may depend and which also change under transformation (3.37) into the new set $\{\boldsymbol{p}'\}$.

We first consider the osmotic pressure Π in a semidilute solution of concentration c. On dimensional grounds, Π has to have the form

$$\Pi = c k_B T f(ca^3, N) \tag{3.39}$$

where f is some dimensionless function. Under transformation (3.37) the concentration changes as

$$c \to \lambda^{-1} c \tag{3.40}$$

and Eqs. (3.38) and (3.39) imply that the function f satisfies the relationship

$$f(ca^3, N) = \lambda^{-1} f(\lambda^{3\nu - 1} ca^3, \lambda^{-1} N) \tag{3.41}$$

for arbitrary λ. By choosing $\lambda = N$ we conclude that the function f depends only on the combination $ca^3N^{3\nu-1}$ and can be written as

$$f(ca^3, N) = \frac{1}{N}\hat{f}(ca^3N^{3\nu-1}) . \tag{3.42}$$

Combining Eqs. (3.39) and (3.42) and introducing the overlap concentration $c_* = a^{-3}N^{1-3\nu}$ [Eq. (3.25)] we finally obtain for the osmotic pressure:

$$\Pi(c) = \frac{c}{N}k_B T\hat{f}\left(\frac{c}{c_*}\right) . \tag{3.43}$$

Eq. (3.43) above holds for both the dilute and the semidilute regimes ($c < c_{**}$), where the details of the interactions are irrelevant. By requiring that this equation reproduces van't Hoff's law at the dilute limit, we first conclude that the scaling function $\hat{f}(x)$ must approach unity for small values of its argument. If we now go to the semidilute regime, we can invoke the *physical* argument that the osmotic pressure in that regime must be independent of the degree of polymerization N. This becomes clear if we consider the entangled state shown in Fig. 11(b) and imagine that we cut each chain in two halves. This imposes the constraint that all N-dependence must vanish from the right-hand side of Eq. (3.42) with the implication that $\hat{f}(x)$ must be a power law of its argument, $\hat{f}(x) \sim x^{\alpha}$, and $\alpha = (3\nu - 1)^{-1}$. Combining the last result with Eq. (3.43) we find *in the semidilute regime*:

$$\Pi(c) \sim \frac{c}{N}k_B T\left(\frac{c}{c_*}\right)^{1/(3\nu-1)} \propto c^{9/4} . \tag{3.44}$$

Thus, scaling theory makes the prediction that the scaling of the osmotic pressure with the concentration in the semidilute regime has the nontrivial exponent $3\nu/(3\nu - 1) = 9/4$ and *not* the classical exponent 2 which is predicted on the basis of the virial expansion in the Flory–Huggins theory, Eq. (3.28). This $\Pi(c) \sim c^{9/4}$ concentration dependence has also been confirmed by experiments [138].

The size of the polymer scales with $N^{3/5}$ in the dilute solution, $c < c_*$, but only with $N^{1/2}$ in the concentrated solution, $c \gg c_*$. Scaling theory can be used to determine the crossover between these two regimes. Repeating the argument used for the osmotic pressure above, we find that the size of the polymer, $R_*(c)$, must be given by an expression of the form

$$R_*(c) = R_*\tilde{f}\left(\frac{c}{c_*}\right) , \tag{3.45}$$

where $R_* \propto aN^{3/5}$ is the size of the isolated chain. Eq. (3.45) above implies once more that the function $\tilde{f}(x)$ must approach unity for small values of its argument. On the other hand, for large concentrations, $R_*(c)$ must scale with $N^{1/2}$ implying that in the semidilute regime the function $\tilde{f}(x)$ must be a power law of its argument, $\tilde{f}(x) \sim x^{\delta}$. Using $c_* \sim N^{1-3\nu}$ [see Eq. (3.25)], we find $\delta = (1 - 2\nu)/(6\nu - 2) = -1/8$. We conclude that within the dilute regime the size of the chain remains constant but above the overlap concentration the chain shrinks according to the power law

$$R_*(c) = R_*\left(\frac{c}{c_*}\right)^{-(2\nu-1)/2(3\nu-1)} \propto c^{-1/8} . \tag{3.46}$$

This concentration dependence of R_* has been confirmed by neutron scattering experiments on labeled chains [139]. Note also that Eqs. (3.36) and (3.46) give the concentration dependence of the screening length ξ as

$$\xi(c) \sim c^{-3/4} . \tag{3.47}$$

3.4. *Effective interactions between polymer chains*

In the preceding sections, we have regarded the polymer chains as flexible strings, ignoring the microscopic details at length scales below the monomer length a. These considerations have brought about the universal scaling laws describing the N-dependence of the size of isolated chains and the concentration dependence of the thermodynamic properties of chain solutions. We can visualize this way of treating the chains if we imagine that we are observing a polymer solution through a microscope which allows us to resolve details of the chain at length scales $l > a$ but not at scales $l < a$. If we take a snapshot of a dilute polymer solution, as seen through this microscope, we will see a picture similar to the one shown in Fig. 13(a). The natural way to describe such a solution in the continuum would be through the introduction of the Hamiltonian given by Eq. (3.22) but now generalized to many chains, namely [134]

$$\beta\mathscr{H}[\boldsymbol{r}_{n\alpha}] = \frac{3}{2a^2}\sum_{\alpha=1}^{N_c}\int_0^N \mathrm{d}n\left(\frac{\partial \boldsymbol{r}_{n\alpha}}{\partial n}\right)^2 + \frac{v(T)}{2}\sum_{\alpha=1}^{N_c}\sum_{\gamma=1}^{N_c}\int_0^N\int_0^N \mathrm{d}n\,\mathrm{d}m\,\delta(\boldsymbol{r}_{n\alpha} - \boldsymbol{r}_{m\gamma}) , \tag{3.48}$$

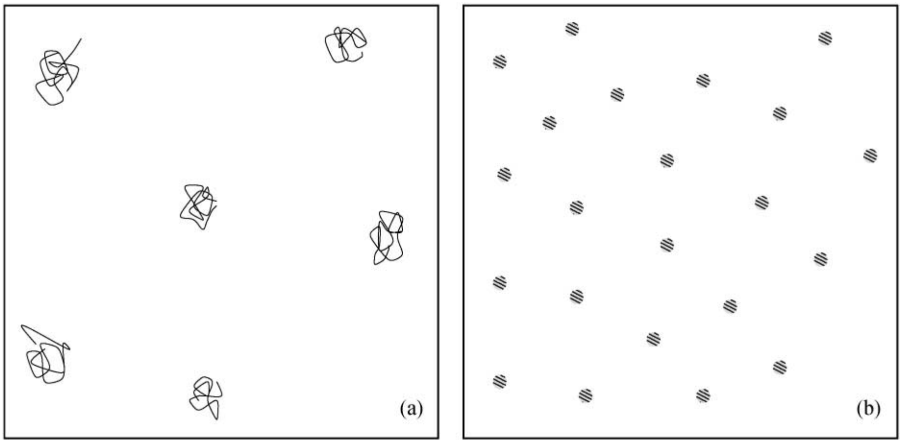

Fig. 13. A dilute polymer solution observed through two different microscopes. In (a) the microscope can resolve details above the monomer length whereas in (b) the microscope can only resolve details above the size of the chain. As a result, all length scales in (b) appear reduced with respect to those in (a) and the objects which appear as flexible chains in (a) show up as “point particles” in (b). Note that the field of view in (b) includes many more particles than in (a).

where $\boldsymbol{r}_{n\alpha}$ is the position vector of the nth monomer in the αth chain and the solution contains N_c chains. The first term in Eq. (3.48) above is the sum of the elastic energies of the chains and the second term includes both the intrachain ($\alpha = \gamma$) and the interchain ($\alpha \neq \gamma$) excluded volume interactions.

We can now make a leap in the length scale at which we observe the polymer solution, by imagining that we are looking at it through a microscope that has a much lower resolving power than the first one; now, all apparent length scales will get reduced by a factor $b > 1$, which is the ratio between the resolving power of the two microscopes. By making the resolving power of the second microscope small enough, we see at some point a picture similar to the one shown in Fig. 13(b): the internal details of the polymers cannot be probed any more and every chain appears to the eye as a diffuse object whose size is given by R_g. In this picture, it is natural to model the chains as point particles and the theoretical language appropriate to describe the properties of the solution is that of an effective Hamiltonian $\mathscr{H}_\mathrm{eff}$ featuring as degrees of freedom the coordinates $(\boldsymbol{R}_1, \boldsymbol{R}_2, \ldots, \boldsymbol{R}_{N_\mathrm{c}}) \equiv \{\boldsymbol{R}\}$ and momenta $(\boldsymbol{P}_1, \boldsymbol{P}_2, \ldots, \boldsymbol{P}_{N_\mathrm{c}}) \equiv \{\boldsymbol{P}\}$ of the centers of mass of every chain and including possibly volume terms, namely

$$\mathscr{H}_\mathrm{eff} = \sum_{i=1}^{N_\mathrm{c}} \frac{\boldsymbol{P}_i^2}{2M} + V_\mathrm{eff}(\{\boldsymbol{R}\}) + \Omega f_0(\rho) \, . \tag{3.49}$$

In Eq. (3.49) above, Ω is the macroscopic volume containing the N_c chains, each having a mass M, $\rho = N_\mathrm{c}/\Omega$ is the density of chains, $V_\mathrm{eff}(\{\boldsymbol{R}\})$ is the sought-for effective interaction between the centers of mass of the polymers and $\Omega f_0(\rho)$ is the volume term. In general, $V_\mathrm{eff}(\{\boldsymbol{R}\})$ will be represented by a sum of two-, three- and higher-order potentials, in agreement with the arguments put forward in Section 2.3.

The physical meaning of the effective potential V_eff follows from the general discussion on effective Hamiltonians presented in Section 2.3. We imagine that we hold the centers of mass of the polymers in solution fixed at the positions $(\boldsymbol{R}_1, \boldsymbol{R}_2, \ldots, \boldsymbol{R}_{N_\mathrm{c}})$ but we allow otherwise the monomers to fluctuate. We take a canonical average over the monomer degrees of freedom and calculate the corresponding partition function. The effective Hamiltonian is then simply $-k_\mathrm{B}T$ times the logarithm of this partition function, see Eqs. (2.33) and (2.34).

In the case at hand, there exist two formal deviations from the general discussion presented in Section 2.3. On the one hand, in the original Hamiltonian, Eq. (3.48) the microscopic degrees of freedom, i.e., the monomer coordinates and momenta, do not appear explicitly. They have been instead substituted with the continuous fluctuating fields $\boldsymbol{r}_{n\alpha}$, where n is thought of as a continuous variable. In fact, the Hamiltonian given by Eq. (3.48) is itself a *coarse-grained*, effective Hamiltonian. On the other hand, the degrees of freedom of the centers of mass do not appear in the original Hamiltonian, i.e., they do not correspond to any "real particles" in the system. However, neither of these two deviations presents a serious difficulty in formally constructing $V_\mathrm{eff}(\{\boldsymbol{R}\})$. The effective potential can still be defined if we start from the probability distribution function $\Psi[\boldsymbol{r}_{n\alpha}]$ of the original degrees of freedom and use the dependence of the new degrees of freedom on the original ones in order to calculate the new distribution function $\Psi_\mathrm{eff}(\{\boldsymbol{R}\})$ for the centers of mass, as described below.

The probability distribution function $\Psi[\boldsymbol{r}_{n\alpha}]$ follows from Eq. (3.48); it is proportional to the Boltzmann factor of the Hamiltonian, i.e.,

$$\Psi[\boldsymbol{r}_{n\alpha}] = Q_{N_\mathrm{c}}^{-1} \exp\{-\beta\mathscr{H}[\boldsymbol{r}_{n\alpha}]\} \tag{3.50}$$

where Q_{N_c} is the partition function of the N_c-chain system, given by[11]

$$Q_{N_c} = \int \prod_{\mu=1}^{N_c} \mathscr{D}\boldsymbol{r}_{n\mu} \exp\{-\beta\mathscr{H}[\boldsymbol{r}_{n\alpha}]\} . \tag{3.51}$$

Assuming that all monomers in every chain have the same mass, it follows that the center-of-mass coordinate $\boldsymbol{R}_\alpha$ of the αth polymer is given by

$$\boldsymbol{R}_\alpha = \sum_{i=1}^{N} \boldsymbol{r}_{i\alpha} . \tag{3.52}$$

From Eqs. (3.50) and (3.52) we can formally calculate the probability distribution Ψ_{eff} of the centers of mass as

$$\Psi_{\text{eff}}(\{\boldsymbol{R}\}) = Q_{N_c}^{-1} \int \prod_{\mu=1}^{N_c} \mathscr{D}\boldsymbol{r}_{n\mu} \exp\{-\beta\mathscr{H}[\boldsymbol{r}_{n\alpha}]\} \prod_{\gamma=1}^{N_c} \delta\left(\boldsymbol{R}_\gamma - \sum_{i=1}^{N} \boldsymbol{r}_{i\gamma}\right) . \tag{3.53}$$

The effective potential V_{eff} now follows if we express this probability distribution as a Boltzmann factor involving this potential, namely

$$\Psi_{\text{eff}}(\{\boldsymbol{R}\}) = \frac{\exp[-\beta V_{\text{eff}}(\{\boldsymbol{R}\})]}{\int \mathrm{d}\boldsymbol{R}^{N_c} \exp[-\beta V_{\text{eff}}(\{\boldsymbol{R}\})]} , \tag{3.54}$$

where $\mathrm{d}\boldsymbol{R}^{N_c}$ is a shorthand for $\mathrm{d}\boldsymbol{R}_1 \mathrm{d}\boldsymbol{R}_2 \ldots \mathrm{d}\boldsymbol{R}_{N_c}$. Eqs. (3.53) and (3.54) finally yield for the effective potential the expression

$$V_{\text{eff}}(\{\boldsymbol{R}\}) = -k_B T \ln\left\{ A \int \prod_{\mu=1}^{N_c} \mathscr{D}\boldsymbol{r}_{n\mu} \exp\{-\beta\mathscr{H}[\boldsymbol{r}_{n\alpha}]\} \prod_{\gamma=1}^{N_c} \delta\left(\boldsymbol{R}_\gamma - \sum_{i=1}^{N} \boldsymbol{r}_{i\gamma}\right)\right\} , \tag{3.55}$$

where the normalization constant A can be chosen appropriately in order to satisfy the desired asymptotic behavior of $V_{\text{eff}}(\{\boldsymbol{R}\})$, as we discuss in Section 3.4.1 below.

3.4.1. Theoretical results

Result (3.55) above is exact but impossible to handle for an arbitrary number of chains. Usually, one resorts to considering two chains only ($N_c = 2$), in which case the resulting effective potential V_{eff} is a function of the separation $R = |\boldsymbol{R}_1 - \boldsymbol{R}_2|$ between the centers of mass of the chains. A theoretical calculation of this $V_{\text{eff}}(R)$ for athermal solvents using renormalization-group techniques has been carried out by Krüger et al. [140]. As there are only two chains in the system, the Hamiltonian of Eq. (3.48) can be written in the form

$$\beta\mathscr{H} = \beta\mathscr{H}_{11} + \beta\mathscr{H}_{22} + \beta\mathscr{H}_{12} , \tag{3.56}$$

where

$$\beta\mathscr{H}_{\alpha\alpha} = \frac{3}{2a^2}\int_0^N \mathrm{d}n \left(\frac{\partial \boldsymbol{r}_{n\alpha}}{\partial n}\right)^2 + \frac{v(T)}{2}\int_0^N\int_0^N \mathrm{d}n\,\mathrm{d}m\,\delta(\boldsymbol{r}_{n\alpha} - \boldsymbol{r}_{m\alpha}) , \tag{3.57}$$

---

[11] In writing down in Eq. (3.51) the partition function as a functional integral over all conformations of the fluctuating fields $\{\boldsymbol{r}_{n\alpha}\}$, fluctuations of the fields corresponding to wavevectors $Q > \Lambda \sim 1/a$ must be excluded because the model does not make sense below the cutoff length $l = a$.

$$\beta\mathscr{H}_{\alpha\gamma} = \frac{v(T)}{2}\int_0^N\int_0^N \mathrm{d}n\,\mathrm{d}m\,\delta(\boldsymbol{r}_{n\alpha} - \boldsymbol{r}_{m\gamma}) \quad \text{with } \alpha \neq \gamma\ . \tag{3.58}$$

Krüger et al. define the effective potential $V_{\mathrm{eff}}(|\boldsymbol{R}_1 - \boldsymbol{R}_2|)$ as [140]

$$V_{\mathrm{eff}}(|\boldsymbol{R}_1 - \boldsymbol{R}_2|) = -k_{\mathrm{B}}T\ln\left\{\frac{\Omega^2}{Q_1^2}\int\mathscr{D}\boldsymbol{r}_1\mathscr{D}\boldsymbol{r}_2\,\hat{\rho}^{(1)}_{\mathrm{cm}}(\boldsymbol{R}_1)\hat{\rho}^{(1)}_{\mathrm{cm}}(\boldsymbol{R}_2)\exp[-\beta(\mathscr{H}_{11} + \mathscr{H}_{22} + \mathscr{H}_{12})]\right\}, \tag{3.59}$$

where Q_1 is the partition function of an isolated chain and $\hat{\rho}^{(\alpha)}_{\mathrm{cm}}(\boldsymbol{R}_\alpha)$ is the one-particle density operator of the center of mass of the αth chain:

$$\hat{\rho}^{(\alpha)}_{\mathrm{cm}}(\boldsymbol{R}_\alpha) = \delta\left(\boldsymbol{R}_\alpha - \sum_{i=1}^{N}\boldsymbol{r}_{i\alpha}\right). \tag{3.60}$$

A comparison between Eqs. (3.55), (3.59) and (3.60) shows that the definition of Krüger et al. is in agreement with the general result (3.55) and that the choice for the normalization coefficient is $A = (\Omega/Q_1)^2$. This choice guarantees that $V_{\mathrm{eff}}(R)$ approaches zero as the distance between centers of mass grows towards infinity.

In addition, definition (3.59) of the effective potential allows for other useful interpretations of this quantity. On the one hand, we can equivalently write

$$V_{\mathrm{eff}}(|\boldsymbol{R}_1 - \boldsymbol{R}_2|) = -k_{\mathrm{B}}T\ln\left[\frac{\tilde{Q}_2(|\boldsymbol{R}_1 - \boldsymbol{R}_2|)}{Q_2(\infty)}\right], \tag{3.61}$$

where

$$\tilde{Q}_2(|\boldsymbol{R}_1 - \boldsymbol{R}_2|) = \Omega^2\int\mathscr{D}\boldsymbol{r}_1\mathscr{D}\boldsymbol{r}_2\,\hat{\rho}^{(1)}_{\mathrm{cm}}(\boldsymbol{R}_1)\hat{\rho}^{(2)}_{\mathrm{cm}}(\boldsymbol{R}_2)\exp[-\beta(\mathscr{H}_{11} + \mathscr{H}_{22} + \mathscr{H}_{12})] \tag{3.62}$$

is the constrained partition function of a system of two chains whose centers of mass are kept at separation $|\boldsymbol{R}_1 - \boldsymbol{R}_2|$. The quantity $Q_2(\infty)$ is nothing else but the product of the two partition functions of the isolated chains, i.e., $Q_2(\infty) = Q_1^2$. Eq. (3.61) above makes the property $V_{\mathrm{eff}}(R \to \infty) = 0$ manifest. On the other hand, Eq. (3.59) shows that the Boltzmann factor $\exp[-\beta V_{\mathrm{eff}}(|\boldsymbol{R}_1 - \boldsymbol{R}_2|)]$ is proportional to the correlation function between the centers of mass in a dilute solution, i.e.

$$\exp[-\beta V_{\mathrm{eff}}(|\boldsymbol{R}_1 - \boldsymbol{R}_2|)] \propto \langle\hat{\rho}^{(1)}_{\mathrm{cm}}(\boldsymbol{R}_1)\hat{\rho}^{(2)}_{\mathrm{cm}}(\boldsymbol{R}_2)\rangle\ . \tag{3.63}$$

The last result is important for the calculation of the effective potential in simulations, as we shall see below.

The result of the renormalization-group study of Krüger et al. [140] is that the effective potential $V_{\mathrm{eff}}(R)$ is extremely well approximated by a *universal* Gaussian function[12]

$$V_{\mathrm{eff}}(R) \cong \varepsilon\exp[-(R/\sigma)^2]\ , \tag{3.64}$$

---

[12] The universality holds for the case under consideration here, where the two chains have the same degree of polymerization and the solvent is athermal. When the temperature becomes relevant or the two chains have different numbers of monomers, corrections to the Gaussian form are necessary, as we discuss in Section 3.4.2 below.

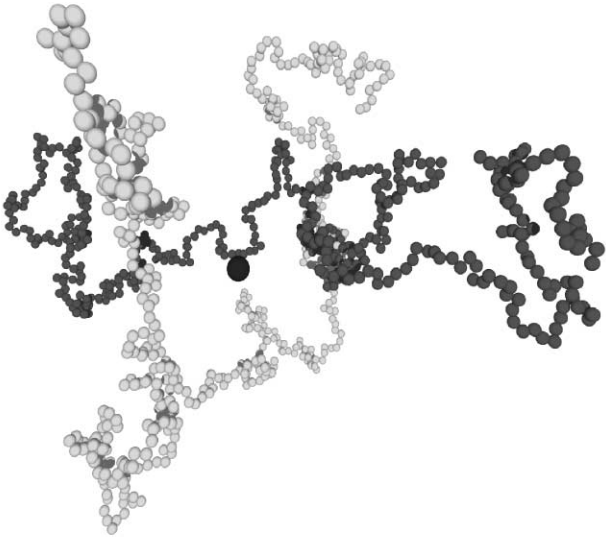

Fig. 14. A snapshot from a simulation involving two self-avoiding polymers. In this configuration, the centers of mass of the two chains (denoted by the big sphere) coincide, without violation of the excluded-volume conditions. (Courtesy of Arben Jusufi.)

where ε is an energy scale of the order of $k_B T$ and σ is a length scale proportional to the radius of gyration R_g of the chain. The effective potential is entropic, i.e., the energy scale is simply proportional to the temperature and the latter is a thermodynamically irrelevant parameter for the polymer solution, as expected for an athermal solvent: all monomer–monomer interactions appearing in the Hamiltonian of Eq. (3.48) are either zero or diverging and this causes the Boltzmann factor, $\exp\{-\beta\mathscr{H}[\boldsymbol{r}_{n\alpha}]\}$, to be temperature independent, with the result that the effective Boltzmann factor, $\exp[-\beta V_{\mathrm{eff}}(R)]$, inherits the same property. On the other hand, it is to be expected that the length scale appearing in the effective potential, σ, must be proportional to R_g, as R_g is the only characteristic length of the chain when the latter is looked upon at these scales.

A striking characteristic of the Gaussian potential of Eq. (3.64) is that, in contrast to the usual interatomic potentials or even potentials between colloidal particles, it does not diverge at the origin. This means that configurations where the centers of mass of the two chains coincide are not forbidden. However, this is to be expected, in view of the fact that the polymers are indeed fractal and not compact objects. The centers of mass of two coils can be at the same place, still leaving room for allowed configurations, in which each chain can fluctuate without intersecting the other, as shown in Fig. 14. Polymer chains are *soft*, *interpenetrable* entities.

3.4.2. Simulation results

Another possibility to determine the effective polymer–polymer potential $V_{\mathrm{eff}}(R)$ is through computer simulations of two chains. In these approaches, the monomers are modeled microscopically as beads interacting by means of a pair potential whose form is chosen so as to include also the effects of the solvent. For athermal solvents a hard-sphere interaction between monomers is usually employed, although soft interactions, such as a purely repulsive "truncated and shifted" Lennard-Jones potential have also been employed in good-solvent conditions [141]. The effects of a solvent of poorer quality are taken into account through an additional attraction between the beads, whose strength can be changed. The connectivity of the chain can be modeled in a number of different ways. For the calculation of $V_{\mathrm{eff}}(R)$, use of Eq. (3.63) is made: the correlation function $G(R)$ between the centers of mass of the two chains at distance R is measured, normalized to unity for large separations and subsequently set equal to the Boltzmann factor $\exp[-\beta V_{\mathrm{eff}}(R)]$.

The earliest simulations on this topic have been performed by Olaj et al. [142–146]. In Refs. [142,145], $V_{\mathrm{eff}}(R)$ was calculated by on-lattice simulations and for athermal chains, i.e., with no other interaction between the neighboring sites on the lattice other than the excluded volume one. In Ref. [144] the work was extended to nonathermal solvents and to off-lattice calculations but the latter were limited to athermal solvents only. In Refs. [143,146], attention was focused on the neighborhood of the Θ-temperature and the effective potential was calculated by separating the attractive and repulsive interactions of the chains in two terms.

Off-lattice simulations of athermal polymers were performed by Grosberg et al. [147], Schäfer and Baumgärtner [148], as well as by Krüger et al. [140] as a complementary approach to the theoretical techniques employed by the same authors, mentioned in the preceding section. In Ref. [147] the monomers were modeled as tangent hard spheres, whereas in Refs. [140,148] they were modeled as hard beads connected by hard, freely rotating rods along the chain (the "pearl-necklace-model"). In all cases, the correlation function $G(R)$ between the two centers of mass was measured and set equal to the Boltzmann factor of the "potential of mean force" $V_{\mathrm{eff}}(R)$. Excellent agreement between theory and simulation was found, confirming in this way that the effective interaction between athermal chains has indeed a Gaussian form.

Off-lattice simulations of nonathermal polymers were carried out by Dautenhahn and Hall [149]. In this work, the monomers along the chain were modeled as tangent spheres and the effective monomer–monomer interaction $v_{\mathrm{mm}}(r)$ was chosen to have the form of a "square-well potential", i.e.

$$v_{\mathrm{mm}}(r) = \begin{cases} \infty & \text{if } r < \Delta\ , \\ -\tau & \text{if } \Delta < r < \lambda\Delta\ , \\ 0 & \text{if } r > \lambda\Delta\ , \end{cases} \tag{3.65}$$

where Δ is the hard-sphere diameter, $\tau > 0$ is an energy scale and λ was chosen to have the value 1.5. The quality of the solvent was modified by changing the ratio $\tau/(k_{\mathrm{B}}T)$: the case $\tau/(k_{\mathrm{B}}T) = 0$ corresponds to athermal solvents and the quality of the solvent gets worse as this parameter increases. The effective potential was measured as follows: first, a statistical weight $W_i(R)$ was attributed to any allowed configuration, compatible with a center-to-center separation R, according to

$$W_i(R) = \exp\left[-\beta \sum_{i \neq j}{}' v_{\mathrm{mm}}(|\boldsymbol{r}_i - \boldsymbol{r}_j|)\right], \tag{3.66}$$

where the sum is carried over all distinct pairs of monomers having coordinates $\boldsymbol{r}_i$ and $\boldsymbol{r}_j$ and the prime denotes the constraint of keeping the centers of mass of the two coils at distance R. Then, the effective potential $V_{\mathrm{eff}}(R)$ was calculated as

$$V_{\mathrm{eff}}(R) = -k_{\mathrm{B}}T\ln\left[\frac{\sum_{i=1}^{M} W_i(R)}{M}\right], \tag{3.67}$$

where M denotes the total number of generated configurations, both accepted and rejected ones. For athermal solvents and for good solvents not too far from the athermal condition, the validity of the Gaussian potential of Eq. (3.64) was confirmed. The energy scale ε in Eq. (3.64) was found to be of the order of a few $k_{\mathrm{B}}T$ and decreasing with increasing degree of polymerization or with worsening of solvent quality. As the Θ-temperature is approached, the effective potential maintains a Gaussian-like core but it develops an attraction at larger center-to-center separations. Olaj et al. [142,143,146] as well as Czech and Hall [150] have taken account of this feature by modeling the effective potential by a sum of two Gaussian terms, one short-range repulsive and one long-range attractive.

Most recently, Louis et al. [151] have independently carried out state-of-the art simulations involving not just two but N_{c} chains and varying the number of chains to cover a very broad range of concentrations, ranging from dilute solutions up to five times the overlap concentration. They confirmed a Gaussian-like form for the effective potential with a prefactor $\varepsilon \approx 2k_{\mathrm{B}}T$. The most important result of this work is that the pair potential picture holds throughout the large concentration range and that the two potential parameters, ε and σ remain constant up to the overlap concentration c_*, changing only very slightly with density above c_*. The density dependence of the potential parameters is modeling the many-body terms, which appear to be very weak in this case.

Moreover, the same authors have shown that employing this effective interaction leads to a very accurate description of the thermodynamics (equation of state) of polymer solutions for a wide range of concentrations, thus confirming the validity of the idea that polymer chains can be viewed as soft colloids [152]. This greatly facilitates the study of polymer solutions, as the monomers drop out of sight and the number of dynamical degrees of freedom is reduced by a factor N, the degree of polymerization. The Gaussian effective interaction has also recently been employed by Louis et al. in their study of the structure of colloid–polymer mixtures [153].

We conclude this section with the remark that the idea of a Gaussian effective interaction between polymer chains dates back to Flory, one of the pioneers of the field, who already in 1950 proposed the so-called Flory–Krigbaum potential [154], $V_{\mathrm{FK}}(R)$, which reads as

$$\beta V_{\mathrm{FK}}(R) = N^2\frac{v_{\mathrm{seg}}^2}{v_{\mathrm{solv}}}\left(\frac{3}{4\pi R_g^2}\right)^{3/2}(1-2\chi)\exp\left(-\frac{3R^2}{4R_g^2}\right), \tag{3.68}$$

where v_{seg} and v_{solv} denote the volumes of a monomer segment and a solvent molecule, respectively. Though the *functional form* of this interaction is correct for athermal or good solvents, several of the quantitative characteristics of the Flory–Krigbaum potential turn out to be wrong: the strength of the interaction is proportional to $N^{1/5}$ (taking into account the scaling $R_g \sim N^{3/5}$), resulting into an interaction which becomes steeper with increasing degree of polymerization, in disagreement with the findings of Dautenhahn and Hall [149]. Moreover, the Flory–Krigbaum potential remains repulsive at all separations above the Θ-point, vanishing identically at the Θ-temperature, $\chi = 1/2$, again in disagreement with the simulation results of Ref. [149].

3.5. The Gaussian core model

In the preceding section, we argued that the effective interaction between the centers of mass of two polymer chains in an athermal solvent can be described in an excellent approximation by an interaction of a Gaussian form. We expect this interaction to be the valid theoretical tool for the statistical description of a many-body system of polymers in solution, at least as far as we stay in the dilute regime. As the concentration is increased, many-body terms will become increasingly relevant. Yet, the statistical–mechanical analysis of a system of point particles interacting by means of a pair-additive Gaussian potential is of significant physical interest for two reasons. On the one hand, because even the missing many-body interactions can be mimicked by introducing density-dependent parameters in the pair potential [22,68,151]. On the other hand, because the peculiarity of a bounded pair interaction brings about some quite interesting new phenomenology in the structure and thermodynamics of the many-body system, one which is unknown for the usual systems interacting by means of potentials which diverge at the origin.

The physical system we consider in the rest of this section is, therefore, a collection of N_c chains or, more general, "colloids" enclosed in a macroscopic volume Ω and interacting by means of the Gaussian pair potential $v(r)$ given by

$$v(r) = \varepsilon e^{-(r/\sigma)^2} , \tag{3.69}$$

where $\varepsilon > 0$ is an energy scale and σ is a length scale. The properties of such a system were first analyzed by Stillinger et al. in the late 1970s [155–159]. Simulations on the fluid state structure of this system have been recently performed by Watzlawek et al. [77,160].

The model has become popular again recently, due to its possible applications in soft matter physics and its property to yield a negative thermal expansion, for a review see Ref. [161]. The relevant thermodynamic parameters are the reduced density $\bar{\rho} \equiv \rho\sigma^3 = N_c\sigma^3/\Omega$ and the reduced temperature $t = k_B T/\varepsilon$. Following the terminology of Ref. [155], we refer to this system as the Gaussian core model (GCM).

3.5.1. Formal properties

The GCM has some particular mathematical properties arising from the form of the interaction and the property of Gaussian functions to be the eigenfunctions of the Fourier transform. These properties, which have been explored by Stillinger et al. [155,159,161] yield important information regarding the phase behavior of the GCM; we present a summary below.

(I) *Hard-sphere limit*: Consider the Boltzmann factor $B(r, \beta)$ of the Gaussian potential:

$$B(r, \beta) = \exp[-\beta\varepsilon e^{-(r/\sigma)^2}] , \tag{3.70}$$

which varies from $\mathrm{e}^{-\beta\varepsilon}$ (for $r \to 0$) to 1 (for $r \to \infty$). We now focus on very low temperatures, $\beta\varepsilon \gg 1$, where $\mathrm{e}^{-\beta\varepsilon} \cong 0$. Of interest are the value of r, $r_*(\beta)$, where $B(r,\beta)$ has the intermediate value 1/2 and the derivative of $B(r,\beta)$ at this point, which are given by the relations

$$r_*(\beta) = \sigma\sqrt{\ln\left(\frac{\beta\varepsilon}{\ln 2}\right)} \tag{3.71}$$

and

$$\left.\frac{\mathrm{d}B(r,\beta)}{\mathrm{d}r}\right|_{r_*(\beta)} = \frac{r_*(\beta)}{\sigma^2}\ln 2 \,. \tag{3.72}$$

The two equations above show that as the temperature approaches zero ($\beta \to \infty$), on the one hand $r_*(\beta)$ approaches infinity and on the other hand the value of the derivative of the Boltzmann factor at $r_*(\beta)$ diverges as well. In other words, with lowering the temperature, the quantity $B(r,\beta)$ looks more and more like a step function with a discontinuity at $r_*(\beta)$ [155]. But this is precisely the Boltzmann factor of a hard-sphere potential having a hard-sphere diameter $r_*(\beta)$. One expects, therefore, that at low temperatures the GCM will display the hard-sphere freezing transition [162–166] from a fluid into a face-centered cubic (fcc) crystal. The coexistence densities between fluid and solid, ρ_f and ρ_s, respectively, and their temperature dependence at low T are determined from the known values in the hard-sphere system [165]: $\rho_\mathrm{f} r_*^3(\beta) = 0.9435$ and $\rho_\mathrm{s} r_*^3(\beta) = 1.0409$. Using Eq. (3.71) for $r_*(\beta)$, it can be seen that the reduced coexistence densities $\rho_\mathrm{f}\sigma^3$ and $\rho_\mathrm{s}\sigma^3$ both approach zero as $T \to 0$. In the zero-temperature limit, the GCM displays coexistence between a fluid and a fcc solid which both have vanishing densities. Using the results above, the equations for the freezing and melting lines, $t_\mathrm{f}(\bar{\rho})$ and $t_\mathrm{m}(\bar{\rho})$ in the $(t,\bar{\rho})$-plane take the form

$$t_\mathrm{f}(\bar{\rho}) = \frac{1}{\ln 2}\exp\left(-\frac{0.962}{\bar{\rho}^{\,2/3}}\right), \tag{3.73}$$

$$t_\mathrm{m}(\bar{\rho}) = \frac{1}{\ln 2}\exp\left(-\frac{1.027}{\bar{\rho}^{2/3}}\right). \tag{3.74}$$

It can again be seen that at $t = 0$ the two lines coalesce at $\bar{\rho} = 0$.

(II) *Convolution property*: Let $\boldsymbol{R} \equiv (\boldsymbol{r}_1, \boldsymbol{r}_2, \ldots, \boldsymbol{r}_{N_\mathrm{c}})$ be a $3N_\mathrm{c}$-dimensional vector, where $\boldsymbol{r}_i$ denotes the position vector of the ith particle in the system. Define a linear, Gaussian-smoothing operator $\mathscr{L}(\lambda)$, acting on an arbitrary function $f(\boldsymbol{R})$ of all coordinates, through the relation

$$[\mathscr{L}(\lambda) * f](\boldsymbol{R}) = (\pi^{1/2}\lambda)^{-3N_\mathrm{c}}\int \mathrm{d}\boldsymbol{S}^{N_\mathrm{c}} \exp[-(\boldsymbol{R}-\boldsymbol{S})^2/\lambda^2] f(\boldsymbol{S}) \,, \tag{3.75}$$

where $\mathrm{d}\boldsymbol{S}^{N_\mathrm{c}} = \mathrm{d}\boldsymbol{s}_1\mathrm{d}\boldsymbol{s}_2 \ldots \mathrm{d}\boldsymbol{s}_{N_\mathrm{c}}$ and

$$(\boldsymbol{R}-\boldsymbol{S})^2 = \sum_{i=1}^{N_\mathrm{c}} (\boldsymbol{r}_i - \boldsymbol{s}_i)^2 \,. \tag{3.76}$$

We now choose $f(\boldsymbol{R})$ to be the total potential energy of the system, $\Phi(\boldsymbol{R})$:

$$\Phi(\boldsymbol{R}) = \sum_{i=1}^{N_\mathrm{c}} \sum_{j=i+1}^{N_\mathrm{c}} \varepsilon \mathrm{e}^{-(\boldsymbol{r}_i - \boldsymbol{r}_j)^2/\sigma^2} \,. \tag{3.77}$$

Then, as a result of the property of the Gaussian function to remain form-invariant under convolutions, the following relation holds [161]:

$$[\mathscr{L}(\lambda) * \Phi](\boldsymbol{R}) = \frac{1}{(1+2\lambda^2)^{3/2}}\Phi\left(\frac{\boldsymbol{R}}{\sqrt{1+2\lambda^2}}\right). \tag{3.78}$$

The smoothed version of the total interaction energy of the GCM is equal to the total interaction energy of a GCM in which the range of the potential has been increased a factor $(1+2\lambda^2)^{1/2}$ and its strength has been reduced by a factor $(1+2\lambda^2)^{3/2}$.

(III) *Duality relations*: We now assume that the N_c particles are arranged on the sites of a Bravais lattice. Let us consider the quantity [159,161]

$$I_X(\rho) = \varepsilon + \lim_{N_c\to\infty}\left(\frac{2\Phi_X}{N_c}\right), \tag{3.79}$$

where the subscript stands for the chosen lattice, ρ for the average density of particles and Φ_X is the total potential energy associated with the lattice arrangement (the 'Madelung energy' of the lattice). Using the translational invariance of a Bravais lattice with respect to lattice vectors and the fact that $v(0)=\varepsilon$, the quantity $I_X(\rho)$ can also be written as

$$I_X(\rho) = \varepsilon\sum_{\{\boldsymbol{R}\}} \mathrm{e}^{-(\boldsymbol{R}/\sigma)^2} \tag{3.80}$$

$$= \varepsilon\int \mathrm{d}\boldsymbol{r}\sum_{\{\boldsymbol{R}\}} \delta(\boldsymbol{r}-\boldsymbol{R})\mathrm{e}^{-(r/\sigma)^2}, \tag{3.81}$$

where $\{\boldsymbol{R}\}$ is the set of Bravais lattice vectors. We now introduce the Fourier representation of the sum of delta spikes:

$$\sum_{\{\boldsymbol{R}\}} \delta(\boldsymbol{r}-\boldsymbol{R}) = \rho\sum_{\{\boldsymbol{K}\}} \mathrm{e}^{\mathrm{i}\boldsymbol{K}\cdot\boldsymbol{r}}, \tag{3.82}$$

where $\{\boldsymbol{K}\}$ is the set of *reciprocal* lattice vectors, forming the reciprocal lattice $\hat{X}$ of X, which is also a Bravais lattice. Introducing Eq. (3.82) into Eq. (3.81) and carrying out the $\boldsymbol{r}$-integration, we obtain

$$I_X(\rho) = \rho\sigma^3\left[\varepsilon\sum_{\{\boldsymbol{K}\}} \mathrm{e}^{-(K\sigma/2)^2}\right]. \tag{3.83}$$

The term in the square brackets on the rhs of Eq. (3.83) above is a sum of Gaussians over Bravais lattice vectors $\{\boldsymbol{K}\}$. A comparison with Eq. (3.80) shows that it must be related to the quantity $I_{\hat{X}}$ of the reciprocal lattice $\hat{X}$. At the same time, the density of points in this lattice is always proportional to ρ^{-1}. In other words, Eq. (3.83) relates the quantity $I_X(\rho)$ with the quantity $I_{\hat{X}}(\alpha\rho^{-1})$, where α is a proportionality constant. This is a so-called *duality relation* which arises from the boundedness of the Gaussian interaction and its property to remain form-invariant under Fourier transformation [159,161].

As a specific (and physically relevant) case, we now consider the choice where X is the body-centered cubic (bcc) lattice and hence $\hat{X}$ is the face-centered cubic (fcc) lattice. For this pair of lattices, Eq. (3.83) takes the form

$$I_{\mathrm{bcc}}(\bar{\rho}) = (\pi^{3/2}\bar{\rho})I_{\mathrm{fcc}}(\pi^{-3}/\bar{\rho}) . \tag{3.84}$$

Eq. (3.84) above has the property that at the "magic density" $\bar{\rho}_* = \pi^{-3/2} \cong 0.1796$ the prefactor at the rhs is equal to unity and the arguments of I_{bcc} and I_{fcc} are equal. This in turn implies that at reduced density $\bar{\rho} = \bar{\rho}_*$ the fcc and bcc lattices are degenerate, i.e., they have the same Madelung energy. Numerical calculations (lattice sums) show that for $\bar{\rho} < \bar{\rho}_*$ the fcc lattice has a lower lattice energy[13] than the bcc, i.e., $I_{\mathrm{fcc}}(\bar{\rho}) < I_{\mathrm{bcc}}(\bar{\rho})$. Combining this fact with Eq. (3.84), we find that for densities $\bar{\rho} > \bar{\rho}_*$ the opposite is true: $I_{\mathrm{fcc}}(\bar{\rho}) > I_{\mathrm{bcc}}(\bar{\rho})$ and the relative stability of the fcc and bcc lattices is exchanged. Below $\bar{\rho}_*$ the fcc wins with respect to bcc and above $\bar{\rho}_*$ the bcc is stable.

A powerful property of the general relation (3.83) is that it allows us to calculate the ground-state energy of a given lattice at very high densities ($\bar{\rho} \to \infty$) by considering the ground-state energy of the *reciprocal* lattice at *very low* densities. In this way, high-density expansions for the lattice energies of a number of lattices have been obtained [159]. For the simple cubic (sc), bcc, and fcc, these expressions read as

$$I_{\mathrm{sc}}(\bar{\rho}) = \varepsilon\pi^{3/2}\bar{\rho}[1 + 6\exp(-\pi^2\bar{\rho}^{2/3}) + \cdots] , \tag{3.85}$$

$$I_{\mathrm{bcc}}(\bar{\rho}) = \varepsilon\pi^{3/2}\bar{\rho}[1 + 12\exp(-2^{1/3}\pi^2\bar{\rho}^{2/3}) + \cdots] \tag{3.86}$$

and

$$I_{\mathrm{fcc}}(\bar{\rho}) = \varepsilon\pi^{3/2}\bar{\rho}\left[1 + 8\exp\left(-\frac{3\pi^2}{2^{4/3}}\bar{\rho}^{2/3}\right) + \cdots\right]. \tag{3.87}$$

The leading term in the high-density expansion of the lattice energies is, according to Eqs. (3.85)–(3.87) above, independent of the lattice structure and equal to $\varepsilon\pi^{3/2}\bar{\rho}$. This is twice the energy per particle corresponding to a *uniform* and *random* (i.e., uncorrelated) distribution of particles interacting by means of the Gaussian potential. To show this, we note that the potential energy per particle in a uniform system is given, quite generally, by the second term on the rhs of Eq. (2.65) and hence we have

$$\frac{2\Phi}{N_c} = 4\pi\rho\int_0^\infty r^2\varepsilon e^{-(r/\sigma)^2}g(r)\,\mathrm{d}r . \tag{3.88}$$

Setting $g(r) = 1$, which means that the positions of the particles are statistically uncorrelated, we obtain precisely

$$\frac{2\Phi_{\mathrm{id}}}{N_c} = \varepsilon\pi^{3/2}\bar{\rho} , \tag{3.89}$$

---

[13] Here we use the term "lattice energy" to denote the quantity $I_X(\bar{\rho})$ which, according to its definition in Eq. (3.79), is equal to twice the ground-state energy per particle plus the "self-energy" ε of a single particle.

where the subscript denotes an "ideal" state where all correlations are absent. The above considerations lead to the conjecture that at very high densities, $\bar{\rho} \to \infty$, all positional correlations between the Gaussian particles are lost and the system resembles an "infinite-density ideal gas" with a radial distribution function $g(r) = 1$. The verification of this conjecture is part of our considerations in Section 3.5.3.

3.5.2. Approximate phase diagram

The properties presented in the preceding section offer the basis for the construction of a semiquantitative phase diagram of the GCM. It has already been pointed out that at low densities and low temperatures a hard-sphere-type freezing takes place, with the freezing and melting lines being given by Eqs. (3.73) and (3.74). At $T = t = 0$, the ground-state configurations have been explored by Stillinger [155] by calculating lattice sums for various candidate crystal structures and choosing the one yielding the lowest ground-state energy. The sc, bcc, fcc, hexagonal close-packed (hcp) and diamond lattices were taken as candidates. For all of them it was checked that configurations where a fraction of sites is multiply occupied are unfavorable, i.e., single-site occupancy always yields the minimum energy for a given lattice structure. As anticipated already in the preceding section, it was found that the zero-temperature phase diagram of the GCM is very simple: the fcc has the lowest energy for $\bar{\rho} < \bar{\rho}_*$ and the bcc for $\bar{\rho} > \bar{\rho}_*$. This leads to a fcc–bcc phase transition with the coexisting densities lying on either side of $\bar{\rho}_*$ being determined by the common-tangent construction.

At zero temperature and for densities $\bar{\rho} \to \infty$, Eqs. (3.79), (3.86) and (3.89) yield the difference between the energy per particle of a bcc-solid and that of a uniform, ideal liquid as

$$\frac{\Phi_{\mathrm{bcc}}}{N_{\mathrm{c}}} - \frac{\Phi_{\mathrm{id}}}{N_{\mathrm{c}}} = -\frac{\varepsilon}{2} . \tag{3.90}$$

In comparison to the solid, the liquid possesses an additional communal entropy arising from the diffusive nature of the particle motions in the translationally invariant state. At finite temperature, this entropy will win over the term $-\varepsilon/2$ above, bringing the free energy of the liquid below that of the solid. Hence, at high densities and small but finite temperatures the bcc-solid will melt. Based on Eqs. (3.85)–(3.87), Stillinger [159] argued that the free energies of all states of the model at high density will differ by amounts proportional to $\exp(-K\bar{\rho}^{2/3})$ and thus conjectured that the freezing and melting lines at the limit $\bar{\rho} \to \infty$ must be given by equations of the form

$$t_{\mathrm{f}}(\bar{\rho}) \propto \exp(-K_{\mathrm{f}}\bar{\rho}^{2/3}) , \tag{3.91}$$

$$t_{\mathrm{m}}(\bar{\rho}) \propto \exp(-K_{\mathrm{m}}\bar{\rho}^{2/3}) \tag{3.92}$$

with the appropriate constants K_{f} and K_{m}. Note the duality between Eqs. (3.73), (3.74), valid for $\bar{\rho} \to 0$, and (3.91), (3.92), valid for $\bar{\rho} \to \infty$. Apart from proportionality constants, one pair can be obtained from the other by the formal substitution $\bar{\rho} \to 1/\bar{\rho}$. Moreover, Eqs. (3.91) and (3.92) show that the slope of the high-density freezing and melting lines are *negative*. Contrary to the usual case, the liquid coexisting with the solid has a *higher* density than the latter.

The freezing and melting lines commence with positive slope at low temperatures and densities and end up with negative slope at low temperatures and high densities. Moreover, the finiteness of the Gaussian interaction implies that crystalline order cannot be maintained at any temperature;

there must be an *upper freezing temperature* t_u above which the system is always in the liquid state.[14] However, the value of t_u cannot be calculated without a detailed numerical study of the GCM.

These theoretical considerations were subsequently complemented by molecular dynamics (MD) simulations by Stillinger and Weber [156,157], performed at some selected points of the $(t,\bar{\rho})$-plane, which allowed for an approximate calculation of the phase diagram of the GCM. A semiquantitative verification of the location of freezing lines for selected temperatures was obtained by Watzlawek [77] on the basis of Monte-Carlo (MC) simulations. The upper freezing temperature has the value $t_u \approx 0.008$ and the corresponding density is $\bar{\rho}_u \approx 0.25$. However, the liquid structure of the GCM had not been studied in detail before. Recently, Lang et al. [160] performed a detailed study of the fluid- and solid-state properties of the model, leading to a quantitative calculation of the phase diagram and establishing the high-density ideal gas behavior of the system. This approach is presented in detail below.

3.5.3. *The fluid state: integral-equation theories*

As mentioned in Sections 3.4.1 and 3.4.2 above, the effective interaction between two athermal polymer coils can be described by a Gaussian potential of the form given by Eq. (3.69) with the prefactor ε being of the order of $k_B T$. This corresponds to reduced temperature $t \sim 1$. The phase transitions of the GCM, on the other hand, take place at reduced temperatures below $t \approx 10^{-2}$, i.e., two orders of magnitude lower. Hence, at the physical parameters which describe polymer solutions, the model displays no phase transitions and describes a system which remains fluid at all concentrations.

As a representative for polymer solutions in physical conditions, we choose the value $t = 0.5$ and examine the structure of the GCM by employing the HNC closure. At such temperatures, the bridge function of the system is indeed expected to be very small, hence the HNC approximation $B(r) = 0$ is a reasonable one, an assumption confirmed also by direct comparison with computer simulations [169]. As usual in theoretical approaches, we adopt as a measure of the density of the system the "packing fraction" η defined as

$$\eta = \frac{\pi}{6}\rho\sigma^3 = \frac{\pi}{6}\bar{\rho}^3 \tag{3.93}$$

and calculate the radial distribution function $g(r)$ and the structure factor $S(Q)$ at fixed temperature $t = 0.5$ for increasing packing fraction η. Results for representative η-values are shown in Fig. 15 for $g(r)$ and in Fig. 16 for $S(Q)$.

Referring to Fig. 15 and in comparison to Fig. 5(a), which shows a typical $g(r)$ for dense fluids, we see that the system differs from the "usual" liquids in two significant ways: on the one hand, there is no *correlation hole*, i.e., no region in the vicinity of $r = 0$ where $g(r)$ vanishes. A Gaussian particle at this temperature does not prohibit the others from fully overlapping with it, at any density. This is

---

[14] This intuitive argument holds for finite interactions which cannot sustain crystals with multiply occupied sites. If multiple occupancy is possible, then the clustering of particles on lattice sites brings about a novel stabilization mechanism for the solid and the upper freezing temperature does not necessarily exist, see Refs. [167,168] or Appendix B.

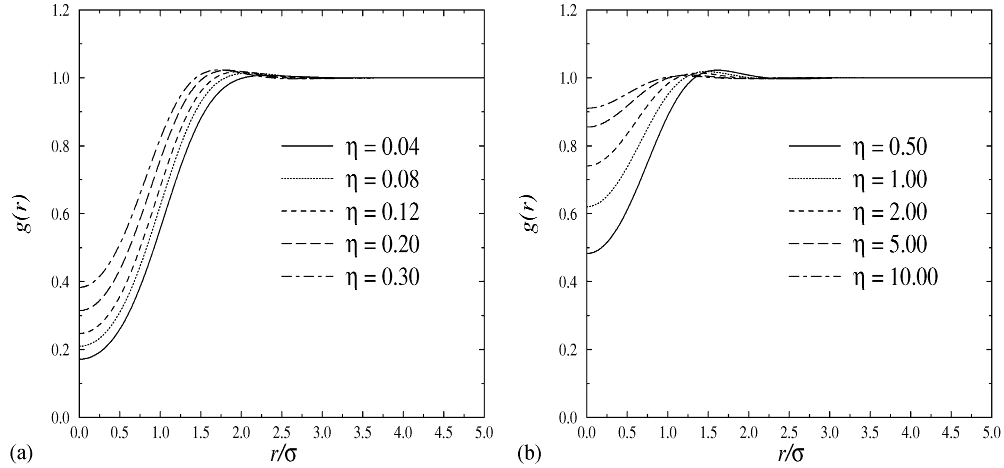

Fig. 15. The radial distribution function $g(r)$ of the Gaussian core model at reduced temperature $t = 0.5$ for increasing packing fraction η. The curves have been calculated using the HNC closure.

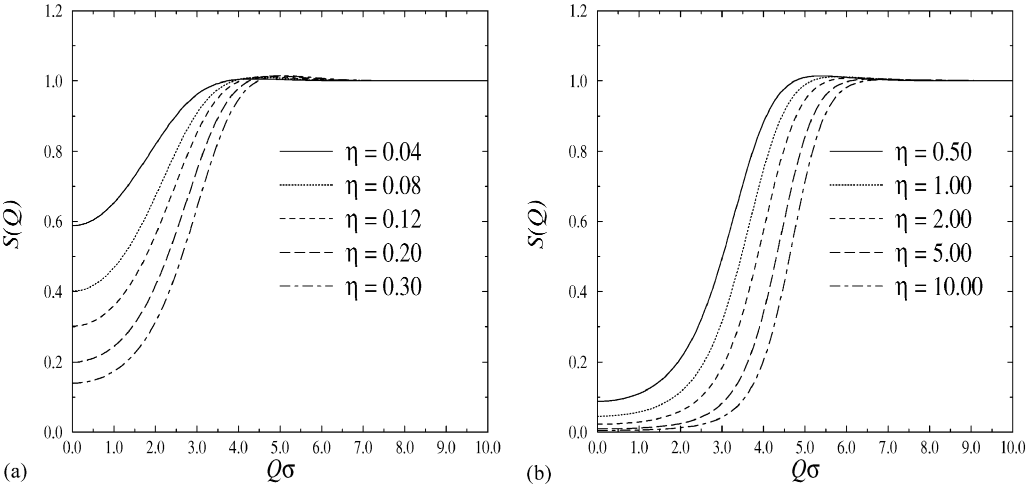

Fig. 16. The structure factor $S(Q)$ of the Gaussian core model at reduced temperature $t = 0.5$ and for the same packing fractions η for which $g(r)$ is shown in Fig. 15.

a consequence of the fact that the interaction itself is finite at $r = 0$, and that the thermal energy $k_B T$ is of the order of the energy barrier, $\varepsilon = 2k_B T$ in this case, thus allowing particles to fully overlap. On the other hand, the value of $g(r)$ at zero separation grows with increasing density and at high packing fractions the radial distribution function $g(r)$ approaches unity for all r-values, see Fig. 15(b). This is a confirmation of the assumption of Stillinger et al. that the system becomes ideal at high packings and it will shortly be shown that this approach to an ideal system also occurs at much lower temperatures.

The structure factor $S(Q)$ of a fluid is a measure of the susceptibility of the system to a spontaneous spatial modulation having wavenumber Q, a property which becomes evident within the framework of the fluctuation–dissipation theorem, where $S(Q)$ appears as a proportionality factor between a weak external potential of wavenumber Q and the associated linear density response [4]. Hence, a structure factor with a high peak at some wavenumber (and at its higher harmonics) is a signal of an incipient transition of the fluid to a spatially modulated system, i.e., a crystal. These considerations together with analysis of freezing data available for a large variety of liquids have led to the introduction of the empirical Hansen–Verlet criterion [170,171], which states that a liquid crystallizes when $S(Q)$ at its highest peak has the quasi-universal value 2.85. The calculated structure factors at $t = 0.5$, shown in Fig. 16 show very little Q-dependence and they lie well below this critical value, pointing to the fact that the system is far away from crystallization. The absence of phase transitions at this temperature has also been confirmed by calculating its free energy through the pressure route (see Section 2.4) and confirming that it is free of nonconvex regions [77]. However, we should keep in mind that this analysis does not yet include the volume terms which, as discussed in Section 2.5, can induce a fluid–fluid phase transition. We will return to this point in Section 3.7.

It is now natural to ask the question how $g(r)$ and $S(Q)$ look at a much lower temperature, in particular close to the approximately calculated upper freezing temperature $t_{\mathrm{u}} \cong 0.008$. This question is relevant because the approximate phase diagram has been calculated by invoking a number of complementary considerations, whereas integral equation theories allow for a more detailed and accurate calculation of the structure and thermodynamics of the liquid. For this purpose we now choose a temperature $t = 0.01$, lying slightly above the estimated value of t_{u}, and calculate $g(r)$ and $S(Q)$ again as functions of η. The availability of Monte-Carlo simulation data for precisely this temperature [77], allows us to make a further test of the integral equation theories applied to this peculiar system.

The softness of the Gaussian interaction excludes the PY-closure as a candidate because the latter is known to work well only for very steeply repulsive potentials and to fail when the interaction is soft. We are therefore going to consider the HNC and the Rogers–Young (RY) closures. HNC Moreover, the peculiarity of the Gaussian interaction to allow for full overlaps between particles implies that a closure must be considered, in which special consideration is given to the value of $g(r)$ at zero separation. An elegant way to achieve this is by making use of the so-called test particle approach of Lee et al. [172–175]. One considers instead of a one-component system a mixture between particles interacting among themselves with the potential $v(r)$ (species 1) and "strong particles", interacting with the former by means of the double interaction, $2v(r)$ (species 2). The mixture is considered at the limit of zero dilution for the strong particles. Lee and Shing [172] have shown that the value of the cavity function $y(r) = \mathrm{e}^{\beta v(r)} g(r)$ at $r = 0$ is given by the relation

$$\ln y(0) = 2\beta\mu_{\mathrm{ex}}^{(1)} - \beta\mu_{\mathrm{ex}}^{(2)}\,, \tag{3.94}$$

where $\mu_{\mathrm{ex}}^{(i)}$ is the excess chemical potential of species i in the mixture.[15] These excess chemical potentials can be expressed entirely in terms of the bridge function $B(r)$ and the associated "star

---

[15] The term "excess chemical potential" means the difference between the total chemical potential and its ideal value, i.e., the value it has when all particles in the system are noninteracting.

function" $S^*(r)$ introduced by Lee [173]. Under certain approximations, $S^*(r)$ can itself be expressed in terms of $B(r)$ [173] and the whole problem reduces to finding a reasonable parameterization for the bridge function. The so-called zero separation closure (ZSEP) is constructed by choosing for $B(r)$ the form proposed by Verlet [176]:

$$B_{\mathrm{ZSEP}}(r) = -\frac{\zeta\gamma^2(r)}{2}\left[1 - \frac{\varphi\gamma(r)}{1+\alpha\gamma(r)}\right], \tag{3.95}$$

where $\gamma(r) = h(r) - c(r)$ is the indirect correlation function and ζ, φ, α are three parameters which have to be determined in order to satisfy three thermodynamic consistency conditions: the consistency between the pressure and compressibility routes (see Section 2.4), the zero separation condition of Eq. (3.94) above and the Gibbs–Duhem relation:

$$\frac{\partial P}{\partial \mu} = \rho\ , \tag{3.96}$$

where P, μ and ρ are the pressure, chemical potential and density, respectively, of a pure system of species 1-particles. Both P and μ can be readily obtained from the correlation functions, within the framework of the ZSEP closure. The ZSEP closure has recently been successfully applied by Fernaud et al. [177] to another system interacting by means of a bounded interaction, the "penetrable spheres model" (PSM) of Likos et al. [167] whose properties are summarized in Appendix B.

We present the obtained results in Figs. 17–19 and we discuss them below. We begin with the RY closure. When the packing is not large enough, typically $\eta \lesssim 0.50$ at this temperature, the RY closure gives results which are in very good agreement with simulations, as can be seen in Figs. 17 and 18. However, above $\eta \approx 0.50$, the $g(r)$ from simulations starts *penetrating* towards $r = 0$, physically meaning that the probability of finding two particles "sitting on top of each other" is

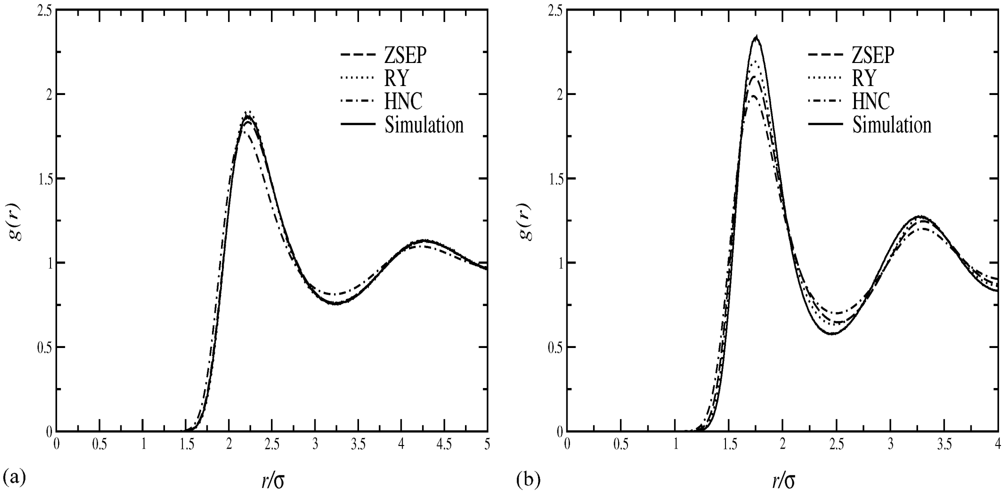

Fig. 17. Comparison for the radial distribution function $g(r)$ between the simulation results and those obtained from the various closures, at $t = 0.01$ and at small values of the packing fraction: (a) $\eta = 0.05$; (b) $\eta = 0.12$.

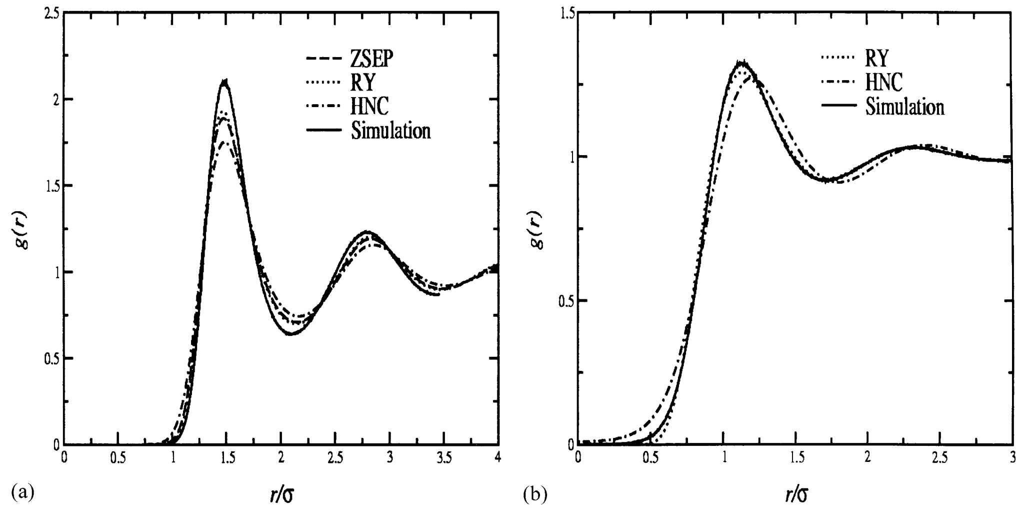

Fig. 18. Same as Fig. 17 but for intermediate packings: (a) $\eta = 0.20$; (b) $\eta = 0.50$.

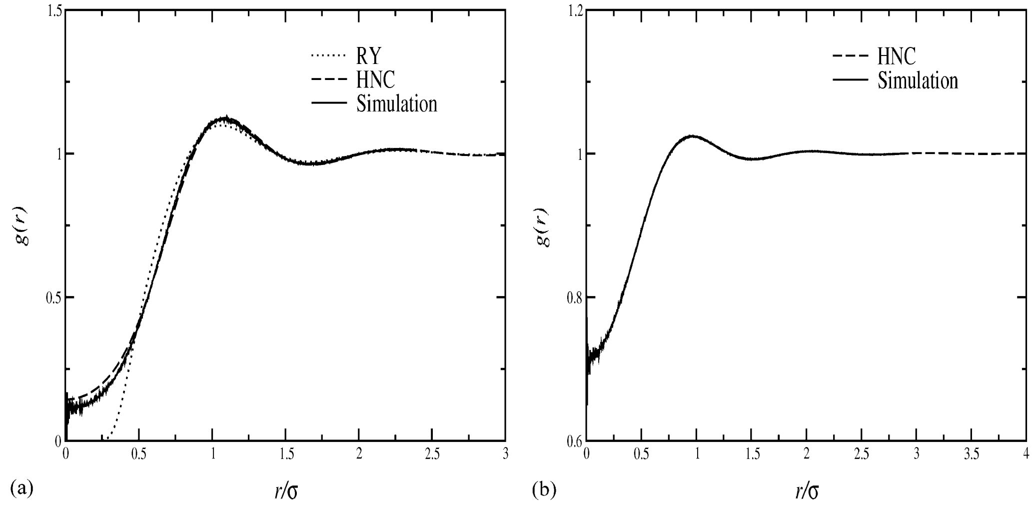

Fig. 19. Same as Fig. 17 but for high packings: (a) $\eta = 1.00$; (b) $\eta = 6.00$, where the simulation result is indistinguishable from the HNC.

finite and there is no "correlation hole" in $g(r)$. This is to be expected for a system with a bounded interaction. However, as can be seen from Fig. 19(a), the RY closure fails to capture precisely this penetration phenomenon, yielding always $g(r)$'s that are *too low* at small separation and making the erroneous prediction that a correlation hole exists.

The reason for this behavior can be traced back in the construction of the RY closure, Eqs. (2.66) and (2.68), where it can be seen that the RY closure always looks like the PY closure at small separations. The latter is however inaccurate for a long-range interaction lacking a hard core. We

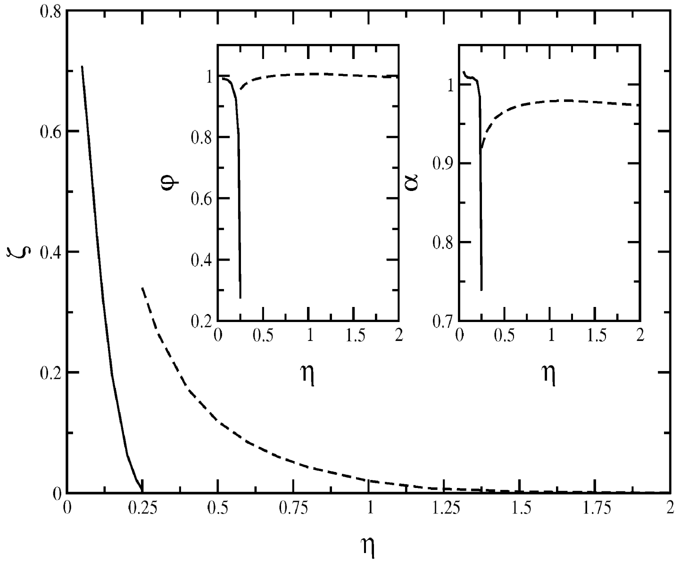

Fig. 20. The self-consistency parameters of the ZSEP closure applied to the Gaussian core model at reduced temperature $t = 0.01$ as functions of the packing fraction η. The solid lines denote the physical and the dashed lines the unphysical branch (see the text).

attempted to modify the RY closure by employing mixing functions yielding a HNC-like small-r behavior and a PY-like large-r behavior. However, these did not yield self-consistency parameters for the whole range of densities. Despite of its inability to correctly describe the high-density penetration of $g(r)$, the standard RY closure yields, nevertheless, a self-consistency parameter α for all densities considered here. In addition, this parameter grows with density, thus pointing to a tendency of the RY closure to reduce to the HNC at high packings.

In view of the failure of the RY-closure, we are led to consider the ZSEP closure which has *precisely* the property that in its implementation the value of $g(r)$ at zero separation plays an important role and is determined self-consistently. In fact, the resounding success of the ZSEP in describing the $g(r)$ of the PSM model (also a bounded interaction) has been mainly attributed to this property [177]. As can be seen from Figs. 17 and 18(a), the ZSEP performs only slightly worse than the RY closure up to a packing fraction $\eta \approx 0.25$. The self-consistency parameters ζ, φ and α of the ZSEP are displayed in Fig. 20. The parameter ζ which appears as an overall factor in the parameterization of the bridge function [see Eq. (3.95)] decreases with density and close to $\eta = 0.25$ it is small enough and the ZSEP practically reduces to the HNC closure.

However, at packing fractions $\eta > 0.25$, a *second branch* of solutions appears, which is denoted by the dashed lines in Fig. 20. This branch is disconnected from the first and hence it causes the $g(r)$ to behave discontinuously at this packing fraction, a result which is clearly unphysical. This second branch produces $g(r)$'s that show *too much penetration* and too little structure, when compared with the simulation results. The reason for this unphysical behavior can be traced to the fact that this second branch corresponds to bridge functions which are *positive* at small separations r. Indeed, from Eq. (3.95), and taking into account that $\gamma(r) \gg 1$ at small separations, we can see that $B_{\mathrm{ZSEP}}(r)$

has the sign of the product $\zeta(\varphi - \alpha)/\alpha$. For the first, physical branch (solid lines in Fig. 20) this combination is *negative* because $\varphi < \alpha$. For the second, unphysical branch, this combination is positive because $\varphi > \alpha$ there. A positive bridge function acts then as an additional "attractive potential" in Eq. (2.59) and causes the overpenetration in $g(r)$ mentioned above.

The appearance of a branch of solutions of the ZSEP for which the bridge function is positive is a sign of internal inconsistency of the closure and in this sense the ZSEP signals its own limits of applicability. Indeed, the bridge function of any system has been shown to be a quasi-universal function, which can always be mapped onto the bridge function of a suitably defined hard-sphere system having a hard-sphere diameter that depends on the characteristics of the interaction and the thermodynamic point under consideration [80]. The bridge function of the HS system is, however, practically exactly known and it is essentially a negative function for all r. Hence, a positive bridge function is physically unacceptable and the second branch of solutions of the ZSEP has to be discarded. The results from this second branch come again into very good agreement with simulation at packing fractions above $\eta \approx 1.00$ because, as seen in Fig. 20, the parameter ζ is already very small there and the bridge function has a negligible contribution to $g(r)$; even the unphysical branch reduces to the HNC at high densities. However, there is no way to bridge the physical solutions at packings $\eta \leq 0.25$ with the HNC-like solutions *within* the ZSEP closure, that is without having to compare with independently produced simulation results.

We comment next on the quality of the HNC. As can be seen from Figs. 17–19, the HNC underestimates the structure at small-to-intermediate packings but yields otherwise reasonable results. It does not suffer from any of the problems of the more sophisticated closures and, in fact, it seems to be the best at high densities. In order to further explore this property (which is supported by the fact that the other two closures tend to the HNC at this limit), we also solved this closure at *extremely high* packing fractions. Here, the highest packing at which we simulated was $\eta = 6.00$, due to time constraints. With increasing η, a very large number of particles would be required in the simulation box in order to obtain reliable results. In view of the fact that the HNC gives results which coincide with those from Monte-Carlo at $\eta = 6.00$ [see Fig. 19(b)], we gain confidence at this closure and apply it for arbitrarily high densities, in order to obtain information on the structure of the very dense fluid. In Fig. 21(a), we show results for $g(r)$ where it can be seen that at very high packings $g(r)$ tends to unity and hence $h(r) = g(r) - 1$ tends to zero. However, this does not mean that the structure factor $S(Q)$ tends to unity as well, as a naive guess based on the definition $S(Q) = 1 + \rho\tilde{h}(Q)$ would imply. The quantity $\tilde{h}(Q)$ tends to zero but at the same time the prefactor ρ diverges, thus giving rise to a nontrivial $S(Q)$.

Results for the corresponding structure factor $S(Q)$ are shown in Fig. 21(b). It can be seen that, for high densities, the peak of $S(Q)$ disappears and the latter looks like a "smoothed step function" with values ranging from zero to one. The value of Q at which the crossover occurs does not scale as a power law of the density but rather shifts to the right by almost a constant every time the packing fraction is increased by an order of magnitude. This hints to a very weak dependence of this crossover value on the density; we return to this point in Section 3.5.4.

The liquid-state correlation functions display an anomalous behavior in comparison with that of "normal" liquids, interacting by means of hard, unbounded interactions. For the latter, the structure grows monotonically with increasing density and eventually the systems freeze. Here, the structure grows up to a packing fraction $\eta \cong 0.12$ at $t = 0.01$ and for higher densities it becomes weaker again. To amply demonstrate this phenomenon we show in Fig. 22 the structure factors

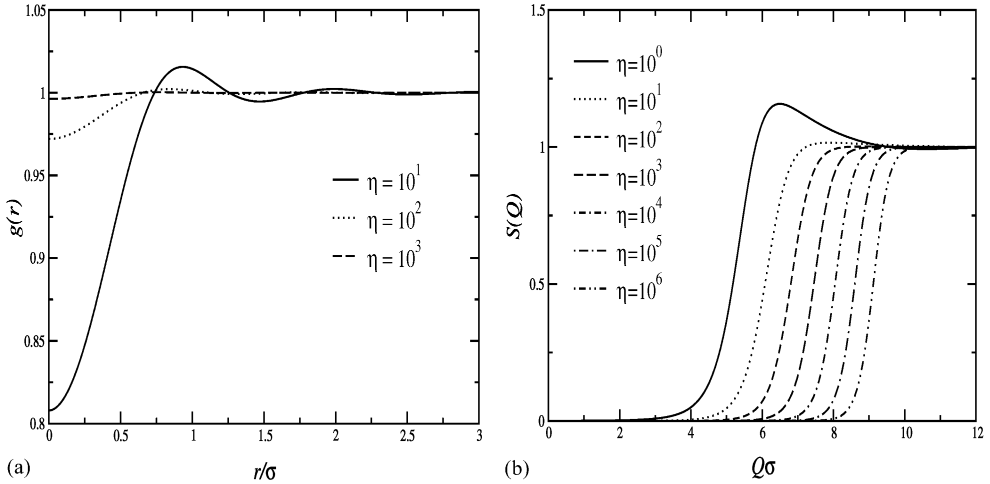

Fig. 21. (a) The radial distribution function $g(r)$ and (b) the structure factor $S(Q)$ as obtained by the HNC closure for $t = 0.01$ and extremely high values of the packing fraction.

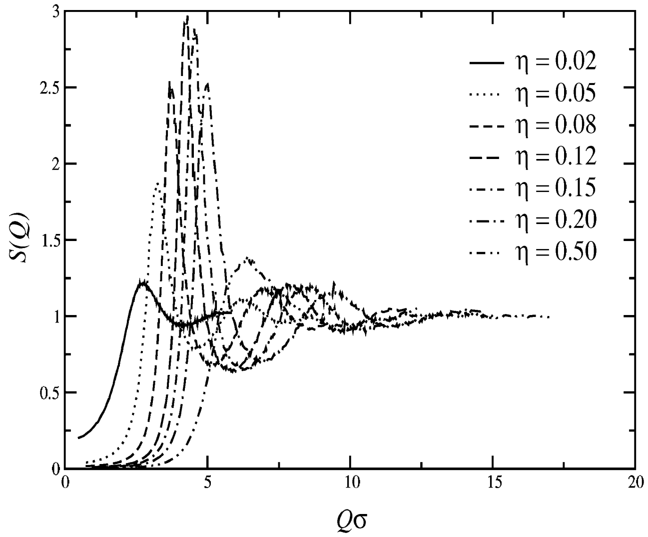

Fig. 22. The structure factor $S(Q)$ of the GCM at $t = 0.01$ for different packing fractions, as obtained by Monte-Carlo simulation.

obtained from the MC simulations for a wide range of densities, where it can be seen that the height of the peak of $S(Q)$ attains its maximum value at $\eta \cong 0.12$. This behavior of $S(Q)$ is closely related to reentrant melting, because the height of the maximum of $S(Q)$ is a diagnostic tool for the freezing transition, according to the Hansen–Verlet criterion [170,171]. The evolution of $S(Q)$ with density shown in Fig. 22 in conjunction with this criterion implies that the system approaches crystallization at about $\eta = 0.12$ and then remelts. The height of the peak at $\eta = 0.12$, which is indeed slightly above the Hansen–Verlet value 2.85, implies that at this temperature the system barely freezes and that $t = 0.01$ is very close to the upper freezing temperature. We will confirm this prediction in Section 3.5.6.

Finally, we have performed MC simulations and solved the HNC closure also at much higher temperatures, $t = 1.00$, corresponding to the physical domain for the effective interactions between polymer chains. There, we found that the HNC accurately reproduces the simulation results at all densities and that the liquid has very little structure, a result which can be easily understood in view of the fact that the thermal energy, which is equal to the interaction strength there, washes out the correlation effects caused by the interactions.

3.5.4. The high-density limit in the fluid state

The results of the preceding section on the structure of the fluid at high densities point out that the correlations are becoming weaker as density grows and that the system approaches some kind of "infinite-density ideal gas" limit, where $g(r) = 1$. This limit was assumed already by Stillinger [155]. There, the internal energy of a high-density fluid was approximated by that of a *random distribution* of points interacting by means of the Gaussian potential, i.e., the positions of the points were assumed to be uncorrelated. The relation $g(r) = 1$ was used explicitly in deriving an estimate for the internal energy of the high-density fluid and it was shown that, in fact, the complete absence of a correlation hole in the fluid raises its internal energy with respect to that of a solid (where a correlation hole is necessarily present) by exactly $\varepsilon/2$ per particle, see Eq. (3.90). Yet, the existence of this ideal-gas limit was *not proven*. Here, we present a density functional mean-field theory which establishes this limit and provides analytic expressions for the correlation functions of the GCM fluid at high densities [160].

An approximate density functional theory amounts to introducing an approximation for the excess part of the free energy functional, see Eq. (2.70). We consider the limit $\rho\sigma^3 \gg 1$. The average interparticle distance $a \equiv \rho^{-1/3}$ becomes vanishingly small in this limit and it holds $a \ll \sigma$, i.e., the potential is extremely long range. Every particle is simultaneously interacting with an enormous number of neighboring molecules and in the absence of short-range excluded volume interactions the excess free energy of the system can be approximated by a simple mean-field term, equal to the internal energy of the system:

$$F_{\mathrm{ex}}[\rho(\boldsymbol{r})] \cong \frac{1}{2}\iint \mathrm{d}\boldsymbol{r}\,\mathrm{d}\boldsymbol{r}'\, v(|\boldsymbol{r}-\boldsymbol{r}'|)\rho(\boldsymbol{r})\rho(\boldsymbol{r}') \tag{3.97}$$

with the approximation becoming more accurate with increasing density and eventually exact at $\bar{\rho} \to \infty$. The direct correlation function $c(|\boldsymbol{r}-\boldsymbol{r}'|;\rho)$ in a fluid of density ρ is given by the second functional derivative of $F_{\mathrm{ex}}[\rho(\boldsymbol{r})]$ with respect to the density [79], namely

$$c(|\boldsymbol{r}-\boldsymbol{r}'|;\rho) = -\lim_{\rho(\boldsymbol{r})\to\rho} \frac{\delta^2 \beta F_{\mathrm{ex}}[\rho(\boldsymbol{r})]}{\delta\rho(\boldsymbol{r})\delta\rho(\boldsymbol{r}')}\ . \tag{3.98}$$

Combining Eqs. (3.97) and (3.98) we find that the direct correlation function (dcf) of the system at high densities becomes independent of ρ and is simply proportional to the interaction:

$$c(r) = -\beta v(r)\ . \tag{3.99}$$

Eq. (3.99) above has a strong similarity with the mean-spherical approximation (MSA) [4,178], introduced as a perturbation theory to study systems interacting by potentials that can be separated into a hard-sphere interaction (diameter σ_{HS}) $v_0(r)$ and a "soft tail" $\phi(r)$. In the MSA, the radial distribution function of the system $g(r)$ vanishes for $r < \sigma_{\mathrm{HS}}$ and the direct correlation function $c(r)$ at $r > \sigma_{\mathrm{HS}}$ is given by $c(r) = -\beta\phi(r)$. The main difference from the MSA here, is that there is *no reference potential* $v_0(r)$ because there are no hard cores in the system. Hence, Eq. (3.99) holds with the *total* interaction on the right-hand side and for the *whole range* of separations r. Moreover, unlike the MSA which is essentially a high-temperature approximation, Eq. (3.99) holds for the whole temperature range, provided that the density is high enough ($\rho\sigma^3 \gg 1$). Of course, the mean-field approximation becomes also valid at high temperatures ($t \gg 1$) irrespective of the density, because there the thermal energy completely dominates over the *bounded* interaction. This happens in contradistinction with diverging interactions, where short-range correlation effects always survive.

The Fourier transform $\tilde{c}(Q)$ of the dcf is obtained easily from Eqs. (3.99) and (3.69), and for the GCM it has the form

$$\tilde{c}(Q) = -\pi^{3/2}\beta\varepsilon\sigma^3 \exp[-(Q\sigma/2)^2] . \tag{3.100}$$

Using the Ornstein–Zernike equation and the ensuing relation $S(Q) = [1 - \rho\tilde{c}(Q)]^{-1}$ we obtain for the structure factor the expression:

$$S(Q) = \frac{1}{1 + \pi^{3/2}\beta\varepsilon\rho\sigma^3 \exp[-(Q\sigma/2)^2]} . \tag{3.101}$$

This analytic expression is compared with the MC result at $\beta\varepsilon = 100$ ($t = 0.01$) and $\eta = 6.00$ in Fig. 23. The excellent agreement between the two demonstrates the validity of the simple

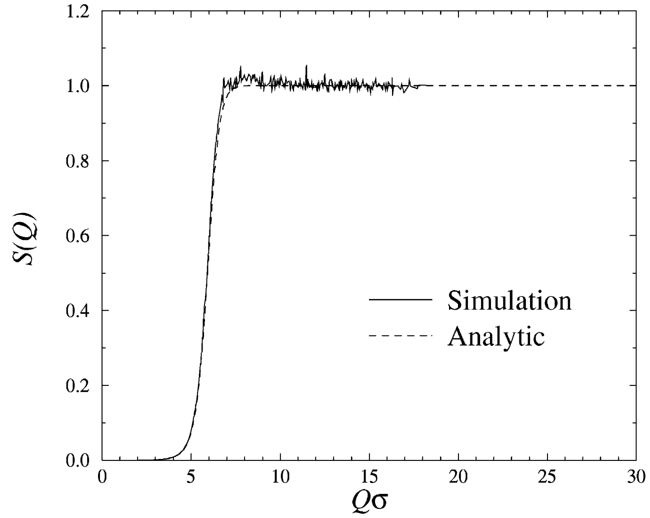

Fig. 23. The structure factor $S(Q)$ of the GCM at $t = 0.01$ and $\eta = 6.00$ as obtained from simulation (solid line) and as given by the analytical expression, Eq. (3.101) (dashed line).

mean-field theory at high densities. Eq. (3.101) shows that at high densities $S(Q)$ is a monotonic function of Q and has the shape of a "smoothed step function" with values ranging from $(\pi^{3/2}\beta\varepsilon\rho\sigma^3)^{-1} \cong 0$ at low Q's to unity at high Q's. The crossover between the two regimes occurs at a characteristic wavenumber Q_* at which $S(Q) = 1/2$ and which, according to Eq. (3.101), is given by

$$Q_*\sigma = 2\sqrt{\ln(\pi^{3/2}\beta\varepsilon\rho\sigma^3)} \,. \tag{3.102}$$

Note the very weak, square root-logarithmic dependence of Q_* on density and the inverse temperature.

Another quantity of interest is the isothermal compressibility χ_T of the system, defined as

$$\chi_T = \left(\Omega\frac{\partial^2 F}{\partial\Omega^2}\right)^{-1} , \tag{3.103}$$

where F is the Helmholtz free energy, and also related to the $Q \to 0$ limit of $S(Q)$ through the compressibility sum rule, Eq. (2.57). Expressions (2.70) and (3.97) yield the Helmholtz free energy in the high-density limit as

$$F = k_B T N[\ln(\rho\Lambda^3) - 1] + \tfrac{1}{2}N\pi^{3/2}\varepsilon\rho\sigma^3 \,. \tag{3.104}$$

From Eqs. (3.103) and (3.104) we obtain

$$\chi_T = \frac{1}{k_B T\rho + \pi^{3/2}\varepsilon\rho^2\sigma^3} , \tag{3.105}$$

which evidently satisfies the compressibility sum rule (2.57) with $S(Q)$ given by Eq. (3.101). We note that at high densities χ_T obeys the scaling

$$k_B T\chi_T \sim t\rho^{-2} \,. \tag{3.106}$$

Moreover, from Eq. (3.104) the pressure $P = -(\partial F/\partial\Omega)$ is obtained as

$$P = k_B T\rho + \tfrac{1}{2}\pi^{3/2}\varepsilon\rho^2\sigma^3 \,. \tag{3.107}$$

The quadratic scaling of the (osmotic) pressure P with the density (at $\rho\sigma^3 \gg 1$) results naturally in the framework of the mean-field theory, under the assumption of a *density-independent* pair potential. Louis et al. [151] combined this fact with the slight concentration dependence of the Gaussian potential parameters for real chains above the overlap concentration, to establish that the full scaling reads as $P \sim \rho^{9/4}$, in full agreement with the predictions of the scaling theory, see Eq. (3.44). The recovery of such a nontrivial result, whose derivation was originally based on considerations about the dependence of the pressure on the degree of polymerization, through a colloidal approach which reduces every chain to a "point particle" is a strong confirmation of the validity of the latter approach.

Since $S(Q) = 1 + \rho\tilde{h}(Q)$, Eq. (3.101) immediately yields an analytic expression for the Fourier transform $\tilde{h}(Q)$ of the correlation function $h(r)$, namely

$$\tilde{h}(Q) = -\frac{\pi^{3/2}\beta\varepsilon\sigma^3\exp[-(Q\sigma/2)^2]}{1 + \pi^{3/2}\beta\varepsilon\rho\sigma^3\exp[-(Q\sigma/2)^2]} \,. \tag{3.108}$$

At low Q's, where the exponential is of order unity, the term proportional to the density in the denominator dominates and $\tilde{h}(Q)$ behaves as $-\rho^{-1} \to 0$ as $\rho \to \infty$. At high Q's, the exponential itself tends to zero. Hence, the function $\tilde{h}(Q)$ vanishes as $\rho \to \infty$ with the leading term being proportional to ρ^{-1}. Consequently, the correlation function $h(r)$ vanishes as well and $g(r) \to 1$ as $\rho \to \infty$. This is the particular "high-density ideal gas" limit of the model. However, a clear distinction must be drawn between this "interacting ideal gas" and the usual ideal gas, in which either the system is noninteracting or an interacting system is considered at the opposite limit, $\rho \to 0$. In the usual ideal gas limit, we have $c(r) = \exp[-\beta v(r)] - 1$, $S(Q) = 1$ and $g(r) = \exp[-\beta v(r)]$. The ideal gas pressure P scales linearly with the density and the ideal compressibility χ_T scales with ρ^{-1}. Here, $c(r) = -\beta v(r)$, $S(Q)$ is not unity in the whole Q range, the pressure scales as ρ^2 [see Eq. (2.64)] and the isothermal compressibility as ρ^{-2} [see Eq. (3.106)]. Nevertheless, the above considerations point out to a kind of interesting *duality* of the GCM in the liquid phase, in which the system is trivially ideal at low densities and becomes again ideal (vanishing correlations) at high densities. This can be thought of as the counterpart for the fluid state of the duality discovered by Stillinger in the crystalline state [159].

The mean-field approximation put forward in this section is not limited to the Gaussian potential. It is valid for all interactions $v(r)$ which are finite, analytic functions and which tend to zero fast enough at infinite separations so that the thermodynamic functions are extensive and the Fourier transform of $v(r)$ exists, as we discuss in Appendix C. In addition, it can now be understood why the HNC showed the best agreement with simulation results among all closures at high densities. As $g(r) \to 1$, and $c(r) \to -\beta v(r)$ in this limit, the exact relation (2.59) forces the bridge function $B(r)$ to vanish. For bounded, analytic potentials decaying fast enough to zero, the HNC becomes *exact* at high densities. A systematic comparison between the HNC, the mean-field approximation and refinements of the latter has been performed in the recent work of Louis et al. [169], confirming the fact that at high densities the mean-field approximation and the HNC become both exact.

3.5.5. The solid: Einstein model

In this section we present the approach employed for the calculation of the free energies of candidate crystalline states of the model. As we are dealing with a soft interaction, a harmonic approximation in the solid is justified and we adopt the simple Einstein model [15,16] as a means to estimate the free energy of the latter. The approach is based on the Gibbs–Bogoliubov inequality [4]. The latter states that the Helmholtz free energy F of a system having Hamiltonian $\mathscr{H}$ is related to the Helmholtz free energy F_0 of a reference system having Hamiltonian $\mathscr{H}_0$ by

$$F \leq F_0 + \langle \mathscr{H} - \mathscr{H}_0 \rangle_0 , \tag{3.109}$$

where the average on the right-hand side is taken in the reference system. The procedure is useful if (i) a simple enough reference Hamiltonian can be chosen, which physically corresponds to a situation close enough to the real one, and in which F_0 and the average $\langle \mathscr{H} - \mathscr{H}_0 \rangle_0$ can be calculated in a straightforward way and (ii) this Hamiltonian contains at least one variational parameter which can be chosen in order to minimize the right-hand side, obtaining in this way a lower upper bound for the true free energy of the system.

In a harmonic solid, a reasonable noninteracting reference system is the Einstein solid, characterized by the Hamiltonian

$$\mathscr{H}_0 = \sum_{i=1}^{N} \left[\frac{\boldsymbol{p}_i^2}{2m} + \frac{k}{2}(\boldsymbol{r}_i - \boldsymbol{R}_i)^2 \right], \tag{3.110}$$

where $\boldsymbol{p}_i$ is the canonical momentum of a particle of mass m, k is the "spring constant" which plays the role of a variational parameter and the set $\{\boldsymbol{R}_i\}$ forms a prescribed Bravais lattice. The real Hamiltonian reads as

$$\mathscr{H} = \sum_{i=1}^{N} \frac{\boldsymbol{p}_i^2}{2m} + \sum_{i=1}^{N} \sum_{j=i+1}^{N} \varepsilon \exp\left(-\frac{|\boldsymbol{r}_i - \boldsymbol{r}_j|^2}{\sigma^2} \right). \tag{3.111}$$

The calculation of the Helmholtz free energy in the Einstein model is a trivial exercise yielding

$$\frac{F_0}{N} = \frac{3}{2} k_{\mathrm{B}} T \ln\left(\frac{\tilde{\alpha}}{\pi} \right) + 3 k_{\mathrm{B}} T \ln\left(\frac{\Lambda}{\sigma} \right), \tag{3.112}$$

where

$$\tilde{\alpha} = \frac{\beta k \sigma^2}{2}. \tag{3.113}$$

The one- and two-particle densities in the reference system are given by a sum of Gaussians and a double sum of products of Gaussians, respectively, where the latter are centered on lattice sites and the sums are carried upon all these sites. As the interaction has itself a Gaussian form, the calculation of the quantity $\langle \mathscr{H} - \mathscr{H}_0 \rangle_0$ reduces to integrals that can be carried out analytically. The final result is very simple and reads as

$$\frac{\langle \mathscr{H} - \mathscr{H}_0 \rangle_0}{N} = \frac{1}{2} \sum_{j \neq 0} n_j \left(\frac{\tilde{\alpha}}{\tilde{\alpha} + 2} \right)^{3/2} \varepsilon \exp\left(-\frac{\tilde{\alpha} X_j^2}{\tilde{\alpha} + 2} \right) - \frac{3 k_{\mathrm{B}} T}{2}. \tag{3.114}$$

The sum on the rhs is carried over all shells of lattice vectors, i.e., sets of lattice vectors of equal length, with the shell $j = 0$ (self-interaction) excluded. The quantity n_j is the number of lattice vectors belonging to a shell and $X_j = |\boldsymbol{R}_j|/\sigma$. It can be easily seen that at $T = 0$, where $\tilde{\alpha} \to \infty$, the first term on the rhs of Eq. (3.114) reduces to the internal energy per particle of the considered crystalline arrangement, the *lattice sum*. At zero temperature there is no variational parameter and the Einstein model becomes exact; the winning phase is the one with the lowest lattice energy. At finite temperatures, the sum of the terms on the rhs of Eqs. (3.112) and (3.114) has to be minimized with respect to $\tilde{\alpha}$ for any given lattice structure. The minimum comes about through the competition of the entropic, logarithmic term on the rhs of Eq. (3.112), which favors delocalization at $\tilde{\alpha} = 0$ and the internal energy term on the rhs of Eq. (3.114) which favors localization at $\tilde{\alpha} \to \infty$. The obtained value is then the estimate for the Helmholtz free energy of the given lattice and the procedure can be repeated for every candidate lattice. We note that the term $3 k_{\mathrm{B}} T \ln(\Lambda/\sigma)$ on the rhs of Eq. (3.112) can be dropped because it occurs for all possible phases of the system, fluid and solid, and does not affect the free energy comparisons between them.

We have performed the minimization for a different number of candidate lattice structures: fcc, bcc, simple cubic, diamond and body-centered orthogonal. We always assumed a lattice with a single occupancy per site, based on the result of Stillinger stating that indeed solids with multiply occupancies are unstable [155]. For the whole range of temperatures $0 \le t \le 0.015$ considered, we always found the fcc and bcc to be the only stable crystals, with the former winning at low densities and the latter at high densities. The quantitative results are presented in Section 3.5.6 below.

3.5.6. *Quantitative phase diagram*

In this section we switch from the variable η to the variable $\bar{\rho} \equiv \rho\sigma^3$ as a measure of the density, in order to allow for a comparison with the approximate results of Stillinger and Stillinger [161]. With the free energy of the crystals obtained by the procedure outlined in Section 3.5.5, the phase diagram can be drawn if the corresponding free energy of the fluid is also known. The latter can be obtained from the results of the integral equation theories outlined in Section 3.5.3.

The Helmholtz free energy of the liquid can be calculated by the virial or the compressibility route (see Section 2.4.1). The RY and ZSEP closures are thermodynamically consistent, hence in these closures both routes yield the same result, but the HNC is not. However, as explained in Section 3.5.3, neither the RY nor the ZSEP yield reliable results for the whole density range. If we were dealing with a usual system, without reentrant melting, then we could have used the RY or the ZSEP results at low or intermediate densities. However, we are interested also in the high-density fluid free energies, where in fact the HNC becomes exact. A combination of low-density results from one closure and high-density results from another is not of much use either, because it would produce unphysical discontinuities in the free energy or its derivatives at the point of switching between the two. We are thus led to employ the HNC closure in the whole density domain in order to perform the thermodynamic integration and obtain the fluid free energy.

The HNC compressibility route yields at low densities fluid free energies that are too low, leading to the erroneous result that the HS-like freezing of the Gaussian fluid into a fcc lattice does not take place. There are two factors playing an important role here: on the one hand, the predicted isothermal compressibilities are too high causing a fluid free energy which is too low and on the other hand, the solid free energy, being a product of the variational procedure outlined in Section 3.5.5, is unavoidably higher than the true one. It is therefore pertinent to follow the HNC virial route in calculating the fluid free energy. The latter leads indeed to an overestimation of the fluid free energy but this compensates for the overestimation of the solid free energy and leads to the physically correct picture of freezing into an fcc solid at the low-density part of the phase diagram. We have thus calculated the fluid free energies through the HNC virial route for a range of temperatures $10^{-5} \le t \le 0.015$ for a range of densities $0 \le \rho\sigma^3 \le 1.00$ and performed the common tangent construction on the resulting free energy density curves to obtain the phase boundaries. The resulting phase diagram is shown in Fig. 24.

The phase diagram obtained is very similar to the approximate one drawn by Stillinger and Stillinger [161]. It shows the sequence of freezing, structural (fcc → bcc) and remelting transitions as well as the upper freezing temperature t_u associated with the corresponding density $\bar{\rho}_u$. The coordinates of this point, where the fluid-bcc coexistence lines turn around, are $(t_u, \bar{\rho}_u) = (0.0102, 0.2292)$. This is in perfect agreement with the preliminary results from Section 3.5.3, where at $t = 0.01$ the structure factor at $\eta = 0.12$, corresponding to $\bar{\rho} = 0.2292$, was found to slightly exceed the Hansen–Verlet value. The fcc–bcc coexistence lines run linearly from the points $\bar{\rho}_{\mathrm{fcc}} = 0.17941$ and $\bar{\rho}_{\mathrm{bcc}} = 0.17977$ at $t = 0$ to the points $\bar{\rho}_{\mathrm{fcc}} = 0.16631$ and $\bar{\rho}_{\mathrm{bcc}} = 0.16667$ at the triple temperature $t_t = 8.753 \times 10^{-3}$. The density gap between the fcc- and bcc-coexisting densities

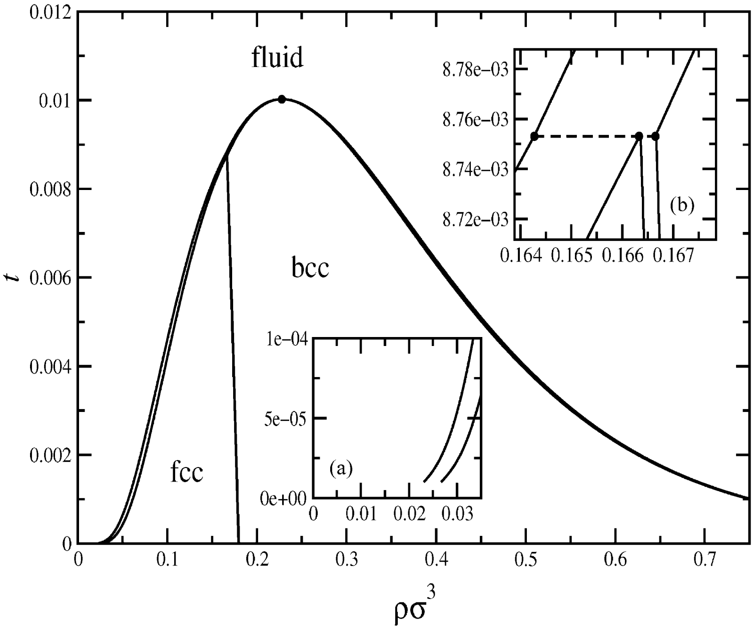

Fig. 24. The phase diagram of the GCM obtained by the approach described in the text. The fcc–bcc coexistence lines are also double lines but they cannot be resolved in the scale of the figure because the fcc–bcc density gap is too small. The full dot marks the point at which the fluid-bcc coexistence curves turn around. The two insets show details of the phase diagram. (a) In the neighborhood of zero densities and temperatures. (b) In the neighborhood of the fluid-fcc–bcc triple temperature, with the dashed line denoting the triple line between these coexisting phases.

remains constant and equal to $\Delta\bar{\rho} = 3.6 \times 10^{-4}$. The density of the coexisting fluid at the triple temperature is $\bar{\rho}_{\text{fluid}} = 0.16431$.

It should be emphasized that, notwithstanding its deceiving appearance in Fig. 24, the point $(t_u, \bar{\rho}_u)$ is *not* a critical point. At $(t_u,\bar{\rho}_u)$, two common tangents between the fluid- and bcc-solid free energies, one lying on the low- and the other on the high-density side of it, coalesce into this single point. No susceptibility diverges and all free energy density curves remain strictly concave up.

It is now pertinent to ask whether the Hansen–Verlet freezing criterion is satisfied for both the low- and the high-density crystallization of the system. To this end, we have performed additional MC simulations at temperatures below t_u and in Fig. 25 we show structure factors at two such temperatures, $t = 0.007$ and 0.005, for increasing values of the density. It can be seen that the Hansen–Verlet criterion is indeed valid for both freezing transitions.

It is of course also possible to calculate the free energies of the various candidate phases in a simulation, by means, e.g., of the virial route in the fluid state and by employing the Frenkel–Ladd method [11,77,179] in the solid state. However, the latter is very time consuming. The very good agreement between the phase boundaries obtained from the approximate theory presented here and the MC results regarding the height of the peak of $S(Q)$ and the spontaneous crystallization of the system in the simulation box, lead us to believe that the phase diagram of Fig. 24 is quantitatively correct.

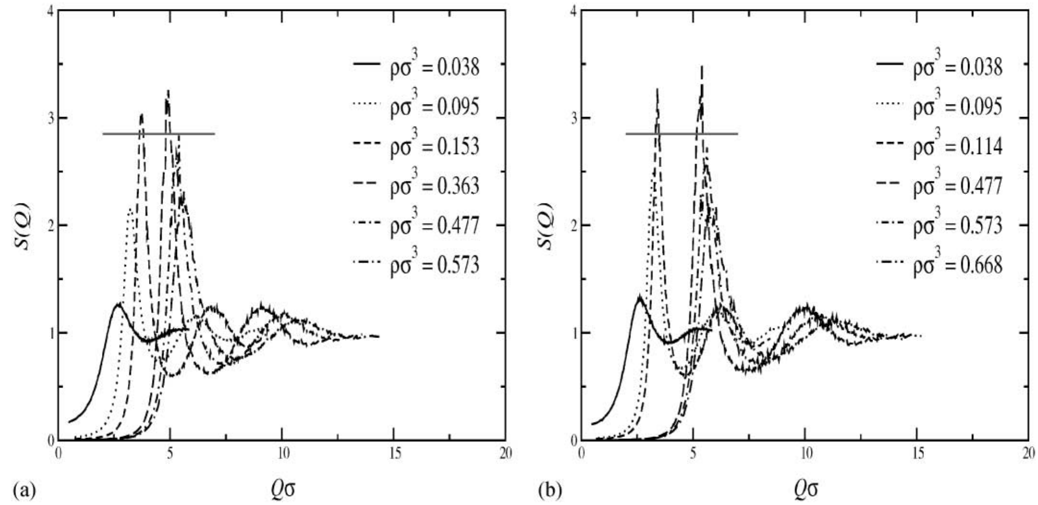

Fig. 25. Structure factors $S(Q)$ for the GCM at (a) $t = 0.007$ and (b) $t = 0.005$ obtained from MC simulations. Densities as indicated in the legends. The straight lines mark the Hansen–Verlet value 2.85. The corresponding structure factors in the regions $0.153 \lesssim \rho\sigma^3 \lesssim 0.363$ for $t = 0.007$ and $0.114 \lesssim \rho\sigma^3 \lesssim 0.477$ for $t = 0.005$ show Bragg peaks, indicating that the GCM has to be in the solid state for these densities.

3.6. The peculiarities of bounded interactions

The Gaussian core model displays a whole range of novel phenomena and properties: an anomalous dependence of the correlation functions on the density, a high-density "ideal gas limit", reentrant melting, an upper freezing temperature, etc. Many of these characteristics arise from the fact that the pairwise interaction does not diverge at zero separation, i.e., it is bounded. However, the topology of the phase diagram of the GCM has some striking similarities with that of star polymers, to be discussed in Section 5, obtained by employing a *diverging* interaction. An upper freezing parameter, above which the systems remain fluid at all densities, as well as reentrant melting appear in both.

Another example of a system interacting by means of a bounded interaction is the so-called "penetrable spheres model" (PSM) [77,167], which is analyzed in Appendix B. The pair potential of the PSM reads as

$$v(r) = \begin{cases} \varepsilon & \text{if } r < \sigma\ , \\ 0 & \text{if } r > \sigma\ , \end{cases} \tag{3.115}$$

where σ is the diameter of the spheres and ε is the height of the energy barrier ($\varepsilon > 0$). Evidently, this is also a bounded interaction but, as shown in Appendix B, the phenomenology and the associated phase diagram of the PSM are quite different from those of the GCM, as can be seen by a comparison between Figs. 24 and 57. In the PSM no reentrant melting occurs and the system seems to freeze at *all* temperatures into increasingly clustered solids [177,180]. The reason for this difference is, evidently, that in the PSM, the particles can build clusters whereas in the GCM this is not favored energetically. Recently, Likos et al. [168], derived an exact criterion establishing whether the phase diagram of a given system interacting by means of a bounded potential will display clustering or reentrant melting behavior. As the presentation of this result would interrupt the flow of the text, we present it in detail in Appendix C.

3.7. The volume terms for polymer solutions

In Eq. (3.49) we wrote down the general expression for the effective Hamiltonian between the centers of mass of polymer chains in a solution, featuring interactions of all orders as well as volume terms. In the preceding sections, however, we only considered the pair-potential approximation, on the one hand, and ignored the volume terms, on the other. Many-body terms are in general very difficult to take into account. Yet, their effect can be mimicked by a density-dependent parameter $\sigma = \sigma(\rho)$ [22,68,151] and therefore we do not expect that they will produce any qualitative change of the phase behavior of the system. The volume terms, on the other hand, can induce phase transitions or modify the phase boundaries, as already discussed in Section 2.5. The main question is whether these terms have a positive or negative curvature with respect to the density. In the temperature range corresponding to real chains in athermal solvents, $t \sim 1$, the GCM displays no phase transitions. Hence, volume terms with a positive curvature will not change the phase behavior of the system. The phase transitions which occur at temperatures below t_u are only of theoretical interest, as there is no physical mechanism to make the energy barrier between real polymer chains two orders of magnitude higher than the thermal energy. Accordingly, we focus on the physical regime of real chains and estimate the volume terms for this case.[16]

Let us visualize every chain as a sphere of typical size σ which is, in general, density-dependent, $\sigma = \sigma(\rho)$. This density dependence corresponds to the physical situation of the shrinking of chains above the overlap concentration, presented in Section 3.3.3. We assume the centers of mass of the chains to be arranged on a lattice having Wigner–Seitz cell of linear extent σ, so that there are no overlaps between the chains and hence no contributions to the free energy of the solution due to interactions. The only change in the free energy, with respect to that of a dilute solution, comes through the cost of compressing N_c chains together. This is an extensive contribution, $\Delta F = N_c f_c(\rho) = \Omega\rho f_c(\rho)$, where $f_c(\rho)$ denotes the free energy cost for the compression of a single chain and depends only on the average density ρ. Accordingly, we take ΔF to be a reasonable estimate for the volume term $\Omega f_0(\rho)$ of Eq. (3.49), with the implication that the estimate for the term $f_0(\rho)$ is

$$f_0(\rho) = \rho f_c(\rho) . \tag{3.116}$$

Associated with the compression of the chain from its natural size $\sigma(0)$ down to a size $\sigma(\rho) < \sigma(0)$ is a free energy cost

$$f_c(\rho) = -4\pi \int_{\sigma(0)}^{\sigma(\rho)} \Pi(r) r^2 \, dr , \tag{3.117}$$

---

[16] The argument that follows has been originally put forward by Hartmut Löwen in the context of star polymer solutions.

where $\Pi(r)$ is the osmotic pressure as a function of the distance from the center of mass of the chain. Considering the space occupied by the chain as a dilute polymer solution of local concentration $\phi(r)$, we have, according to Eq. (3.30):

$$\Pi(r) = k_B T \frac{\phi(r)}{N} . \tag{3.118}$$

Moreover, following Flory-type arguments, we assume a uniform monomer distribution $\phi(r) = \phi$ given as the average number of monomers in the volume occupied by the chain, i.e.,

$$\phi \propto \frac{N}{\sigma^3(\rho)} \tag{3.119}$$

with some geometrical proportionality constant of order unity. Gathering the results from Eqs. (3.117)–(3.119) we obtain

$$f_c(\rho) \propto k_B T \left[\left(\frac{\sigma(\rho)}{\sigma(0)} \right)^{-3} - 1 \right] . \tag{3.120}$$

The dependence of the chain size on density[17] was determined in Section 3.3.3. The size of the chain remains constant and equal to $\sigma(0)$ up to the overlap density ρ_* but afterwards it decays as $\rho^{-1/8}$, i.e.,

$$\frac{\sigma(\rho)}{\sigma(0)} = \begin{cases} 1 & \text{for } \rho < \rho_* , \\ \left(\dfrac{\rho}{\rho_*} \right)^{-1/8} & \text{for } \rho > \rho_* . \end{cases} \tag{3.121}$$

Eqs. (3.116), (3.120) and (3.121) imply that the term $f_0(\rho)$ *vanishes* for $\rho < \rho_*$ and for $\rho > \rho_*$ it has the density dependence:

$$f_0(\rho) \propto \rho_* \left[\left(\frac{\rho}{\rho_*} \right)^{11/8} - \left(\frac{\rho}{\rho_*} \right) \right] \quad (\rho > \rho_*) . \tag{3.122}$$

The linear term in Eq. (3.122) above is irrelevant and the first term has a positive second derivative with respect to the density. The volume terms do not produce any "hidden" phase transitions.

3.8. Concluding remarks

In this section we looked at the theory of polymer solutions from different points of view: the mean-field-type Flory theory for isolated chains and Flory–Huggins theory of solutions, the powerful scaling theory and the theory of effective interactions between centers of mass of the polymers. All these approaches are complementary in nature, as they offer different ways of

---

[17] In Section 3.3.3, the dependence of the polymer size on the *monomer* concentration c was considered, whereas here we look at its dependence on the *chain* concentration ρ. However, the two are related by the simple proportionality $c = N\rho$ and all scaling results for the c-dependence can simply be taken over for the ρ-dependence.

looking into the same problem. Depending on the questions asked, one could offer more insight than the other. This freedom to look at the system from various different points of view and to collect results from different theories, synthesizing them into a new picture, is quite usual and has been proven to be very fruitful in the field of complex fluids. In the coming sections, we will see how ideas from polymer and colloidal science come together in a unified new picture of effective interactions between more and more complex objects or mixtures.

We have seen how polymer chains can be thought of as very soft, interpenetrable spheres with an extent of the order of their radius of gyration. New phenomena, induced by this extreme softness, such as the inability to freeze the system above a certain upper temperature, arise. When steep interactions between the particles are present, these phenomena disappear. In the following section, we are going to make a big leap in the hardness of the constituent particles of the system and turn our attention to the interactions between hard colloidal particles which include in the mixture an additional, smaller component. We first go from “extremely soft” polymers to “extremely hard” colloidal particles and later, in Section 5, we will make an attempt to bridge the gap between these two borderline cases, by considering the hybrid colloidal system of star polymers.

4. Depletion interactions

In this section we discuss the ways in which an attraction between hard, index-matched colloidal particles can be introduced and tuned by the addition of a smaller component, such as nonadsorbing polymer. The quantitative characteristics of this attraction, commonly known as depletion interaction, are presented and their dependence on the size and concentration of the smaller component is analyzed. Subsequently, the effect of the depletion interaction on the macroscopic phase behavior of the colloidal suspension is discussed and it is demonstrated that a variation of the depth and/or range of the attraction can lead to a rich topology of phase diagrams. The latter can involve a single fluid and a single solid phase, two fluids and one solid or one fluid and two solids, depending on the quantitative characteristics of the depletion interaction.

4.1. Hard spheres

Depletion interactions are ubiquitous in mixtures of colloidal particles with smaller entities, when the latter experience an excluded volume interaction with the former. These interactions are purely entropic in nature. Therefore, it is pertinent to consider in some generality the – sometimes quite unexpected – effects of entropy. We start by considering the simplest physical system dominated by entropy, namely the hard-sphere (HS) system. This corresponds to a collection of particles of diameter σ, interacting by means of the potential:

$$v(r) = \begin{cases} \infty & \text{if } r < \sigma , \\ 0 & \text{if } r > \sigma . \end{cases} \tag{4.1}$$

In the HS system the interaction energy vanishes manifestly, as particles overlaps are excluded and for nonoverlapping configurations the interaction energy is equal to zero. Therefore, it is entropy alone that governs the phase behavior of the system. In particular, the equilibrium configuration at any given density $\rho = N/\Omega$ of N particles in the macroscopic volume Ω is the one that maximizes the free volume available to each particle. A common dimensionless measure of the density is the packing fraction η, defined as the fraction of the total volume Ω which is covered by the spheres and which is given by the relation

$$\eta = \frac{\pi}{6}\rho\sigma^3 . \tag{4.2}$$

The maximum or close-packing value of η is $\eta_{\mathrm{CP}} = \pi\sqrt{2}/6 \cong 0.74$ and it materializes for the fcc and the hcp crystalline arrangements [15]. The HS system undergoes an entropically driven freezing transition from a fluid, at low and intermediate densities, into a fcc-solid, at high densities [162–166,181]. The fluid freezes at packing fraction $\eta_{\mathrm{f}} = 0.494$ and the solid melts at packing fraction $\eta_{\mathrm{m}} = 0.545$. It is an apparent paradox that entropy drives a phase transition from a disordered into an ordered phase [182]. However, in the ordered phase the self-organization of the particles into a lattice allows for an increase of the free volume available to every one, in comparison to the free volume available in a diffusive, amorphous state as the liquid. This is an example of an *entropically driven* phase transition. The earliest example of such a transition is described in a classic paper by Onsager [183] for a system of hard rods. In the HS system, the temperature is irrelevant and its phase diagram is very simple and is schematically depicted in Fig. 26.

For many years, the HS system was a very useful but purely theoretical construction. A purely hard potential does not materialize in atomic systems. However, with the advance of colloidal science, it became possible to prepare samples which are extremely close in their behavior to an ideal HS system. By index-matching the particles with the surrounding solvent, the van der Waals

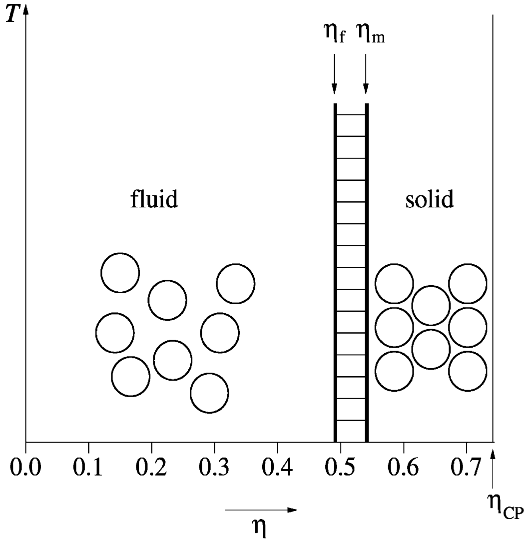

Fig. 26. The phase diagram of the HS system. The thick vertical lines are freezing and melting lines and their location is temperature-independent. The shaded region is the liquid–solid coexistence region.

attraction can be drastically reduced (see Section 2.2) and the interaction between the colloids is then dominated by the repulsive cores [184–186]. The equation of state of such a fluid was experimentally measured and found to be in excellent agreement with its theoretical counterpart for a HS system [187]. Using an appropriately prepared PMMA/decalin/CS_2 system, Pusey and van Megen [188,189] performed an experimental study of the phase behavior of the HS system, and observed the freezing and melting transitions at densities which are practically identical with those predicted from theory.

4.2. The depletion mechanism

Let us now consider a slightly more complicated system, i.e., a *mixture* of two kinds of spheres, large (diameter σ) and small (diameter τ). Following the terminology introduced in Section 2.3, we call the former species 1 and the latter species 2. Spheres of species 1 interact with each other by means of the HS potential, i.e., $v_{11}(r)$ is given by Eq. (4.1) above. To simplify the discussion, we assume that the small spheres do not interact with each other, i.e., $v_{22}(r) = 0$ but they have a HS interaction with the large ones. Thus, the interaction potential v_{12} is given by

$$v_{12}(r) = \begin{cases} \infty & \text{if } r < (\sigma + \tau)/2\ , \\ 0 & \text{if } r > (\sigma + \tau)/2\ . \end{cases} \tag{4.3}$$

We now consider just two large spheres in a sea of small ones, and kept fixed at distance R from each other, as shown in Fig. 27. According to the general theory presented in Section 2.3, the effective potential $V_{\mathrm{eff}}(R)$ between these two spheres, appropriately normalized so that it vanishes for $R \to \infty$, will be given by the expression

$$V_{\mathrm{eff}}(R) = v_{11}(R) - k_{\mathrm{B}} T \ln\left[\frac{Z_2(R)}{Z_2(\infty)}\right], \tag{4.4}$$

where $Z_2(R)$ is the configurational partition function of the small spheres in the presence of the large.[18] Due to the excluded volume interaction of Eq. (4.3) above, the small spheres are excluded from a sphere of diameter $\sigma + \tau$ surrounding each large sphere. The spherical shell with thickness $\tau/2$ surrounding each large sphere, depicted as a lightly shadow region in Fig. 27, is called the *depletion layer*. Every large sphere creates for the small an excluded volume equal to the sum of the sphere volume *plus* the volume of the depletion layer.

As all interactions are purely entropic in origin, $Z_2(R)$ is just the number $W(R)$ of (quantum) states that are available to the small particles in the presence of the large ones, and $k_{\mathrm{B}} \ln Z_2(R)$ is the corresponding entropy $S_2(R)$. Eq. (4.4) takes then the form

$$V_{\mathrm{eff}}(R) = v_{11}(R) - T[S_2(R) - S_2(\infty)]\ . \tag{4.5}$$

Let us now compare the two configurations shown in Figs. 27(a) and (b). In (a), the center-to-center separation R between the large spheres is larger than $\sigma + \tau$ and their depletion layers do not

---

[18] When only two large spheres are present, the configurational partition function of the small ones depends only on the magnitude R of the vector $\boldsymbol{R}$ separating the centers of the large ones, cf. Eq. (2.37) in Section 2.3.

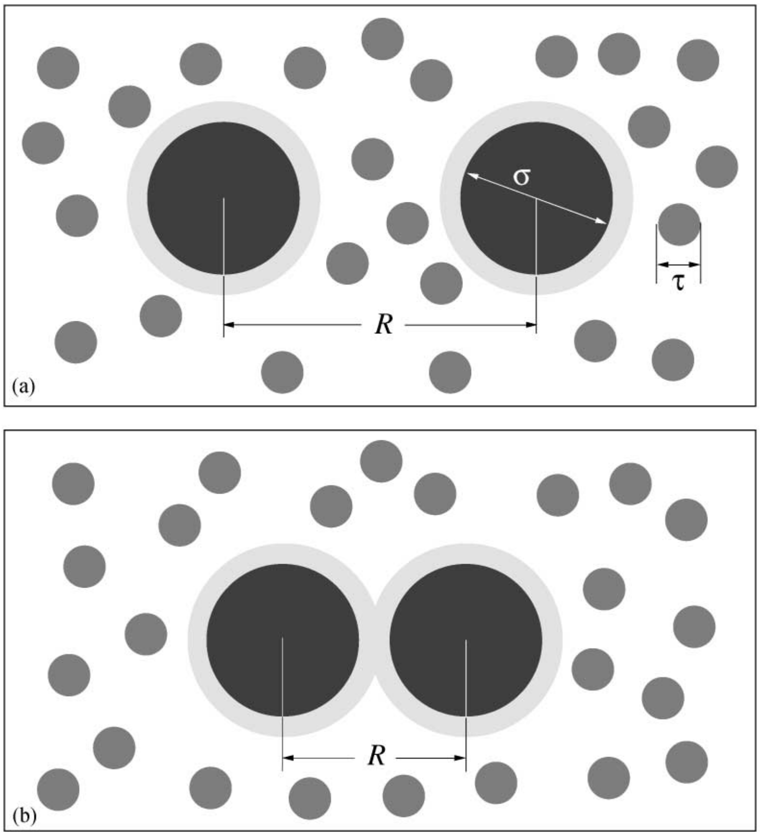

Fig. 27. The depletion mechanism. In (a), the depletion layers between the large spheres of diameter σ, denoted by the lightly shadowed rings, do not overlap but in (b) they do. In this way, the available volume to the small spheres of diameter τ is increased and the two large spheres in (b) experience an effective attraction.

overlap. Hence, the total excluded volume for the small particles is twice the sum of the volume of each large sphere and the volume of its depletion layer. In (b), we have $R < \sigma + \tau$ and the depletion layers overlap. The total excluded volume for the small particles is smaller with respect to (a), by an amount equal to the volume of the lens-shaped domain formed by the overlapping depletion layers. Thus, the total *available* volume in (b) is *larger* than that in (a) by exactly the same amount, with the implication that $S_2(R)$ is larger in (b) than in (a), as the total available volume uniquely determines the entropy of noninteracting particles. According, then, to Eq. (4.5) the effective potential $V_{\mathrm{eff}}(R)$ between the large spheres vanishes for $R > \sigma + \tau$ but it develops an attractive part for $\sigma < R < \sigma + \tau$, getting deeper as R gets smaller because with decreasing R the overlap volume between the depletion layers increases.

A similar conclusion can also be reached by realizing that in the situation shown in Fig. 27(a) every large sphere is being hit by the small ones symmetrically from all sides, whereas in that in Fig. 27(b), where the small spheres are excluded from the region between the two large ones, there is an unbalanced pressure exerted on the two spheres by the small ones from the "outside", thus pushing the two closer together. This consideration makes it plausible that the depletion mechanism, though sketched above for a special kind of mixture, must be in fact quite general whenever large and small entities which exclude each other are being brought together in a mixture.

The simple model for the depletion interaction presented above, was introduced by Asakura and Oosawa [190] and later developed independently by Vrij [191] as a model of a mixture between colloidal particles and nonadsorbing(free) polymers, and it is known as the Asakura–Oosawa (AO) model.[19] In view of the fact that the polymer–polymer interaction is a soft Gaussian with height of order unity (see Section 3.4), and hence vastly weaker than the hard colloid–colloid and colloid–polymer interactions, the approximation of noninteracting polymers appears to be a reasonable one. In the following section we proceed with a quantitative analysis of the ensuing interaction potential within the AO model because the latter, due to its simplicity, allows for analytical calculations and can be viewed as the "Ising model" for the depletion interaction. We will comment on its accuracy at the end of the following section.

4.3. The depletion potential: quantitative results

4.3.1. Mixtures of hard spheres and polymers

The interactions between hard spheres or walls mediated through free, nonadsorbing polymer coils is a problem which has been studied extensively in experiments [76,193–196], by integral equation theories [153,197,198], scaling theory, field theory and renormalization group techniques [199–207] and by simulations [208,209]. The simplest theoretical framework is provided by the AO model, in which the calculation of the depletion potential between two colloidal spheres is a straightforward exercise that reduces to the calculation of the volume of the lens-shaped overlap domain formed by the depletion layers of the two colloids. It is useful to introduce the chemical potential μ_2 or the corresponding activity $z_2 = \Lambda_2^{-3}\exp(\beta\mu_2)$ of pure ideal polymers in a reservoir that are in thermal, chemical and mechanical equilibrium with the polymers in the mixture, through a semipermeable membrane that allows the passage of polymers but not of colloids. The result is the AO depletion potential $V_{\mathrm{AO}}(R) \equiv -k_{\mathrm{B}}T\ln Z_2(R)$ which reads as [67,190,191]:

$$V_{\mathrm{AO}}(R) = \begin{cases} -k_{\mathrm{B}}Tz_2\sigma^3\dfrac{\pi(1+q)^3}{6}\left[1 - \dfrac{3R}{2(1+q)\sigma} + \dfrac{R^3}{2(1+q)^3\sigma^3}\right] & \text{for } \sigma < R < \sigma + \tau\ , \\ 0 & \text{for } R > \sigma + \tau\ , \end{cases} \tag{4.6}$$

where $q = \tau/\sigma$. For polymer chains, τ is of the order of their radius of gyration R_g. The depletion potential is purely entropic in origin, as manifested by the fact that it scales with the thermal energy $k_{\mathrm{B}}T$ and is, evidently, attractive. Its range is $\sigma + \tau$ and can be externally controlled by changing the spatial extent of the added polymers by varying, e.g., the solvent quality or their degree of polymerization (see Section 3).

As the polymers in the reservoir are ideal, their osmotic pressure Π and their activity z_2 are related by

$$\Pi = k_{\mathrm{B}}Tz_2\ . \tag{4.7}$$

---

[19] The AO model should be distinguished from the related *AO approximation* [192]. In the latter, the polymers are *explicitly* modeled as ideal chains, whereas in the former as interpenetrating spheres, see also Ref. [152].

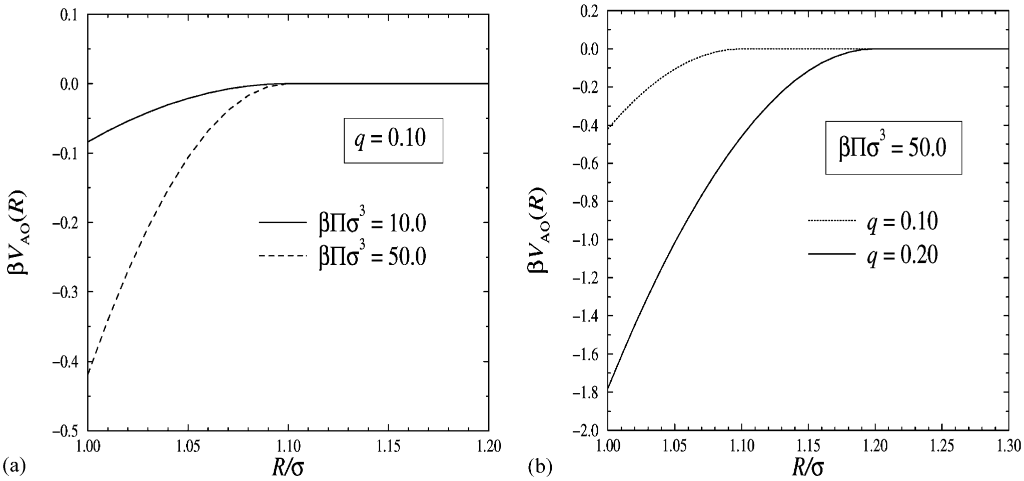

Fig. 28. The Asakura–Oosawa depletion potential [second and third lines in Eq. (4.8) above] for different parameter values: (a) $q = 0.10$ at $\beta\Pi\sigma^3 = 10.0$ and 50.0; (b) $\beta\Pi\sigma^3 = 50.0$ for $q = 0.10$ and 0.20.

Putting everything together, we obtain the effective interaction $V_{\mathrm{eff}}(R)$ between two colloidal spheres in the AO model as

$$\beta V_{\mathrm{eff}}(R) = \begin{cases} \infty & \text{for } R < \sigma\,, \\ -\,\beta\Pi\sigma^3 \dfrac{\pi(1+q)^3}{6}\left[1 - \dfrac{3R}{2(1+q)\sigma} + \dfrac{R^3}{2(1+q)^3\sigma^3}\right] & \text{for } \sigma < R < (1+q)\sigma\,, \\ 0 & \text{for } R > (1+q)\sigma\,. \end{cases} \quad (4.8)$$

The depth of the effective potential can also be externally controlled by changing the osmotic pressure of the polymer solution, i.e., their density and it is also affected by changing q. A plot of the depletion potential $V_{\mathrm{AO}}(R)$ for different values of the corresponding parameters is shown in Fig. 28, where it can be seen that changing the concentration and size of the polymers allows us to tune the depletion attraction. Verma et al. [193] measured the depletion attraction between a pair of micron-sized colloidal spheres in DNA solutions using a line-scanned optical tweezer and found excellent agreement with the predictions of the AO theory.

The original analysis in Refs. [190,191] was based on considering only two large colloidal spheres in the presence of a sea of interpenetrating ones. However, according to the general discussion in Section 2.3, effective interactions are rigorously defined for an arbitrary number of large particles, not just two. Though to achieve this is prohibitively complicated in general, the task has been accomplished for the case of the AO model in the recent work of Dijkstra et al. [67], who used exact diagrammatic expansions of the partition function in terms if Mayer bonds. Three *exact* results have now been established through this work, namely the following:

1. The effective *pair potential* between the colloids is given by Eq. (4.8), irrespective of the colloid density, i.e., the Asakura–Oosawa depletion potential is *exact* on the pair level.

2. The effective Hamiltonian is free of third- and higher-order interactions when the size ratio q does not exceed the magic value[20] $q_* = 2\sqrt{3}/3 - 1 \cong 0.1547$.
3. The volume term $f_0(\rho)$ of the model (where ρ is the colloid density) is linear in ρ and therefore irrelevant for the determination of phase boundaries.

Hence, a mapping of the AO model with a size ratio $q \leq q_*$ into an effective one-component system featuring the effective interaction given by Eq. (4.8) is *exact*. Dijkstra et al. took advantage of this property but also extended their study to models with $q > q_*$, finding that the missing many-body terms do not have a significant effect on the phase behavior of the AO model [67].

The AO model provides an excellent reference system for the study of colloid–polymer mixtures. Nevertheless, quantitative discrepancies between theoretical predictions based on it and experiments have been recently reported [153,211], even though the polymers were in Θ-like conditions and hence it appeared reasonable to treat them as noninteracting.[21] It is not clear yet whether these discrepancies are due to the shortcomings of the integral equation approaches applied to solve the AO model or in the higher-order interactions missing from the latter [153]; however, possible suspects are the oversimplified assumptions of the vanishing polymer–polymer interactions on the one hand and of the hard-sphere like interaction between polymers and colloids on the other. As a result, theoretical efforts to devise realistic interactions between these entities have been recently undertaken [152,212–214].

A depletion attraction also develops between a colloidal sphere and a flat wall, when smaller free polymers are present in the mixture. Once more, the depletion potential can be calculated in the framework of the Asakura–Oosawa model [192]. Rudhardt et al. [76] performed direct measurements of this potential in mixtures of colloids and nonionic polymers using total internal reflection microscopy (TIRM) [72–75], finding excellent agreement with the theoretical predictions. The depletion *force* was measured by Ohshima et al. [194] using laser radiation pressure and it was found that the observed force almost coincides with the theoretically predicted one. However, it should be noted that in recent TIRM-measurements of the sphere–wall depletion potential, deviations from the Asakura–Oosawa form have been observed [195,196], which have been attributed to the existence of additional, dispersion forces between the sphere and the wall.

Finally, the depletion potential between two flat walls mediated by *real* (as opposed to ideal, i.e., noninteracting) polymer chains was calculated recently by Bolhuis et al. [152], employing the Gaussian model for the chain–chain interaction (see Section 3.4.2). The results were compared with those arising from the AO *approximation* [192], which is itself more accurate than the AO *model* in this case.[22] It was found that, although the resulting depletion interaction is qualitatively similar to the AO approximation, the latter is a rather poor one from the quantitative point of view, even at

---

[20] 'Magic' because it corresponds to the case when a small sphere passes exactly into the free space formed by three large ones touching each other in an equilateral configuration, see also Ref. [210].

[21] Note, however, that at the Θ point it is not the effective interaction between coils that vanishes but rather the second virial coefficient of the monomer–monomer interaction potential, see Sections 3.3.1 and 3.4.2.

[22] For the case of two flat walls, the AO model predicts a depletion interaction that has the form of an attractive linear ramp up to wall separations $d = 2R_g$ and vanishes thereafter, whereas the AO approximation yields an interaction that decays smoothly to zero [152,190].

low polymer densities. An important difference is that the real depletion interaction displays a slight repulsive "hump" at a distance $d \cong 2R_g$ between the walls, a feature absent from both the AO approximation and the AO model. This repulsion is caused by the correlations between the interacting coils and is also present (and much more enhanced) in the case of hard-sphere mixtures, as we discuss below.

4.3.2. Hard-sphere mixtures

When dealing with a mixture of large (diameter σ_1) and small (diameter σ_2) hard spheres, the simple analysis of the AO model does not hold any more. The pair interactions between species α and β ($\alpha, \beta = 1, 2$), $v_{\alpha\beta}(r)$, are now given by

$$v_{\alpha\beta}(r) = \begin{cases} \infty & \text{if } r < (\sigma_\alpha + \sigma_\beta)/2 \,, \\ 0 & \text{if } r > (\sigma_\alpha + \sigma_\beta)/2 \end{cases} \tag{4.9}$$

and the hard repulsion among the small spheres brings about correlation effects which cause the depletion interaction between the large ones to deviate significantly from the Asakura–Oosawa form [Eq. (4.6)], especially at intermediate and high concentrations of the small component.[23]

An exact expression for the depletion *force* between two large hard spheres has been derived by Attard [216,217] and has been employed in simulation studies of depletion by Dickman et al. [218]. It was found that the depletion potential between two large spheres (as well as that between a sphere and a wall) develops repulsive parts and has an oscillatory behavior, due to correlation effects between the small spheres. Götzelmann et al. applied density functional theory combined with the Derjaguin approximation [219] and later performed an improved calculation of the depletion interaction where the Derjaguin approximation was disposed off [220].

Roth et al. [221,222] employed the so-called test particle approach to the calculation of the depletion interaction. The starting point in this approach is the definition of the effective potential in the *grand canonical ensemble*, where the central quantity is the grand partition function $\Xi(\{\mu_i\}, T)$, with $\{\mu_i\}$, $i = 1, 2, \ldots, \nu$ denoting the chemical potentials of the species in a ν-component mixture, which are held fixed. With $\Omega(R, \{\mu_i\}, T) = -k_B T \ln \Xi(R, \{\mu_i\}, T)$ being the grand potential of a mixture containing two large spheres fixed at center-to-center distance R, the effective potential between two large spheres is given by [221,222]

$$V_{\text{eff}}(R) = v_{11}(R) - k_B T \ln\left[\frac{\Xi(R, \{\mu_i\}, T)}{\Xi(\infty, \{\mu_i\}, T)}\right], \tag{4.10}$$

cf. Eq. (4.4). Equivalently, one can express the effective potential in terms of the one-body direct correlation functions [79] $c^{(1)}(\{\mu_i\})$ of the small component as

$$V_{\text{eff}}(R) = v_{11}(R) - c^{(1)}(R, \{\mu_i\}, T) + c^{(1)}(\infty, \{\mu_i\}, T) \,, \tag{4.11}$$

where the first argument in the one-body direct correlation functions denotes the distance at which the big spheres are held. The function $c^{(1)}(R, \{\mu_i\}, T)$ can be calculated by a density functional approach employing Rosenfeld's fundamental measure functional [98,99], and in this way Roth

---

[23] The simpler case of a one-dimensional mixture of long and short hard rods was considered in detail in the recent work of Lekkerkerker and Widom [215].

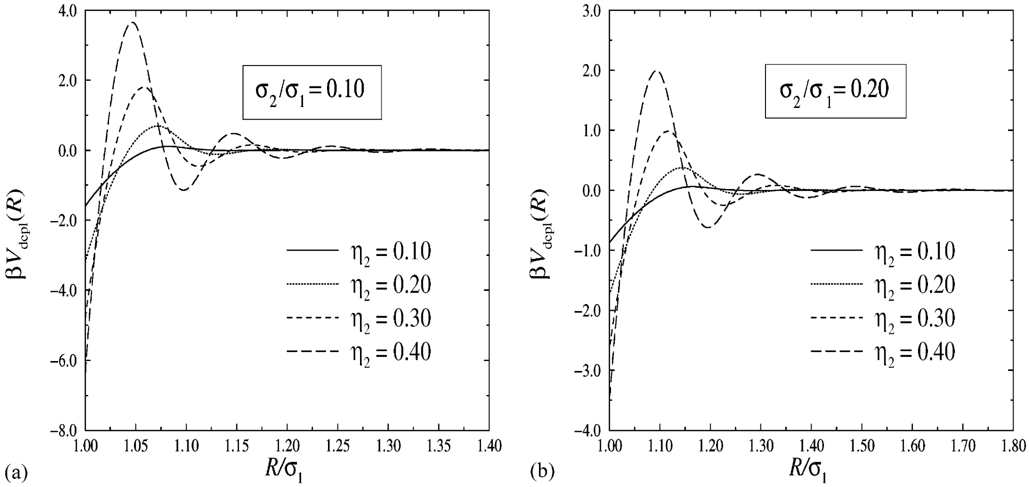

Fig. 29. The depletion potential $V_{\mathrm{depl}}(R)$ between two large hard spheres at center-to-center distance R due to the presence of a sea of small ones, at different packing fractions η_2 of the small. (a) Size ratio $\sigma_2/\sigma_1 = 0.10$ and (b) size ratio $\sigma_2/\sigma_1 = 0.20$. Notice the effects of η_2 and of the size ratio on the range and strength of the depletion. The curves were produced using the analytical fit to the density-functional results given in Ref. [221].

et al. have performed a calculation of the depletion potential in hard-sphere mixtures which compares extremely well with simulation results [221,222]. The calculation was further extended to depletion forces near curved surfaces, for both cases of positive and negative surface curvatures [223].

Representative results for the depletion potential between two large hard spheres in a sea of small ones, as a function of the packing fraction of the small spheres, $\eta_2 = \pi\rho_2\sigma_2^3/6$, are shown in Fig. 29. The characteristic oscillations become more pronounced with increasing η_2 and only at very low values of η_2 is the depletion similar to the AO model (cf. Fig. 28). The depletion potential has also been experimentally measured by Crocker et al. [224] using a line-scanned optical tweezer, and very good agreement with the theoretical predictions has been obtained [221].

Once more, the aforementioned results were obtained by considering two isolated large spheres in the presence of many small ones. A full, statistical–mechanical treatment of the two-component system was performed by Dijkstra et al. [64,66] and the theoretical results using the depletion picture of Götzelmann et al. [219] were compared with those from a direct simulation of the two-component mixture and its phase behavior [65,66]. As far as the quality of the depletion picture is concerned, the main conclusions now read as follows:

1. Contrary to the results for the simpler, AO model, the pair potential approximation is never exact, i.e., higher-order effective interactions between the large spheres are always present, no matter how small the size ratio σ_2/σ_1 is.
2. Application of the effective depletion potential of Götzelmann et al. [219] in an effective, one-component description of the mixture, yields nevertheless results for the phase behavior of the system, which are very close to those obtained from a full, two-component direct simulation.

Hence, the missing many-body terms have a negligible effect on the macroscopic behavior of the system.

3. As for the AO model, the volume term $f_0(\rho)$ is a linear function of ρ and does not affect the phase boundaries.

Another full statistical–mechanical approach to the depletion interactions in hard-sphere mixtures was employed recently by Méndez-Alcaraz and Klein [225] for binary as well as for the much richer case of a *ternary* mixtures. The same approach was employed by König and Ashcroft [226] for a ternary hard-sphere mixture, motivated by the search for suitable size ratios that could stabilize hard-sphere quasi-crystals.[24] Here, the Percus–Yevick closure for the full, three-component system was solved and the obtained radial distribution function for the largest component was inverted in a pseudo-one-component fashion, in order to obtain an effective potential for the large spheres. The characteristic oscillations of the depletion potential were once again found.

The approach of Méndez-Alcaraz and Klein [225] has as a starting point the structure-based definition of the effective liquid introduced by Andelman [228] and further elaborated by Heno and Regnaut [229]. This amounts to the requirement that a multi-component treatment of the mixture should give the same correlation functions for the component under consideration as the effective one-component treatment, a property already mentioned in Section 2.3.1. Cuesta and Martínez-Ratón [230] have recently employed a powerful density functional approach to analyze the effects of the degrees of freedom that have been traced out on the effective direct correlation function of the remaining component. For a short description of integral equation techniques applied to multicomponent liquids and the inversion procedure, see Appendix D.

Depletion forces between two spheres immersed in a suspension of a smaller, hard-sphere-Yukawa system were calculated by density functional theory by von Grünberg and Klein [231]. We finally note that entropically driven depletion interactions between hard-spheres also occur in mixtures of spheres and hard rods. Here, the situation is more complicated because of the rod geometry and of the existence of additional parameters in the problem, such as the aspect ratio of the rods. Approximate expressions for the rod-induced depletion interaction have been derived in the recent years [232–235].

4.4. Tuning the attractions

Irrespective of the detailed microscopic interactions between the large colloids and the smaller components, the resulting depletion interaction has the property that its characteristics can be externally *tuned*: its range can be altered by changing the size of the small particles, whereas this size as well as their density affects its depth (strength) as well as the correlation effects (see Section 4.3.2 above). This flexibility has allowed us to make quantitative predictions about the possibility of existence of a liquid phase in a given system.

Since the pioneering work of van der Waals [236], it is known that there is no fundamental difference between a liquid and a gas; both phases have the same spatial symmetries and the only

---

[24] Two-component hard-sphere quasi-crystals are thermodynamically unstable [227] and in practice most three-dimensional quasi-crystals are indeed ternaries [210].

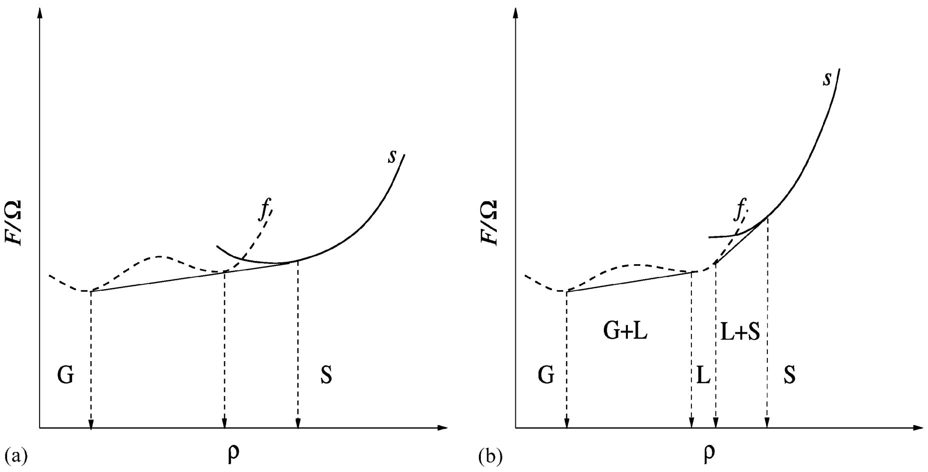

Fig. 30. Free energy density F/Ω vs. average density ρ curves, for the fluid f (dashed curve) and the solid s (solid curve). (a) At the triple temperature T_t, a gas (G) coexists with a liquid phase of vanishing extent and a solid (S). (b) At a higher temperature, a liquid phase (L) appears between the gas and the solid and the fluid part of the free energy curves still has nonconvex parts, i.e., the considered temperature lies below the critical temperature T_c of the liquid–gas coexistence. The thin solid lines are common tangents and the vertical dashed lines point to the coexistence densities, denoted by the arrows.

reason why we differentiate between them is the fact that they *can* be found in a two-state coexistence. However, due to their fundamental similarity, this phase coexistence terminates at a critical point at some temperature T_c. Moreover, three phases, gas, liquid and solid, can coexist at the triple temperature T_t. A *necessary* requirement for the existence of a liquid–gas-phase transition is the presence of an attractive part in the interaction potential between the molecules of a certain species, which gives rise to the "van der Waals loop", i.e., to nonconvex parts in the free energy density vs. density curves of the substance. Yet, the above condition is by no means *sufficient*. Though a van der Waals loop is always caused by the attractions, the question of whether a liquid–gas transition materializes or not depends crucially on the competition with the solid phase. In Fig. 30, we sketch the free energy curves for a system in which $T_t < T_c$. Here, the fluid free energy curve has nonconvex parts above the triple temperature. The phase diagram of such a system will feature three phases, gas, liquid and solid, the coexistence line of the first two terminating at a critical point.

However, a second scenario is also possible. As shown in Fig. 31, the gas–liquid coexistence curve can also be *metastable* with respect to the gas–solid coexistence and hence it will not materialize in practice because it will always be preempted by the crystallization transition. The attractions are not strong enough to bring about a van der Waals loop which will survive the competition with the crystal *before* reaching the critical point and the system has *no liquid phase*, just one fluid and one solid phase.

The crucial parameter that determines which of the two above-mentioned scenarios materializes is the ratio of the range of the attraction to the range of the hard-core repulsion, schematically the parameter q in the Asakura–Oosawa potential, Eq. (4.8). The pioneering theoretical work on the subject was performed by Gast et al. [237] who applied perturbation theory by splitting the

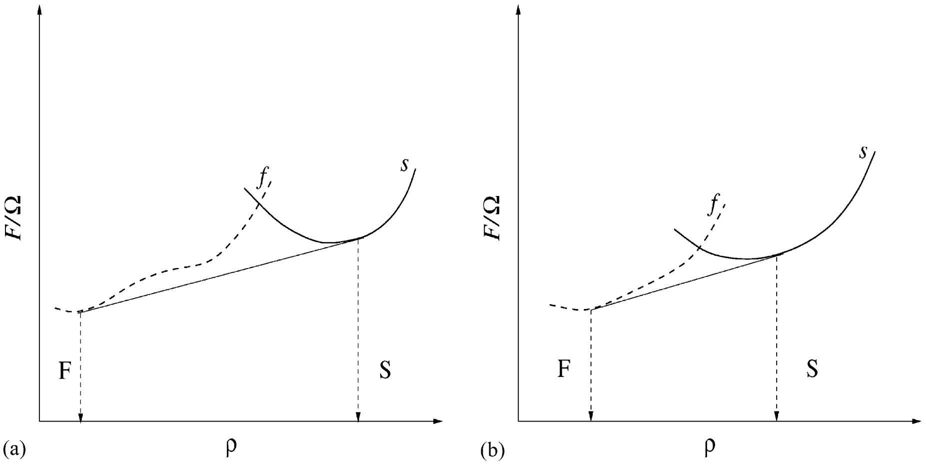

Fig. 31. Same as Fig. 30 but for a system with a single fluid phase F. (a) At a temperature below the critical temperature T_c of a putative gas–liquid coexistence, a broad coexistence region between a low-density fluid and a dense solid appears. (b) At the critical temperature T_c, the fluid free energy branch is already flat but the common tangent still connects a low-density fluid with a high-density solid. A gas–liquid transition is always preempted by crystallization.

interaction into a HS reference part and an attractive tail. This approach received the criticism that it assumed the same polymer concentration on coexisting phases [22,238–240]. Therefore, Lekkerkerker et al. [241] applied a free-volume approximation which allows for polymer partition between the two phases and does not work from the outset with the Asakura–Oosawa potential [67]. It was found that a single fluid phase, and thus a simple fluid–solid coexistence exists when $q \lesssim 0.32$ and for larger values of this parameter, the usual phase diagram with two fluid phases and one solid phase is recovered. The detailed study of Dijkstra et al. [67] revealed that the liquid–gas coexistence disappears for $q \leq 0.4$. These results are in semiquantitative agreement with those obtained from the experiments of Ilett et al. [242]. Here, the varied parameter was the ratio of the radius of gyration R_g of the free, nonadsorbing polymer to the radius a of the colloidal particles, $\zeta = R_g/a$. It was found that the crossover between the two topologies of the phase diagram occurs at $\zeta \sim 0.25$. Similar conclusions have been reached for colloid–polymer systems in two spatial dimensions [243]. A liquid–gas transition is also suppressed by freezing in highly asymme tric HS mixtures, as demonstrated in the recent works of Dijkstra et al. [66] and of Velasco et al. [244].

Similar conclusions for the change in the topology of the phase diagram have been reached by Hagen and Frenkel [245] in their simulation study of a HS-attractive Yukawa (HSAY) system, where the decay parameter $\kappa\sigma$ of the Yukawa tail has been varied. The simulations yielded that the liquid phase disappears for $\xi \equiv \kappa\sigma \geq 6.0$, whereas a simple perturbation theory by the same authors gives the crossover value $\xi \geq 7.4$. In the last few years, a number of theoretical studies on the question of stability of the liquid phase have been carried out, by employing families of intermolecular potentials depending on some parameters which control the range of the attractions. The hard-sphere-attractive Yukawa system was studied by Mederos and Navascués [246] using density functional theory. Hasegawa [247] studied the HSAY system as well as the so-called $m - n$ potential, a natural extension of the Lennard-Jones 6–12 potential to arbitrary powers

$n = 2m$, using perturbation theory. Daanoun et al. [248] introduced a van der Waals approach for both liquids and solids and studied the phase diagrams of model systems interacting by means of square–well and HS-attractive inverse-power potentials, using the range of the square well and the exponent of the inverse power as tuning parameters for the range of the attraction. Coussaert and Baus [249] extended this approach to attractive Yukawa potentials, the Hamaker–van der Waals potential of Eq. (2.10) and to the AO-potential of Eq. (4.8). Tejero et al. [16,250] applied first-order perturbation theory based on the Gibbs–Bogoliubov inequality to evaluate the free energy of simple fluids interacting by means of a double Yukawa potential. Though the detailed results of these studies depend on the chosen potential and the approximations made, the rule of thumb that emerges from the above-mentioned work is that when the range of the attractions is more than, approximately, 20% of the range of the repulsions, the liquid phase is stable and the phase diagram of the system features two fluid and one solid phases. Below this value, the liquid–gas transition disappears. The fact that the liquid–gas transition becomes metastable has the important consequence of speeding up crystal nucleation, as demonstrated by ten Wolde and Frenkel [251,252] in the context of crystallization of globular proteins.

We finally remark that another physical system where the question of the existence of a liquid phase has occupied the literature for quite some time [247,253–259] is that of a macroscopic collection of C_{60} molecules (fullerenes).[25] C_{60} molecules are widely believed to interact by means of the Girifalco potential [260] whose attractive part has a range lying close to the above-mentioned 20% borderline value. There has been contradictory evidence in the literature, both for [253,261] and against [262] the existence of the liquid phase in this system. Recent, state-of-the-art simulations seem to verify that the system indeed possesses a liquid phase at high temperatures but its range of stability is narrow and limited between 1880 and 1980 degrees Kelvin [259].

It is now natural to pose the question what happens when the range of the attractions is further reduced, below 20% of the repulsions. The evolution of the phase diagram is schematically shown in Fig. 32. After the liquid–gas coexistence has moved into the metastable regime, and for ranges of the attraction less than, roughly, 5% of the repulsion, an isostructural fcc–fcc transition between a low-density and a high-density crystal appears, terminating at a critical point [263,264]. The system has then two solid phases and one fluid phase.[26] The phase diagram of substances with very short-range attractions is a "mirror image" of the phase diagram of system with long-range attractions. The fact that most atomic substances have attraction ranges well above the 20% limit, means that the liquid phase is common and can coexist with a gas of a dramatically lower density. Hence, we have been (mis-)guided to introduce the liquid phase of matter as a third phase between crystals and gases, though it does not fundamentally differ from the latter. If the common materials in our everyday life had short-range attractions instead, then we would have probably been led to believe that there are two "kinds" of fcc crystals, as we would be used to find them in coexistence with each other. The isostructural fcc–fcc transition is a phenomenon that can take place only in

---

[25] Fullerenes have a diameter of 0.71 nm [260] and hence they are almost colloidal particles.

[26] The phase diagram in Fig. 32 is drawn, conventionally, on the temperature–density plane. For entropic attractions caused by depletion, such as the AO potential of Eq. (4.8), there is no temperature in the system and then T has to be interpreted as some other parameter that controls the depth of the attraction, such as the osmotic pressure Π or the fugacity z_2 of the polymers.

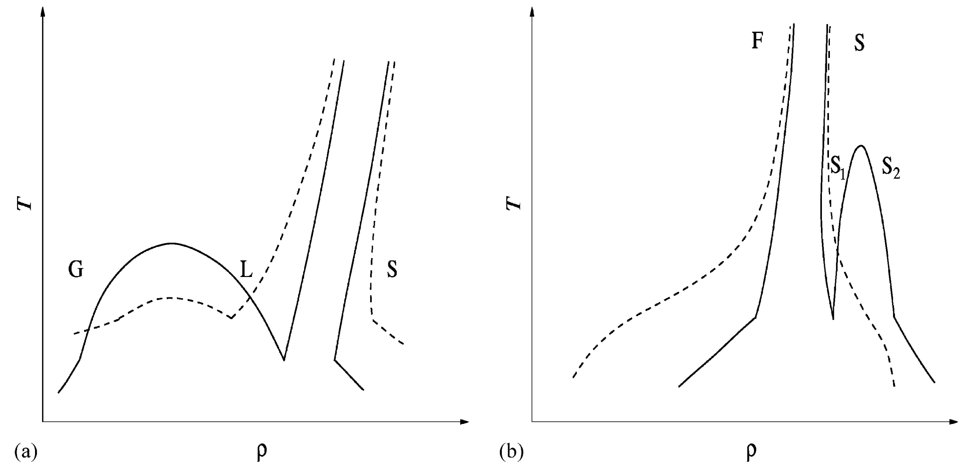

Fig. 32. Schematic evolution of the temperature–density phase diagram of a generic substance, as the range of the attraction is reduced. (a) At ranges significantly larger than 20% of the hard core repulsion (solid lines), three phases, gas (G), liquid (L) and solid (S) are present but as the attraction approaches this borderline value (dashed lines), the critical and triple temperatures are approaching each other and the range of stability of the liquid phase is reduced. (b) At ranges of the attraction below 20%, a single fluid phase (F) and a single solid phase (S) exist (dashed lines). When the range of the attractions is further reduced, below approximately 5% of the repulsion, an isostructural phase transition between two solids of the same symmetry, S_1 and S_2, takes place and the phase diagram looks specular to the one shown in (a) (solid lines).

colloidal systems, where the attractions can be tailor-cut by tuning their range, and has attracted considerable interest in the last few years. We therefore devote the next section to a more detailed review of some theoretical work done on this novel phenomenon.

4.5. Solid-to-solid isostructural transitions

Solid-to-solid isostructural transitions have been discovered for the first time in the early 1980s in the simulation studies of Young and Alder [265], conducted for a 'square-well' (SW) system characterized by the interparticle potential:

$$v(r) = \begin{cases} \infty & \text{if } r < \sigma\ , \\ -\varepsilon & \text{if } \sigma < r < (1+q)\sigma\ , \\ 0 & \text{if } r > (1+q)\sigma\ , \end{cases} \tag{4.12}$$

where ε is the depth of the potential ($\varepsilon > 0$) and $(1+q)\sigma$ is its range. Young and Alder considered a long-range attractive potential, with $q = 0.5$ and found an fcc–fcc transition. The latter is induced in the crystal lattice by the second nearest neighbors, whose distance from a given particle is $\sqrt{2}$ times that of the nearest neighbors. Indeed, in an open solid where only the first neighbors of a given particle are inside its attractive well, the free energy density is a convex function of the density. Above a characteristic threshold density at which the second neighbors also fall inside the well in a dense solid, the free energy density drops due to the abrupt decrease in the internal energy and it develops a nonconvex part. This mechanism brings about the fcc–fcc transition. However, there is no real potential steep enough at this distance to stabilize the solid in a more condensed state by means of the second-neighbor attraction; therefore, this transition was considered to be an artifact of the steepness of the square–well potential [264,265]. If the range of the square–well potential becomes even longer, allowing particles within the third, fourth, etc., shells to interact, a whole spectrum of thermodynamically stable isostructural solids coexisting at different densities may be observed. However, this is again merely an artifact due to the unrealistic steepness of the square–well potential tail; for smooth potentials, this transition does not occur. On the other hand, if the attraction is *short range*, then the isostructural transition *survives* even when the square–well attraction is smoothed out, i.e., replaced by a continuous attractive tail of comparable range. This is the subject of the following section.

4.5.1. Short-range attractive interactions

The fcc–fcc isostructural transition in square–well was rediscovered in the mid-1990s by Bolhuis and Frenkel [263,264], with the important difference that in this study the SW potential was *short range*. In this simulation study, the fcc–fcc transition was found to occur for ranges of the attraction up to a threshold $q_c \cong 0.07$; for large q-values, it was preempted by the melting transition. Moreover, the critical density was found to grow with decreasing potential range, approaching its close-packing value $\rho_{CP} = \sqrt{2}/\sigma^3$ at $q = 0$, where the whole density coexistence region disappears and the coexistence line degenerates into a vertical segment in the temperature–density phase diagram [264]. The critical temperature T_c of the fcc–fcc transition was found to be practically constant, $k_B T_c/\varepsilon \cong 1.75$, regardless of the q-value.

Moreover, in Ref. [264], the form of the attractive potential was modified into a Yukawa tail, i.e., the hard-sphere-attractive Yukawa (HSAY) potential was also introduced:

$$v(r) = \begin{cases} \infty & \text{if } r < \sigma , \\ -\varepsilon\sigma \exp[-\kappa(r-\sigma)]/r & \text{if } r > \sigma . \end{cases} \tag{4.13}$$

It was found that, in contrast to the Young–Alder case [265], where the fcc–fcc transition does not survive the replacement of the long-range SW tail with a Yukawa one, for short-range attractions it does. The range of the attraction is governed by the parameter $\xi \equiv \kappa\sigma$; a fcc–fcc transition was found to place in the HSAY system for values above $\xi_c \cong 25$ and for smaller ξ-values (longer-range attractions), the fcc–fcc transition of the HSAY system is again preempted by melting. The simulation study was accompanied by theoretical calculations based on the uncorrelated cell model, which confirmed the overall picture qualitatively but did not provide quantitative agreement with the Monte-Carlo data [264].

The discovery of this fcc–fcc transition motivated a number of theoretical approaches attempting to reproduce the simulation result quantitatively and offer insight into the novel phenomenon. A simple, van der Waals-type theory was first proposed by Tejero et al. [248], yielding the correct dependence of the phase diagram on the range of the SW potential but a rather low threshold value for the disappearance of the fcc–fcc transition, $q_c \cong 0.015$.

Likos et al. [266] proposed a density functional approximation based on the Gibbs–Bogoliubov inequality [4]. First, the SW-potential of Eq. (4.12) was separated into a reference part, $v_0(r)$ and a perturbation part, $\phi(r)$:

$$v(r) = v_0(r) + \phi(r) , \tag{4.14}$$

where $v_0(r)$ is the HS potential given by Eq. (4.1) and $\phi(r)$ is given by

$$\phi(r) = \begin{cases} 0 & \text{if } r < \sigma\,, \\ -\varepsilon & \text{if } \sigma < r < (1+q)\sigma\,, \\ 0 & \text{if } r > (1+q)\sigma\,. \end{cases} \tag{4.15}$$

Subsequently, the Gibbs–Bogoliubov inequality was invoked (see Section 3.5.5), relating the Helmholtz free energy F of a system characterized by the Hamiltonian $\mathscr{H}$ to the free energy F_0 of a reference system having Hamiltonian $\mathscr{H}_0$ by

$$F \le F_0 + \langle \mathscr{H} - \mathscr{H}_0 \rangle_0\,. \tag{4.16}$$

Choosing the HS-interaction as the reference Hamiltonian, and applying Eq. (4.16) for a uniform (homogeneous) fluid we obtain

$$F(\rho_1) \le F_0(\rho_1) + \frac{1}{2}N\rho_1 \int g_0(r;\rho_1)\phi(r)\,\mathrm{d}\boldsymbol{r}\,, \tag{4.17}$$

where N is the number of particles in the specified volume Ω, $\rho_1 = N/\Omega$ is the number density, and $g_0(r;\rho_1)$ is the radial distribution function of the reference (HS) system. On the other hand, a crystalline solid is characterized by a *strongly nonuniform* one-particle density, $\rho(\boldsymbol{r})$. According to the basic theorem of density functional theory [79], the Helmholtz free energy of a nonuniform (inhomogeneous) system is a *unique functional* of the one-particle density, $F = F[\rho(\boldsymbol{r})]$. Applying the Gibbs–Bogoliubov inequality to this case, we obtain

$$F[\rho(\boldsymbol{r})] \le F_0[\rho(\boldsymbol{r})] + \frac{1}{2}\int g_0^{(2)}(\boldsymbol{r},\boldsymbol{r}';[\rho(\boldsymbol{r})])\rho(\boldsymbol{r})\rho(\boldsymbol{r}')\phi(|\boldsymbol{r}-\boldsymbol{r}'|)\,\mathrm{d}\boldsymbol{r}\,\mathrm{d}\boldsymbol{r}'\,, \tag{4.18}$$

where $g_0^{(2)}(\boldsymbol{r},\boldsymbol{r}';[\rho(\boldsymbol{r})])$ is the pair distribution function of the solid, which is also a unique functional of the one-particle density [79]. We can also write $g_0 = h_0 + 1$, for both uniform and nonuniform phases, introducing the pair correlation function h_0 of the reference system.

The Gibbs–Bogoliubov inequality is used in most cases in a variational sense: on the right-hand side, one or more variational parameters are introduced, and these are varied until an optimal upper bound for the sought-for Helmholtz free energy is obtained. A usual variational parameter is the diameter of the reference HS-interaction, for example. However, there is no such freedom here, since the partition of the potential is determined by the potential parameters uniquely, see Eqs. (4.14) and (4.15). Thus, as a first approximation, the Gibbs–Bogoliubov inequality has been treated as an *equality*, i.e.

$$F(\rho_1) = F_0(\rho_1) + \frac{1}{2}N\rho_1\int \phi(r)\,\mathrm{d}\boldsymbol{r} + \frac{1}{2}N\rho_1 \int h_0(r;\rho_1)\phi(r)\,\mathrm{d}\boldsymbol{r} \tag{4.19}$$

for the homogeneous phase, and

$$F[\rho(\boldsymbol{r})] = F_0[\rho(\boldsymbol{r})] + \frac{1}{2}\int \rho(\boldsymbol{r})\rho(\boldsymbol{r}')\phi(|\boldsymbol{r}-\boldsymbol{r}'|)\,\mathrm{d}\boldsymbol{r}\,\mathrm{d}\boldsymbol{r}' + \frac{1}{2}\int h_0^{(2)}(\boldsymbol{r},\boldsymbol{r}';[\rho(\boldsymbol{r})])\rho(\boldsymbol{r})\rho(\boldsymbol{r}')\phi(|\boldsymbol{r}-\boldsymbol{r}'|)\,\mathrm{d}\boldsymbol{r}\,\mathrm{d}\boldsymbol{r}' \tag{4.20}$$

for the inhomogeneous one. The last term in Eqs. (4.19) and (4.20) describes the effect on the internal energy from the correlations that arise due to HS-repulsions alone. As a last approximation, the attractive part was treated in the *mean-field approximation*, i.e., this last term was ignored for both the liquid and the solid. Ignoring the correlations in the crystal phase is a very reasonable approximation, because there most of the structure of the two-particle density $\rho^{(2)}(\boldsymbol{r},\boldsymbol{r}')$ comes from the product $\rho(\boldsymbol{r})\rho(\boldsymbol{r}')$. The approximation is less well justified in the liquid phase; yet, it was introduced as a way of treating the fluid and the solid on equal footing, yielding the final approximate expressions for the free energies as

$$F(\rho_l) = F_0(\rho_l) + \frac{1}{2}N\rho_l\int\phi(r)\,\mathrm{d}\boldsymbol{r} \tag{4.21}$$

for the liquid, and

$$F[\rho(\boldsymbol{r})] = F_0[\rho(\boldsymbol{r})] + \frac{1}{2}\int\rho(\boldsymbol{r})\rho(\boldsymbol{r}')\phi(|\boldsymbol{r}-\boldsymbol{r}'|)\,\mathrm{d}\boldsymbol{r}\,\mathrm{d}\boldsymbol{r}'\;, \tag{4.22}$$

for the solid.

For the liquid phase, the excess free energy per particle of the HS reference system is given very accurately by the Carnahan–Starling equation of state [267]. The final expression for the fluid free energy in this approximation reads as

$$\frac{\beta F(\rho_l)}{N} = \ln(\rho_l\sigma^3) - 1 + \frac{\eta(4-3\eta)}{(1-\eta)^2} - \frac{2\pi\varepsilon\rho_l\sigma^3}{3k_\mathrm{B}T}[(1+q)^3-1] + 3\ln(\Lambda/\sigma)\;, \tag{4.23}$$

where T is the temperature, $\eta = \pi\rho_l\sigma^3/6$ is the packing fraction of the HS-liquid, and Λ is the thermal de Broglie wavelength; the last term in Eq. (4.23), being identical at a given temperature for both liquid and solid phases, does not affect the comparisons between those and can be therefore dropped.

For the solid having average density $\rho_\mathrm{s} = N/\Omega$, a usual and accurate parameterization for the one-particle density $\rho(\boldsymbol{r})$ has been adopted, modeling this quantity as a sum of isotropic Gaussians centered around lattice sites, i.e.

$$\rho(\boldsymbol{r}) = \left(\frac{\alpha}{\pi}\right)^{3/2}\sum_{\{\boldsymbol{R}\}}\exp[-\alpha(\boldsymbol{r}-\boldsymbol{R})^2]\;, \tag{4.24}$$

where $\{\boldsymbol{R}\}$ is the set of lattice vectors of the given Bravais lattice. The limit $\alpha \to 0$ corresponds to completely delocalized Gaussians, and it was be taken to correspond to the uniform liquid, whereas the Gaussians become more and more localized as α grows. Denoting by $\rho_{\boldsymbol{K}}$ the Fourier components of $\rho(\boldsymbol{r})$, and by $\mu_{\boldsymbol{K}} \equiv \rho_{\boldsymbol{K}}/\rho_\mathrm{s}$ the dimensionless Fourier components, the parameterization of Eq. (4.24) immediately implies

$$\mu_{\boldsymbol{K}} = \mathrm{e}^{-K^2/4\alpha}\;, \tag{4.25}$$

where $\{\boldsymbol{K}\}$ is the set of reciprocal lattice vectors (RLVs) of the given lattice, and $K \equiv |\boldsymbol{K}|$.

The ideal free energy of the reference system, $F_0^{\mathrm{id}}[\rho(\boldsymbol{r})]$, is known exactly, see Eq. (2.70). The excess free energy of the nonuniform reference system, $F_0^{\mathrm{ex}}[\rho(\boldsymbol{r})]$, was calculated by using the modified weighted density approximation (MWDA) of Denton and Ashcroft [93]. The MWDA is known to give excellent results for HS-systems, and is computationally straightforward. Denoting by $f_1(\rho)$ the free energy per particle of the uniform system at density ρ, the MWDA approximates the excess free energy of the *nonuniform* system by that of a *uniform* system, but evaluated at a specified *weighted density* $\hat{\rho}$, i.e.,

$$\beta F_0^{\mathrm{ex}}[\rho(\boldsymbol{r})] = N f_1(\hat{\rho}) \ . \tag{4.26}$$

The weighted density $\hat{\rho}$ is evaluated self-consistently as a weighted average over $\rho(\boldsymbol{r})$; in the Gaussian approximation, $\hat{\rho}$ is determined by solving the implicit equation:

$$\hat{\rho}(\rho_s,\alpha) = \rho_s\left[1 - \frac{1}{2\beta f_1(\hat{\rho})}\sum_{\boldsymbol{K}\neq 0} \mathrm{e}^{-K^2/2\alpha}\tilde{c}_0(\boldsymbol{K};\hat{\rho})\right] , \tag{4.27}$$

where $\tilde{c}_0(\boldsymbol{K};\hat{\rho})$ stands for the Fourier transform of the direct correlation function of the uniform reference liquid at wavevector $\boldsymbol{K}$, and at density $\hat{\rho}$. Finally, the mean-field internal energy U of the fcc-solid [the second term in the rhs of Eq. (4.22)] is most easily evaluated in Fourier space, where the double integral turns into a sum over the RLVs of the lattice, yielding the expression

$$\frac{\beta U}{N} = \frac{\rho_s\sigma^3}{2}\sum_{\{\boldsymbol{K}\}} \mathrm{e}^{-K^2/2\alpha}\beta\tilde{\phi}(K) \ , \tag{4.28}$$

where

$$\tilde{\phi}(K) = \frac{4\pi}{K\sigma^3}\int_0^\infty r\sin(Kr)\phi(r)\,\mathrm{d}r \tag{4.29}$$

is the Fourier transform of the perturbation potential $\phi(r)$. For any given average solid density $\rho_s\sigma^3$, the sum in the rhs of Eq. (4.22) has been minimized with respect to the localization parameter α and the obtained minimum was taken as the approximate value of the free energy of the solid.

The phase diagrams obtained by means of this theory for different values of q are shown in Fig. 33(a). It can be seen that an isostructural fcc-to-fcc transition does take place. The mean-field theory overestimates the critical temperature T_c of the fcc–fcc transition by about 20% but it correctly yields the insensitivity of T_c to the range of the attraction. Moreover, the theory reproduces the simulation results for the critical density ρ_c quite well [266].

The separation of the triple from the critical temperature becomes smaller with increasing q. Within the range of q which examined in Ref. [266] the dependence of the triple temperature as well as the critical temperature on q was found to be linear. By fitting the data for the triple and critical temperatures with straight lines, it was found that the threshold value of q at which the fcc–fcc transition disappears is $q_c = 0.08235$. This threshold is larger than the value $q_c \cong 0.07$ obtained in the simulations by about 18%, a discrepancy that can be traced back to the above-mentioned overestimation of the critical temperature in this theory.

The theory of Ref. [266] has received the criticism that it neglects the correlations in the fluid and solid phases [269,270] and hence it is inaccurate for the case of *long-range* square–well attractions, where these correlations are crucial in bringing about a quantitatively reasonable estimate of the liquid–gas transition. Correlation effects in both phases have been taken into account in the subsequent work of Rascón et al. [271], within the framework of the perturbation weighted density

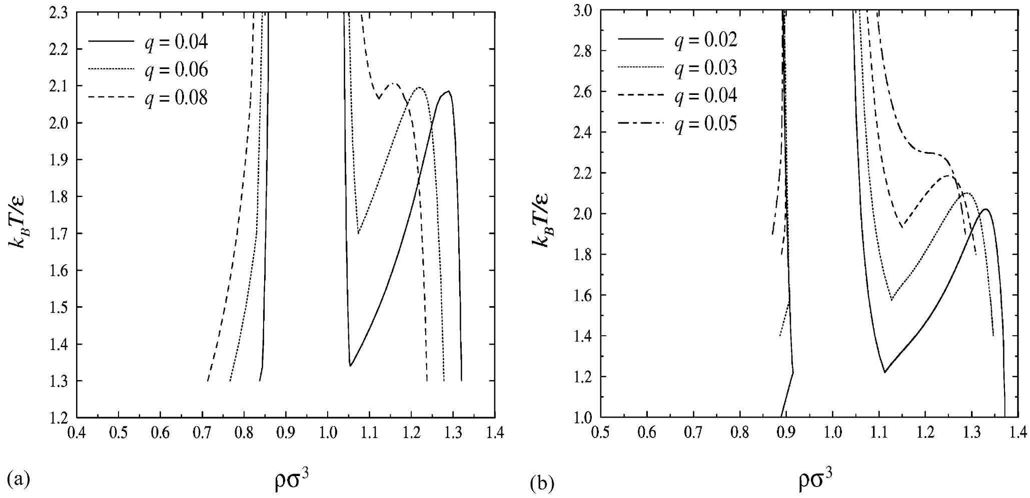

Fig. 33. The phase diagram of the narrow square–well system as obtained by density functional theory. (a) Result of the density functional perturbation theory approximation of Ref. [266]. (b) Result of the nonperturbative approach of Ref. [268]. (Redrawn from Refs. [266,268], respectively.)

approximation (PWDA) [272,273]. The threshold value was predicted to be $q_c \cong 0.06$ but the critical temperature was seriously overestimated and found to be $k_B T_c/\varepsilon \cong 2.70$. An improved perturbation theory developed later by the same authors [274] brought the theoretical result for T_c in much closer agreement with simulation.

The isostructural transition in the SW system has also been studied by Likos and Senatore [268] in a *nonperturbative* way, that is, without the separation of the interaction into a HS reference and a perturbation part. The full SW potential was treated in both the fluid and the solid phases. The structural and thermodynamic properties of the former were obtained by employing the analytical approximation of Nezbeda [275] to the Percus–Yevick solution of the SW potential. The free energy of the solid phases was calculated again by means of the MWDA, but the latter now performed for the *full* interaction. The excess free energy of a SW fcc-solid was calculated by mapping the latter onto an effective SW liquid, i.e., by employing Eqs. (4.26) and (4.27) for the full system. The results are shown in Fig. 33(b). The nonperturbative approach brings the theoretical results in better agreement with simulation as far as the critical temperature is concerned, as it predicts a lower value of T_c than its perturbative counterpart. The threshold value of q is now predicted to be $q_c \cong 0.05$, hence the nonperturbative and the perturbative approaches bracket the simulation result $q_c \cong 0.07$. At the same time, the nonperturbative approach brings about a weak dependence of the critical temperature on the attraction range, a feature that is at odds with the simulation results.

A question of considerable theoretical interest is in which universality class the new, isostructural critical point belongs. Both the perturbation theory mean-field approximation [266] and the nonperturbative density functional approach [268] predict mean-field-type critical exponents in the neighborhood of the critical point; in particular the exponent β, defined through $(\rho - \rho_c) \sim (T - T_c)^\beta$ as $T \to T_c^-$, has been found to have the classical value 1/2. However, in view of the

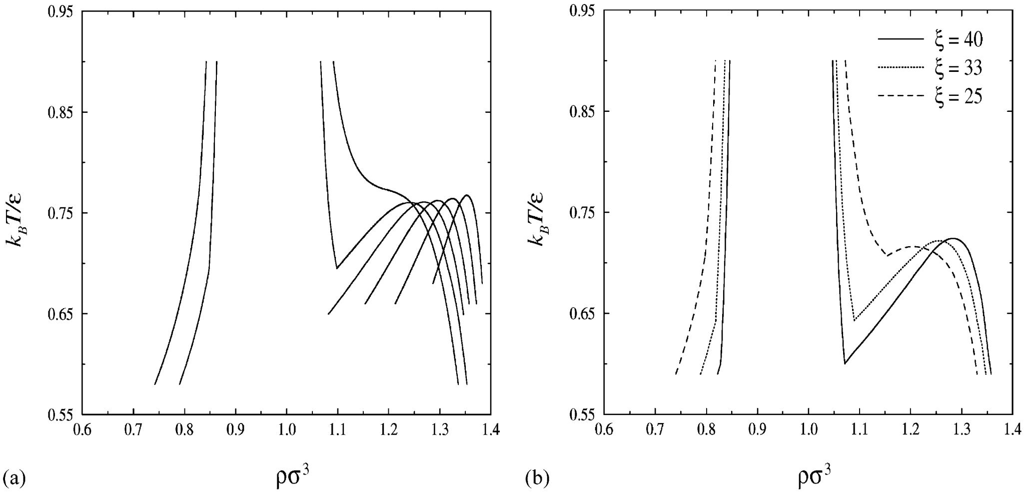

Fig. 34. The phase diagram of hard-sphere-attractive Yukawa systems with short-range attractions, as obtained by the density functional approach of Ref. [277]. (a) Percus–Yevick input for the correlation functions of the reference HS system. The decay parameter of the Yukawa potential has the values, from right to left: $\xi = 100$, 67, 50, 40, 33 and 25. For the last value of ξ the fcc–fcc transition is just preempted by melting. (b) Verlet–Weiss input for the reference HS system. Notice that here, for the value $\xi = 25$ the fcc–fcc transition is still barely not preempted by melting. (Redrawn from Ref. [277].)

approximations involved in the above-mentioned theories, which are inadequate to take into account the nature of the critical fluctuations, the prediction of classical exponents is of questionable value. Chou and Nelson [276] have proposed a field-theoretical approach in two dimensions, in which it is demonstrated that in the neighborhood of the critical point, if dislocations are excluded, coupling of the density fluctuations to the elastic degrees of freedom leads indeed to mean-field critical exponents. Hence, although the fcc–fcc critical point is the mirror image of the liquid–gas critical point, it need not necessarily belong to the same (Ising) universality class with the latter.

The perturbative approach of Ref. [266] was extended to short-range hard-sphere attractive Yukawa systems [Eq. (4.13)] by Németh and Likos [277]. The MWDA was once again employed in the calculation of the free energy of the reference system in the crystalline phase and for the direct correlation function of the HS system both the Percus–Yevick [4] and the more accurate, Verlet–Weiss [278] expressions were employed. The ensuing phase diagrams for varying values of the dimensionless Yukawa decay parameter $\xi = \kappa\sigma$ are shown in Fig. 34.

As can be seen from a comparison between Figs. 34(a) and (b), a weak dependence of the phase diagram on the quality of the HS input has been found. In particular, the Percus–Yevick input yields the crossover value $\xi_c \cong 25$ for the range of the attraction where the fcc–fcc coexistence disappears, whereas use of the Verlet–Weiss input brings this value slightly up. The agreement with the simulation result of Bolhuis et al. [264] is excellent, also as far as the critical temperature is concerned. The theoretical prediction for the latter lies within 4% of the simulation result [277].

The isostructural transition in the HSAY system was also studied by Hasegawa [247] and by Rascón et al. [279], using different approximations of density functional perturbation theory. In

Ref. [247] better agreement with simulation was found for T_c in comparison with that of Németh and Likos [277] but the threshold value ξ_c was overestimated and found to be $\xi_c \cong 40$. In the work of Rascón et al. [279], the critical temperature was overestimated by about 13% and the critical threshold was found to be $\xi_c \cong 50$. Nevertheless, both approaches have the advantage with respect to the work of Németh and Likos that their domain of applicability is not limited to short-range attractive Yukawa tails only.

The above phenomena take place in three spatial dimensions. In two dimensions, an isostructural transition between two triangular crystals still takes place but near the critical point there exists an intervening hexatic phase [276,280]. Though the occurrence of the fcc–fcc transition in three dimensions is an indisputable theoretical fact, it has not been experimentally observed to-date, because it is extremely sensitive to polydispersity which is unavoidable in colloidal suspensions. The experimental verification of this novel phenomenon remains, therefore, a problem for the future.

4.5.2. Short-range repulsive interactions

Though the focus of this section has been on attractive depletion interactions up to now, the phenomenon of solid-to-solid isostructural transitions is not limited to these. Kincaid et al. [281] studied a system interacting by means of a short-range square-shoulder (SS) potential of the form

$$v(r) = \begin{cases} \infty & \text{if } r < \sigma\ , \\ \varepsilon & \text{if } \sigma < r < (1+q)\sigma\ , \\ 0 & \text{if } r > (1+q)\sigma\ , \end{cases} \tag{4.30}$$

where $\varepsilon > 0$. Using perturbation theory, they found that an isostructural solid-to-solid transition takes place in this system. The same system was later studied by means of Monte-Carlo simulation by Bolhuis and Frenkel [282]. The range of repulsions covered went up to $q = 0.08$. The square-shoulder system has the property that it reduces to a pure hard-sphere system of diameter $(1+q)\sigma$ at $T = 0$ and to a pure hard-sphere system of diameter σ at $T = \infty$. Hence, two different packing fractions can be defined, one related to the spheres of diameter σ, called η and given by Eq. (4.2), and one related to the spheres of diameter $(1+q)\sigma$, called $\bar{\eta}$ and defined as

$$\bar{\eta} = \frac{\pi}{6}\rho(1+q)^3\sigma^3\ . \tag{4.31}$$

At $T = 0$ the system displays the usual HS freezing transition with packing fractions at coexistence given by $\bar{\eta}_f = 0.494$ and $\bar{\eta}_m = 0.545$ for the fluid and the solid, respectively (see Section 4.1). Moreover, as $T \to 0$, the fcc–fcc binodals mark the phase coexistence between two closely packed fcc solids, having packing fractions $\bar{\eta}_{CP} = \pi\sqrt{2}/6$ and $\eta_{CP} = \pi\sqrt{2}/6$. Contrary to the case of the SW potential, there is no triple point between the two fcc phases and the fluid phase. If only fcc-solids are considered, then the freezing binodals remain disconnected from the fcc–fcc binodals all the way down to $T = 0$. The critical density of the isostructural transition was found to increase with decreasing range of attractions, as in the case of the SW system; finally, the critical temperature of this transition was found to be $k_B T_c/\varepsilon \cong 1.5$ for $q = 0.01$ and slightly decreasing with increasing range of repulsion q [282]. The fcc–fcc transition in the square-shoulder systems exists for values of q as high as 0.15, whereas for the square–well system it becomes metastable to freezing already at $q_c \cong 0.07$.

A density functional perturbation theory for the SS system was put forward by Denton and Löwen [283], employing the same approximations as those of Ref. [266] for the SW system. In this work, attention was focused on the fcc–fcc transitions only and the freezing was not considered. For two values of q considered, $q = 0.03$ and 0.08, very good agreement with simulation was found, with the theoretical coexistence curves showing a systematic drift to higher densities but with the critical temperature being obtained to within 7% of the simulation value [283].

Though the theory of Denton and Löwen is simple in its implementation and yields satisfactory results for a given range of temperatures, it has the disadvantage that it is essentially a high-temperature expansion [see also Eqs. (4.22) and (4.28)]. At sufficiently low temperatures it does not automatically reduce to a HS theory for the system of hard spheres with diameter $(1 + q)\sigma$. Motivated by this, Lang et al. [284] proposed a nonperturbative density functional approach for the SS system analogous to the one put forward by Likos and Senatore for the SW system [268]. Instead of being separated into a HS reference and a perturbation part, the square-shoulder potential was treated here in full.

Liquid-state data for the square-shoulder system were calculated for a number of repulsion ranges and with a variety of integral equation theories and then compared with simulation. This liquid input, and in particular the excess free energy per particle and the direct correlation function of the liquid were subsequently employed to perform a mapping of the solids into effective liquids, within the framework of the MWDA [93].

The analysis revealed an unexpected, albeit now well-understood, sensitivity of the theoretical prediction for the critical temperature on the liquid input. In particular, if the Nezbeda approximation to the Percus–Yevick direct correlation function is employed [275], then an unreasonably high value of the critical temperature, $k_B T_c/\varepsilon \cong 6.0$ is obtained (cf. $k_B T_c/\varepsilon \cong 1.5$ in the simulation). However, if a direct correlation function derived from a higher-quality closure is employed, such as the Rogers–Young (RY) [81] or the optimized random phase approximation (ORPA) [285], then the critical temperature comes much closer to the simulation result and lies in the range $0.9 \le k_B T_c/\varepsilon \le 1.3$, depending on the width of the repulsive shoulder. The reason of this spectacular reduction of T_c was traced back to the fact that the Nezbeda–Percus Yevick direct correlation function vanishes identically for $r > (1 + q)\sigma$ and is negative otherwise. However, the RY and ORPA dcf's, which are both superior to the PY result, possess a positive tail at $r > (1 + q)\sigma$ which causes the change mentioned above.

The phase diagram obtained from this theory, using the ORPA liquid input, is shown in Fig. 35. The critical temperature is *underestimated* and it shows a stronger dependence on the width of the repulsive potential with respect to the Monte-Carlo results, a feature also encountered in the corresponding theory for square–well systems [268]. In view of the above-mentioned sensitivity of the results on liquid-state input, it is possible that this could be remedied if the even more accurate RY liquid input was employed.

Phase diagrams of systems interacting by means of short-range repulsive potentials were also studied in some generality by Rascón et al. [286], who employed exact zero-temperature considerations in combination with density functional perturbation theory combined with an approximate expression for the two-particle density in the solid phase. The square-shoulder and the hard-sphere

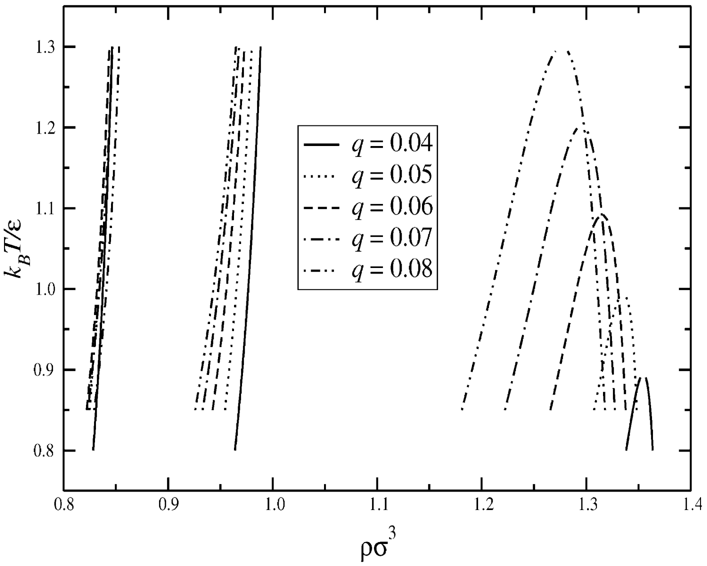

Fig. 35. Phase diagrams of square-shoulder fluids obtained by employing the MWDA-mapping of the full system [284] described in the text. The almost vertical lines on the left are liquidus and solidus lines, whereas the bell-shaped curves on the right are coexistence lines between two fcc-solids. (Redrawn from Ref. [284].)

repulsive Yukawa (HSRY) systems were considered in detail.[27] For the SS system, the results of Ref. [286] are in good agreement with simulation and they bring about the additional feature that a bcc-solid, a bcc–fcc, and a *bcc–bcc isostructural transition* are predicted to exist at very low temperatures, in the density region between the freezing and the fcc–fcc isostructural binodals, as shown in Fig. 36.

As far as the HSRY system is concerned, a marked discrepancy with the case of the attractive tails appears, namely that the isostructural transition does *not* survive the smoothing of the repulsive shoulder into a repulsive Yukawa tail. This makes it rather improbable that such a transition will be experimentally observed, since realistic repulsive potentials are smooth. Hence, though the repulsive potentials bring about broader coexistence regions than the attractive ones, and are therefore more likely to survive the polydispersity, this advantage is of little practical use if they cannot survive a smoothing of the repulsion. Rascón et al. [286] have shown that the crucial parameter for the existence of an isostructural transition in repulsive systems is the value of the *derivative* of the repulsion at contact between the hard particles.

We finally note that combinations of attractive and repulsive tails have also been studied, leading to exotic phase diagrams, displaying liquid–gas *and* solid–solid isostructural transitions and even a *quadruple point* where four phases are in coexistence with each other [287].

---

[27] The HSRY pair potential is given by Eq. (4.13) with the replacement $-\varepsilon \to \varepsilon$.

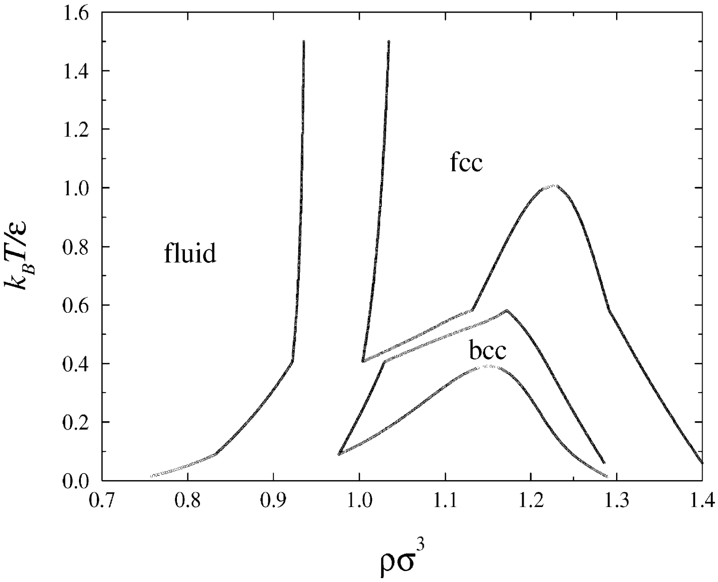

Fig. 36. The phase diagram of a square-shoulder system with shoulder width $q = 0.12$, obtained by employing the theory of Ref. [286]. (Courtesy of Andreas Lang.)

4.6. Concluding remarks

In this section we focused our attention on systems interacting primarily via a hard repulsion that can be subsequently "dressed" with an effective attraction caused by additional smaller components, such as free, nonadsorbing chains. The colloidal particles considered here were hard and this property alone guarantees the existence of a freezing transition. The main consideration, then, was how one can tune the attractions caused by the additional component and one important question that we have been able to answer is: *How much attraction is needed to make a liquid?*

The hard colloids considered here are the extreme opposite of the soft, penetrable polymer chains considered in the preceding section. There, we saw (in the context of the Gaussian core model, Section 3.5) that the freezing transition is not guaranteed to take place if the potential is too weak in comparison with the typical thermal energy of the particles. Hence, it is of great importance to be able also to consider systems which are intermediate between the extremely soft polymer chains and the extremely hard colloids and in which the steepness of the repulsions can be somehow tuned. The appropriate physical system which allows to build a bridge between these two is a collection of star-shaped polymers and a detailed study of the structure and thermodynamics of such assemblies is the topic of the following section. By studying star polymers we will attempt to give an answer to a question which is specular to the one mentioned in the previous paragraph, namely: *How much repulsion is needed to make a solid?*

5. Star polymers

In this section we consider systems which are intermediate between the polymer chains and the hard colloidal particles and provide a natural bridge between the two. These are solutions of star-shaped polymers, chemically synthesized by attaching a number of polymer chains to a common center. The resulting macromolecular aggregates are on average spherical in shape and can be viewed as colloidal particles. An effective interaction between star polymers in good solvents is theoretically derived and confirmed by direct comparison with experiments and simulations. This ultrasoft, logarithmic interaction is subsequently employed in the investigation of the structural and phase behavior of star polymer solutions, resulting in a rich variety of phases and an unexpected behavior of the fluid correlation functions. The corresponding effective interaction in Θ-solvent conditions is also discussed and its features are compared with those of the aforementioned interaction in good solvent conditions.

5.1. General considerations

Star polymers are macromolecular entities consisting of f polymeric chains chemically anchored to a common center. The number of arms f is also called *functionality* of the stars. When the degree of polymerization N is the same for all chains, one talks about *regular* stars. In this section, we are going to be dealing exclusively with long arms, $N \gg 1$, so that the universal scaling results of Section 3 can be applied. In this limit, the microscopic dimensions of the central core where the arms are attached become irrelevant when compared with the overall size of the star and hence we will be making the further simplification of treating the core of the stars as vanishingly small. Related systems are sterically stabilized colloidal particles (see Section 2.2.2) or micelles, which have star-like behavior at the limit where the size of the core particle becomes much smaller than the extent of the tethered polymeric brush [19,288,289].

Star polymers have attracted considerable interest in the recent past [290–292]. The reason for that is threefold. First, from a technical point of view, star polymers are important in several industrial applications [290]. One example are hydrogenated polyisoprene star polymers,[28] where they are used as viscosity index modifiers in oil industry applications due to their excellent shear stability. Further, commercial star polymers are brought into action in coating materials, as binders in toners for copying machines, and in several pharmaceutical and medical applications [290]. Second, from an experimental point of view, the recent synthesis of regular star polymers with various possible numbers of arms by Roovers and coworkers [293,294] made it possible to explore the physics of well-defined model systems, which are monodisperse in both the number of arms and the degree of polymerization. Important examples are polyisoprene stars with $f = 8,18$ [295] and polybutadiene stars with $f = 32, 64, 128$ [294], both synthesized by anionic polymerization. Thereafter, the static properties of stars can be studied by small-angle neutron scattering (SANS) (see Section 5.4), light scattering and small-angle X-ray scattering (SAXS). Quasi-elastic

---

[28] "Shellvis", distributed by Shell Chemical Co. [290].

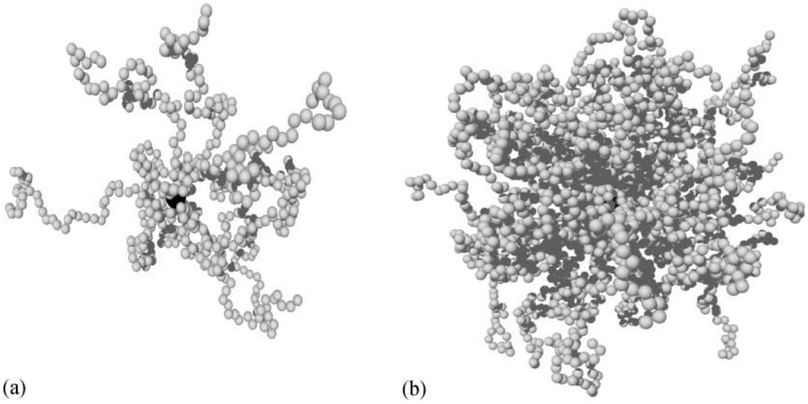

Fig. 37. Snapshots of star polymers in good solvents as obtained from MD simulations employing the model of Grest et al. [330] with: (a) $f = 10$, $N = 50$, and (b) $f = 50$, $N = 50$. For small f, the star looks like a fractal, aspherical object whereas for large f it resembles a spherical, colloidal particle. (Taken from Ref. [331].)

neutron scattering experiments using neutron spin-echo spectroscopy [296], as well as dynamical light scattering are used to study the collective and single-chain dynamics of arms of the star polymers, for a recent review see Ref. [290]. Third, star polymers constitute an important soft-condensed matter system, linking the fields of polymer physics and colloid physics, thus attracting also interest from a purely theoretical point of view. Star polymers with small arm numbers ($f = 1,2$) resemble linear polymers. Thus, their chain-averaged configurations show a considerable asphericity [297–299], although their averaged number density of monomers, $c(r)$, is spherically symmetric around the center of mass of the polymer. With increasing arm number f, the asphericity of the stars has been shown to decrease considerably [300–307], leading to "stiff" spherical particles in the limit of high f. This evolution of the shape of the star with increasing functionality is shown in Fig. 37. It is essentially in the limit $f \gg 1$ where a description of star polymers as sterically stabilized colloidal particles holds. This polymer–colloid hybrid character of star polymers has been explored in a number of publications dealing with the structural [288,290,295,308–319] and dynamical [288,311,312,320–329] properties of star polymers.

The synthesis of star polymers is an art of its own. Producing samples with a narrow molecular weight distribution, i.e., as monodisperse as possible, is a major challenge for the chemist. The problem of polydispersity becomes more acute as the functionality grows. Typically, anionic polymerization is employed to produce branches with narrow molecular weight distributions and postpolymerization linking, involving the still active chain ends, can then be done to produce branched polymers with a predetermined number of arms. These species are then excellent models for testing the theories. The two most common linking agents are chlorosilanes and divinylbenzene. We will not go any deeper into this specialized domain here; for more details we refer the reader to the review of Grest et al. [290]. Moreover, in line with the spirit of this work, we will not discuss the dynamical properties of star polymer solutions in this section, rather only the static ones. The latter are amenable to a treatment through an effective Hamiltonian, to be introduced in Section 5.6.

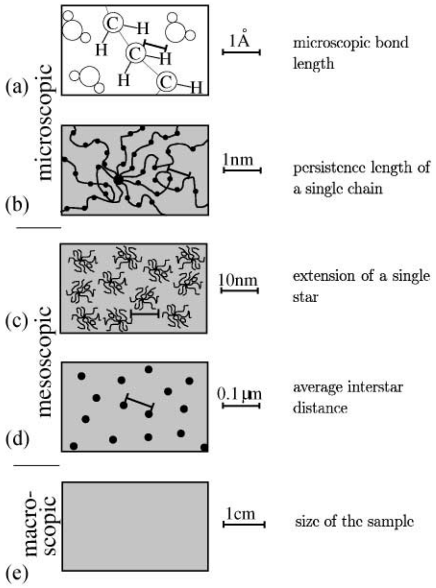

Fig. 38. The various length scales at which a star polymer solution can be looked upon, ranging from microscopic to macroscopic and covering in this way about eight orders of magnitude.

5.2. Length scales of a star

Solutions of star polymers can be looked upon in a vast range of length scales, depicted schematically in Fig. 38. It is the task of the physicist, and indeed the central goal of the field of statistical physics, to bridge this enormous gap. Starting from microscopic interactions, one would like to be able to predict the macroscopic behavior of the system and the ways in which it reacts to external "fields", such as stress, pressure, temperature, etc. Faced with such a question, it has to be decided at which length scale we start. At truly microscopic scales, of the order of an Ångstrom, one sees the individual monomer and solvent molecules, as shown in Fig. 38(a). Here, the detailed chemistry and the molecular interactions play the dominant role and determine the structure of the system at these scales; the properties are highly *nonuniversal*. However, as already mentioned in Section 3, if one looks at the chains at length scales one order of magnitude larger, a certain universality appears. All chains can be modeled as self-avoiding, fluctuating strings.[29] The situation is depicted in Fig. 38(b), where it can be seen that the inner of the star looks there like a semidilute polymer solution (see Section 3.3). This is the favorite starting point of a physicist because in this way the universal properties of the chains can be exploited in order to derive an equally universal, effective interaction between the centers of the stars, by tracing out the monomer degrees of freedom.

---

[29] The self-avoidance is present in a good solvent, whereas in a Θ-solvent the chain conformations are those of ideal chains (see Section 3.2.) We will be dealing in this section almost exclusively with good solvents, though.

It is to be expected, on physical grounds, that this interaction will be vanishingly small when the interstar separation is much larger than their typical size and it will attain high values when they overlap. This brings into the game the next length scale, shown in Fig. 38(c), which is the size of the stars. In what follows, we will discuss this length scale in more detail, including its dependence on f, N and solvent quality. Once this effective interaction has been established, though, the size of the star is automatically built in it and one can look at the system at even larger length scales, of the order a micron, as shown in Fig. 38(d). The stars have dropped out of sight as “hairy objects” there and they have been replaced by their centers, viewed as point particles. Thereafter, the known rules of statistical mechanics can be applied to make the next leap in length and predict the properties of the system at macroscopic scales.

We now turn our attention to the scales that characterize the size of the star. One common such length, which is also directly measurable in static scattering experiments is the *radius of gyration* R_g. Denoting by $\boldsymbol{r}_i$ the instantaneous position of the ith monomer in a star, the radius of gyration is defined as [290]

$$R_g = \left[\frac{1}{(Nf)^2}\sum_{i=1}^{Nf} \langle(\boldsymbol{r}_i - \boldsymbol{r}_{\mathrm{cm}})^2\rangle\right]^{1/2}, \tag{5.1}$$

where $\langle \ldots \rangle$ denotes an average over all monomer configurations and $\boldsymbol{r}_{\mathrm{cm}}$ denotes the center of mass of the star, given by

$$\boldsymbol{r}_{\mathrm{cm}} = \frac{1}{Nf}\sum_{j=1}^{Nf} \boldsymbol{r}_j . \tag{5.2}$$

Combining Eqs. (5.1) and (5.2) we obtain

$$R_g = \left[\frac{1}{2(Nf)^2}\sum_{i=1}^{Nf}\sum_{j=1}^{Nf} \langle(\boldsymbol{r}_i - \boldsymbol{r}_j)^2\rangle\right]^{1/2} . \tag{5.3}$$

Eqs. (5.1) and (5.3) can be compared with the definition of R_g for a linear chain, Eqs. (3.2) and (3.3). For chains obeying Gaussian statistics (ideal chains), it has been shown [290,332] that R_g of the whole star is related to the radius of gyration $R_g^{(1)}$ of a single arm through[30]

$$R_g = \sqrt{\frac{3f-2}{f}}R_g^{(1)} . \tag{5.4}$$

Additional length scales, which are useful in experiments, are the so-called *hydrodynamic radius* R_{H} and the *viscosity radius* R_{V}, which are both dynamical quantities related to the hydrodynamic drag of an equivalent sphere and whose definitions are based on the Stokes–Einstein relation for a suspension of spheres [290].

From a theoretical point of view and as far as the static properties of stars are concerned, another useful measure of the star size is the *corona radius* R_{c}, defined as the distance from the center of the stars in which all monomers are “inside”. Associated with this concept is the simplifying

---

[30] It should be emphasized that the gyration radius $R_g^{(1)}$ of a single arm *in the star* is not the same as the gyration radius of a free, linear polymer given by Eq. (3.2).

assumption that the average monomer concentration $c(r)$ around the star center vanishes identically beyond the corona radius R_c. As there are Nf monomers in the whole star, R_c is defined through the "conservation law" [333]:

$$4\pi \int_0^{R_c} r^2 c(r)\, dr = Nf . \tag{5.5}$$

In Section 5.3 we will discuss a standard model for the conformation of an isolated star, which gives an explicit scaling law for the quantity $c(r)$ and thus allows for the calculation of R_c through Eq. (5.5) above. However, even without knowing the function $c(r)$, the size of a star can be estimated by employing Flory-type arguments, similar to those presented in Section 3.1 for the free chains ($f = 1$). There, it was argued that associated with a single chain is an elastic free energy $F_{el}(R)$, given by Eq. (3.7), and an interaction free energy $F_{int}(R)$, given by Eq. (3.9), and that the size of the single chain is determined as the value at which the sum of the two is minimized. The procedure can be generalized to a star [334]. As there are now f chains, the elastic free energy $F_{el}(R)$ is given by

$$F_{el}(R) = \frac{3k_B T}{2} \frac{fR^2}{Na^2} , \tag{5.6}$$

where a is the monomer length. Moreover, in order to consider the extension of stars in both good and Θ-solvent conditions, let us also introduce the ternary-contact parameter w which plays a role analogous to that of the excluded volume parameter v for binary contacts [29]. Typically, w is of order unity. Applying a mean-field picture and taking into account that the average monomer concentration in a star of size R is $(Nf)/R^3$, we obtain for the interaction free energy the expression

$$F_{int}(R) \cong k_B T \left[v \frac{(Nf)^2}{2R^3} + wa^6 \frac{(Nf)^3}{R^6} \right] . \tag{5.7}$$

In good solvent conditions the pair term in $F_{int}(R)$ dominates over the ternary term and the latter can be ignored. In Θ conditions, where $v = 0$, the ternary term has to be kept under consideration. Adding $F_{el}(R)$ and $F_{int}(R)$ and minimizing with respect to R, we obtain from Eqs. (5.6) and (5.7) that the typical size R_* of the star scales as

$$R_* \sim f^{1/5} N^{3/5} \quad \text{(good solvent)} , \tag{5.8}$$

$$R_* \sim f^{1/4} N^{1/2} \quad (\Theta \text{ solvent}) . \tag{5.9}$$

Note that the N-scaling is the same as for a single chain, whereas the additional f-scaling expresses the stretching of the chains due to the star-shaped architecture. These scaling laws hold for both static scales defined above, the gyration radius R_g and the corona radius R_c. Indeed, as will be shown in the following section, the two differ by a simple proportionality constant of order unity.

5.3. Conformations of a single star

5.3.1. Scaling theory

Though the Flory argument predicts the scaling of the overall star size, it does not say anything about the conformation of an isolated star and, in particular, about the monomer concentration

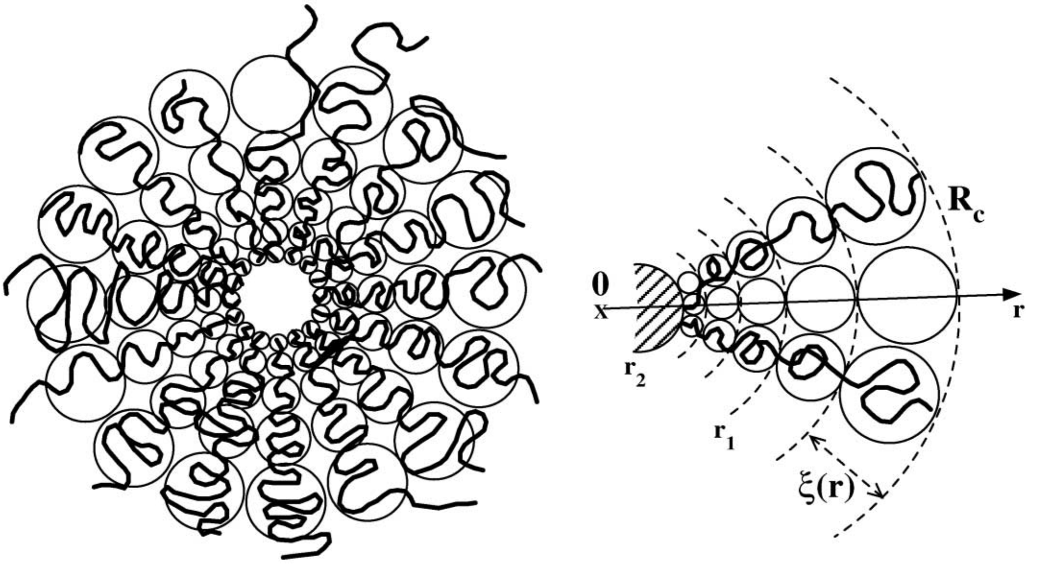

Fig. 39. The Daoud–Cotton [333] blob model of a star.

$c(r)$. The latter is a very useful quantity, as it plays an important role in the determination of the scattering function of a single star, the so-called *form factor* and also in the derivation of an effective potential between stars. An elegant and transparent way to obtain this quantity is by employing scaling theory in the framework of the standard *blob model* of a star, introduced by Daoud and Cotton [333] in analogy to polymer chains grafted on a flat surface [335,336]. This geometrical model is displayed in Fig. 39.

In the Daoud–Cotton model, the inner of the star is regarded as a succession of concentric shells of blobs, each blob in the shell having size $\xi(r)$. The spherical blobs are closely packed and within each one every chain behaves as if it were free, i.e., the effects of the neighboring chains are not present. By purely geometrical arguments, it follows that the blob size $\xi(r)$ scales as

$$\xi(r) \sim r f^{-1/2} . \tag{5.10}$$

Let $n(r)$ be the number of monomers inside a blob centered at r. A local swelling parameter $\alpha(r)$ can then be defined as the ratio between the swollen and ideal blob size $\xi_0(r)$:

$$\alpha(r) = \frac{\xi(r)}{\xi_0(r)} . \tag{5.11}$$

The ideal and swollen sizes are given by Eqs. (3.5) and (3.12), respectively, yielding the result

$$\alpha^5(r) \sim \bar{v} n^{1/2}(r) , \tag{5.12}$$

where $\bar{v} \equiv v a^{-3}$ is a dimensionless excluded volume parameter. Depending on the value of $\alpha(r)$, one distinguishes three separate regions of the star, namely the following.

(I) *The swollen region*: Here, the blobs are swollen, i.e., they size $\xi(r)$ scales with the number of monomers $n(r)$ with the Flory exponent 3/5 [see Eq. (3.12)], yielding the following scaling laws for the various quantities of interest:

$$n(r) \sim \left(\frac{r}{a}\right)^{5/3} \bar{v}^{-1/3} f^{-5/6} , \tag{5.13}$$

$$\alpha(r) \sim \left(\frac{r}{a}\right)^{1/6} f^{-1/12} \bar{v}^{1/6} , \tag{5.14}$$

$$c(r) \sim a^{-3} \left(\frac{r}{a}\right)^{-4/3} \bar{v}^{-1/3} f^{2/3} . \tag{5.15}$$

The last equation, combined with the scaling law for the osmotic pressure Π in a semidilute polymer solution, Eq. (3.44), yields the scaling of the local osmotic pressure inside the star as

$$\Pi(r) \sim f^{3/2} r^{-3} . \tag{5.16}$$

Using the Flory–Huggins theory result $\Pi \sim c^2$, arising from the virial expansion in Section 3.3.1, would have led to the erroneous scaling $\Pi(r) \sim r^{-8/3}$.

The extent of the swollen region ranges from the outermost of the star, $r = R_c$, down to a distance r_1 from the center (see Fig. 39), at which the local scaling factor $\alpha(r)$ attains the value unity. From Eq. (5.14) we obtain this value as

$$r_1 \sim f^{1/2} \bar{v}^{-1} a . \tag{5.17}$$

(II) *The unswollen region*: The results for the swollen region are based on the assumption that the blob size $\xi(r)$ exceeds the size of the thermal blob $l_c \cong a\bar{v}^{-1}$ [29], where the latter is a measure of the distance over which the behavior of the chain is ideal; on longer scales the chain is self-avoiding. However, as $\xi(r)$ becomes smaller with approaching the star center, [see Eq. (5.10)], at distances $r < r_1$ from the center the blobs have their ideal size, $\alpha(r) = 1$, and this leads to the scaling relations:

$$n(r) \sim \left(\frac{r}{a}\right)^{2} f^{-1} , \tag{5.18}$$

$$c(r) \sim a^{-3} \left(\frac{r}{a}\right)^{-1} f^{1/2} . \tag{5.19}$$

The unswollen region persists down to a distance r_2 from the center (see Fig. 39), where the local concentration $c(r)$ reaches the value unity and the star resembles a melt. From Eq. (5.19) we obtain this value as

$$r_2 \sim a f^{1/2} . \tag{5.20}$$

(III) *The core*: At distances $0 < r < r_2$, the concentration is unity, the blob size coincides with the monomer size and the chains are completely stretched. In this *core* region of the star there are N_c monomers. With $R_{\rm core}$ denoting the core size, the scaling laws read as

$$f N_c \sim \left(\frac{r_2}{a}\right)^{3} , \tag{5.21}$$

$$N_c \sim f^{1/2} , \tag{5.22}$$

$$R_{\text{core}} \sim N_c a , \tag{5.23}$$

$$c(r) \sim a^{-3} . \tag{5.24}$$

Combining the results of this section with the definition of the corona radius R_c, Eq. (5.5), the scaling of the latter is obtained as

$$R_c \sim \left[Nf + \frac{1}{10}\frac{f^{3/2}}{\bar{v}^2} + \frac{1}{6} f^{3/2} \right]^{3/5} \bar{v}^{1/5} f^{-2/5} a . \tag{5.25}$$

Integrating in Eq. (5.5) from a lower limit equal to zero, is tantamount to ignoring the size of the microscopic particle on which the chains are attached. Depending on the degree of polymerization N (length of the chains), the strength of the excluded volume interactions $\bar{v}$ and the functionality f, one can distinguish three regimes for the N-, f- and $\bar{v}$-dependencies of the star size, as follows:

Regime R_c

$$N \gg f^{1/2}\bar{v}^{-2} \to N^{3/5}\bar{v}^{1/5}f^{1/5}a , \tag{5.26}$$

$$f^{1/2}\bar{v}^{-2} \gg N \gg f^{1/2} \to N^{1/2}f^{1/4}a , \tag{5.27}$$

$$f^{1/2} \gg N \to (Nf)^{1/3}a . \tag{5.28}$$

If the conditions of (5.26) hold, then most of the star is in the swollen region, so that the core and the unswollen part of the star can be ignored. The scaling of (5.26) confirms the Flory prediction of Eq. (5.9) for good solvents, whereas the scaling of (5.27) the Flory prediction in Eq. (5.9) for Θ-solvents. As can be seen from Eqs. (5.26) and (5.27) above, the spatial extension of stars is larger than that of an isolated chain with the same degree of polymerization, due to stretching of the chains caused by the star architecture. At the same time, stars are smaller than a single chain with a degree of polymerization Nf; the latter has an extent which scales as $f^{3/5}N^{3/5}$ in good solvents and as $f^{1/2}N^{1/2}$ in Θ-solvents. At the same time, the above equations demonstrate that the quality of the solvent alone is not sufficient to determine the scaling behavior of the stars; if the chains are short, then the star can show Θ-type behavior even in a good solvent. In this case, the whole of the star will be in the unswollen region and then the scaling relation (5.27) will be satisfied.

We are going to be considering the case of stars with *long chains* in a *good solvent*, so that the swollen region will dominate throughout the extent of the star and the scaling relation (5.26) will hold. In this situation, a relationship between the corona radius R_c and the radius of gyration R_g can be established, when the latter is interpreted in a "mechanical" sense as the expectation value of r^2 evaluated with the probability distribution $c(r)$. With the latter given by the scaling law $c(r) \sim r^{-4/3}$, it holds

$$R_g^2 = \frac{\int_0^{R_c} r^{-4/3} r^4 \, \mathrm{d}r}{\int_0^{R_c} r^{-4/3} r^2 \, \mathrm{d}r} = \frac{5}{11} R_c^2 . \tag{5.29}$$

Results on isolated star polymers in Θ-solvent conditions can be found in Refs. [290,305–307,320,337,338]. An effective pair potential describing accurately experimental SANS data for star polymer solutions in the neighborhood of the Θ point was introduced by Likos et al. [316] and is described in some detail in Appendix E.

5.3.2. Simulations

The conformations of isolated stars and the associated predictions of the scaling theory have been tested in a number of microscopic Monte-Carlo and molecular dynamics simulations, both on-lattice [302,305,307,339–341] and off-lattice [78,292,303,330,338,342,343]. Whereas in on-lattice simulations a coarse-grained model of description is employed automatically, in off-lattice simulations a model microscopic interaction between the beads is used, for a recent review see Ref. [341].

A common model for the monomer–monomer interactions in off-lattice simulations in good solvents has been introduced by Grest et al. [330]. All monomers are assumed to interact by means of the purely repulsive truncated and shifted Lennard-Jones (LJ) potential, $V_0(r)$, given by

$$V_0(r) = \begin{cases} 4\varepsilon\left[\left(\dfrac{r}{\sigma_{\mathrm{LJ}}}\right)^{12} - \left(\dfrac{r}{\sigma_{\mathrm{LJ}}}\right)^{6} + \dfrac{1}{4}\right] & \text{if } r < 2^{1/6}\sigma_{\mathrm{LJ}}\ , \\ 0 & \text{if } r > 2^{1/6}\sigma_{\mathrm{LJ}}\ , \end{cases} \tag{5.30}$$

where ε sets and energy and σ_{LJ} a length scale. The good solvent quality is modeled by the purely repulsive nature of the interaction. On the other hand, the connectivity of the chains is modeled by an *additional* interaction between monomers on the same chain, which is given by the so-called *finite extendible nonlinear elastic* (FENE) potential $V_{\mathrm{FENE}}(r)$:

$$V_{\mathrm{FENE}}(r) = \begin{cases} -15\varepsilon\left(\dfrac{R_0}{\sigma_{\mathrm{LJ}}}\right)^{2}\ln\left[1 - \left(\dfrac{r}{R_0}\right)^{2}\right] & \text{if } r < R_0\ , \\ \infty & \text{if } r > R_0 \end{cases} \tag{5.31}$$

with $R_0 = 1.5\sigma_{\mathrm{LJ}}$. For small f, $f \lesssim 6$, the interior of the star is not too dense and standard MC simulations are efficient. However, as f increases, it becomes dense and hence one has to employ either MD simulations or local stochastic MC methods [344,345]. In addition, it is necessary to attach the chains to a core of microscopic dimensions, so that problems with overlaps of the innermost monomers can be avoided [78]. In this case, the size of the core has to be taken into account in testing the predictions of the scaling theory regarding the size of the star, as in the latter the core size is assumed to be vanishingly small [78]. A detailed study of chains tethered on a spherical particle of nonnegligible extent can be found in Ref. [346].

The scaling law regarding the behavior of the monomer density $c(r)$, Eq. (5.15), is tested by averaging the latter quantity during the simulation run and plotting $\ln[f^{-2/3}c(r)]$ against $\ln r$. In this way, the exponent $-4/3$ has been confirmed in a number of simulations, for a broad range of arm numbers, ranging from $f = 3$ up to 270 [290]. The scaling of the star size with N and f is difficult to be verified in a simulation if the corona radius R_c is used as a measure; there always exists a diffuse layer of polymer beyond the scaling regime, whereas in the Daoud–Cotton model an artificially sharp drop of the monomer density to zero at a distance $r = R_c$ from the center is assumed. Therefore, the gyration radius R_g, Eq. (5.1), is used to characterize the star size. The latter is suitable for a simulation, as its calculation amounts to taking averages over configurations. The predictions of the Daoud–Cotton model have been confirmed, both in on-lattice [78,302,305,307,331,339,347] and off-lattice [292,306,330,348] simulations.

5.4. Scattering methods and the form factor

A scattering experiment provides information about the correlations in reciprocal space. If we are dealing with an isolated star or with a very dilute solution, where interstar correlations can be ignored, scattering provides information about the molecular weight, size and monomer–monomer correlations *inside* the star. In concentrated solutions, it also provides information about interstar correlations, as we shall see below. The central result that connects the measured scattering intensity $I(Q)$ at an angle θ from an incident radiation of wavelength λ with the spatial distribution of scatterer, reads as [28,290,349]

$$I(Q) = \int \bar{\rho}(\mathbf{r}')\bar{\rho}(\mathbf{r}-\mathbf{r}')\exp(i\mathbf{Q}\cdot\mathbf{r})\,\mathrm{d}\mathbf{r}\,\mathrm{d}\mathbf{r}' , \tag{5.32}$$

where $Q = 4\pi\sin(\theta/2)/\lambda$ is the scattering vector and $\bar{\rho}(\mathbf{r})$ denotes the spatial distribution of scattering density. In the case of small-angle neutron scattering (SANS), the *coherent* scattering intensity $I(Q)$ can also be expressed as [290]

$$I(Q) = N_{\mathrm{s}}\frac{\Delta\rho^2}{N_{\mathrm{A}}}\mathscr{S}(Q) , \tag{5.33}$$

where N_{s} is the number of scatterers (stars) in the system, N_{A} is Avogadro's constant, $\mathscr{S}(Q)$ is the static scattering factor and $\Delta\rho^2 = (\rho_{\mathrm{m}} - \rho_{\mathrm{s}})^2$ is the contrast factor between the scattering length densities of the monomers, ρ_{m}, and the solvent, ρ_{s}. The scattering length density ρ_i of the component i in the mixture is calculated as [350]

$$\rho_i = \frac{\sum_z b_z}{v_i} , \tag{5.34}$$

where b_z is the coherent scattering length of an atom z in the solvent or of a repeat unit in a polymeric molecule and v_i is the respective volume; the sum is carried, hence, over all atoms in a molecule or in the repeat unit. In SANS one takes advantage of the fact that neutrons and protons scatter neutrons differently in order to develop a very useful technique called *labeling*. Indeed, neutrons have a positive scattering length density, whereas protons a negative one, indicating that wavefunction of the incident neutrons in the beam changes phase upon scattering on protons. Hence, by selectively replacing hydrogen atoms with deuterium ones, one can tune the scattering length density of the scatterers (stars) or parts of them with that of the solvent, without affecting the relevant, chemical properties of the substance. In this way, in a SANS experiment, it can be arranged that only parts of a star show contrast with the solvent or that single stars be made visible in a sea of others, when the latter are index matched with the solvent and the former are not.

When scattering from a very dilute solution is performed, the static scattering factor $\mathscr{S}(Q)$ is known as the *form factor* $P(Q)$ of the object and it contains information about its molecular weight, size and mass distribution. Indeed, in the limit $Q \to 0$, the probe is too coarse to detect anything else but the number of scatterers in the sample and hence it delivers information about the average density or, equivalently, the molecular weight of the stars. At larger scattering vectors, $Q \sim R_g^{-1}$ the stars can be viewed as diffuse, spherical objects of size R_g and hence information about the radius of gyration R_g is gained. For $\xi_{\max}^{-1} < Q < a^{-1}$, where $\xi_{\max}$ denotes the size of the outermost blob in the Daoud–Cotton model and a the monomer length, the scattering can be understood by covering the star with spheres of radius Q^{-1} and in the absence of strong correlations among their positions, the latter scatter incoherently. The resulting scattering intensity is then the number of spheres times the form factor of a single sphere. As the latter contains a single, self-avoiding polymer chain, the form factor at these high Q-values is expected to scale as that of a chain, yielding the power-law dependence $P(Q) \sim Q^{-1/\nu}$, see Eq. (3.15). These various regimes are brought together in a compact form for $P(Q)$ introduced by Dozier et al. [295] which reads as

$$V_W P(Q) = V_W \exp\left[-\frac{(QR_g)^2}{3} \right] + \frac{4\pi\alpha}{Q\xi} \frac{\sin[\mu \tan^{-1}(Q\xi)]}{[1+(Q\xi)^2]^{\mu/2}} \Gamma(\mu) , \tag{5.35}$$

where V_W denotes the molar volume, $\mu = 1/\nu - 1$, ξ is the average blob size, $\alpha \sim \bar{v}(\xi/a)^{1/\nu}$ and $\Gamma(\mu)$ is the gamma function. According to Dozier et al. [295], the quantities V_W,α,ξ and R_g are to be treated as free fit parameters, whereas the exponent ν is fixed at its Flory value 3/5, yielding $\mu = 2/3$. The Dozier form factor yielded excellent fits for an array of data obtained for stars with $f = 8$–128 arms [314]. Other common functional forms for $P(Q)$, which also include a few fit parameters, are that of Alessandrini and Carignano [351], based on renormalization group techniques and the form factor parameterization of Beaucage [352,353], which reads as

$$V_W P(Q) = V_W \exp\left[-\frac{(QR_g)^2}{3} \right] + B\left(\frac{[\mathrm{erf}(1.06 \cdot QR_g/\sqrt{6})]^3}{QR_g} \right)^{d_f} \equiv G(Q) + F(Q) . \tag{5.36}$$

The first term is identical with the Dozier fit of Eq. (5.35) whereas the term $F(Q)$ is substantial at high Q values and reflects the short range, i.e., monomer correlations. The quantities V_W, R_g, B and d_f are again fit parameters.

Finally, we point out that the form factor can also be measured in a standard simulation. For a system of point masses, $P(Q)$ can be given as a sum over all monomers of the star,

$$\begin{aligned} P(Q) &= \frac{1}{(Nf)^2} \sum_{i=1}^{Nf} \sum_{j=1}^{Nf} \langle \exp[\mathrm{i}\boldsymbol{Q}\cdot(\boldsymbol{r}_i - \boldsymbol{r}_j)] \rangle \\ &= \frac{1}{(Nf)^2} \left\langle \left| \sum_{i=1}^{Nf} \exp(\mathrm{i}\boldsymbol{Q}\cdot\boldsymbol{r}_i) \right|^2 \right\rangle . \end{aligned} \tag{5.37}$$

The star form factor has been calculated in the simulation studies of Refs. [330,338].

5.5. *Concentration effects*

Up to now, we have only considered isolated stars. Now, we assume that there are N_s stars included in the volume Ω, having therefore an average density $\rho = N_s/\Omega$. In analogy with the considerations set forth in Section 3.3 for free chains, one can also distinguish for star polymers between dilute, semidilute and concentrated solutions. The quantity that separates the two first regimes is the so-called *overlap density* ρ_*, defined as the density at which the stars start to overlap within their coronae and estimated by $\rho_* R_c^3 \cong 1$.[31] From Eq. (5.26) we obtain the scaling of ρ_* as

$$\rho_* \sim N^{-9/5}\bar{v}^{-3/5} f^{-3/5} a^{-3} . \tag{5.38}$$

The behavior of star solutions as a function of concentration was studied theoretically within the blob model by Daoud and Cotton [333] and also later by Witten and Pincus [308] and by Witten et al. [309]. The main results from these approaches are summarized below.

According to Daoud and Cotton [333], above the overlap concentration the star solution looks as follows: around each star there is a region of space with size

$$\chi \sim (a^3 c)^{-3/4}\bar{v}^{-1/4} f^{1/2} a , \tag{5.39}$$

where the star has a single star behavior. At the overlap concentration c_*, χ is evidently of the order of the corona radius R_c. However, for distances larger than χ, there is a screening of the interaction and all the blobs from different stars have *the same* size $\xi(c)$, where ξ is the density screening length of semidilute polymer solutions introduced in Section 3.3.2 and whose concentration dependence is given by Eq. (3.47); in more detail:

$$\xi(c) \sim (a^3 c)^{-3/4}\bar{v}^{-1/4} a = \chi f^{-1/2} . \tag{5.40}$$

Witten et al. [308] argued about the concentration dependence of the osmotic pressure Π of the solution as follows. Below the overlap concentration, in the dilute solution regime, the osmotic pressure $\Pi(\rho)$ follows a van't Hoff law analogous to Eq. (3.30) for isolated chains, namely

$$\Pi = \rho k_B T \quad (c < c_*) . \tag{5.41}$$

However, far above the overlap concentration, $c \gg c_*$, the solution looks like a semidilute polymer solution with a blob size ξ and hence the osmotic pressure will be given by

$$\Pi = k_B T \xi^{-3} \quad (c > c_*) . \tag{5.42}$$

As $\xi \sim c^{-3/4}$, Eq. (5.42) is in full agreement with the general result $\Pi \sim c^{9/4}$, Eq. (3.44). The two expressions, Eqs. (5.41) and (5.42) have a mismatch at the overlap concentration c_*. The former yields $\Pi(c_*) \cong k_B T R_c^{-3}$ whereas the latter $\Pi(c_*) \cong k_B T R_c^{-3} f^{3/2}$, see Eq. (5.40). In passing from the dilute to the semidilute regime, the pressure increases sharply by a factor $f^{3/2}$ when the concentration changes by only a factor of order unity. Witten et al. [308] argued further that this implies a corresponding drop in the osmotic compressibility $\chi_{osm} = (c\partial\Pi/\partial c)^{-1}$ and, as the latter is related to the low-wavevector limit of the structure factor $S(Q)$ by $c k_B T \chi_{osm} = S(0)$ [Eq. (2.57)], this implies that, above c_*, the *decrease* in $S(0)$ scales with $f^{3/2}$. The decrease in $S(0)$ is accompanied by an increase by the same amount in $S(QR_c \cong 1)$ which signals a strong ordering at a length scale R_c. This spatial ordering, a precursor of an incipient crystalline state, becomes stronger with increasing f, hence it is to be expected that stars with a high functionality will freeze more easily than stars with a lower one [308].

---

[31] Notice that the *monomer* concentration c and the *star* concentration ρ are connected by the relation $c = Nf\rho$.

The argument was then carried further, to concentrations much above the overlap concentration, $c \gg c_*$. There, the star centers are swimming in a sea of blobs of constant size in a semidilute polymer solution. The system is perfectly homogeneous, without any physical reasons for crystalline ordering, and the center–center structure factor $S(Q)$ is deprived of any significant structure. Given that a crystal was predicted to occur at $c \cong c_*$, the scenario put forward by Witten et al. [308], was that the stars would freeze and remelt, i.e., present the reentrant melting scenario similar to the one we already encountered for the Gaussian core model in Section 3.5.6. Associated with such a phase diagram topology is the existence of a "lower freezing functionality" $f_{\rm l}$, such that star polymer solutions with $f < f_{\rm l}$ will not freeze at any density. Witten et al. [308] predicted $f_{\rm l} \cong 100$, stating that this estimate could also be off by an order of magnitude in either direction. As we shall see in the following sections, all these predictions have been confirmed and a precise result for $f_{\rm l}$ has been derived by using the modern approach of introducing an effective Hamiltonian for the center-to-center interactions between stars [315,317,319].

The above predictions have been experimentally verified by both SAXS and SANS experiments on monodisperse solutions of star polymers [290,310,313,314,354] as well as on block copolymer micelles [288,289,355–358]. In SANS experiments, performed for $f = 8$, 18, 32, 64 and 128, the scaling theory predictions about the nonmonotonic behavior of the maximum of $S(Q)$, as well as the absence of freezing for low functionalities, $f \leq 32$, has been confirmed, whereas the samples with $f = 64$ and 128 arms displayed Bragg peaks above the overlap concentration [354]. On the other hand, in the SAXS experiments with copolymer micelles, McConnell et al. [355,356,358] observed the predicted macrocrystal ordering into a fcc or bcc crystal for hard and soft micelle–micelle interactions, respectively. Moreover, in a later series of SAXS experiments, the predicted reentrant melting (order to disorder) transition was also observed above the overlap density [289,357,358]. In addition, a second freezing and a second subsequent reentrant melting were observed for the softest micellar solution, i.e., for the micellar system with the longest arms, which is physically the closest to the stars [289,357,358]. Similarly, recent SAXS experiments by Ishizu et al. on solutions of many-armed star polymers [359] and on star copolymers [360–362] above the overlap concentration, revealed macrocrystal ordering into a bcc lattice which changed into a mixture of bcc and fcc crystallites upon increasing the concentration. For a recent review of these experiments, we refer the reader to Ref. [363].

In full analogy with the case of free chains presented in Section 3.3.3, the increase of concentration above c_* causes the stars to shrink. Daoud and Cotton [333] have shown that the size $R_{\rm c}$ of the stars remains constant up to the overlap concentration c_* but thereafter two regimes can be distinguished in which $R_{\rm c}$ decreases with the following power laws:

$$R_{\rm c} \sim (ca^3)^{-3/4}\bar{v}^{-1/4}f^{1/2}a \quad \text{for } c_* < c < c_1 \ , \tag{5.43}$$

$$R_{\rm c} \sim N^{1/2}(ca^3)^{-1/8}\bar{v}^{1/8}a \quad \text{for } c \gg c_1 \ , \tag{5.44}$$

where the characteristic concentration c_1 scales as

$$c_1 \sim c_* f^{2/5} \ . \tag{5.45}$$

Notice that the $R_{\rm c} \sim c^{-3/4}$ of (5.43) regime occurs only if the concentration window $c_* < c < c_1$ is broad enough, i.e., for sufficiently high-arm numbers. For small-arm numbers, only the $R_{\rm c} \sim c^{-1/8}$ of (5.44) will be seen. The shrinkage of the radius of gyration in 18-arm stars above the overlap concentration has been observed experimentally, using zero-average contrast methods [290,295,310,314]. The size of the star was found to be constant up to c_* and in a double-logarithmic plot a slope of $-1/8$ was found above c_*. No sign of the $c^{-3/4}$ dependence in this volume fraction range has been observed, pointing that for $f = 18$ the region $c_* < c < c_1$ is not wide enough.

5.6. Effective interactions between star polymers

We now wish to study the properties of star polymer solutions by employing the language of effective interactions. By tracing out the monomeric degrees of freedom associated with the fluctuating arm chains, we will introduce an effective potential between the remaining star centers, treated as point particles. In this way, we will view star polymers as colloidal particles and, as will be shown shortly, they will turn out to be ultrasoft ones.

5.6.1. Theory

The pioneering idea for deriving the effective interaction is due to Witten and Pincus [309]. Let us first consider the case $f = 1$, i.e., two free chains, keep one of the ends of each chain at a separation r from each other and consider the effective interaction between them, due to all the remaining monomers that are free to fluctuate.[32] According to its definition, Eq. (2.33), the sought-for effective interaction will be given by

$$\beta v(r) = \beta v_{\mathrm{mm}}(r) - \ln\left[\frac{Q_2(r)}{Q_2(\infty)}\right], \tag{5.46}$$

where $v_{\mathrm{mm}}(r)$ is the direct monomer–monomer interaction, $Q_2(r)$ is the constrained partition function of the system when the two ends are kept fixed at separation r and the denominator on the right-hand side serves the purpose of sending the effective interaction to zero when this separation tends to infinity, see also Eq. (3.61). The direct interaction $v_{\mathrm{mm}}(r)$ is, in a good solvent, a steep repulsion having the range of the monomer size, i.e., at most a few Ångstroms. On the other hand, it is expected on physical grounds that the second term on the rhs of Eq. (5.46) will be of much longer range, typically of the gyration radius of the chains, cf. Eq. (3.64). Hence, we omit the term $v_{\mathrm{mm}}(r)$ from our considerations below and focus only on the second term, which is mediated by all the traced out degrees of freedom.

Let us consider the case where r is of the order of the monomer length, a. Then, the bulk of the system will look like a single fluctuating chain with $2N$ monomers. Accordingly, the partition function $Q_2(r \sim a)$ will be given by the general result, Eq. (3.24), with $N \to 2N$, namely

$$Q_2(r \sim a) \propto \tau^{2N}(2N)^{\gamma-1}\ . \tag{5.47}$$

---

[32] In Section 3.4 we considered another effective interaction between free chains, namely that between their centers of mass. Here we consider the one between their endpoints and the two are evidently different from each other.

On the other hand, as already discussed in Section 3.4.1, the quantity $Q_2(\infty)$ is simply Q_1^2 and using Eq. (3.24) we obtain

$$Q_2(\infty) \propto \tau^{2N} N^{2(\gamma-1)} . \tag{5.48}$$

Eqs. (5.47) and (5.48) yield the result

$$\frac{Q_2(r \sim a)}{Q_2(\infty)} \propto N^{1-\gamma} . \tag{5.49}$$

The ratio on the left-hand side is dimensionless and, when the chains are looked upon at scales where the microscopic details are not visible, it can only depend on the dimensionless ratio r/R, where R denotes the typical chain size. At the same time, it is a power law in N and the latter enters the combination r/R only through the dependence of the chain size on the degree of polymerization, $R \propto N^{\nu}$. The consequence is that $Q_2(r \sim a)/Q_2(\infty)$ must be a power law in r/R,

$$\frac{Q_2(r \sim a)}{Q_2(\infty)} \propto \left(\frac{r}{R}\right)^{x} \propto N^{-x\nu} . \tag{5.50}$$

Eqs. (5.49) and (5.50) imply $x = (\gamma - 1)/\nu$. Though the derivation is based on the assumption $r \sim a$, the result of Eq. (5.50) can be extended up to $r \sim R$. Indeed, at these distances one expects the effective interaction to have fallen practically to zero, as the two chains do not overlap, and Eq. (5.50) yields $Q_2(r \sim R)/Q_2(\infty) = 1$ there, with the implication that $\beta v(r)$ from Eq. (5.46) vanishes. The scaling argument yields the correct physical behavior at both extreme cases, $r \sim a$ and $r \sim R$, hence we can write, using Eq. (5.46),

$$\beta v(r) = -\frac{\gamma - 1}{\nu} \ln\left(\frac{r}{R}\right) \quad (r \leq R) . \tag{5.51}$$

Note the ultrasoft, logarithmic divergence of the effective interaction as $r \to 0$.

Witten and Pincus [309] considered next the opposite case, $f \gg 1$. By employing the Daoud–Cotton blob picture, assigning a free energy $k_B T$ to reach blob and counting (geometrically) the number of blobs per star, the partition function Q_1 of an isolated star was calculated as

$$Q_1 \propto [N f^{(\nu-1)/(2\nu)}]^{-\nu f^{3/2}} . \tag{5.52}$$

As before, it holds $Q_2(\infty) = Q_1^2$, hence

$$Q_2(\infty) \propto [N f^{(\nu-1)/(2\nu)}]^{-2\nu f^{3/2}} . \tag{5.53}$$

The scaling argument is now repeated as above: when two such stars are brought at a center-to-center distance $r \sim b$, where b is a typical blob size, the picture is identical to that of a single star with $2f$ arms, with the implication

$$Q_2(r \sim b) \propto [N(2f)^{(\nu-1)/(2\nu)}]^{-\nu(2f)^{3/2}} . \tag{5.54}$$

From Eqs. (5.53) and (5.54) the ratio of the partition functions is obtained as

$$\frac{Q_2(r \sim b)}{Q_2(\infty)} \propto N^{-\nu\theta(f)} , \tag{5.55}$$

where $\theta(f) \propto f^{3/2}$. Invoking once more the argument that this ratio can only depend on r/R and that $R \propto N^{\nu}$, the effective star–star interaction is obtained as [309]

$$\beta v(r) = -\alpha f^{3/2} \ln\left(\frac{r}{R}\right) \quad (r \le R) \tag{5.56}$$

with the unknown proportionality factor α. The logarithmic divergence is recovered again. However, this effective potential is still not complete. Three questions have to be answered, namely the following:

(a) What is the value of the prefactor α?
(b) Precisely at which length scale R does the logarithmic interaction cease to be valid?
(c) To which functional form does the interaction cross over for separations $r > R$, given that an abrupt crossover to zero for such distances is evidently unphysical?

These issues were addressed by Likos et al. [315], who introduced a complete effective interaction potential between star centers for arbitrary f. The way in which the various parameters were chosen is discussed below:

(a) By matching expression (5.51), valid for $f = 1$ with expression (5.56), valid for $f \gg 1$, it was postulated that $\alpha = (\gamma - 1)/\nu = 5/18$ for all f. This assumption evidently gives the exact result for $f = 1$ and, for $f = 2$, it yields for the prefactor $\alpha f^{3/2}$ the value 0.786, which is very close to the exact value 0.8 calculated by means of renormalization group techniques by des Cloizeaux [364]. Moreover, recent renormalization group calculations show that the functional form $(5/18)f^{3/2}$ yields excellent agreement with the "exact" value, at least up to $f = 6$ [365–368].
(b) The logarithmic interaction was assumed to set in whenever significant overlap between the blobs of the two stars takes place. Thereafter, the length scale R was fixed as the length at which the outermost blobs of the two stars fully overlap. Hence, by defining $\sigma/2$ as the distance from the star center to the center of the outermost blob (see Fig. 39), the logarithmic interaction was assumed to be valid for $r \le \sigma$.
(c) For distances $r \ge \sigma$, the interaction was *postulated* to have a Yukawa form, with the decay length given by the diameter of the outermost blob, $\xi_{\max} = 2\sigma/\sqrt{f}$, as dictated by geometry. This is intuitively clear, as the blob size is the only relevant length scale at weak overlaps between the chains.

By combining the logarithmic with the Yukawa form and matching them at $r = \sigma$ by requiring that both the potential and its first derivative (the force) be continuous there, the effective star–star interaction was put forward as [315]

$$\beta v(r) = \begin{cases} \dfrac{5}{18} f^{3/2}\left[-\ln\left(\dfrac{r}{\sigma}\right) + \dfrac{1}{1+\sqrt{f}/2}\right] & \text{for } r \le \sigma\,, \\[2ex] \dfrac{5}{18} f^{3/2} \dfrac{1}{1+\sqrt{f}/2}\left(\dfrac{\sigma}{r}\right) \exp\left[-\dfrac{\sqrt{f}(r-\sigma)}{2\sigma}\right] & \text{for } r \ge \sigma\,. \end{cases} \tag{5.57}$$

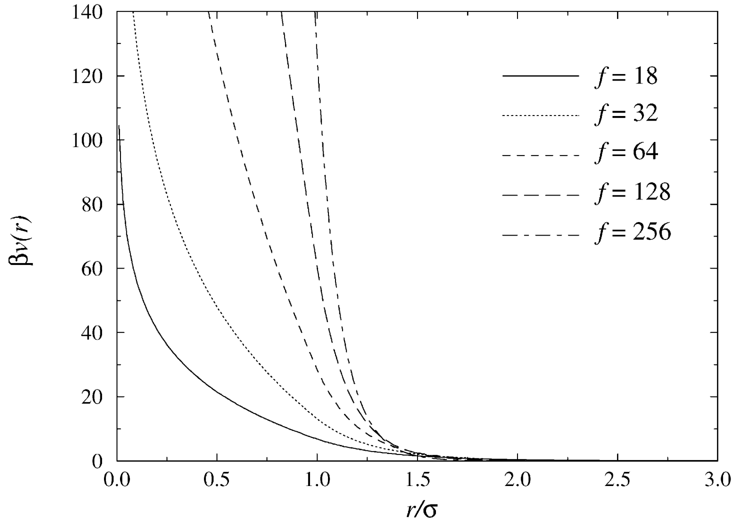

Fig. 40. The effective star–star potential of Eq. (5.57) for a number of different f-values. Notice that the potential becomes harder with increasing f, tending eventually to a HS interaction for $f \to \infty$.

The potential is shown in Fig. 40 for various values of the functionality f. It can be seen that, as all interactions in the system were assumed to be of the excluded volume type (athermal solvents), the effective potential scales with the temperature and the latter becomes thermodynamically irrelevant. However, another "thermodynamic parameter" appears in its place controlling the stiffness of the interaction, namely the functionality f. As can be seen, the interaction has an ultrasoft logarithmic core, featuring a divergence as $r \to 0$ which is slower than any power law. Yet, this divergence becomes steeper as f grows and, formally, the interaction reduces to a hard sphere potential for $f \to \infty$. As anticipated in Section 5.1, the number of arms acts as a tunable parameter which allows us to control the steepness of the interaction, interpolating in this way at the level of the pair potential between soft, fractal chains and hard colloids. The physical picture of the stars becoming increasingly compact objects for increasing f is reflected in the stiffening of the effective potential.

The logarithmic core was also derived by Pincus [61], using independent arguments based on the r-dependence the osmotic pressure in the interior of the star, given by Eq. (5.16). A similar interaction potential, being logarithmic for short distances but decaying exponentially for larger ones, has been introduced by Buitenhuis and Förster [369] in order to fit viscoelasticity measurements performed on copolymer micelles. As far as star polymer systems are concerned, the pair potential of Eq. (5.57) has been tested against experimental data and also against calculations from molecular dynamics simulations, obtaining results that strongly support its validity. We present these comparisons in the following sections.

5.6.2. Experiments

One way to test the validity of potential (5.57) is to compare theoretical predictions with experimental observations regarding the scattering intensity for a wide spectrum of concentrations.

When scattering from a concentrated solution the static scattering factor $\mathscr{S}(Q)$ in Eq. (5.33) becomes the product of the form factor $P(Q)$ and the structure factor $S(Q)$. For a given interaction potential, the latter can be calculated theoretically by means some integral equation theory, as discussed in Section 2.4.1.

A detailed comparison between theory and SANS data from a series of solutions of 18-arm polyisoprene (PI) stars was performed by Likos et al. [315]. In performing such comparisons, the smearing effects arising from the finite resolution of the experimental apparatus have to be taken into account. This is done by convolving the product $P(Q)S(Q)$ with the resolution function $R(Q_0, Q)$, where Q_0 is the considered wavevector, yielding the result [cf. Eq. (5.33)]

$$I(Q_0) = N_s \frac{\Delta\rho^2}{N_A} \int P(Q)S(Q)R(Q, Q_0)\,\mathrm{d}Q \,. \tag{5.58}$$

The resolution function is usually modeled as a Gaussian, centered at Q_0 and having a width which depends on both the uncertainty of the wavelength of the incident neutron beam and on the uncertainty of the scattering angle [315,370]:

$$R(Q, Q_0) = \frac{1}{\sqrt{2\pi}\Delta Q} \exp\left[-\frac{1}{2}\frac{(Q - Q_0)^2}{(\Delta Q)^2} \right], \tag{5.59}$$

where $(\Delta Q)^2 = (2\pi\Delta\theta/\lambda)^2 + (Q_0\Delta\lambda/\lambda)^2$, with $\Delta\theta$ being the uncertainty in the angle and $\Delta\lambda/\lambda$ the relative uncertainty in the wavelength. For the form factor $P(Q)$ the Dozier form [295] of Eq. (5.35) was employed, whereas the structure factor $S(Q)$ was calculated using the Rogers–Young closure, [81] given by Eqs. (2.66) and (2.67).

The synthesis of the arms started with deuterated PI and secondary butyl lithium as initiator and proceeded with protonated PI. The still living polymer chains were coupled to the 18-functional chlorosilane linking agent $[CH_2Si(CH_2CH_2SiCl_3)_3]_2$. The result of the synthesis is a labeled 18-arm star with a near-monodisperse molecular weight distribution, where each arm commences with 27 protonated monomers in the core and continues with 81 monomers to the deuterated shell. The molecular weight of the arm is 8000 g/mol. The solvent and the deuterated shell have the same scattering length density and in the experiment only the protonated core is visible.

The SANS experiments were performed at the FRJ-2 reactor of the Forschungszentrum Jülich. Using fully deuterated methylcyclohexane as solvent, samples covering polymer volume fractions ϕ in the range $5 \times 10^{-4} \le \phi \le 0.3$ were investigated. The solutions were studied in 1 mm quartz cells, resulting in sample transmission between 55% and 85%. The SANS experiments were carried out at a neutron wavelength $\lambda = 7$ Å, employing sample-detector distances of 1.25, 2, 4, and 8 m. In this way a range of momentum transfer 0.005 $\text{Å}^{-1} \le Q \le 0.25$ Å^{-1}, where $Q = (4\pi/\lambda)\sin(\theta/2)$ and θ is the scattering angle was covered. The scattering due to the empty cell and the solvent, as well as the incoherent scattering of the deuterated part of the star and the calculated incoherent background caused by the protonated part of the polymer were subtracted. The resulting Q-dependence of the scattered intensity $I(Q)$ after scaling by the volume fraction ϕ is shown in Fig. 41.

In attempting to fit the experimental data for the total scattering intensity $I(Q)$ with the theoretical predictions based on an analytic pair potential, one has to take into consideration the fact that the star size itself has a dependence on the concentration ϕ, as was earlier found experimentally [290,295,310,314], see Eq. (5.44). Accordingly, the length σ must also have a

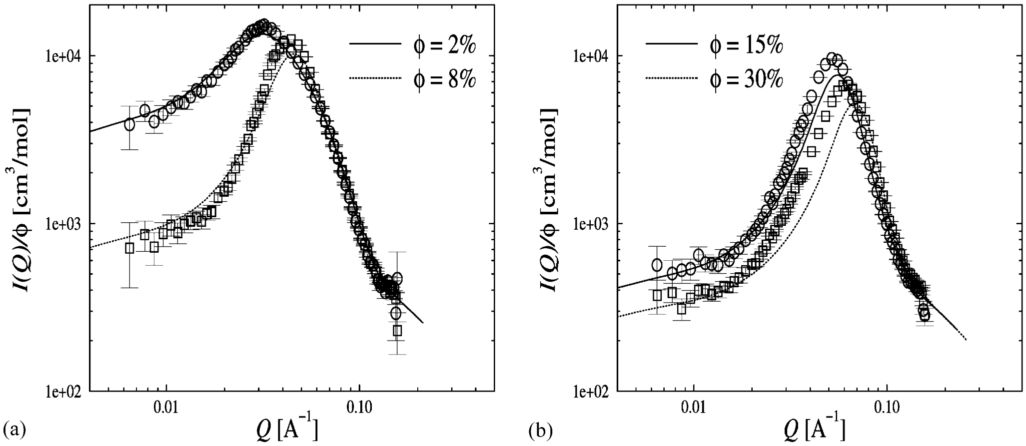

Fig. 41. Experimental (symbols) and theoretical (lines) results for the scattering intensities $I(Q)$ scaled with polymer volume fraction ϕ. From top to bottom (a) $\phi = 2\%$ and 8%; (b) $\phi = 15\%$ and 30%. The overlap volume fraction is $\phi_* = 10\%$ for this sample. (Redrawn from Ref. [315].)

ϕ-dependence, $\sigma = \sigma(\phi)$, to account for the influence of the deformation of the star on the pair interaction. This dependence was fixed as follows: for the lowest concentration considered, $\phi = 2\%$ σ was obtained by optimizing the agreement between the theoretical prediction and the experimental results. For the potential given by Eq. (5.57), the value $\sigma(\phi = 2\%) = 96$ Å was obtained. At the same concentration, the experimentally measured radius of gyration is $R_g(\phi = 2\%) = 76.1$ Å [370]. This fixed once and for all the ratio $\sigma/R_g \equiv \tau = 1.26$. For all other concentrations ϕ, it was set $\sigma(\phi) = \tau R_G(\phi)$, where $R_g(\phi)$ was read off from the experimental results [370]. In this way, the fit contained *no adjustable parameters* since σ did not vary arbitrarily with ϕ, but rather dictated by the measured values of the size of the star.

In Fig. 41 we show representative results for $\phi = 2\%,\ 8\%,\ 15\%$, and 30%. It can be seen that the fit is quite satisfactory for the whole range of concentrations. In particular, the osmotic compressibility of the solution, being proportional to $I(Q \to 0)$ is given correctly for all concentrations, as well as the general shape and wavenumber $Q_{\max}$ at which the scattering intensity displays a maximum. The height of the peak is underestimated by the theory and the agreement worsens somewhat as the concentration grows. However, at high values of ϕ the decoupling between form- and structure factors implied in writing down $I(Q) \propto P(Q)S(Q)$ becomes questionable and this is a possible source of discrepancies between theory and experiment. The logarithmic-Yukawa potential is the first that gave semiquantitative agreement between theory and experiment for such a wide range of concentrations. Earlier attempts to fit the experimental results with a hard-sphere-Yukawa interaction, for example, failed at and beyond the overlap concentration [370]. Indeed, the existence of a “soft core”, such as the logarithmic term in the potential is crucial at high concentrations where the stars start interpenetrating. We finally note that a similar comparison was recently performed for $f = 57$-arm samples, yielding again a very satisfying agreement between theory and experiment [371]. There, the intermediate, $\sigma \sim c^{-3/4}$ shrinking of the star size of Eq. (5.43) had also to be employed, indicating that for large f the region $c_1 < c < c_*$ region mentioned in Section 5.5 exists.

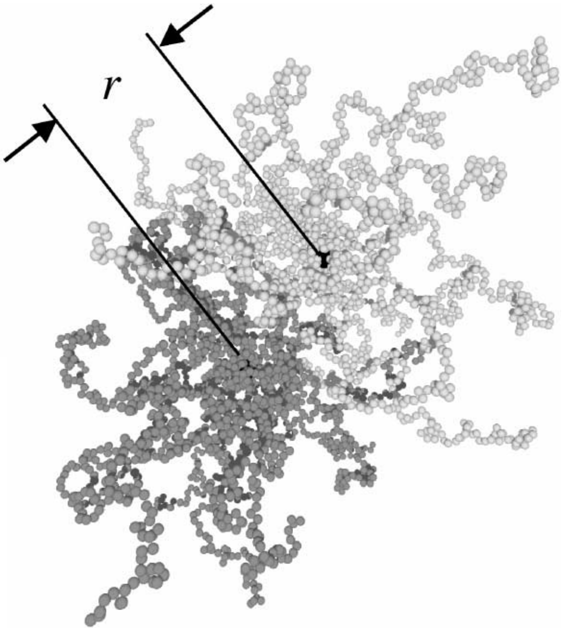

Fig. 42. Typical configuration for two stars with $f = 30$ and $N = 50$, as obtained from a snapshot during the MD simulation of Ref. [78], with r denoting the distance between their centers. (Courtesy of Arben Jusufi.)

5.6.3. Simulations

As mentioned in Section 2.3.3, it is possible in a standard simulation to measure the effective force between the remaining degrees of freedom after the remaining ones have been traced out. For the case of star polymers, Jusufi et al. [78] performed extensive molecular dynamics simulations for a large variety of combinations of arm numbers and degrees of polymerization of the stars. The simulations involved two star polymers, whose centers were kept fixed at a distance r, as shown in Fig. 42, while the monomeric degrees of freedom in the arms were moved.

The monomer–monomer interactions used were the truncated and shifted Lennard-Jones potential of Eq. (5.30) between all monomers and, in addition, the FENE potential of Eq. (5.31) for monomers along the same chain. Due to the large number of arm numbers f, which could not be accommodated in the small region at the center of the star [330,338], the arms had to be attached on a spherical particle of microscopic size $R_p \sim \sigma_{LJ}$, with the precise value depending on the number of arms and the degree of polymerization. Accordingly, the interactions between the monomers and the central particle were introduced. All monomers had a repulsive interaction $V_0^p(r)$ of the truncated and shifted Lennard-Jones type with the central particle,

$$V_0^p(r) = \begin{cases} \infty & \text{if } r \leq R_p \,, \\ V_0(r - R_p) & \text{if } r > R_p \,, \end{cases} \tag{5.60}$$

whereas the innermost monomers in the chain an additional attractive potential $V^{\mathrm{p}}_{\mathrm{FENE}}(r)$ of the FENE type, namely

$$V^{\mathrm{p}}_{\mathrm{FENE}}(r) = \begin{cases} \infty & \text{if } r \le R_{\mathrm{p}} , \\ V_{\mathrm{FENE}}(r - R_{\mathrm{p}}) & \text{if } r > R_{\mathrm{p}} . \end{cases} \tag{5.61}$$

Accordingly, the effective force $\boldsymbol{F}_i$ acting on the ith star was calculated as

$$\boldsymbol{F}_i = \left\langle -\nabla_{\boldsymbol{R}_i}\left[\sum_{k=1}^{2fN} V^{\mathrm{p}}_0(|\boldsymbol{r}_k - \boldsymbol{R}_i|) + \sum_{l=1}^{f} V^{\mathrm{p}}_{\mathrm{FENE}}(|\boldsymbol{r}_l - \boldsymbol{R}_i|)\right]\right\rangle , \tag{5.62}$$

where the first sum is carried over all $2fN$ monomers of both stars and the second only over the f innermost monomers of the chains of the considered star. The direct force between the two central particles did not need to be considered, as the distance was always kept at values where this force was vanishing.

In comparing with the force derived through the r-derivative of the potential of Eq. (5.57), two issues have to be addressed: on the one hand, the length scale entering the theoretical potential is σ, whereas in a simulation it is the radius of gyration R_g which is measured. On the other hand, the theoretical potential was derived under the assumption that there was no microscopic particle on which the chains are grafted, whereas in the simulations a central particle of radius R_{p} was introduced. The first question was addressed as follows: the gyration radius R_g calculated in simulations was used as the basic length scale for the simulation data and the latter were fitted by the theoretical result using a least-squares fit and using σ as a single-fit parameter. Afterwards, it was checked how the optimal value of σ scales with R_g as obtained from the single star simulations. The procedure is consistent if the ratio $\lambda = \sigma/R_g$ is independent of f. This is precisely what was found and, in addition, the relationship $\sigma = 1.26R_g$ was found, in full agreement with the corresponding ratio used in the comparison of theory with the SANS data (see Section 5.6.2). Hence, experiment, theory and simulation come to a perfect agreement with each other. The finite size of the core was taken into account as follows: by making a plot of the inverse force vs. the distance, s straight line was found for small interstar distances, consistent with the prediction $|\boldsymbol{F}(r)| \propto r^{-1}$. However, this straight line crossed the horizontal axis not at $r = 0$ but at $r = R_d \approx R_{\mathrm{p}} + \sigma_{\mathrm{LJ}}/2$, i.e., it showed a divergence at a finite distance between the star centers, which has clearly to be attributed to the presence of the finite cores. As R_d is also a microscopic length scale, it is irrelevant at the scales upon which the stars are looked and therefore the star–star distance was normalized by subtracting $2R_d$.

The results are shown in Fig. 43, where an excellent agreement between theory and simulation can be seen. It should be noted that the kink in the theoretical force curves appearing at $r = \sigma$ stems from the fact that, by construction, the potential is continuous there only up to its first derivative, i.e., the force. The second derivative of $\beta v(r)$ has a jump there, however, and this shows up as a kink in the force vs. distance curves. Moreover, the Yukawa tail of the potential was carefully checked by plotting the logarithm of the force against distance for $r > \sigma$ [78] and finding that the simulation data fell on a straight line, whose slope was given by the decay length of the effective potential of Eq. (5.57). Hence, the latter has been confirmed also by the simulation and it is a valid theoretical tool for a colloidal approach to the structure and thermodynamics of star polymer solutions.

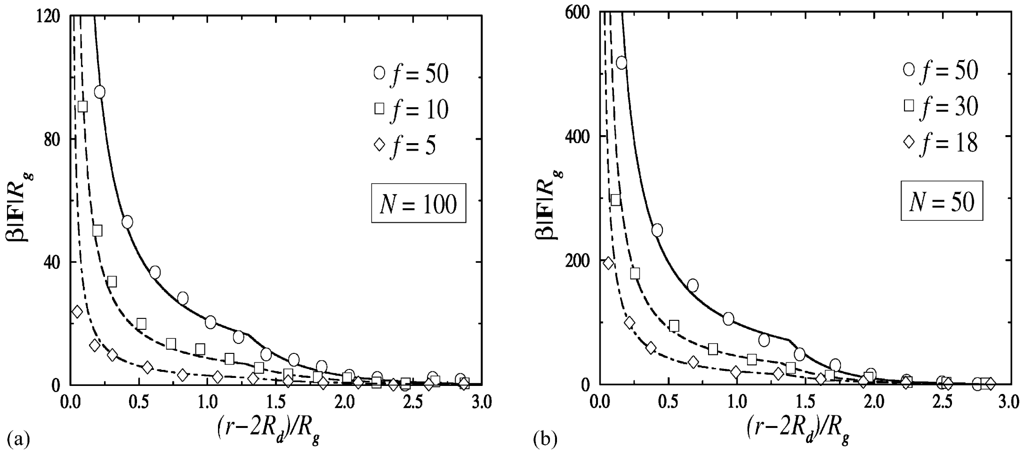

(a) (b)

Fig. 43. Simulation results (symbols) and the theoretical prediction (lines) for the magnitude of the reduced effective force $\beta|F|R_g$ between the centers two star polymers, plotted against the normalized distance $(r - 2R_d)/R_g$. (a) $N = 100$ for $f = 5$, 10 and 18; (b) $N = 50$ for $f = 18$, 30 and 50.

5.7. Anomalous structure factor

A wealth of information regarding the macroscopic behavior of star polymer solutions can be gained by calculating structural liquid properties with the logarithmic-Yukawa potential of Eq. (5.57) as input. Watzlawek et al. [77,317] carried out extensive Monte-Carlo simulations, accompanied by integral equation theories in order to calculate $g(r)$ and $S(Q)$ for a wide range of densities and arm numbers. As a dimensionless measure of the former, again the "packing fraction" η of the solution was introduced:

$$\eta = \frac{\pi}{6}\rho\sigma^3 . \tag{5.63}$$

Taking $\rho_*\sigma^3 \cong 1$ as an estimate for the overlap density ρ_*, the corresponding overlap packing fraction $\eta_* \cong 0.5$ can be introduced. Attention was focused on the case $f = 32$ which turns out to be interesting.

The Rogers–Young closure [81] yielded results that were practically identical with those from MC simulations. In Fig. 44(a), we show the resulting structure factor $S(Q)$ for small and intermediate packing fractions. An anomalous evolution of $S(Q)$ with η can be seen, which is quite similar to that observed in the Gaussian core model, see Fig. 22. As for the GCM, this behavior strongly suggests a reentrant melting scenario. The structure factor increases up to about the overlap packing fraction η_* and thereafter it decreases again. This is in full agreement with the scaling predictions of Witten et al. [308,309] who indeed predicted this phenomenon to occur at about the overlap concentration. Moreover, a decrease in the intensity of the highest peak of $S(Q)$ above η_* has also been observed experimentally [77,310,314,354] in star polymer solutions but is otherwise unknown for the usual, "hard" interactions, such as the Yukawa potential [372–380].

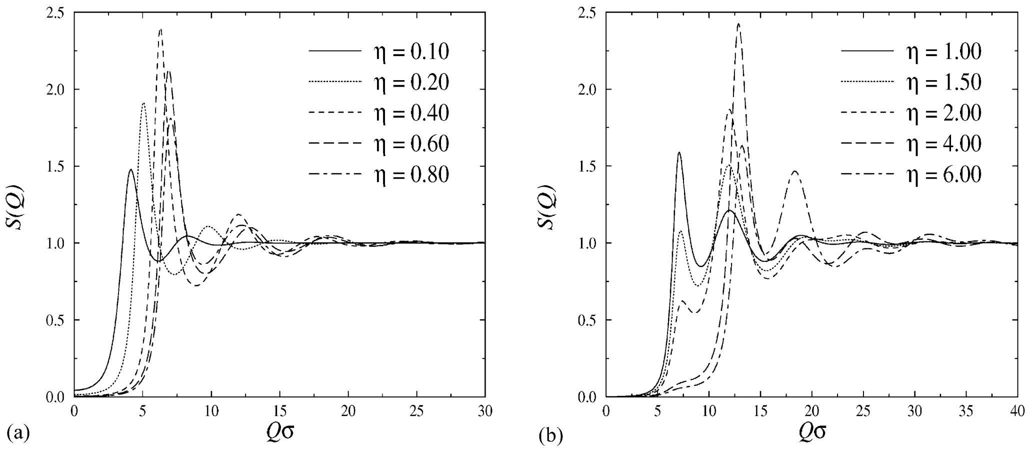

Fig. 44. The structure factor $S(Q)$ obtained by employing the interaction of Eq. (5.57) and solving the Rogers–Young closure for $f = 32$: (a) Intermediate and (b) high packing fractions.

Invoking the Hansen–Verlet criterion [170,171] in conjunction with the results displayed in Fig. 44(a), a preliminary prediction can be made, namely that for $f = 32$ the system does not freeze. The further evolution of the structure factor $S(Q)$ with density can be seen in Fig. 44(b). Though the second peak remains at twice the position of the first up to $\eta = 0.60$, at packing $\eta = 0.80$ the position of the first peak is practically unchanged with respect to that at $\eta = 0.60$, but the second peak now *moves closer* to the origin and increases in height. This trend persists as η grows and already at $\eta = 1.50$ the second peak is already higher than the first, which shows a clear trend of disappearing at higher densities, as it will be confirmed shortly.

This anomaly in the structure factor can be traced to the crossover of the interaction from a Yukawa to a logarithmic form *and* the softness of the logarithmic potential. Indeed, above the overlap concentration the system always tries to maintain one coordination shell *outside* the logarithmic part, where the interaction is weak. At the same time, the softness of the logarithmic core allows two things to happen: on the one hand, qualitatively, the system remains always fluid which would not have been the case if the core were harder. On the other hand, more quantitatively, the softness of the logarithm allows for a rather broad first peak of the radial distribution function which can accommodate enough particles so as to allow for the second peak to occur immediately outside $r = \sigma$.

The unusual shape of the structure factor can be understood by means of the existence in the system of these two different length scales: one length scale $a \approx \rho^{-1/3}$, which is manifestly density dependent and one length scale b ($b \gtrsim \sigma$) which is density-independent. Below η_* only the first length scale appears but above η_* both are present. Let us call Q_n the position of the nth peak of the structure factor. The first peak of $S(Q)$ corresponds, roughly, to the length scale b, i.e., $Q_1 \approx 2\pi/b$ and the second peak to the length scale $b - a$, i.e., $Q_2 \approx 2\pi/(b - a)$. The first peak of the structure factor disappears altogether when the density is such that $b - a = a$ or $b = 2a$; the structure factor has a main peak at a position dictated only by the density, when the length b is twice the length a in such a way that $g(r)$ has exactly two oscillations of wavelength a between $r = 0$ and b. Since $b \approx \sigma$, it turns out that the density must be such that $a \approx \sigma/2$.

The scenario repeats itself upon further increase of the density. The main peak is lowered and the one that used to be the third at low densities grows, etc. The mechanism that brings about this scenario is no other but the development of more and more oscillations inside the logarithmic core in the function $g(r)$. In fact, one can repeat the argument about the "magic" packing fraction η_2 above for an arbitrary number of oscillations as follows: the structure factor $S(Q)$ will be dominated by a single length scale whenever there is an integer number of oscillations m between $r = 0$ and $b \approx \sigma$. Given the magic packing fraction η_2, it is straightforward to show that the general magic packing fraction η_m will be related to η_2 by

$$\eta_m = \left(\frac{m}{2}\right)^3 \eta_2, \quad m = 3, 4, 5, \dots \ . \tag{5.64}$$

Using $\eta_2 = 3.40$ we obtain $\eta_3 = 11.475$, $\eta_4 = 27.20$ and $\eta_5 = 53.125$. The structure factor for these magic values is shown in Fig. 45. It can be seen clearly that for the mth magic value, $S(Q)$ has a dominant peak located at the position $2\pi m/\sigma$. As the order m grows, the height of the dominant peak also decreases slightly and some substructure develops in $S(Q)$. However, the main length scale comes from the m oscillations of the radial distribution function $g(r)$ in the logarithmic core.

The above results can be summarized by making a log–log plot of the positions of the first few peaks of the structure factor against the packing fraction η, as shown in Fig. 46. We emphasize here that when we talk about the nth peak we actually mean "the peak which is the nth if we extrapolate at low enough densities so that we are in a regime where the liquid is normal". The reason for this

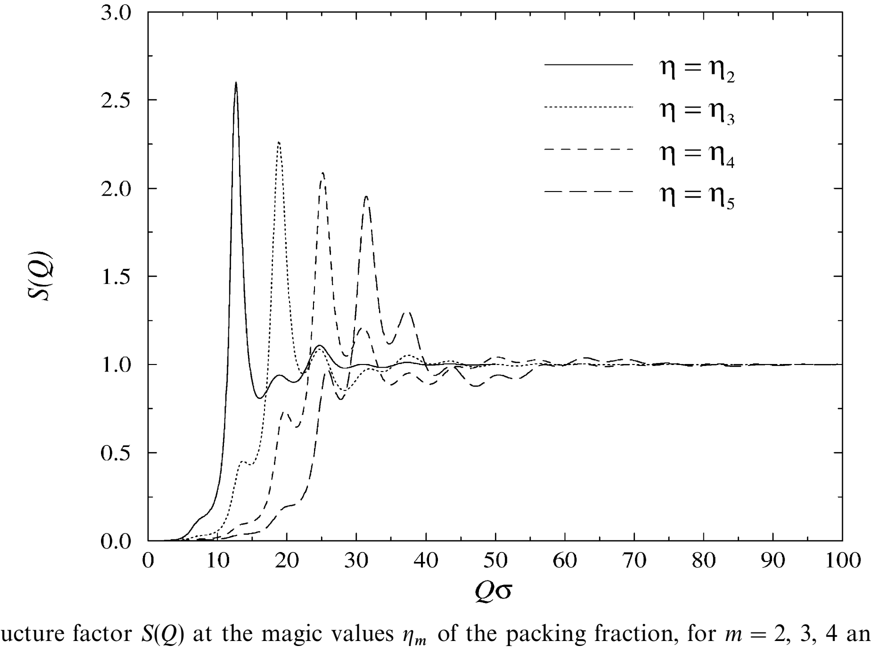

Fig. 45. The structure factor $S(Q)$ at the magic values η_m of the packing fraction, for $m = 2$, 3, 4 and 5. (Taken from Ref. [317].)

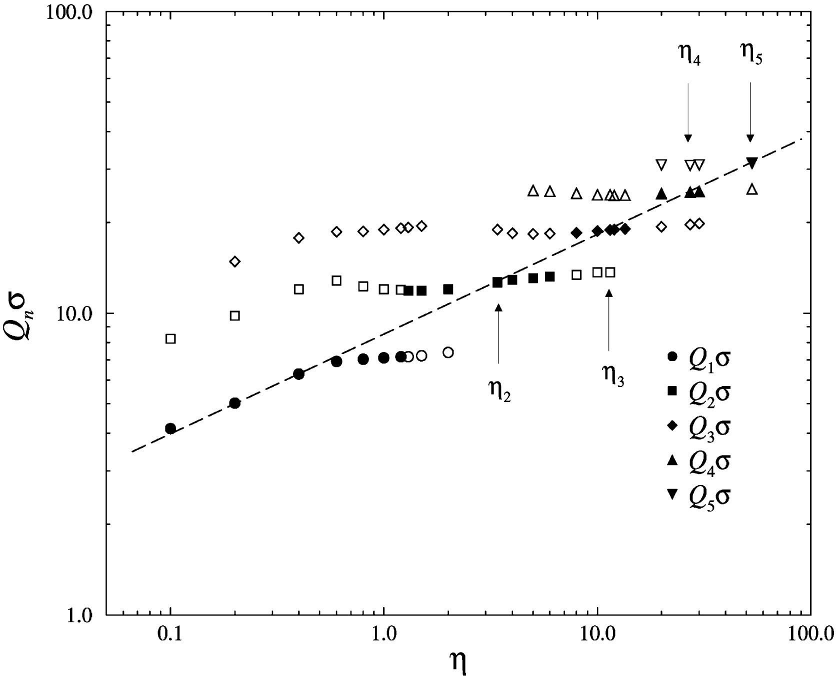

Fig. 46. Double logarithmic plot of the positions of the various peaks of $S(Q)$ against the packing fraction η. The filled symbols indicate the highest peak (see the text for details). The arrows indicate the locations of the magic packing fractions η_m and the straight line has slope 1/3. (Taken from Ref. [317].)

distinction is that as η grows the low-order maxima of the structure factor disappear, as explained above, and as a result what used to be a second-order maximum becomes now first order, etc. This is manifested in Fig. 46 by the fact that the curves representing the positions of the various maxima Q_n stop at some value of η. Moreover, since a higher-order peak overtakes a lower-order one in height before the latter completely disappears, we indicate the highest peak in Fig. 46 by the filled symbols.

Referring to Fig. 46, the following remarks can be made: the fluid interacting by means of the potential given by Eq. (5.57) is normal for packing fractions $\eta \leq \eta^* = 0.50$. Indeed, in this regime on the one hand the first maxima follow the scaling $Q_1 \propto \rho^{1/3}$ and on the other hand the higher-order maxima Q_n are located in positions $Q_n = nQ_1$, both features being a manifestation of the existence of a *single* length scale $\rho^{-1/3}$ in the structure of the system. Above the overlap density ρ_* the scaling breaks down. However, if we extrapolate the straight line with slope 1/3 which characterizes the normal regime to higher densities, we find that it passes precisely through the main maxima at the magic packing fractions η_m. Indeed, at those values of the density the length scales $\rho^{-1/3}$ and σ are commensurate and we have an accidental scaling of the main peak of $S(Q)$ with the 1/3-power of the density. However, the higher-order peaks of $S(Q)$ are still not located at integer multiples of the first one and we are dealing with an unusual fluid for densities exceeding the overlap density ρ_*.

5.7.1. Effective hard-sphere mapping

In order to make a further test of the Hansen–Verlet-based indication that the $f = 32$ system does not freeze, Watzlawek et al. [77,317] also performed a hard-sphere mapping of the system. Following an idea of Kang et al. [381], an effective hard-sphere diameter σ_{HS} was defined, crudely representing the particle repulsion embodied in the pair potential of Eq. (5.57), as follows. The pair potential $v(r)$ was divided into a short-ranged reference potential $V_0(r)$ and a longer-ranged perturbation potential $W(r)$ at a suitably chosen break point λ, namely

$$v(r) = V_0(r) + W(r) , \tag{5.65}$$

where $V_0(r)$ is given by

$$V_0(r) = \Theta(\lambda - r)[v(r) - F(r)] . \tag{5.66}$$

Here, $\Theta(r)$ is the Heaviside step function, and $F(r)$ will be defined soon. According to Eqs. (5.65) and (5.66), the perturbation potential $W(r)$ is given by

$$W(r) = \Theta(\lambda - r)F(r) + \Theta(r - \lambda)v(r) . \tag{5.67}$$

The effective hard-sphere diameter σ_{HS} is density dependent when the specific choice for λ and $F(r)$, applied successfully in Refs. [381,382], is used. This density dependence arises from the identification of λ with the nearest-neighbor distance a_{fcc} of the fcc structure, i.e.,

$$\lambda = a_{\mathrm{fcc}} \equiv (\sqrt{2}\rho^{-1})^{1/3} . \tag{5.68}$$

Furthermore, the function $F(r)$ was chosen as

$$F(r) = V(\lambda) - \left[\frac{\mathrm{d}v(r)}{\mathrm{d}r}\right]_{r=\lambda} (\lambda - r) , \tag{5.69}$$

guaranteeing that both $V_0(r)$ and $\mathrm{d}V_0(r)/\mathrm{d}r$ are vanishing at $r = \lambda$. Having specified λ and $F(r)$, σ_{HS} was then calculated from $V_0(r)$ by the well-known Barker–Henderson (BH) approximation [383]

$$\sigma_{\mathrm{HS}} = \int_0^{\infty} \mathrm{d}r[1 - \mathrm{e}^{-\beta V_0(r)}] , \tag{5.70}$$

or, alternatively, by a scheme proposed by Weeks, Chandler and Anderson (WCA) [381,382,384]. The BH approximation yielded results which are practically identical to the ones from the WCA; thus only the BH results will be discussed below.

In Fig. 47, the resulting effective HS packing fraction $\eta_{\mathrm{HS}} \equiv (\pi/6)\rho\sigma_{\mathrm{HS}}^3$, is shown, which is in general density-dependent. It is hence plotted as a function of the "true" packing fraction η, depending furthermore on the value of f as additional parameter. Obviously, η_{HS} is increasing linearly with η for $\eta \lesssim 0.1$, and it reaches a maximum value depending on f at certain packing fractions $0.4 \lesssim \eta \lesssim 0.7$, which are again depending on f. For $\eta \geq 0.74$, η_{HS} remains constant for all densities.

Since the mapping onto an effective HS system gives quite reliable results in predicting the freezing transition [381,382], the value of η_{HS} was used as an indication for the existence of a freezing transition in the original system. Hard spheres freeze in a fcc structure at $\eta_{\mathrm{f}} = 0.494$ (see Section 4.1) and therefore this specific value was taken in order to explore a possible freezing transition of star polymers from Fig. 47. Obviously, for $f \leq 32$, η_{HS} never exceeds 0.494 for all η,

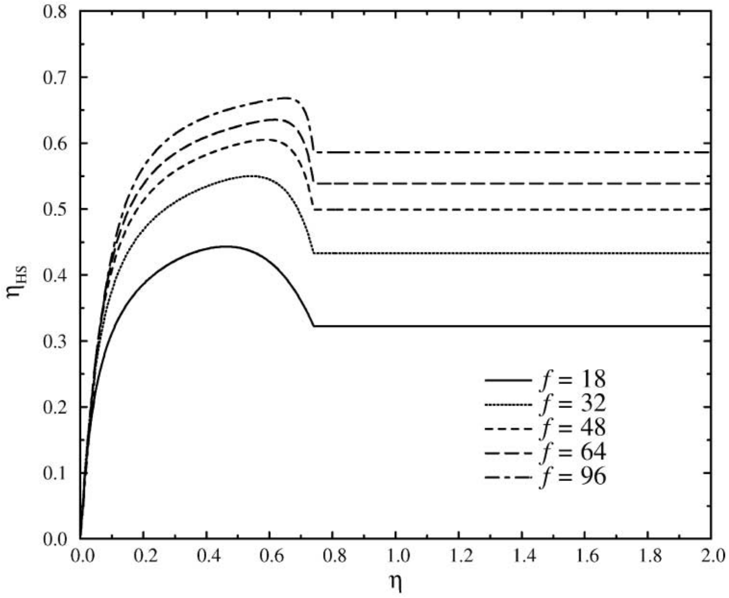

Fig. 47. The effective HS packing fraction η_{HS} as a function of the true packing fraction η, for a number of different arm numbers f. (Taken from Ref. [317].)

leading to the conclusion that the system remains fluid at *all densities*. For $f > 32$ on the other hand, η_{HS} attains values larger than 0.494 at least in a limited window of packing fractions η. Consequently, there is a lower freezing arm number $f_1 \simeq 32$, meaning that the system never freezes for $f \leq f_1$, but freezes presumably at least in a limited range of densities for $f > f_1$.

As can be further seen from Fig. 47, there is a range of arm numbers $f_1 < f \lesssim 64$, where η_{HS} exceeds 0.494 only for $0.2 \lesssim \eta \lesssim 0.7$, which implies a reentrant melting phenomenon at $\eta \simeq 0.7$. Moreover, star polymers with $f \gtrsim 64$, seem to show a liquid phase for $\eta \lesssim 0.2$, followed by a solid phase for *all* higher densities.

5.8. The phase diagram of star polymer solutions

Taking the pair potential of Eq. (5.57) for granted, it is then possible to trace out in detail the phase diagram of the system. Clearly, as the temperature is irrelevant, the appropriate thermodynamic parameters are concentration and arm number, hence the phase diagram must be drawn on the (η, f)-plane. This was done by Watzlawek et al. [77,319,385] using Monte-Carlo simulations as well as theoretical calculations of the free energies of the various phases.

The free energy of the fluid phase can be calculated theoretically by means of the compressibility or virial routes (see Section 2.4.1). In fact, having solved the thermodynamically consistent Rogers–Young closure for a range of densities and arm numbers, it is guaranteed that these two routes will yield identical results. In order to measure the fluid free energy in a simulation, the technique of *thermodynamic integration* must be employed [10,11]. Here, the arm number f, entering the effective interaction as a pseudo-inverse temperature, is used as a thermodynamic variable. Subsequently, a series of simulations is performed for *fixed* packing fraction η but variable f, starting at $f = 0$, where the system is an ideal gas, and ending at any desired f-value. Denoting by $U(f,\eta)$ the excess internal energy and by $F_{\mathrm{fl}}(f,\eta)$ the Helmholtz free energy of the fluid, it is easy to verify that the following relation holds:

$$\frac{\partial \beta F_{\mathrm{fl}}(f,\eta)}{\partial f} = \left\langle \frac{\partial \beta U(f,\eta)}{\partial f} \right\rangle , \tag{5.71}$$

where $\langle \cdots \rangle$ denotes a canonical expectation value. Thereafter, the quantity $\beta F_{\mathrm{fl}}(f,\eta)$ can be calculated through the relationship

$$\beta F_{\mathrm{fl}}(f,\eta) = N_{\mathrm{s}}\left[\ln\left(\frac{6\eta}{\pi}\right) - 1\right] + \int_0^f \left\langle \frac{\partial \beta U(f',\eta)}{\partial f'} \right\rangle_{f'} \mathrm{d}f' + 3N_{\mathrm{s}} \ln\left(\frac{\Lambda}{\sigma}\right) , \tag{5.72}$$

where N_{s} is the number of stars in the macroscopic volume Ω, $\langle \cdots \rangle_{f'}$ means that the expectation value must be taken at fixed f' and also the logarithmic ideal free energy terms have been added explicitly [see Eq. (2.70)]. As usual, the last term in the rhs of Eq. (5.72) is an unimportant constant and can be dropped. The expectation value of the f'-derivative can furthermore be expressed as an integral over the radial distribution function, namely

$$\begin{aligned}\left\langle \frac{\partial \beta U(f',\eta)}{\partial f'} \right\rangle_{f'} &= \left\langle \sum_{i<j} \frac{\partial \beta v(|\mathbf{r}_i - \mathbf{r}_j|;f')}{\partial f'} \right\rangle_{f'} \\ &= 12 N_{\mathrm{s}} \eta \int_0^\infty \frac{\partial \beta v(x;f')}{\partial f'} g(x;f',\eta) x^2 \,\mathrm{d}x \, .\end{aligned} \tag{5.73}$$

Here, $x = r/\sigma$, $g(x;f',\eta)$ is the radial distribution function which can be measured in a standard simulation and which depends also on f' and η and $\beta v(x;f')$ is the pair potential of Eq. (5.57), with its f'-dependence marked in the argument list. Eqs. (5.72) and (5.73) allow for the calculation of the fluid Helmholtz free energy in a simulation.

As far as the solid phases are concerned, Watzlawek et al. [77,319] considered a large number of candidate crystal structures and the competition among them. The structures were the fcc, bcc and simple cubic (sc) lattices, but also the more "exotic" diamond (diam), face-centered orthogonal (fco), body-centered orthogonal (bco), orthogonal (orth) and diamond orthogonal (diao) structures [15]. In the last four, "orthogonal" structures, produced by stretching the conventional unit cells of the original ones by an arbitrary amount and keeping the conventional cell volume fixed, the ratios of the lattice constants a, b and c in the three spatial directions act as additional degrees of freedom which have to be relaxed so that a minimum of the free energy can be achieved. We note that the bco structure reduces to the bcc for $a{:}b{:}c = 1{:}1{:}1$ and to the fcc for $a{:}b{:}c = 1{:}1{:}\sqrt{2}$ [15]. The calculation of the free energies of the candidate solid phases commenced with the lattice sums (formally the free energies at $f \to \infty$) which already give strong indications about the surviving phases at finite f and proceeded with the Frenkel–Ladd method in the simulation [11,77,179,319] and within the framework of the Einstein model (Section 3.5.5) in the purely theoretical considerations. The analysis was carried out for a wide range of arm numbers, $18 \leq f \leq 512$ and packing fractions, $0 \leq \eta \leq 1.5$. The common tangent construction yielded then the phase diagram shown in Fig. 48.

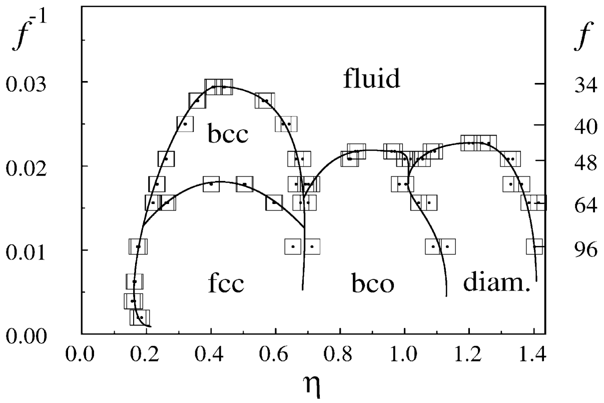

Fig. 48. The phase diagram of star polymer solutions in a good solvent, as obtained from the simulations, drawn on the (η,f)-plane. The squares indicate the phase boundaries. The lines, drawn as a guide to the eye, should in principle be double but the density gaps between coexisting phases are so narrow that this would only crowd the figure without adding significant information. (Taken from Ref. [319].)

For $f \lesssim f_1 = 34$, the fluid phase is the only stable one and freezing is impossible at all densities. The order-of-magnitude estimate of Witten et al. [308], $f_1 \cong 100$, has been made precise. The same holds for the reentrant melting scenario, which has also been confirmed, with the bcc crystal being nested between a low- and a high-density liquid at about the overlap packing fraction $\eta_* \cong 0.50$. For $f \geq f_1$, four stable crystal structures exist and, depending on f, a given system will have at least one stable crystalline phase. In the domain of intermediate densities, $0.2 \lesssim \eta \lesssim 0.7$, the bcc phase is stable for $f_1 < f \lesssim 54$, whereas for $f \gtrsim 70$ the fcc crystal wins. In the regime $54 \lesssim f \lesssim 70$, the system will first freeze into a bcc lattice but then it will undergo a structural phase transition into a fcc crystal. The interplay between bcc and fcc can be easily understood here, as at these densities only the Yukawa tail of the interaction is visible to the particles. Hence, for large f (strong screening), packing effects dominate and stabilize the fcc, whereas for smaller f energy plays an important role stabilizing the more open, bcc structure. This is completely analogous to the phase behavior observed in charge-stabilized colloids [375,378,379] as well as in copolymer micelles [288,289,355,356]. The HS-type behavior, formally corresponding to $f \rightarrow \infty$ sets in at very high f-values, typically $f \cong 10\,000$, due to an interplay between the steeply increasing logarithmic core and the Yukawa tail, for details see Ref. [77].

Quite more unexpected phases show up for high packing fractions, $\eta \gtrsim 0.7$. An bco phase with a strong anisotropy along its three principal space axes is stable in the region $0.70 \lesssim \eta \lesssim 1.1$ and a diamond lattice becomes stable for $1.1 \lesssim \eta \lesssim 1.4$. The density domain in which these phases show up is precisely the one in which the fluid displays an anomalous structure factor with two length scales, $\rho^{-1/3}$ and σ. Moreover, at these densities the particles start to overlap within their ultrasoft logarithmic cores. Hence, a close relationship exists between ultrasoftness, $S(Q)$-anomalies in the fluid and the exotic crystal structures, as explained below.

The ratios of the lattice constants in the bco crystal turned out to be nearly independent of f and increasing from $b/a \cong 2.24$ and $c/a \cong 1.32$ at $\eta = 0.7$ to $b/a \cong 3.14$ and $c/a \cong 1.81$ at $\eta = 1.0$. This means that, throughout the range of stability of the bco phase, the anisotropy in the conventional unit cells leads to a strong interpenetration of the particle coronae along one of the three lattice axes (the one with the smallest lattice constant). In this way, the nearest-neighbor distance is smaller than σ whereas all other neighbors are kept at distances larger than σ. This can be intuitively understood from the form of the interaction potential (5.57). Due to the very weak divergence at small r, the energy penalty for overlaps within the logarithmic core is not prohibitively large. At the same time, the potential falls rapidly enough at distances $r > \sigma$, so that it becomes energetically favorable to have two neighbors very close to a central particle and all remaining ones outside the σ-range rather than 12 (fcc) or 8 (bcc) nearest neighbors, all of them at distances larger than the nearest-neighbor distance in the bco but nevertheless within the σ-range.

The same argumentation leads to an understanding of the stability of the diamond lattice. As the density increases further, the bco becomes unstable with respect to a lattice in which two more neighbors enter into the corona and the diamond lattice with four nearest neighbors is stabilized. Again, the simulations revealed that in the domain of stability of the diamond, the second neighbors are kept outside the corona. Hence, both the ultrasoft character of the logarithmic potential and the crossover to a Yukawa tail at $r = \sigma$ are necessary to stabilize the diamond crystal. This phenomenon is unknown for the usual, hard pair potentials and, in fact, there exists a widespread belief in the literature that three-body interactions are necessary for such a stabilization [386–390].

The information about the stability of the bco and diamond phases is already hidden in the radial distribution function $g(r)$ of a stable liquid with $f = 40$ arms, lying slightly above the domains of stability of these phases. Indeed, this $g(r)$ shows a pronounced peak close to the origin and the fluid state coordination number is about two above the stability domain of the bco and four above that of the diamond. The same is seen in the angle-averaged $g(r)$'s of the solid phases [77]. A very similar effect was found by Broughton and Li [391] for the bond-angle-dependent Stillinger–Weber potential [386], which was *constructed* with the goal of stabilizing the diamond lattice. Here, however, the latter has been stabilized *for the first time* by means of a simple, radially symmetric pair interaction *alone*. Moreover, the second freezing observed in experiments on starlike copolymeric micelles that was mentioned in Section 5.5 [289,357,358], can now be understood as the freezing of the system into the anisotropic bco phase, see Fig. 48.

The phase diagram has been drawn solely on the basis of the pair interaction of Eq. (5.57). Neither the effects of the neglected many-body forces nor those of the volume terms have been taken into account yet. These are discussed in the following section.

5.9. The three-body forces and the volume terms

Effective triplet interactions in good-solvent star polymer solutions were analyzed recently by von Ferber et al. [392], using an analytical short-distance expansion inspired by scaling theory on the one hand and computer simulations on the other. Three stars were positioned in an equilateral triangle configuration, as shown in Fig. 49. The total force on one star was measured in a MD simulation by a method identical to the one presented in Section 5.6.3 and it was then compared with the sum of the two pair forces from the remaining two, as predicted by the pair potential of Eq. (5.57), for varying size of the edge length r of the equilateral triangle.

As a first result, it was found that triplet forces become relevant only when three stars start to have triple overlaps within their coronae, yielding an packing fraction which is much higher than

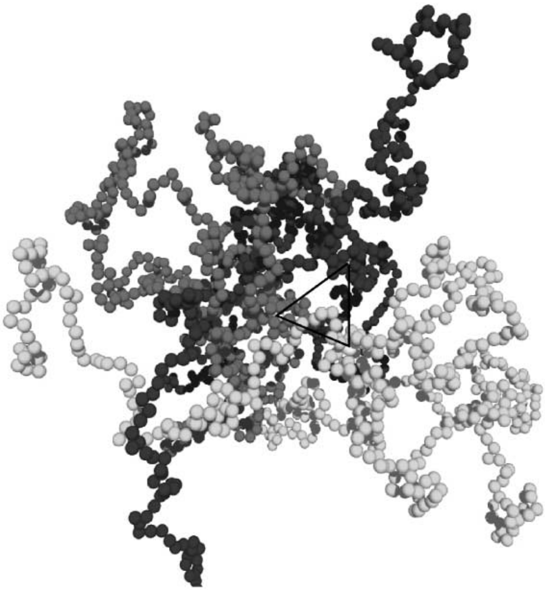

Fig. 49. Snapshot from a simulation of three stars with $f = 5$ arms and $N = 100$ monomers per arm. The cores are located at the corners of the depicted equilateral triangle. (Taken from Ref. [392].)

the highest shown in Fig. 48. Hence, the phase diagram shown there remains unaffected by the presence of three-body forces. Moreover, the triplet force was found to be *attractive*, i.e., the total force turns out to be smaller than the sum of the two-body forces. This can be understood intuitively, if one imagines that the force arises from an overlap between the stars' coronae. In a geometry with a triple overlap, the sum of the three two-body overlaps overestimates the total overlap volume, as it counts the triplet overlap three times. On a quantitative basis, it was found that independently of the arm numbers and of r, in the full region described by the logarithmic potential, the relative deviation of the force caused by the triplet forces is equal to $(3^{3/2} - 3)/(2^{3/2} - 2) \cong -0.11$ [392]. At very high concentrations, where the system looks like a semidilute polymer solution, the pair-potential approximation breaks down, however. This was established in the work of von Ferber et al. [392], through the investigation of the general M-body forces in the limit when the interstar distances go to zero. It was found that the contribution from a cluster of M stars increases with M and even diverges for $M \to \infty$.

The volume terms for star polymer solutions can be estimated in a way quite analogous to the one presented in Section 3.7 for the linear chains [385]. As long as the stars do not overlap and the star size has the dilute limit value, $\sigma(0)$, the volume terms vanish. Above the overlap density ρ_*, nontrivial volume terms $\Omega f_0(\rho)$ appear, which are given by Eqs. (3.116) and (3.117). However, the interior of the star is now a semidilute polymer solution, not a dilute one as was the case for free chains. Accordingly, the osmotic pressure $\Pi(r)$ in the star interior will not be given by Eq. (3.118) but rather by the scaling law, Eq. (5.16). Introducing the latter into Eq. (3.117) we obtain the equation

$$f_c(\rho) \propto -4\pi f^{3/2} \ln\left[\frac{\sigma(\rho)}{\sigma(0)}\right]. \tag{5.74}$$

The volume terms come about from the shrinking of the stars above ρ_*. Using Eq. (3.121), which holds also for star polymers [see Eq. (5.44)], we obtain the result that the volume terms vanish for $\rho < \rho_*$ but above the overlap density they have the form

$$f_0(\rho) \propto f^{3/2} \rho \ln\left(\frac{\rho}{\rho_*}\right) \quad (\rho > \rho_*) \tag{5.75}$$

with a positive constant of proportionality (compressing the stars results into a free energy cost). The curvature of the term $f_0(\rho)$ is positive, $f_0''(\rho) \propto f^{3/2}/\rho$. Hence, it does not bring about any hidden phase transitions (see Section 2.5) and its only effect is to narrow the density gaps between the coexisting phases. In addition, the prefactor $f^{3/2}$ gives this term a very high curvature at high functionalities, so that the density gaps, which are already very narrow (see Fig. 48), will virtually vanish for $f > 10$, thus leading to essentially isochoric phase transitions [106].

5.10. Polydisperse stars

The above considerations were based on the assumption that the star polymers in the solution are perfectly monodisperse. However, in reality, there is always a distribution of arm numbers f, resulting also in a distribution of sizes of the stars, according to Eq. (5.26). Therefore, a generalization of the effective potential of Eq. (5.57) to two stars of different functionalities, f_1 and f_2 is of great interest. The desired effective potential $v_{f_1 f_2}(r)$ was derived by von Ferber et al. [393] using field-theoretical methods and then confirmed by direct comparison with MD simulations.

In Ref. [393], the short-distance behavior of the effective potential $v_{f_1 f_2}(r)$ was derived using renormalization group arguments combined with the so-called *cone approximation* of Ohno [394]. Here, we present a simple scaling argument, which follows parallel lines with that presented in Section 5.6.1 for the monodisperse case. Let $Q_{f_1 f_2}(r)$ be the partition function of two stars, one having functionality f_1 and the other f_2, with their centers held at distance r apart. The effective interaction $\beta v_{f_1 f_2}(r)$ is given by

$$\beta v_{f_1 f_2}(r) = -\ln\left[\frac{Q_{f_1 f_2}(r)}{Q_{f_1 f_2}(\infty)}\right], \tag{5.76}$$

see also Eq. (5.46). We assume that all chains in both stars have the same degree of polymerization N. At center-to-center separations $r \sim b$, where b is the blob size, the two stars resemble a *single* star with a total of $f_1 + f_2$ arms, having a partition function $Q_{f_1 + f_2}$. The latter is given by Eq. (5.52), therefore we obtain

$$Q_{f_1 f_2}(r \sim b) \propto [N(f_1 + f_2)^{(\nu - 1)/(2\nu)}]^{-\nu (f_1 + f_2)^{3/2}}. \tag{5.77}$$

On the other hand, we have $Q_{f_1 f_2}(\infty) = Q_{f_1} Q_{f_2}$, with Q_f denoting the partition function of a star with f arms and Eq. (5.52) once more implies

$$Q_{f_1 f_2}(\infty) \propto [N f_1^{(\nu - 1)/(2\nu)}]^{-\nu f_1^{3/2}} [N f_2^{(\nu - 1)/(2\nu)}]^{-\nu f_2^{3/2}}. \tag{5.78}$$

Taking into account that the typical size R of the stars scales as $R \sim N^{\nu}$, and using the scaling argument of Section 5.6.1 combined with Eqs. (5.76)–(5.78), the effective potential for distances $r \leq R$ is obtained as

$$\begin{aligned}\beta v_{f_1 f_2}(r) &= -\alpha' \theta(f_1, f_2) \ln\left(\frac{r}{R}\right) \\ &\equiv -\Theta_{f_1 f_2} \ln\left(\frac{r}{R}\right),\end{aligned} \tag{5.79}$$

where α' is a proportionality constant and $\theta(f_1, f_2)$ is obtained from Eqs. (5.77) and (5.78) as

$$\theta(f_1, f_2) = (f_1 + f_2)^{3/2} - (f_1^{3/2} + f_2^{3/2}) . \tag{5.80}$$

The proportionality constant α' is determined by requiring that for $f_1 = f_2 = f$, the expression for $\Theta_{f_1 f_2} = \alpha' \theta(f_1, f_2)$ reduces to that for monodisperse stars, given by Eq. (5.57), namely

$$\Theta_{ff} = \tfrac{5}{18} f^{3/2} . \tag{5.81}$$

From Eqs. (5.80) and (5.81) we readily obtain

$$\Theta_{f_1 f_2} = \frac{5}{36} \frac{1}{\sqrt{2} - 1} [(f_1 + f_2)^{3/2} - (f_1^{3/2} + f_2^{3/2})] . \tag{5.82}$$

It can be easily shown that $\Theta_{f_1 f_2} > 0$ for all $f_1, f_2 > 0$.

Let σ_f be twice the distance from the center of a star with functionality f to the center of its outermost blob, the latter having a diameter $2\sigma_f/\sqrt{f}$. For the monodisperse case, the outermost blob diameter sets the decay length κ_f^{-1} of the Yukawa interaction, see Eq. (5.57). In full analogy with the considerations put forward in the derivation of the monodisperse pair potential, the logarithmic form was assumed to be valid when the center-to-center distance becomes smaller than σ, where σ is given by the arithmetic mean of σ_{f_1} and σ_{f_2}:

$$\sigma = \frac{\sigma_{f_1} + \sigma_{f_2}}{2} . \tag{5.83}$$

Moreover, for larger distances, the effective potential was postulated to have a Yukawa-type decay, with a decay length κ^{-1} which is again given as the arithmetic mean of the two decay lengths $\kappa_{f_1}^{-1}$ and $\kappa_{f_2}^{-1}$, namely

$$\kappa^{-1} = \frac{\kappa_{f_1}^{-1} + \kappa_{f_2}^{-1}}{2} . \tag{5.84}$$

With the above definitions, and requiring once more continuity of the effective potential and its derivative at $r = \sigma$, the center-to-center effective potential $\beta v_{f_1 f_2}(r)$ was introduced, which reads as

$$\beta v_{f_1 f_2}(r) = \begin{cases} \Theta_{f_1 f_2} \left[-\ln\left(\dfrac{r}{\sigma}\right) + \dfrac{1}{1 + \kappa\sigma} \right] & \text{for } r \leq \sigma , \\ \Theta_{f_1 f_2} \dfrac{1}{1 + \kappa\sigma} \left(\dfrac{\sigma}{r}\right) \exp[-\kappa(r - \sigma)] & \text{for } r \geq \sigma . \end{cases} \tag{5.85}$$

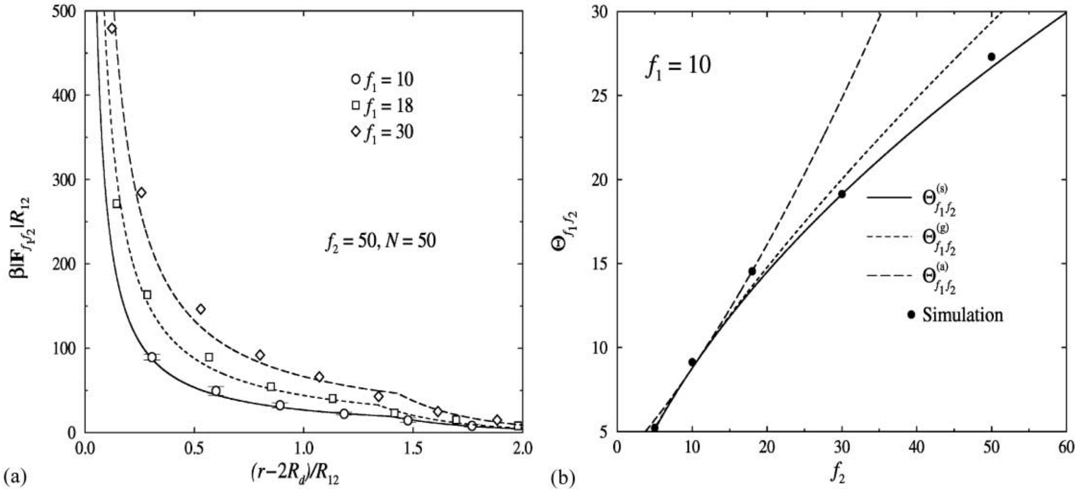

Fig. 50. (a) Simulation results (symbols) and theoretical results (lines) for the reduced effective force $\beta|\boldsymbol{F}_{f_1 f_2}|R_{12}$ vs. reduced distance $(r - 2R_d)/R_{12}$ between two stars of functionalities f_1 and f_2. Here $R_{12} = \sigma/2$ and R_d is the core size, as in Fig. 43. (b) Simulation results for the prefactor $\Theta_{f_1 f_2}$ for $f_2 = 5 \dots 50$ and $f_1 = 10$ fixed, in comparison to three different theoretical predictions. $\Theta^{(s)}_{f_1 f_2}$ is given by Eq. (5.82).

The above potential reduces by construction to the monodisperse expression of Eq. (5.57) for $f_1 = f_2 = f$. Its validity was further confirmed by performing molecular dynamics simulations for various combinations of arm numbers and performing the same comparison with the one presented in Section 5.6.3 for the monodisperse case. Representative results are shown in Fig. 50(a).

From a theoretical point of view, the nontrivial result of this analysis is the scaling prediction of Eq. (5.82) for the prefactor $\Theta_{f_1 f_2}$. In sterically stabilized systems with a size polydispersity the arithmetic mean of the radii is taken as the interaction radius, whereas in charge stabilized colloidal suspensions with charge polydispersity, the interaction is proportional to the product of the two charges, thus leading to a prefactor that is the geometric mean of the two charges. Hence, possible choices for $\Theta_{f_1 f_2}$ could have been the "arithmetic mean":

$$\Theta^{(a)}_{f_1 f_2} = \frac{5}{18}\left(\frac{f_1 + f_2}{2}\right)^{3/2} \tag{5.86}$$

or the "geometric mean":

$$\Theta^{(g)}_{f_1 f_2} = \frac{5}{18}(\sqrt{f_1 f_2})^{3/2} \,. \tag{5.87}$$

However, although all three expressions (5.82), (5.86) and (5.87) yield similar results for f_1 and f_2 not too different from each other, comparison with the simulation results has shown that only the scaling result, Eq. (5.82) is valid for high asymmetries [393], as shown also in Fig. 50(b).

5.11. Concluding remarks

In this section we have seen how star polymers with f chains attached on a common center can be viewed as ultrasoft colloidal particles, physically and formally interpolating between flexible chains and hard spheres. The effective interaction between star centers has been proven to have a logarithmic form, $\beta v(r) \sim f^{3/2} \ln(r/\sigma)$ when two stars overlap within their coronae, with the number of arms controlling the steepness of the repulsion. We have found that there exists a lower freezing arm number, $f_l = 34$, such that solutions of stars with functionalities $f \le f_l$ remain fluid at all densities. In that respect, the phase diagram of star polymers has a topological resemblance to that of the Gaussian core model (GCM), displaying also reentrant melting. This similarity exists although the GCM features a bounded interaction and the stars a diverging one. On the other hand, there exist systems with bounded interactions that can always freeze, see Appendix C. It is therefore not the boundedness of the interaction but rather its steepness that decided whether there is enough repulsion for the system to freeze.

A widely studied class of pair potentials in three dimensions are the so-called power-law interactions, $v(r) = \varepsilon(r/\sigma)^{-m}$, with $m \ge 1$ being an integer.[33] Power laws are scale free and so is the logarithm; as m becomes smaller, the power-law potentials become softer and the logarithm can be thought of as the most natural next step in increasing the softness of the scale-free interactions. Though usual power-law potentials bring about freezing at all temperatures, we have just seen that the logarithm does not.[34] Hence, the crossover between the "freezing at every temperature" behavior and the "reentrant melting behavior" for *diverging* interactions must occur somewhere between the $m = 1$ OCP case and the logarithmic repulsion of the star polymers.

The ultrasoftness of the logarithm lies in the heart of quite a few novel predicted and observed phenomena in star polymer solutions, including an anomalous structure factor and the stability of very anisotropic (body-centered orthogonal) and very open (diamond) crystals in the phase diagram. We have seen in this section yet another example of engineering the molecular architecture so that a specific macroscopic behavior can be achieved. In the following section, we will briefly discuss a few other interesting cases in which the molecular architecture can be tailor-cut and which are the object of current investigations.

6. Current work

In this section we give a brief account of current and planned work on colloidal and biological systems of increasing complexity. By adding hard colloidal particles in a star solution, one obtains a mixture of hard and soft entities, whose macroscopic behavior can be very rich. With the introduction of charge on the chains of the star polymers, one constructs polyelectrolyte stars,

---

[33] Note that in d dimensions, the system has a thermodynamic limit only if $m > d$; for the values $m \le d$, a "neutralizing background" has to be introduced in order to guarantee stability, as in the famous case of the one-component plasma (OCP), corresponding to the Coulomb interactions between charged particles, $m = 1$ at $d = 3$.

[34] Here we are loosely speaking of f as an inverse temperature.

where the chains are stretched and where additional counterions are present into the solution. Finally, by grafting a charge pattern on cylindrical colloids, such as the double helices of the DNA molecules, a novel type of effective interaction appears, depending on both the separation and the relative orientation of the two molecules in a nontrivial manner that features a coupling between translational and rotational configurations.

6.1. Star polymer–colloidal mixtures

A natural extension of the investigations on the phase behavior of star polymers is to consider *mixtures* of stars and hard, colloidal particles. As discussed in Section 4, mixtures of colloids and *linear* polymer chains have been studied in some detail and it has been established that the polymers induce a depletion interaction between the large colloids, whose range and strength can be tuned by changing the size and density of the polymer. By replacing the linear chains with stars, more possibilities open up to tune the effective colloid–colloid interactions. By varying the functionality f, the hardness of the colloid–star interaction can be changed and in this way the gap between colloid-linear chain and hard-sphere mixtures can be naturally bridged. In addition, it is anticipated that by changing the size ratio between colloids and stars and the composition of the mixture, a wide range of phenomenology, such as fluid–fluid, mixing–demixing, solidification transitions, etc., can be observed.

A full statistical–mechanical treatment of the mixture requires knowledge of three interaction potentials, $v_{cc}(r)$ between the colloids, $v_{ss}(r)$ between the stars and the cross-interaction $v_{sc}(r)$ between stars and colloids. Let us denote with σ_c the diameter of the colloids and with σ_s that of the stars, where σ_s here has the meaning of the parameter σ of Section 5.6. The interaction $v_{ss}(r)$ has been derived there, having a logarithmic form for separations smaller than σ_s and a Yukawa decay for separations larger than σ_s; however, it should be kept in mind that the Yukawa-like decay of $v_{ss}(r)$ was based on the blob picture, which does not hold for small functionalities, $f \lesssim 10$. For these cases, Jusufi et al. [214] found that $v_{ss}(r)$ is given by a modified version of Eq. (5.57), namely the following:

$$\beta v_{ss}(r) = \begin{cases} \dfrac{5}{18} f^{3/2}\left[-\ln\left(\dfrac{r}{\sigma_s}\right) + \dfrac{1}{2\tau^2\sigma_s^2}\right] & \text{for } r \le \sigma_s\ , \\ \dfrac{5}{18} f^{3/2} \dfrac{1}{2\tau^2\sigma_s^2} \exp[-\tau^2(r^2 - \sigma_s^2)] & \text{for } r \ge \sigma_s\ , \end{cases} \tag{6.1}$$

where τ is a fit parameter [213,214]. For the colloid–colloid interaction $v_{cc}(r)$, a hard-sphere potential, Eq. (4.1) is assumed.

The cross interaction $v_{sc}(r)$ was derived recently by Jusufi et al. [214], using an idea due to Pincus [61]. Let us suppose that the star and the colloid have center-to-center distance $r < (\sigma_c + \sigma_s)/2$, so that the polymer brush of the former is compressed due to the presence of the latter, as shown in Fig. 51. In this way, an effective repulsion sets in between the two centers, as the volume available to the brushes is diminished by the presence of the colloid. The *force* between the star and the colloid can then be calculated by integrating the osmotic pressure from the star along the spherical section of contact between the two particles [61]. A simple integration of the force over r yields then the effective potential $v_{sc}(r)$.

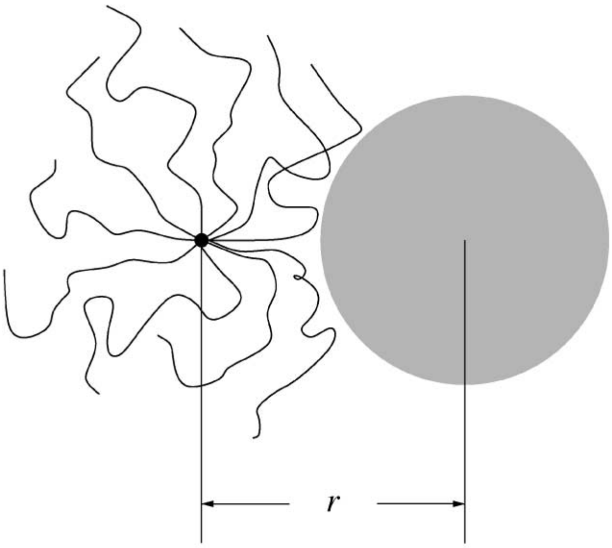

Fig. 51. Sketch of a star polymer and a colloidal particle interacting with each other through the compression of the brush of the former.

At not too close star–colloid approaches, the assumption can be made that the monomer density profile of the star remains unaffected by the presence of the colloid and is given by the scaling law of Eq. (5.15), implying a dependence of the osmotic pressure on the distance from the center of the star given by Eq. (5.16). Then, by integrating the normal component of this osmotic pressure to the surface over the spherical sector of contact between the star and the colloid, the force between the two can be analytically calculated as a function of the center-to-center separation r. It turns out that the scaling law $\Pi(r) \sim r^{-3}$ also holds for close approaches between the particles [395,396]. Hence, this law was taken to hold for the part of the star for which the power laws hold and for the decay of the pressure at the outermost part of the star, a Gaussian functional form was assumed [395]. For details on the theoretical derivation of the star–colloid interaction, we refer the reader to Refs. [214,213] and in what follows we present the main result of this approach, in which the star–colloid interaction $v_{\mathrm{sc}}(r)$ is given through

$$\beta v_{\mathrm{sc}}(r) = \begin{cases} \infty & \text{for } r < \dfrac{\sigma_{\mathrm{s}}}{2}\,, \\ \Lambda f^{3/2} \dfrac{\sigma_{\mathrm{c}}}{2r}\left[-\ln\left(\dfrac{2z}{\sigma_{\mathrm{s}}}\right) - \left(\dfrac{4z^2}{\sigma_{\mathrm{s}}^2} - 1\right)\left(\xi_1 - \dfrac{1}{2}\right) + \xi_2\right] & \text{for } \dfrac{\sigma_{\mathrm{s}}}{2} \le r \le \dfrac{\sigma_{\mathrm{c}} + \sigma_{\mathrm{s}}}{2}\,, \\ \Lambda f^{3/2} \dfrac{\sigma_{\mathrm{c}}}{2r}\left[\dfrac{\xi_2[1 - \mathrm{erf}(\kappa z)]}{1 - \mathrm{erf}(\kappa \sigma_{\mathrm{s}})}\right] & \text{for } \dfrac{\sigma_{\mathrm{c}} + \sigma_{\mathrm{s}}}{2} \le r\,, \end{cases} \tag{6.2}$$

where $z = r - \sigma_{\mathrm{c}}/2$ is the distance from the star center to the surface of the colloid. The constants are $\xi_1 = 1/(1 + 2\kappa^2\sigma_{\mathrm{s}}^2)$ and $\xi_2 = \sqrt{\pi}\xi_1 \exp(\kappa^2\sigma_{\mathrm{s}}^2)(1 - \mathrm{erf}(\kappa\sigma_{\mathrm{s}}))/(\kappa\sigma_{\mathrm{s}})$, while Λ and κ are fit

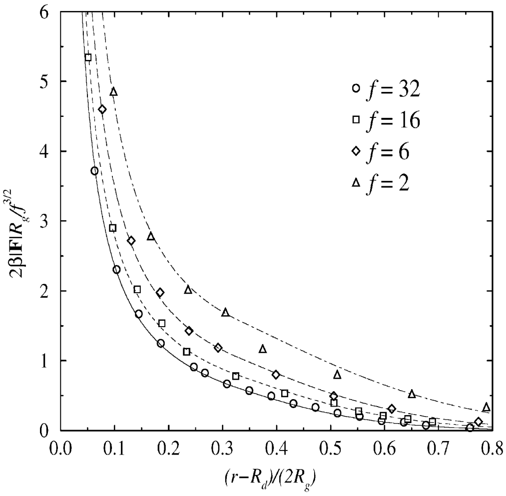

Fig. 52. The force between a star polymer and a flat wall as obtained by simulation (points) and theory (lines), for different values of *f*, expressed as a function of the distance between the star center and the wall. The star core of radius R_d has to be subtracted, as explained in Section 5.6.3. Note that the forces have been divided by a factor $f^{3/2}$.

parameters, determined by a comparison between the theoretically predicted force stemming from expression (6.2) above and the force measured in a simulation, as we explain below.

The star–colloid interaction diverges logarithmically at contact between the star center and the surface of the colloid ($z \to 0$), a result confirmed independently by field-theoretical considerations [397]. This can be understood by considering a star near a *flat* hard wall: similarly with the case of two stars, a single star with *f* arms near a hard wall resembles a star with 2*f* arms in a solvent and then the arguments of Section 5.6.1 lead to a logarithmic behavior at small *z*.

The force between a star and a colloidal particle can also be measured in a simulation, applying the method described in Section 5.6.3. The relationship between the theoretical length scale σ_s and the radius of gyration of the star, R_g, which is the only quantity accessible in a simulation (or in an experiment) was fixed in the same way as done in the case for two stars, namely the ratio $\lambda = \sigma_s/R_g$ was kept fixed at the value $\lambda = 1.26$ for all *f*, see Section 5.6.3. A comparison between the theoretical predictions and results from molecular dynamics for the case $\sigma_s/\sigma_c = 0$ (star polymer against a flat wall) is shown in Fig. 52 below.

The experimentally relevant parameters are the arm number *f* of the stars as well as the size ratio $q = \sigma_g/\sigma_c$, where $\sigma_g = 2R_g$ is the diameter of gyration of the stars. To access the thermodynamics of the mixture theoretically, Dzubiella et al. [213] applied the Rogers–Young closure for binary mixtures (see Appendix D), taking the above-mentioned three potentials as input. The structure of binary mixtures is described by three partial static structure factors $S_{\alpha\beta}(Q)$, with α, $\beta = \mathrm{c,s}$ which are output from the integral equations. Indication of a demixing transition is the divergence of all structure factors at the long-wavelength limit $Q \to 0$. It is more convenient to consider the so-called *concentration structure factor* $S_{\mathrm{con}}(Q)$, defined as

$$S_{\mathrm{con}}(Q) = x_s^2 S_{\mathrm{cc}}(Q) + x_c^2 S_{\mathrm{ss}}(Q) - 2x_c x_s S_{\mathrm{cs}}(Q)\ , \qquad (6.3)$$

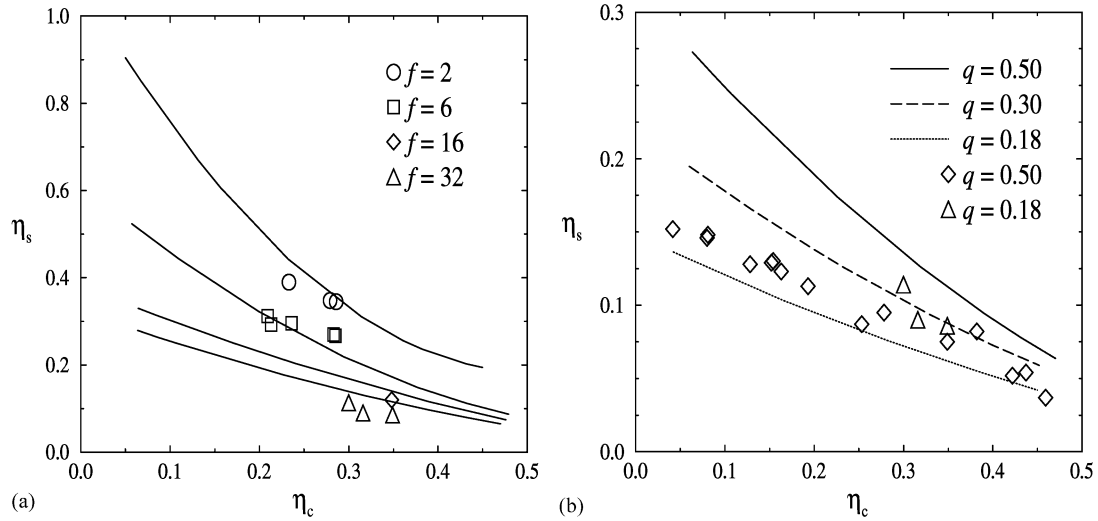

Fig. 53. Binodals for the mixing-demixing transition in star polymer-colloid mixtures. (a) Size ratio $q \cong 0.5$, for different arm numbers, $f = 2$, 6, 16 and 32. The symbols mark experimental results, compared with the theory (lines) for $q = 0.5$. The binodals move downwards with increasing f. (b) Fixed arm number $f = 32$ for different size ratios q. The symbols denote the experimental and the lines the theoretical results.

where x_i ($i = \mathrm{c}, \mathrm{s}$) denotes the concentration of the ith component. The divergence is caused by long-ranged density and concentration fluctuations near the phase transition and marks the so-called *spinodal instability* of the mixture against phase separation. The $Q \to 0$ limit provides also a way to thermodynamics, through the relation [398]

$$\lim_{Q \to 0} S_{\mathrm{con}}(Q) = k_{\mathrm{B}} T \left[\frac{\partial^2 g(x_{\mathrm{c}}, P, T)}{\partial x_{\mathrm{c}}^2} \right]^{-1} . \tag{6.4}$$

The function $g(x_{\mathrm{c}}, P, T)$ is the Gibbs free energy $G(x_{\mathrm{c}}, N, P, T)$ divided by the total particle number N and P denotes the pressure of the mixture.

If the function $g(x_{\mathrm{c}})$ has concave parts the systems shows phase coexistence and the phase boundaries can be calculated by the common tangent construction: at constant pressure P and temperature T, coexistence between two phases A and B with colloid concentrations $x_{\mathrm{c,A}}$ and $x_{\mathrm{c,B}}$ respectively, is warranted if

$$g'(x_{\mathrm{c,A}}) = g'(x_{\mathrm{c,B}}) \tag{6.5}$$

and

$$x_{\mathrm{c,A}} g'(x_{\mathrm{c,A}}) - g(x_{\mathrm{c,A}}) = x_{\mathrm{c,B}} g'(x_{\mathrm{c,B}}) - g(x_{\mathrm{c,B}}) , \tag{6.6}$$

where the prime denotes a derivative with respect to the argument. These conditions ensure the equality of the chemical potentials, $\mu_{i,\mathrm{A}} = \mu_{i,\mathrm{B}}$, for each component in the two phases.

Results from this procedure for different values of f and size ratio are shown in Fig. 53, together with the experimental results. It can be seen that very good agreement between the two is obtained, for a large range of arm numbers and size ratios. Of particular importance is the fact that this is achieved *without* the use of any free parameters in the theory. Investigations of the accompanying freezing transition of these systems are the subject of current research.

6.2. Polyelectrolyte stars

An effective mechanism to stabilize colloidal suspensions is to attach on the colloidal particles *charged* polymer chains, also known as *polyelectrolytes* [61]. In the limit where the size of the central particle is much smaller than the extent of the grafted brush, then one talks about polyelectrolyte stars. These are the generalization of star polymers for the case where the chains carry a net charge [334].

The study of the properties of an isolated polyelectrolyte star and of the effective interaction between two such macromolecular entities is complicated by the presence of more parameters in the problem than for the case of neutral stars. Electroneutrality requires that the net charge of the chains be compensated by the presence in the solution of counterions. The fraction of charged monomers and the valence of the counterions are therefore two additional degrees of freedom and more involved situations can appear, depending on the presence of added salt and the possibility of recombination of free counterions with the charged monomers on the chains [334]. Associated with these is the question of the fraction of counterions that remain trapped in the interior of the star, the so-called *bound counterions*, as opposed to those that can diffuse in the solution, and which are called *free counterions*.

The simplest case is that in which there is no added salt and no recombination, the star is strongly charged and has a large number of arms. These are called *osmotic stars* [334]. In this situation, the vast majority of the counterions are bounded and the arms of the star are fully stretched, thus giving rise to a $c(r) \sim r^{-2}$ power-law dependence of the monomer density from the center of the star [334]. This implies in turn that the arms of the star are rod-like (stiff), possessing a fractal dimension $D = 1$, to be compared with the fractal dimension $D = 5/3$ for neutral stars. This rod-like behavior has been observed experimentally in charged block copolymer micelles [399].

The conformation of a single polyelectrolyte star can be studied via molecular dynamics simulations, in full analogy with the approach described in Section 5.3.2. In Fig. 54 a typical configuration of such a star is shown, where it can be seen that the arms are indeed stretched. However, there exist some deviations from full stretching at the outermost region of the star, leading to a scaling of the form $c(r) \sim r^{-7/4}$ rather than r^{-2} predicted in Ref. [334]. Detailed investigations of the dependence of this exponent on functionality and charging fraction, are currently under way [400].

As far as the effective interaction between two polyelectrolyte stars is concerned, things are somewhat more complicated in comparison with the case of neutral stars, due to the presence of the counterions. In the neutral star case, an effective repulsion between the star centers comes about as a result of the self-avoidance of the chains. Here, for close approaches, the important factor seems to be the increase of the packing fraction of the bound counterions [61], whose osmotic pressure dominates over that of the rod-like chains. According to Pincus [61], this would lead to a force between the stars which is independent of the center-to-center separation. Yet, quite a few questions remain unanswered, namely the fraction of counterions which are free, the relative contributions of electrostatic and steric interactions and the long-range behavior of the effective potential.

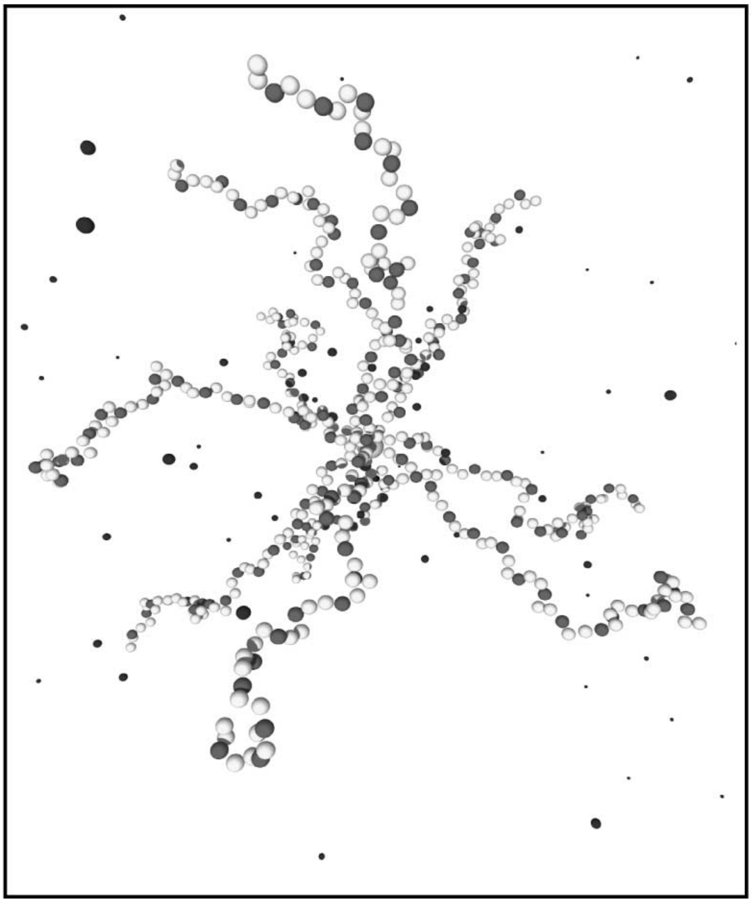

Fig. 54. Simulation snapshot of a polyelectrolyte star with $f = 10$ arms and $N = 50$ monomers per arm. Every third monomer along each chain is charged and is denoted by the dark bead on the chain. The free spheres denote the counterions. Note the stretching of the arms in comparison with the uncharged star having the same f and N values and shown in Fig. 37(a). (Courtesy of Arben Jusufi.)

Starting from simulation results regarding the conformation of isolated stars, conclusions can be drawn on the fraction of bound counterions and the effective force can be therefore theoretically calculated. The latter can be also measured in a MD simulation in order to test the validity of the theoretical approach. Then, the correlation functions of a many-body system consisting of polyelectrolyte stars can be calculated and the results can be compared with experimentally measured scattering data. Work along these lines is currently under way [401].

6.3. Amphoteric polyelectrolytes

Amphoteric polyelectrolytes or *polyampholytes* are again polymer chains but ones that carry on the backbone charges of *both* signs. The *net* charge on the chain depends on the pH of the solution and the pH at which this charge is zero is called the *isoelectric point* of the polyampholyte.

A natural polyampholyte which is of great interest due to its applications in food processing [60], photography [402], electrochemistry [403], biology, implant medicine and engineering is gelatin. Gelatin is widely used as a stabilizer in colloidal suspensions. The polyampholyte adsorbs onto the surface of the colloids and the ensuing stabilization arises as a result of the electrostatic and steric forces between the macromolecules.

A number of methods have been employed to study the stabilizing effects resulting from gelatin adsorption [404]. Most relevant are the direct measurements of the forces between layers of gelatin adsorbed on mica cylinders through the use of the surface force apparatus (SFA). Kawanishi et al. [69] explored the force between layers of gelatin adsorbed to mica surfaces both above and below its isoelectric point ($\mathrm{pH} = 5.1$) using a SFA. The adsorbed amount of gelatin was calculated from the mean refractive index of the medium between the mica sheets. The authors reported a dependence of the adsorbed amount and the range of the layer interactions on the pH and ionic strength of the solutions. The measured force vs. distance curves were fit with a linearized, constant-potential electrostatic interaction [12].

Kamiyama and Israelachvili [62] performed adsorption and SFA measurements on gelatin adsorbed onto mica from aqueous NaCl solutions. Particular attention was paid to the effect of ionic strength and pH on the excess adsorbed gelatin and on the force between the plates as a function of their separation. They found that the amount of added salt has a marginal effect on the adsorption properties, but a rather pronounced effect on the force between the plates: for high salt concentrations, the force is dominated by the steric effects, i.e., the compression energy between two overlapping gelatin layers, which is very well described by the Alexander–de Gennes equation [335,405]. On the other hand, if the salt concentration is low, the electrostatic double-layer repulsion between the plates is not screened and the forces display long-range tails quantifiable via an electrostatic repulsion [12].

As investigators have recently reported, molecular scale measurements of the structure and amount of adsorbed gelatin onto model surfaces using X-ray reflectometry [406] and neutron reflectometry, it is now possible to provide a detailed molecular-level description of polyampholyte adsorption onto macroscopic surfaces and the consequent colloidal forces. Other methods have been attempted to quantify the forces acting between more microscopic surfaces, such as the rheology measurements of Howe et al. [407]. In their work, the viscosity of oil in water emulsions stabilized with gelatin was characterized and a phenomenological model used to extract pair potentials. Although the results for the stabilizing force due to adsorbed gelatin were within the realm of expectation, the method relies on phenomenological modeling and hence it is not predictive.

Given this previous work, questions remain regarding the adsorption properties of gelatin onto *highly curved surfaces*, such as afforded by colloidal latex particles, and the resultant interaction between two such coated particles. Recently, it has been demonstrated that accurate measurements of the structure of gelatin adsorbed on colloidal particles can be achieved through a combination of methods that includes dynamic light scattering, small angle neutron scattering, viscometry, densitometry, and solution depletion with fluorescent labeled gelatin [408,409]. Motivated by these accurate measurements of adsorption properties of gelatin on colloids, Likos et al. [410] performed recently a fit of the scattering data from gelatin-coated latex colloidal suspensions for a wide range of concentrations, using an effective interaction potential which was expressed as the sum of the electrostatic and steric interactions. For the former, the screened Coulombic interaction of

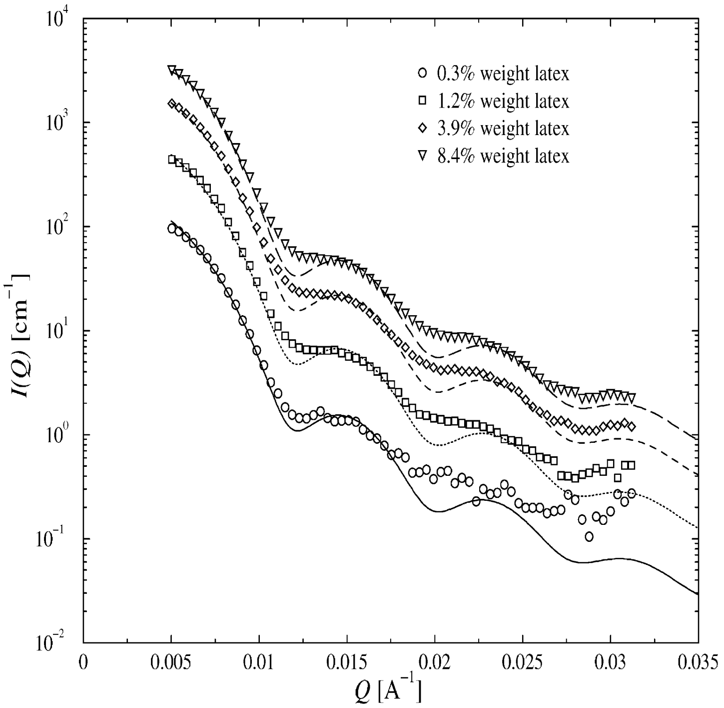

Fig. 55. SANS measured scattering from solutions of gelatin-coated latex particles (points) and the corresponding theoretical results (lines), for various latex concentrations. The discrepancies at the minima of the intensity are due to polydispersity effects in the sample, which are neglected in the theoretical approach. (Taken from Ref. [410].)

Eq. (2.19) was used, but with the weak van der Waals term $V_{\mathrm{vdW}}(r)$ ignored. For the latter, the Derjaguin approximation on the the Alexander–de Gennes expression [335,405] was employed, yielding the steric potential $\beta V_{\mathrm{st}}(r)$ as

$$\beta V_{\mathrm{st}}(r) = \begin{cases} \infty & \text{if } r < 2R\,, \\ f(y) & \text{if } 2R < r \le 2(R+L)\,, \\ 0 & \text{if } 2(R+L) < r\,, \end{cases} \tag{6.7}$$

where R is the radius of the colloidal particles, L is the thickness of the adsorbed gelatin layer and $y = (r - 2R)/(2L)$. The function $f(y)$ is given by

$$f(y) = \frac{16\pi R L^2}{35 s^3}\left[28(y^{-1/4} - 1) + \frac{20}{11}(1 - y^{11/4}) + 12(y - 1)\right] \tag{6.8}$$

with s denoting the distance between anchoring points of the gelatin on the colloidal surface. With all parameters read off from the experiment, the scattering intensities were described very accurately by the theoretical model above; a typical example is shown in Fig. 55.

However, it must be noted that in the samples studied, a rather high amount of salt, having concentration 10 mM, was present, causing a very strong screening of the electrostatic potential, see Eq. (2.17). Therefore, the hard core turned out to play the most important role in the electrostatic interaction. The clear separation between charge- and compression-effects employed in Ref. [410] is possible due to the strong screening of the additional charges of the polyampholyte by the ions of the added salt. A truly rigorous test of the potential would also include variation in the added salt concentration as well as the colloid concentration. This will be the subject of future work.

6.4. Columnar assemblies of DNA molecules

We finally report on current work on a system which is colloidal in nature, as far as the length scales of the molecules involved are concerned, but different from all systems described before in the sense that these molecules do not possess spherical symmetry. We consider a columnar assembly of *parallel*, *rigid* DNA molecules. The DNA molecule has a persistence length of about 500 Å; molecules shorter than this will therefore behave as rigid rods. The diameter of the DNA cylinder is about 20 Å and as long as the average interaxial separation of neighboring DNA molecules remains below approximately 40 Å, the cylinders remain parallel; at larger separations they begin to tilt. In the domain where the rods are parallel to each other, it is therefore a reasonable physical approximation to treat the DNA molecules as infinitely long cylinders, since their length is much larger than their diameter. Equivalently, one can think of them as a *two-dimensional* system of interacting discs.

Each DNA molecule has grafted on it a double-helical pattern of phosphate charges. Hence, the effective interaction between the centers of the discs will depend not only on the radial separation between them, but on the relative orientation of the helices as well. The model can be mapped on a "spin system" of particles (discs) carrying on their backs an additional spin degree of freedom [411]. The effective interaction between the centers of two such discs has been derived in the framework of the linearized Poisson–Boltzmann approximation by Kornyshev and Leikin [411] and has the form of a generalized XY-spin model, including not only the usual $\cos(\phi)$ interaction but also all the higher harmonics, $\cos(n\phi)$, where ϕ denotes the angle between the spins. The effective force was also measured in the recent simulations of Allahyarov and Löwen [412]. On the basis of this interaction, zero-temperature statistical–mechanical studies of the macroscopic ordering of the spin degrees of freedom on a fixed, triangular lattice, have revealed a variety of phases and phase transitions of the first and second kind between them [413]. The extension of this approach to finite temperatures and the inclusion of the fluid phase in these considerations are currently under way.

7. Summary and conclusions

In this work we have reviewed recent progress made on the field of soft condensed matter physics, regarding the static properties of suspensions or solutions of spherical macromolecular entities. We have seen that a very powerful technique for the study of such systems is the introduction of the *effective Hamiltonian* in which only the relevant (large) degrees of freedom show up, and all the other (small) degrees of freedom are traced out. Their effect is to influence certain parameters that appear in the effective interaction, for example its range, depth (in the case of attractions) and softness (in the case of repulsions). The effective Hamiltonian allows us then to proceed by employing the well-known techniques from the statistical mechanics of the one-component systems, including the various approximations of liquid-state theory, density functional theory, cell models, etc. In doing so, care must always be taken of the fact that the parameters appearing in the effective Hamiltonian depend in general on the chemistry and composition of the components that have been traced out and also that the process of effectively reducing the system to one component generates the volume terms which can influence its thermodynamics. Moreover, the pair-potential picture is in general only an approximation (albeit usually an excellent one) and hence it must be used with caution; many-body forces and their effects have to always be examined a posteriori in order to ensure the validity of the pair-potential approximation.

It is the task of statistical physics and physicists to start from microscopic interactions and predict macroscopic behavior. The field of colloidal physics offers us the possibility to think the other way around. Given a certain macroscopic behavior that is either observed or desired, what kind of microscopic interaction must be present in order to cause it? As this interaction can be *externally controlled* for colloidal systems, they offer us a unique opportunity to tune it and to engineer soft matter at the molecular level.

Acknowledgements

I am indebted to Hartmut Löwen for offering me the opportunity to work with him for a number of years, for his enthusiasm, ideas, support and for creating a stimulating research environment, both at Forschungszentrum Jülich and at the University of Düsseldorf, where the bulk of this work has been carried out. I thank additionally the members of the group for the creative atmosphere, the discussions and fun we had together. Elshad Allahyarov, Joachim Dzubiella, Ansgar Esztermann, Christian von Ferber, Reimar Finken, Holger Harreis, Martin Heni, Zsolt Németh, Ralf Pierre, and Matthias Schmidt. Cord Kielhorn and Alexander Schlensog offered invaluable help with all computer matters and in this way they greatly assisted to the completion of this work.

I am especially grateful to three colleagues with whom I collaborated intensively on most of the research subjects covered here: Arben Jusufi was offering security, confirming with his simulations the reasonable theoretical approximations and trashing the silly ones. Andreas Lang could finish a demanding computation at time scales that were smaller than mine by orders of magnitude. Finally, Martin Watzlawek has been a constant source of inspiration, ideas and lively discussions on almost everything included in this work and has read and re-read this document, returning it with many marginalia. I hope he will be pleased to see how many of his comments found their way into the final version.

Many colleagues have further assisted through collaborations, discussions, suggestions and hints on the literature, and I wish to thank them for their contributions. Basil Abbas (Jülich), Neil Ashcroft (Ithaca), Peter Bolhuis (Cambridge), Irene D'Amico (Torino), Alan Denton (Fargo), Anne Denton (Fargo), Erich Eisenriegler (Jülich), Bob Evans (Bristol), María José Fernaud (Madrid), George Fytas (Heraklion), Gerhard Kahl (Vienna), Anja König (Ithaca), Enrique Lomba (Madrid), Ard Louis (Cambridge), Andreas Poppe (Jülich), Dieter Richter (Jülich), Yasha Rosenfeld (Beer-Sheva), Roland Roth (Bristol), Gaetano Senatore (Trieste), Jörg Stellbrink (Jülich), Abe Vaynberg (Delaware), Dimitris Vlassopoulos (Heraklion), Herbert Wagner (Munich), and Norman Wagner (Delaware). A few words of appreciation should be said, in memory of the late Professor Klaus W. Kehr, who offered me warm hospitality during the two years of my stay at the Forschungszentrum Jülich, under his capacity as director of the IFF Theory II Institute.

The research reported here has been supported, in various stages, by the Alexander von Humboldt Foundation, the European Communities through the Human Capital and Mobility Programme, the Forschungszentrum Jülich through a Research Fellowship and the Deutsche Forschungsgemeinschaft through the SFB 237.

Note added in proof

During the production of this document, another review on effective interactions in colloidal suspensions, putting emphasis on charged colloids, has appeared in the literature [436].

Appendix A. Elastic constants from the theory of the harmonic solid

In this appendix we give a brief account of the way in which the elastic constants can be derived from the classical theory of the harmonic crystal. We follow closely the discussion in Ref. [15]. Suppose that each particle in a monatomic solid has been displaced from its equilibrium position $\boldsymbol{R}$ by a vector $\boldsymbol{u}(\boldsymbol{R})$ having Cartesian components $u_\alpha(\boldsymbol{R})$ ($\alpha = 1, 2, 3$). The set of all vectors $\{\boldsymbol{R}\}$ forms, of course, a Bravais lattice. The harmonic potential energy associated with the displacements of all particles is given through the equation

$$U^{\mathrm{harm}} = \frac{1}{4} \sum_{\mu,\nu=1,2,3} \sum_{\boldsymbol{R} \neq \boldsymbol{R}'} [u_\mu(\boldsymbol{R}) - u_\mu(\boldsymbol{R}')]\phi_{\mu\nu}(\boldsymbol{R} - \boldsymbol{R}')[u_\nu(\boldsymbol{R}) - u_\nu(\boldsymbol{R}')] . \tag{A.1}$$

The second sum is carried over all distinct pairs of Bravais lattice vectors. Moreover, $\phi(\boldsymbol{r})$ is the interparticle pair potential and

$$\phi_{\mu\nu}(\boldsymbol{r}) = \frac{\partial^2 \phi(\boldsymbol{r})}{\partial x_\mu \partial x_\nu} \tag{A.2}$$

with the Cartesian components x_α ($\alpha = 1, 2, 3$) of the position vector $\boldsymbol{r}$. By introducing the matrix $\boldsymbol{D}(\boldsymbol{R} - \boldsymbol{R}')$ with entries

$$D_{\mu\nu}(\boldsymbol{R} - \boldsymbol{R}') = \delta_{\boldsymbol{R},\boldsymbol{R}'} \sum_{\boldsymbol{R}''} \phi_{\mu\nu}(\boldsymbol{R} - \boldsymbol{R}'') - \phi_{\mu\nu}(\boldsymbol{R} - \boldsymbol{R}') , \tag{A.3}$$

Eq. (A.1) takes the more compact form:

$$U^{\mathrm{harm}} = -\frac{1}{4} \sum_{\boldsymbol{R},\boldsymbol{R}'} [\boldsymbol{u}(\boldsymbol{R}) - \boldsymbol{u}(\boldsymbol{R}')]\boldsymbol{D}(\boldsymbol{R} - \boldsymbol{R}')[\boldsymbol{u}(\boldsymbol{R}) - \boldsymbol{u}(\boldsymbol{R}')] , \tag{A.4}$$

where the double sum is now carried over all Bravais lattice pairs. The connection of harmonic theory with the theory of elasticity comes if we consider a very long-wavelength disturbance of the atoms from their equilibrium positions, which allows us to Taylor expand the displacement $\boldsymbol{u}(\boldsymbol{R}')$ around $\boldsymbol{u}(\boldsymbol{R})$ and write[35]

$$\boldsymbol{u}(\boldsymbol{R}') \approx \boldsymbol{u}(\boldsymbol{R}) + (\boldsymbol{R}' - \boldsymbol{R})\cdot\nabla\boldsymbol{u}(\boldsymbol{R})|_{\boldsymbol{r}=\boldsymbol{R}}\ . \tag{A.5}$$

Substituting Eq. (A.5) into Eq. (A.4) results into

$$U^{\mathrm{harm}} = \frac{1}{2}\sum_{\boldsymbol{R},\mu\nu\sigma\tau}\left(\frac{\partial}{\partial x_\sigma}u_\mu(\boldsymbol{R})\right)\left(\frac{\partial}{\partial x_\tau}u_\nu(\boldsymbol{R})\right)E_{\sigma\mu\tau\nu}\ , \tag{A.6}$$

where the entries of the fourth-rank tensor $E_{\sigma\mu\tau\nu}$ are given by

$$E_{\sigma\mu\tau\nu} = -\frac{1}{2}\sum_{\boldsymbol{R}} R_\sigma D_{\mu\nu}(\boldsymbol{R})R_\tau\ . \tag{A.7}$$

The slow spatial variation of the displacements $\boldsymbol{u}(\boldsymbol{R})$ allows us to rewrite Eq. (A.6) as an integral:

$$U^{\mathrm{harm}} = \frac{1}{2v}\sum_{\mu\nu\sigma\tau}\int \mathrm{d}\boldsymbol{r}\left(\frac{\partial}{\partial x_\sigma}u_\mu(\boldsymbol{r})\right)\left(\frac{\partial}{\partial x_\tau}u_\nu(\boldsymbol{r})\right)E_{\sigma\mu\tau\nu}\ , \tag{A.8}$$

where v stands for the elementary unit cell volume.

The energy of the crystal should remain unchanged under a rigid rotation. An elementary rotation by an angle $\delta\omega$ along an arbitrary axis $\hat{\boldsymbol{n}}$ passing through the origin results in displacements:

$$\boldsymbol{u}(\boldsymbol{R}) = \delta\omega(\hat{\boldsymbol{n}}\times\boldsymbol{R})\ . \tag{A.9}$$

Substituting Eq. (A.9) into Eq. (A.8) and requiring $U^{\mathrm{harm}} = 0$ for arbitrary rotations, we find that U^{harm} can depend on the derivatives $(\partial u_\mu/\partial x_\sigma)$ only through the symmetrical combination (the strain tensor):

$$\mathscr{E}_{\sigma\mu} = \frac{1}{2}\left(\frac{\partial u_\mu}{\partial x_\sigma} + \frac{\partial u_\sigma}{\partial x_\mu}\right)\ . \tag{A.10}$$

As a result, we can write Eq. (A.8) as

$$U^{\mathrm{harm}} = \frac{1}{2}\sum_{\mu\nu\sigma\tau}\int \mathrm{d}\boldsymbol{r}\,\mathscr{E}_{\sigma\mu}c_{\sigma\mu\tau\nu}\mathscr{E}_{\tau\nu} \tag{A.11}$$

with the elastic constants:

$$c_{\sigma\mu\tau\nu} = -\frac{1}{8v}\sum_{\boldsymbol{R}}\left[R_\sigma D_{\mu\nu}R_\tau + R_\mu D_{\sigma\nu}R_\tau + R_\sigma D_{\mu\tau}R_\nu + R_\mu D_{\sigma\tau}R_\nu\right]\ . \tag{A.12}$$

Assuming spherically symmetric interactions between nearest neighbors, using Eqs. (A.3) and (A.12) above and taking a simple cubic crystal, we obtain for the elastic constant c_{xxxx} Eq. (2.4) of the main text.

---

[35] For a vector field $\boldsymbol{u}(\boldsymbol{R})$ the quantity $\nabla\boldsymbol{u}$ is a matrix with elements $(\nabla\boldsymbol{u})_{\mu\nu} = \partial u_\mu/\partial x_\nu$.

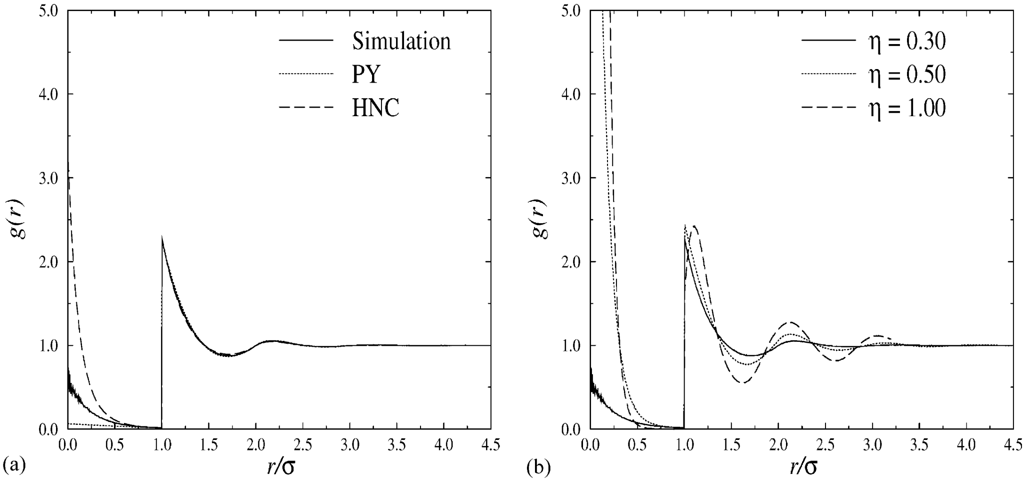

Fig. 56. (a) Comparison between theoretical and simulation results for the radial distribution function of the penetrable spheres model at reduced temperature $t = 0.2$ and at packing fraction $\eta = 0.30$. Notice that the PY closure underestimates the values of $g(r)$ inside the core, whereas the HNC overestimates it. (b) Simulation results for $g(r)$ at the same temperature, $t = 0.2$, at higher packing fractions. Notice the dramatic increase of the value of $g(r)$ at $r = 0$ with increasing packing fraction. The values are $g(0) = 18.5$ at $\eta = 0.50$ and $g(0) = 120$ at $\eta = 1.00$. (Simulation results: courtesy of Martin Watzlawek.)

Appendix B. The penetrable spheres model

In this appendix we present briefly the structural and phase properties of another system with bounded interactions between its constituent particles, the penetrable spheres model (PSM) [167]. The pair potential $v(r)$ between the particles is

$$v(r) = \begin{cases} \varepsilon & \text{if } r < \sigma\,, \\ 0 & \text{if } r > \sigma\,, \end{cases} \tag{B.1}$$

where σ is the diameter of the spheres and ε is the height of the energy barrier ($\varepsilon > 0$). There are N particles in the volume Ω and the density is $\rho = N/\Omega$. The packing fraction η and reduced temperature t are defined as $\eta = \pi\rho\sigma^3/6$ and $t = k_B T/\varepsilon$. Early considerations on the zero-temperature phase diagram of the PSM date back to the work of Marquest and Witten [414] who modeled in this way the interaction between micelles in a solvent. Virial coefficients were studied by Katsura and Abe [415]. Klein et al. have examined some fundamental mathematical properties of a related Kac potential [416,417], in which the range and height of the interaction are not independent quantities, and later performed molecular dynamics simulations on the same model [418].

Clearly, the PSM reduces to the hard sphere (HS) model at $T = 0$. A striking feature of this potential is that it does not differentiate between partial and full overlaps between the spheres: regardless of the separation between the sphere centers, a constant energy cost $\varepsilon > 0$ has to be paid as long as this separation is smaller than the sphere diameter σ. Intuitively, this leads to the conclusion that the spheres will tend to have full overlaps, because in this way the available volume for the remaining spheres will be maximized. This property was confirmed by computer simulations of the fluid state of the system [77,167]. Typical results are shown in Fig. 56. The radial distribution function shows an accumulation of particles at $r = 0$, i.e., a tendency of the spheres to "sit on top of each other".

This unique characteristic of the interaction, makes again the usual closures for the study of the liquid state useless. As shown in Fig. 56(a), the PY closure seriously underestimates the value of $g(r)$ at $r = 0$, whereas the HNC seriously overestimates it (at least at low temperatures). One closure that successfully deals with the problem to date, is the ZSEP closure mentioned in Section 3.5.3 [Eq. (3.95)], which has been employed in the recent work on this model by Fernaud et al. [177]. An alternative method, yielding less spectacular agreement for $g(r)$ inside the core but having the serious advantage of treating liquid and solid phases within the same theoretical framework, is based on the extension of Rosenfeld's fundamental measures free energy density functional to bounded interactions and has been recently proposed by Schmidt [180,419]. In view of the difficulties encountered with the conventional integral equation theories, the calculations of the free energy for the fluid phase in Ref. [167] were based entirely on computer simulations.

It is expected that the system will display a freezing transition into a fcc-solid at finite temperatures, inherited from the underlying HS-freezing transition at $t = 0$. For the fcc-solid, the close-packing value of η is $\eta_{\mathrm{CP}} = \pi\sqrt{2}/6 \cong 0.74$; when $\eta \leq \eta_{\mathrm{CP}}$, it is possible to arrange the particles on the sites of the fcc-lattice without overlaps. At $t = 0$ no configuration with $\eta > \eta_{\mathrm{CP}}$ is allowed, due to the hard-sphere exclusion. However, at finite temperatures η can be arbitrarily large. In Ref. [167] attention was focused on the low-temperature domain of the phase diagram, where the solid phases of the system can be analyzed by some mapping into an effective hard-sphere solid.

The property of "clustering", i.e., the tendency of the particles to form composite particles (clusters) in which a number of them sit on top of each other, is already manifest in the shape of the radial distribution function $g(r)$ of the liquid state. This mechanism of creating "free space" is an efficient means to stabilize solid phases as well. Indeed, when the packing fraction slightly exceeds the close-packing value η_{CP}, then the formation of pairs on a few lattice sites will cost an energy ε for every pair formed but otherwise it will have the effect of increasing the lattice constant, so that *additional overlaps* between particles or clusters on neighboring sites are avoided. On the contrary, if no pairs are formed, then every particle will have to overlap with *all* of its neighbors, thus bringing about a much higher energy cost. It must be emphasized that the efficiency of this mechanism lies precisely in the fact that the interaction energy is *constant* irrespective of the degree of overlap. In the Gaussian core model of Section 3.5, for example, this mechanism does not work. The Gaussian potential increases fast enough with decreasing interparticle distance so that there it is always preferable to have partial overlaps with all 12 nearest neighbors in the fcc lattice (eight in the bcc) than any nonzero fraction of doubly (or more) occupied lattice sites in the solid. The clustering mechanism is, of course, not limited to pair formation. Triplets, quadruplets, etc., are expected to form as the packing fraction increases.

Based on these considerations, Likos et al. [167] put forward a variational procedure for determining the free energy of a solid, which simultaneously determines the fractions of lattice sites occupied by pairs and triplets. The formalism is readily generalizable to any order of clustering but the analysis was limited to pairs and triplets only, on practical grounds.[36] Let the number of lattice sites be denoted by N_s, with N_1 of them being occupied by single particles, N_2 by pairs and N_3 by triplets. The partial fractions s, z and w of multiply occupied sites are defined as

$$s \equiv \frac{N_1}{N_s}, \quad z \equiv \frac{N_2}{N_s} \quad \text{and} \quad w \equiv \frac{N_3}{N_s} . \tag{B.2}$$

Clearly, $s + z + w = 1$ and $N = (1 + z + 2w)N_s$. The result of the formation of composites is that the "clustered solid" has a lattice constant which corresponds not to η but to a new, *effective* packing fraction γ which is lower and related to η by

$$\gamma = \frac{\eta}{1 + z + 2w} . \tag{B.3}$$

The additional, physically motivated assumption, is that at packings $\eta > \eta_{\mathrm{CP}}$ the system will find it favorable to create as many clusters as possible so as to bring about an effective packing γ which is below η_{CP}. This way, the energy cost will come entirely from the sphere overlaps in the clusters themselves; otherwise, the lattice cell will now be large enough, so that the expensive, multiple overlaps with the neighbors will be avoided.

On the basis of these considerations and by employing a cell model for the clustered solid [88–91,420], the variational expression for the free energy per site of the clustered solid, $\tilde{f}(\eta, t; z, w)$ reads as [167]

$$\tilde{f}(\eta, t; z, w) = f_0(\gamma) + \left(\frac{z + 3w}{1 + z + 2w}\right)t^{-1} + \left(\frac{z \ln 2 + w \ln 6}{1 + z + 2w}\right)$$
$$+ \frac{1}{1 + z + 2w}[z \ln z + w \ln w + (1 - z - w)\ln(1 - z - w)] , \tag{B.4}$$

where $f_0(\gamma)$ is the free energy per site of a hard-sphere fcc-solid at packing fraction $\gamma < \eta_{\mathrm{CP}}$ and γ is given by Eq. (B.3). In Eq. (B.4) above the energy costs ε and 3ε associated with every doubly and triply occupied site, respectively, the indistinguishability of particles sitting on the same site and the mixing entropy arising from all possible ways of choosing the N_2 and N_3 sites that are occupied by clusters are taken into account. The quantities z and w are variational parameters, as there are no chemical potentials controlling the site occupancy, hence the free energy per particle of the solid is given by

$$f(\eta, t) = \min_{\{z,w\}} \tilde{f}(\eta, t; z, w) . \tag{B.5}$$

For the quantity $f_0(\gamma)$ the very accurate result from the density functional approximation of Denton and Ashcroft [93] was used. The results of the variational calculation were successfully tested against those from Monte-Carlo simulations.

Putting together the simulation results for the free energy of the fluid with the cell model-variational results for the free energy of the solid, the phase diagram shown in Fig. 57 was

---

[36] Though the term "on practical grounds" sounds rather innocent, in fact it is not: the minimization of a function of a very large number of parameters can sometimes be a highly nontrivial numerical task.

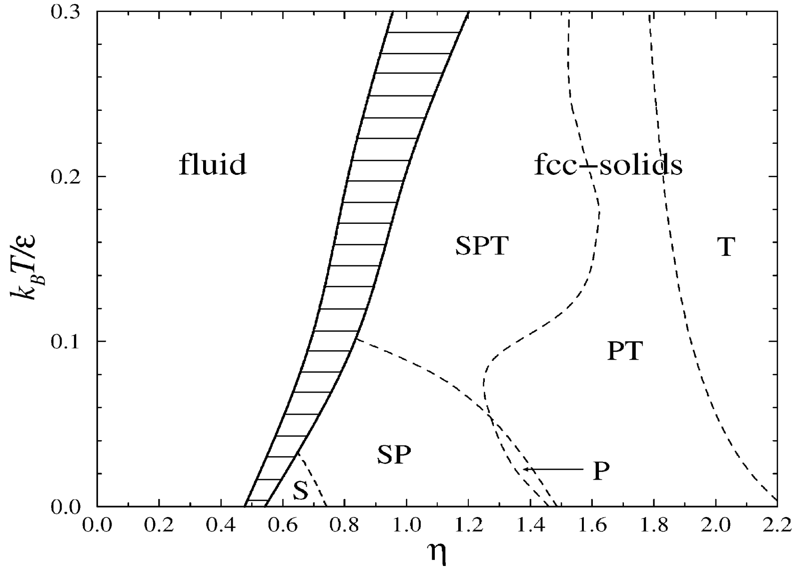

Fig. 57. The phase diagram of the penetrable spheres model. The thick lines denote the first-order freezing transition and the shaded region is the liquid–solid coexistence region. The dashed lines denote continuous clustering transitions in the solid. As explained in the text, the region of stability of the T-solid is artificially enlarged due to the lack of the possibility of formation of four-particle clusters in the theory. (Redrawn from Fig. 8 of Ref. [167].)

obtained. The terminology to characterize the various solids appearing there has the following meaning:

(i) S-solid if $s = 1$, $z = w = 0$;
(ii) SP-solid if $0 < s < 1$, $0 < z < 1$ and $w = 0$;
(iii) P-solid if $s = 0$, $z = 1$ and $w = 0$;
(iv) PT-solid if $s = 0$, $0 < z < 1$ and $0 < w < 1$;
(v) SPT-solid if $0 < s < 1$, $0 < z < 1$ and $0 < w < 1$, and
(vi) T-solid if $s = z = 0$, $w = 1$.

The typical scenario that materializes is the following: for packing fractions $\eta < \eta_{\mathrm{CP}}$, we have the usual S-solid, as there is no particular gain for clusters to be formed. At higher densities, pairs start to appear and an SP-solid is formed. The pair fraction grows with density at the expense of the singly occupied sites. Depending on the temperature, the fraction of pairs may reach the value unity at about $\eta \approx 2\eta_{\mathrm{CP}}$ before any triplets appear, thus forming a P-crystal. As temperature grows, triplets appear while both s and z are nonzero, thus giving rise to a SPT-solid. By further increase of the density, the single-occupancy sites disappear altogether and a PT-solid emerges. Then, the pairs start being replaced by triplets completely and a T-solid takes the place of the PT-solid. However, it should be noticed that the region of stability of the T-phase is artificially enlarged. The reason is that, in order to determine with accuracy the stability for a given type of clusters, at least the next type of cluster must be put into the theory, i.e., quadruplets or even quintuplets for the T-solid and so on.

The fractions of multiply occupied sites change continuously from zero to finite values and thus in Ref. [167] the loci of vanishing s, z and w were identified with "second-order clustering transitions" in the solid. It was later shown by Schmidt [180] that these are not lines of sharp thermodynamic transitions but rather diffuse boundaries separating a region where the occupancy number is exponentially suppressed from a region where it is not. Nevertheless, the overall picture shown in Fig. 57 was also confirmed in the density functional work of Ref. [180], although the liquid–solid coexistence lines found are somewhat different from the ones presented here.

Irrespective of the quantitative details, the results of Refs. [167,180], as well as some considerations of Fernaud et al. based entirely on liquid structure [177], all point to the same result for the phase behavior of the PSM. The freezing transition into an fcc-solid with clustered sites persists to arbitrarily high temperatures, running approximately along the "diagonal" of the (t, η)-plane, $t = \eta$, as the temperature grows. The freezing line does not "turn around" as in the case of the Gaussian core model, there is no upper freezing temperature and hence no reentrant melting for the PSM at high densities.

Appendix C. Clustering or reentrant melting? An exact result

In this appendix, we examine in full generality the phase behavior of systems whose constituent particles interact by means of potentials which do not diverge at the origin, are free of attractive parts and decay fast enough to zero as the interparticle separation r goes to infinity. By employing a mean-field-density functional theory which is shown to become exact at high temperatures and/or densities, we establish a criterion which determines whether a given system will freeze at all temperatures or it will display reentrant melting and an upper freezing temperature [168].

We will work with a general interaction $v(r) = \varepsilon\phi(r/\sigma)$ satisfying the requirements put forward above. Here, ε and σ are an energy and a length, respectively, and $\phi(x)$ is some dimensionless function. The latter does *not* have to be analytic, i.e., discontinuities in the potential or its derivatives are allowed. The positivity of the interaction, $\phi(r) \geq 0$ guarantees that the system is stable [421] and the fast decay to zero at $r \to \infty$ that the Fourier transform (FT) of $\phi(r)$, called $\tilde{\phi}(Q)$, exists. Let us call $\hat{\phi}(Q) = \sigma^{-3}\tilde{\phi}(Q)$ the dimensionless FT. Without loss of generality, we assume $\phi(0) = 1$. For more concreteness we introduce in addition the family of bounded potentials $v_\xi(r)$ depending on a tunable parameter ξ,

$$v_\xi(r) = \varepsilon\,\frac{1 + \mathrm{e}^{-\sigma/\xi}}{1 + \mathrm{e}^{(r-\sigma)/\xi}}\,, \tag{C.1}$$

where ξ is a "smoothing parameter" having dimensions of length. The case $\xi = 0$ recovers the PSM whereas as ξ grows the interaction becomes smoother. Due to its resemblance to the Fermi–Dirac distribution, we call this family the Fermi distribution model (FDM).[37] The additional factor

---

[37] Other choices are also possible, for example a family of the form $v_m(r) = \varepsilon\exp[-(r/\sigma)^m]$, where m is a positive integer. In this way one recovers the PSM for $m = \infty$ and the GCM for $m = 2$.

$1 + \mathrm{e}^{-\sigma/\xi}$ in the numerator of the rhs of Eq. (C.1) ensures that the potential varies from ε at $r = 0$ to zero at $r \to \infty$, for all ξ.

We introduce dimensionless measures of temperature and density as

$$t = \frac{k_{\mathrm{B}} T}{\varepsilon} = (\beta\varepsilon)^{-1} , \tag{C.2}$$

$$\eta = \frac{\pi}{6}\rho\sigma^3 = \frac{\pi}{6}\bar{\rho} , \tag{C.3}$$

where k_{B} is Boltzmann's constant and $\rho = N/V$ is the density of a system of N particles in the volume V. We will refer to η as the "packing fraction" of the system.

The key idea for examining the high-temperature and/or high-density limit of such model systems in three and higher dimensions is the following. We consider, in general, a spatially modulated density profile $\rho(\boldsymbol{r})$ which does not vary too rapidly on the scale σ set by the interaction. At high densities, $\rho\sigma^3 \gg 1$, the average interparticle distance $a \equiv \rho^{-1/3}$ becomes vanishingly small, and it holds $a \ll \sigma$, i.e., the potential is extremely long range. Every particle is simultaneously interacting with an enormous number of neighboring molecules and in the absence of short-range excluded volume interactions the excess free energy of the system [79] can be approximated by a simple mean-field term, equal to the internal energy of the system:

$$F_{\mathrm{ex}}[\rho(\boldsymbol{r})] \cong \frac{1}{2}\iint \mathrm{d}\boldsymbol{r}\,\mathrm{d}\boldsymbol{r}'\, v(|\boldsymbol{r} - \boldsymbol{r}'|)\rho(\boldsymbol{r})\rho(\boldsymbol{r}') \tag{C.4}$$

with the approximation becoming more accurate with increasing density. Then, Eq. (C.4) immediately implies that in this limit the direct correlation function $c(r)$ of the system, defined as [79]

$$c(|\boldsymbol{r} - \boldsymbol{r}'|; \rho) = -\lim_{\rho(\boldsymbol{r}) \to \rho} \frac{\delta^2 \beta F_{\mathrm{ex}}[\rho(\boldsymbol{r})]}{\delta\rho(\boldsymbol{r})\delta\rho(\boldsymbol{r}')} , \tag{C.5}$$

becomes independent of the density and is simply proportional to the interaction, namely

$$c(r) = -\beta v(r) . \tag{C.6}$$

Using the last equation, together with the Ornstein–Zernike relation [4], we readily obtain an analytic expression for the structure factor $S(Q)$ of the system as

$$S(Q) = \frac{1}{1 + \bar{\rho} t^{-1} \hat{\phi}(Q)} . \tag{C.7}$$

Bounded and positive-definite interactions have been studied in the late 1970s by Grewe and Klein [416,417]. The authors considered a slightly different model than the one considered here, namely a Kac potential of the form

$$v(r) = \gamma^d \psi(\gamma r) , \tag{C.8}$$

where d is the dimension of the space and $\gamma \geq 0$ is a parameter controlling the range *and* strength of the potential. Moreover, $\psi(x)$ is a nonnegative, bounded and integrable function:

$$0 \leq \psi(x) \leq A < \infty, \qquad C = \int \mathrm{d}^d\boldsymbol{x}\, \psi(x) < \infty. \tag{C.9}$$

Grewe and Klein were able to show rigorously that at the limit $\gamma \to 0$, the direct correlation function of a system interacting by means of potential (C.8) is given by Eq. (C.6) above. The connection with the case we are discussing here is straightforward: as there are no hard cores in the system or a lattice constant to impose a length scale, the only relevant length is set by the density and is equal to $\rho^{-1/3}$ in our model and by the parameter γ^{-1} in model (C.8). In this respect, the limit $\gamma \to 0$ in the Kac model of Grewe and Klein is equivalent to the limit $\rho \to \infty$ considered here. However, in the Kac model the strength of the interaction goes to zero simultaneously with the increase in its range. Moreover, the validity of the mean-field expression at large but finite densities has not been tested in detail. There is also a certain similarity between the ideas put forward here and the considerations on freezing for systems featuring of diverging interactions at infinite or very large numbers of spatial dimensions [422–425]. However, in the latter case, the direct correlation function is given by the Mayer function $f(r) = \exp[-\beta v(r)] - 1$ of the interaction potential and not by $-\beta v(r)$ as in the case at hand.

We employ the mean-field idea as a physically motivated *working hypothesis* for now and, by direct comparison with simulation results, we will show later that it is indeed valid even at moderate densities. Within the framework of this theory, an exact criterion can be formulated, concerning the stability of the liquid phase at high temperatures and densities. The function $\phi(r)$ was assumed to be decaying monotonically from unity at $r = 0$ to zero at $r \to \infty$. For the function $\hat{\phi}(Q)$, there are two possibilities: (i) It has a monotonic decay from the value $\hat{\phi}(Q = 0) = \sigma^{-3}\int \mathrm{d}\boldsymbol{r}\, \phi(r) > 0$ to the value $\hat{\phi}(Q) = 0$ at $Q \to \infty$. We call such potentials Q^{+}*-potentials*. Obviously, the Gaussian interaction belongs to this class. (ii) It has oscillatory behavior at large Q, with the implication that it is a nonmonotonic function of Q, attaining necessarily negative values for certain ranges of the wavenumber. We call such potentials $Q^{\pm}$*-potentials*. Long-range oscillations in Q-space imply that $\phi(r)$ changes more rapidly from unity at $r = 0$ to zero at $r \to \infty$ in the $Q^{\pm}$-class than in the Q^{+} one. Moreover, let us call Q_{*} the value of Q at which $\hat{\phi}(Q)$ attains its minimum, *negative* value.

If we are dealing with a $Q^{\pm}$-potential Eq. (C.7) implies that $S(Q)$ has a maximum at precisely the wavevector Q_{*} where $\hat{\phi}(Q)$ attains its negative minimum, $-|\hat{\phi}(Q_{*})|$. This maximum becomes a *singularity* at the "spinodal line" $\bar{\rho} t^{-1}|\hat{\phi}(Q_{*})| = 1$, signaling the so-called Kirkwood instability of the system [417,418,426,427]. The theory has a divergence, implying that the underlying assumption of a uniform liquid is not valid and the system must reach a crystalline state. Indeed, on the basis of the fluctuation–dissipation theorem, $S(Q)$ can be interpreted as a response function of the density to an infinitesimal external modulating field at wavenumber Q [4] and a diverging value of this response function clearly signals an instability. If the Fourier transform of $\phi(r)$ has negative Fourier components, then an increase in temperature can be compensated by an increase in density in the denominator of Eq. (C.7), so that $S(Q_{*})$ will have a divergence at all t. We thus conclude that $Q^{\pm}$*-systems freeze at all temperatures*.

If we are dealing with a Q^{+}-potential ($\hat{\phi}(Q)$ monotonic), then Eq. (C.7) implies that $S(Q)$ is also a monotonic function of Q at high densities [160]. For such potentials, one can always find a temperature high enough, so that the assumptions of Eq. (C.4) hold and then Eq. (C.7) forces the conclusion that freezing of the system is impossible at such temperatures. This does not imply, of course, that such systems do not freeze at all; one simply has to go to a low enough temperature and density, so that the mean-field assumption does not hold and the interaction is much larger than the thermal energy. Then, the system will display a hard-sphere type of freezing, to be discussed more explicitly below. An upper freezing temperature t_u must exist for Q^+-potentials, implying that such systems must remelt at $t < t_u$ upon increase of the density. Hence, we reach the conclusion that *Q^+-systems display an upper freezing temperature and reentrant melting*. The criterion says nothing about the crystal structure of the solid, however, which always depends on the details of the interaction as well as the density [160,161].

For potentials in the Q^+-class, the mean-field arguments presented above hold not only at high temperatures but also at low ones, provided that the requirement $\rho\sigma^3 \gg 1$ is satisfied, because these are molten at high densities for all nonzero temperatures. The validity of the mean-field theory for Q^+-type systems, even at very low temperatures, was confirmed recently by direct comparison with simulation results for the particular case of the Gaussian potential [160]. If the potential is in the $Q^\pm$-class, the mean-field approximation holds provided that the system is not already frozen, as we will confirm shortly. Moreover, both kinds of systems display an unusual kind of "high-density ideal gas" limit. Indeed, taking expression (C.7) for $S(Q)$ and using the relation $S(Q) = 1 + \bar{\rho}\hat{h}(Q)$ [4], where $\hat{h}(Q)$ is the dimensionless Fourier transform of the pair correlation function $h(r)$ of the uniform fluid, we obtain

$$\hat{h}(Q) = -\frac{t^{-1}\hat{\phi}(Q)}{1 + \bar{\rho}t^{-1}\hat{\phi}(Q)} . \tag{C.10}$$

At low Q's, where $\hat{\phi}(Q)$ is of order unity, the term proportional to the density in the denominator dominates in the limit of high densities and $\hat{h}(Q)$ scales as $-1/\bar{\rho} \to 0$. At high Q's, the Fourier transform $\hat{\phi}(Q)$ in the numerator is itself small, with the result that $\hat{h}(Q)$, and hence also the correlation function $h(r)$, is approaching zero. This, in turn, means that the radial distribution function $g(r) = h(r) + 1$ is very close to unity in this limit and deprived of any significant structure for all values of r and it only has some small structure at small r, which is in fact more pronounced for $Q^\pm$-potentials than for Q^+ ones. In this limit, the hypernetted chain closure (HNC) becomes exact, as the exact relation $g(r) = \exp[-\beta v(r) + h(r) - c(r) + B(r)]$, combined with the limits $g(r) \to 1$, $h(r) \to 0$ and $c(r) \to -\beta v(r)$ forces the bridge function $B(r)$ to vanish. Moreover, Eqs. (C.7) and (C.10) reveal that the systems obey a scaling law, namely that the functions $S(Q)$ and $th(r)$ do not depend on $\bar{\rho}$ and t separately but only on the ratio $\bar{\rho}/t$.

Systems in the $Q^\pm$-class freeze before the spinodal is reached. In order to make quantitative predictions, we invoke the empirical Hansen–Verlet freezing criterion [170,171], which states that a system crystallizes when $S(Q)$ at its main peak reaches the value 2.85. Combining this with Eq. (C.7), we find the equation of the freezing line $t_f(\eta)$ as

$$t_f(\eta) = 2.942|\hat{\phi}(Q_*)|\eta . \tag{C.11}$$

The value $|\hat{\phi}(Q_*)|$ determines the slope of the freezing line at the high (t,η) part of the phase diagram.

We now wish to put these arguments in a strong test, using the concrete family of the FDM, given by Eq. (C.1). First of all, we have calculated the Fourier transform of the potential $v_\xi(r)$ of Eq. (C.1) numerically, establishing that members of the FDM with $\xi > \xi_c = 0.49697$ belong to the Q^+ class and members with $\xi < \xi_c$ to the $Q^\pm$ one. Moreover, we have taken the cases $\xi = 0$ (the PSM), $\xi = 0.1$ (both smaller than ξ_c) and $\xi = 0.6$ (larger than ξ_c) and performed standard

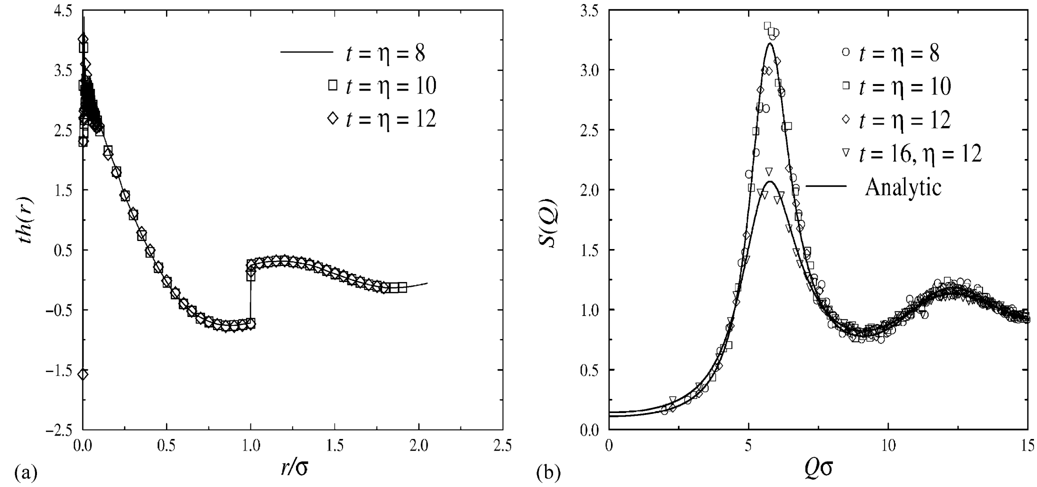

Fig. 58. (a) The product $th(r)$ for a FDM with $\xi = 0$ (PSM), along the diagonal $t = \eta$ at high packing fractions, as obtained from MC simulations. The results close to $r = 0$ are noisy due to poor statistics there. All results collapse onto a single curve. (b) The corresponding structure factors $S(Q)$, shown together with the analytical result of Eq. (C.12).

Monte-Carlo (MC) NVT simulations for various values of temperature and density. We note that the analytical expression (C.7) takes for the PSM the form

$$S(Q) = \left[1 + 24\eta t^{-1}\left(\frac{\sin(Q\sigma) - (Q\sigma)\cos(Q\sigma)}{(Q\sigma)^3}\right)\right]^{-1} . \tag{C.12}$$

The high-temperature–high-density freezing line of Eq. (C.11) takes for $\xi = 0$ the form $t_f(\eta) = 1.0617\eta$. To test the analytical expression of Eq. (C.12), we move along the "diagonal" $t = \eta$, a combination that lies almost on the theoretically predicted freezing line. In Fig. 58 we show the comparison of the analytical results with those obtained from the MC simulations for $S(Q)$ and we also demonstrate that the MC curves for the quantity $th(r)$ all collapse onto a single line. This amply demonstrates the validity of the mean-field approximation for such an extreme case of a $Q^{\pm}$-potential. Moreover, MC simulations at selected points deeply inside the region $t < t_f(\eta)$ displayed Bragg peaks. The corresponding freezing line for the case $\xi = 0.1$ takes the form $t_f(\eta) = 0.731\eta$. In Fig. 59 we show a comparison between simulation and analytical results based on the mean-field approximation for selected points in the fluid phase, showing once more that the mean-field approximation is extremely accurate.

The maximum of the structure factor of the fluid is located at $Q = Q_*$, independently of the density. The freezing density has a linear dependence on the temperature and hence it assumes arbitrarily high values with increasing t. Taking the lattice constant of the incipient solid to be given by the length scale $a = 2\pi/Q_*$, we see that for *arbitrary* average density, the solid maintains a constant lattice spacing. This implies that more and more particles cluster on lattice sites and, in fact, the average occupation number of the sites is proportional to the density. The possibility to freeze at all temperatures is therefore inseparably connected with the phenomenon of clustering in the crystalline state.

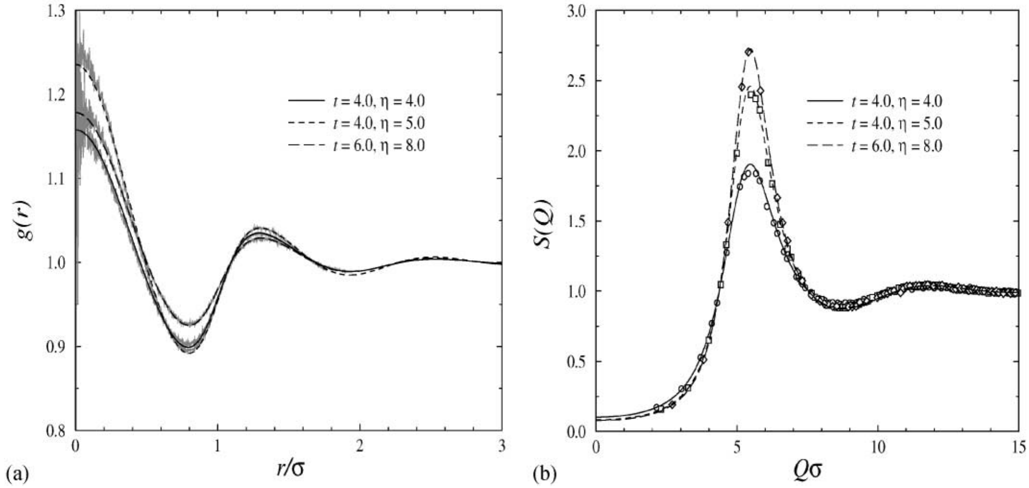

Fig. 59. (a) The radial distribution function and (b) the structure factors for a FDM with $\xi = 0.1$, at selected (t,η) points. In (a) the light-shaded lines are the Monte-Carlo results and the dark ones the analytical, in (b) the points are Monte-Carlo and the lines the theoretical results.

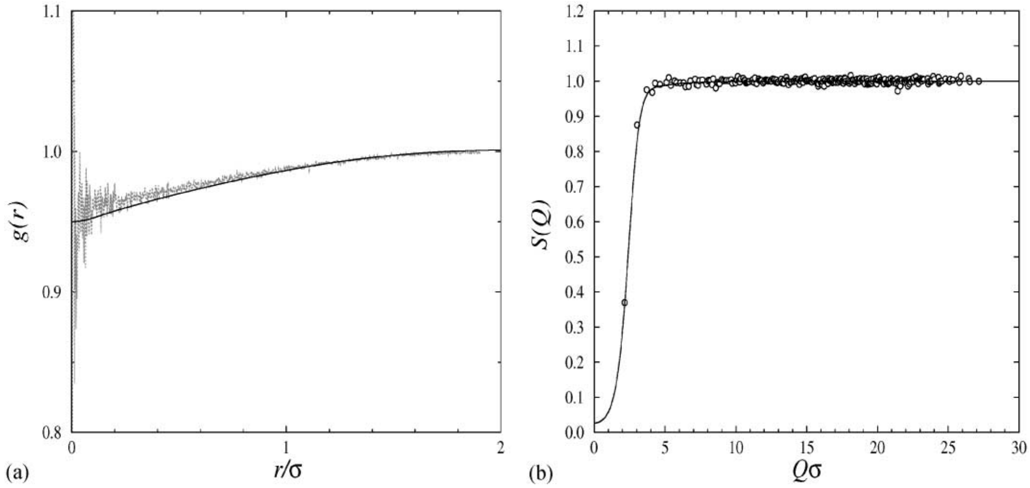

Fig. 60. Same as Fig. 59 but for a value $\xi = 0.6$ at the point $t = 5.0$ and $\eta = 4.0$. Note the lack of structure in $g(r)$ and the corresponding absense of a length scale in $S(Q)$, which looks very similar to the high-density structure factor of the Gaussian core model displayed in Fig. 23.

The pronounced structure of the pair correlation functions of the two models with $\xi < \xi_c$ of Figs. 58 and 59 can be now compared with the lack of any significant structure for the case $\xi = 0.6 > \xi_c$, at $t = 5.0$ shown in Fig. 60. This system belongs to the Q^+-class and the considered temperature is higher than its upper freezing temperature by orders of magnitude. It remains fluid at all densities at this temperature and it forms an "ideal liquid" in which pair correlations are negligible.

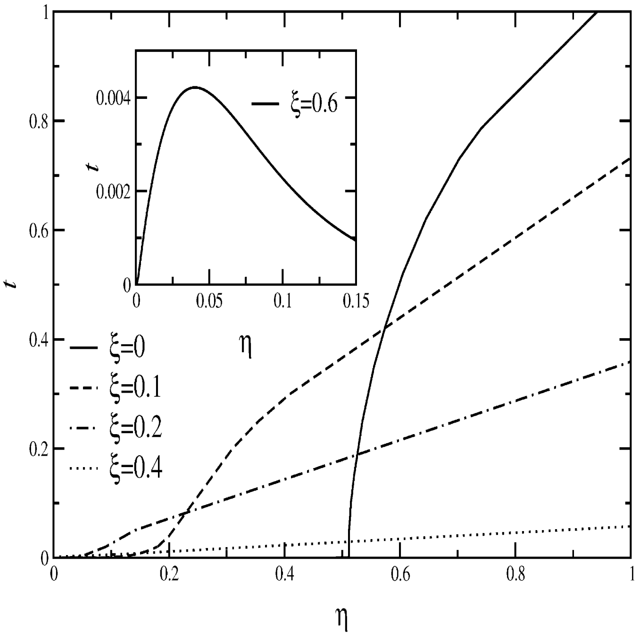

Fig. 61. The evolution of the phase diagram of $Q^{\pm}$-FDMs with ξ. To the right of the freezing lines the system is solid and to the left fluid. Inset: the phase diagram of a Q^{+}-FDM with $\xi > \xi_c$, obtained by solving the HNC and employing the Hansen–Verlet criterion. Below the bell-shaped curve the system is solid and above fluid.

We now turn to the opposite limit of the low-temperature–low-density part of the phase diagram. There, following the original ideas of Stillinger [155], a HS mapping can be performed, as follows. The Boltzmann factor $\exp[-\beta v(r)]$ of the potential varies monotonically from the value $\exp(-\beta\varepsilon) \cong 0$ (since $\beta\varepsilon \gg 1$ there) at $r = 0$ to unity at $r \to \infty$ and has a close resemblance to that of a hard-sphere system. Defining an effective hard sphere diameter σ_{HS} through $\exp[-\beta v(\sigma_{\mathrm{HS}})] = 1/2$ and using the result that the freezing line of hard spheres is given by $\rho\sigma_{\mathrm{HS}}^3 \cong 1$, the low-temperature and low-density freezing line of the system can be drawn and it goes to $\rho = 0$ at $t = 0$ [155]. We have taken this expression for the low-t and low-η freezing line of the FDM and combined it with the analytic expression at the opposite limit, Eq. (C.11), in order to draw schematically the evolution of the phase diagram of the FDM as a function of ξ, for $\xi < \xi_c$. The results are shown in Fig. 61. With increasing ξ, the slopes of the high-t freezing lines decrease; at the limit $\xi \to 0$, corresponding to the PSM, the low-t freezing line approaches the horizontal axis vertically, as is dictated by the fact that the PSM becomes equivalent to the HS system there [167]. In the inset of Fig. 61, we show the phase diagram for a system with $\xi = 0.6 > \xi_c$, showing reentrant melting behavior. The evolution of the phase diagram from a clustering to a reentrant melting behavior can be easily visualized from this picture.

To summarize, we have established a criterion for the topology of the phase diagrams resulting from repulsive, bounded interactions, which is very simple in its formulation and states that if the Fourier transform of the pair potential is positive definite, then the system shows reentrant melting but if not then it freezes at all temperatures, into clustered crystals with multiply occupied sites.

Appendix D. Integral equation theories for multicomponent mixtures

Let us consider a ν-component liquid mixture, consisting of $N_1, N_2, \ldots, N_\nu$ particles of species $1, 2, \ldots, \nu$, respectively, enclosed in the macroscopic volume Ω. The partial density ρ_i of species i, is given by $\rho_i = N_i/\Omega$. The pair structure of the system is fully described by $\nu(\nu+1)/2$ independent correlation functions $h_{ij}(r)$, $i \le j = 1, 2, \ldots, \nu$, because symmetry with respect to exchange of the indices dictates $h_{ij}(r) = h_{ji}(r)$. Associated with the total correlation functions are the direct correlation functions (dcf's) $c_{ij}(r)$. For the same reasons, there exist only $\nu(\nu+1)/2$ independent dcf's. The Fourier transforms of $h_{ij}(r)$ and $c_{ij}(r)$ are denoted by $\tilde{h}_{ij}(Q)$ and $\tilde{c}_{ij}(Q)$, respectively.

The Ornstein–Zernike (OZ) relation for one-component systems at density ρ, Eq. (2.58), takes in Fourier space the algebraic form:

$$\tilde{h}(Q) = \tilde{c}(Q) + \tilde{c}(Q)\rho\tilde{h}(Q)\,, \tag{D.1}$$

where $\tilde{h}(Q)$ and $\tilde{c}(Q)$ are the Fourier transforms of the total and direct correlation functions $h(r)$ and $c(r)$, respectively. The generalization of the OZ relation for multicomponent mixtures takes the form [428]:

$$\tilde{\boldsymbol{H}}(Q) = \tilde{\boldsymbol{C}}(Q) + \tilde{\boldsymbol{C}}(Q)\cdot\boldsymbol{D}\cdot\tilde{\boldsymbol{H}}(Q)\,, \tag{D.2}$$

where $\tilde{\boldsymbol{H}}(Q)$ and $\tilde{\boldsymbol{C}}(Q)$ are $\nu \times \nu$ symmetric matrices with elements:

$$[\tilde{\boldsymbol{H}}(Q)]_{ij} = \tilde{h}_{ij}(Q) \quad \text{and} \quad [\tilde{\boldsymbol{C}}(Q)]_{ij} = \tilde{c}_{ij}(Q) \tag{D.3}$$

and $\boldsymbol{D}$ is a $\nu \times \nu$ diagonal matrix of the partial densities

$$[\tilde{\boldsymbol{D}}]_{ij} = \rho_i \delta_{ij}\,. \tag{D.4}$$

The OZ matrix equation (D.2) above, generates $\nu(\nu+1)/2$ independent algebraic equations for the $\nu(\nu+1)$ unknown functions $\tilde{h}_{ij}(Q)$ and $\tilde{c}_{ij}(Q)$. The system becomes, in principle, solvable if one provides an additional $\nu(\nu+1)/2$ *closure equations* between these functions. These are chosen from the same family of closures mentioned in Section 2.4.1, by adding indices to the correlation functions and to the corresponding pair potentials. For example, the Rogers–Young closure generalization to multicomponent mixtures, given by Eq. (2.66) for $\nu = 1$, reads for a multicomponent mixture as

$$g_{ij}(r) = \exp[-\beta v_{ij}(r)]\left[1 + \frac{\exp[\gamma_{ij}(r) f(r)] - 1}{f(r)}\right] \quad (i = 1, 2, \ldots, \nu \text{ and } i \le j)\,, \tag{D.5}$$

where $g_{ij}(r) = h_{ij}(r) + 1$, $\gamma_{ij}(r) = h_{ij}(r) - c_{ij}(r)$ and $v_{ij}(r)$ is the pair interaction between species i and j. As for the case $\nu = 1$, the function $f(r)$ is given by

$$f(r) = 1 - \exp(-\alpha r)\,. \tag{D.6}$$

Usually, a *single* self-consistency parameter α is employed for all components, as there is a single thermodynamic consistency requirement to be fulfilled, i.e., the equality of the "virial" and "fluctuation" total compressibilities of the mixture. Yet, multi-parameter generalizations of the RY closure have also been proposed [429], invoking the partial compressibilities of the individual components. For $\alpha = 0$ one recovers the PY and for $\alpha = \infty$ the HNC multicomponent closures. For a HS mixture, the PY closure can be analytically solved [430–432].

Suppose now that the full, ν-component system has been solved by means of a chosen integral equation theory and all correlation functions are known. If we are interested in deriving an effective potential $V^{\mathrm{eff}}_{\lambda\lambda}(r)$ acting between particles of species λ only, where the rest of the system has been traced out, we can perform the following inversion: consider the partial correlation function $\tilde{h}_{\lambda\lambda}(Q)$ and use the one-component OZ relation (D.1) to derive an effective one-component dcf $\tilde{c}^{\mathrm{eff}}_{\lambda\lambda}(Q)$ as

$$\tilde{c}^{\mathrm{eff}}_{\lambda\lambda}(Q) = \frac{\tilde{h}_{\lambda\lambda}(Q)}{1 + \rho_\lambda \tilde{h}_{\lambda\lambda}(Q)} \, . \tag{D.7}$$

Note that $\tilde{c}^{\mathrm{eff}}_{\lambda\lambda}(Q) \neq \tilde{c}_{\lambda\lambda}(Q)$ because the former includes all the effects on the λ-species mediated by the remaining $\nu - 1$ degrees of freedom. The mathematical structure of the contributions of these degrees of freedom to the effective direct correlation function $\tilde{c}^{\mathrm{eff}}_{\lambda\lambda}(Q)$ has been analyzed in the recent work of Cuesta and Martínez-Ratón [230] in a powerful and elegant way, within the framework of density-functional theory. With $\gamma^{\mathrm{eff}}_{\lambda\lambda}(r) = h_{\lambda\lambda}(r) - c^{\mathrm{eff}}_{\lambda\lambda}(r)$, the effective potential $V^{\mathrm{eff}}_{\lambda\lambda}(r)$ can be found by inverting the closure

$$g_{\lambda\lambda}(r) = \exp[-\beta V^{\mathrm{eff}}_{\lambda\lambda}(r)]\left[1 + \frac{\exp[\gamma^{\mathrm{eff}}_{\lambda\lambda}(r) f(r)] - 1}{f(r)}\right] . \tag{D.8}$$

This procedure manifestly fulfills the requirement that an effective one-component description of the system should leave all the correlation functions of the considered species unchanged, as mentioned in Section 2.3.1. Yet, there are three caveats: (a) The multicomponent IETs, Eq. (D.5) are approximate in nature. (b) The inversion procedure can be very sensitive to the closure employed for the inversion. If the multicomponent IETs have been solved and a given self-consistency parameter α for the function $f(r)$ has been found, it is *not* a priori clear that the *same* parameter α should be employed in the inversion, Eq. (D.8). Clearly, every different inversion closure yields a different pair potential. (c) The procedure produces necessarily an effective *pair* potential, whereas in the correlation function $g_{\lambda\lambda}(r)$ the effects of all higher-order interactions are hidden. As a result, one obtains effective potentials depending on the density of the considered species λ, as well as on the temperature and the densities of the remaining species.

Appendix E. Star polymer solutions in the neighborhood of the Θ point

The vast majority of the analysis presented in Section 5 dealt with star polymer solutions in good or even athermal solvents, where a universality exists and the self-avoidance of the chains is the rule of the game. This analysis does not apply if the solvent is in the neighborhood of the Θ point. Here, we present briefly a recent colloidal approach to this situation [316], which resulted into an effective interaction between star polymers in Θ-like conditions, yielding, as expected on physical grounds, a more penetrable pair potential than that of Eq. (5.57). As for the good solvent case, small-angle neutron scattering experiments were performed on a star solution, and the resulting intensity spectra were described theoretically by means of an effective potential.

The star polymer under investigation was built of polybutadiene and contained $f = 64$ arms. For all solutions, fully deuterated 1,4-dioxane served as a solvent. For the measurements, solutions of two different concentration regimes were prepared. First, a dilution series of three dilute solutions was mixed in order to determine the form factor of the star. Thereby, star volume fractions of 0.0032, 0.0080 and 0.0127 were chosen. Additionally, a solution was prepared in order to investigate the ordering phenomena. Its volume fraction was 0.104, which is close to the overlap concentration. The value for the overlap concentration was estimated in advance using previous results [294].

The stock solution for the dilution series was generated by mixing the polymer and the solvent first and afterwards heating the mixture to 40°C. Thereby, the polymer was dissolved completely. Turbidity measurements yielded a Θ-temperature of 31.5°C for this solvent. Therefore, the dilution of the stock solution was performed in a heat bath at 40°C. The SANS experiments were performed at five different temperatures, 40°C, 50°C, 60°C, 70°C and 80°C. The accuracy of the temperature was 1°C. Measurements of the second virial coefficient of the solution yielded the Θ-temperature T_Θ is determined to 31°C. In accordance with this result, turbidity measurements revealed $T_\Theta = 31.5^\circ\mathrm{C}$.

The theoretical investigation had as a starting point the theory of Milner et al. [433]. The latter is a self-consistent field (SCF) approach in order to describe the density profile and free energy of polymers grafted on flat plates, suitable for the case at hand, in which the grafting density is high and the self-avoidance is weak. Moreover, the free energy cost (effective interaction) between two such plates being brought close to each other at distances smaller than twice the equilibrium brush extension has been calculated in the same work. Subsequently, Mewis et al. [434] extended the approach to spherical particles coated with polymer by employing the Derjaguin approximation, and Genz et al. [435] used this pair interaction to investigate the applicability of hard-sphere equations of state to polymerically stabilized colloidal suspensions. Referring the reader to the original papers for the details of the derivation [433–435], we only cite here the final expression for the pair potential. Denoting by R the radius of the particle on which the chains are grafted and by L the height of the polymeric brush, the effective potential $\beta v(r)$ reads as

$$\beta v(r) = \begin{cases} \infty & \text{if } r < 2R\,, \\ U_0\left[-\ln y - \frac{9}{5}(1-y) + \frac{1}{3}(1-y^3) - \frac{1}{30}(1-y^6)\right] & \text{if } 2R < r < 2(R+L)\,, \\ 0 & \text{if } 2(R+L) < r\,. \end{cases} \tag{E.1}$$

where $y = (r-2R)/(2L)$ and the prefactor U_0 is given by

$$U_0 = \frac{\pi^2 L^3 f}{48 N a^2 R} \tag{E.2}$$

with a denoting the monomer length and N the degree of polymerization. The radius R has been identified with the innermost part of the star (the core, see Section 5.3.1), whereas the values of the parameters a, N and L have been read off directly from the experimental data [316]. This also included an *increase* in the size of the star with temperature, which is to be expected as a result of improving solvent quality.

Using now the pair potential described above and employing the Rogers–Young closure [81] the structure factor $S(Q;T)$ was calculated for each temperature and for the experimentally measured density ρ. The latter was obtained by the formula $\rho = \phi N_\mathrm{A}/V_W$, where $\phi = 10.4\%$ and V_W had a slight variation from 819 000 cm^3/mol at $T = 40^\circ\mathrm{C}$ to 839 000 cm^3/mol at $T = 80^\circ\mathrm{C}$. For the form factor, the Beaucage fit, Eq. (5.36), was used and the total scattering intensity was then calculated by means of Eq. (5.58).

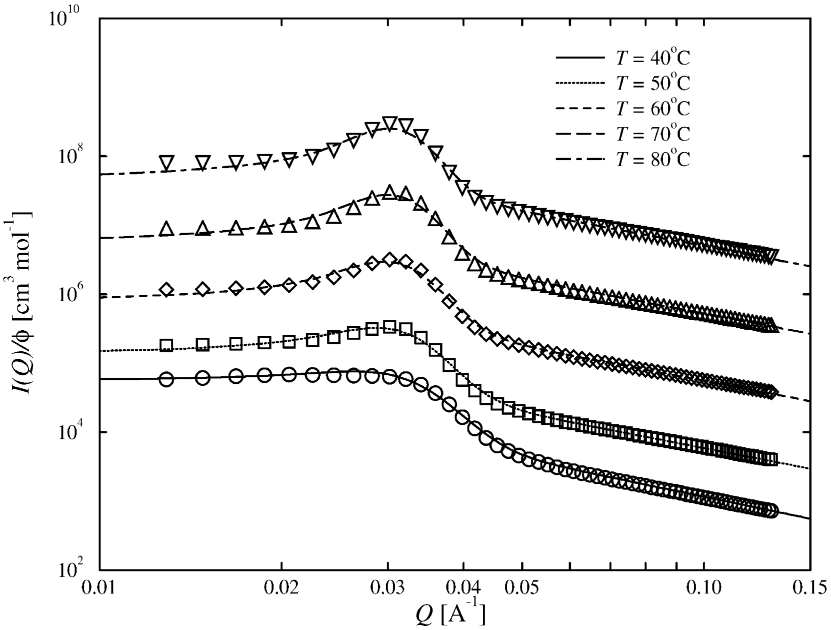

Fig. 62. Theoretical (curves) against experimental (points) total scattering intensities for stars in the vicinity of the Θ point. The theoretical curves have been obtained by the procedure described in the text. For clarity, the data have been multiplied by constants: 50°C:5, 60°C:50, 70°C:500, 80°C:5000. (Taken from Ref. [316].)

The results are shown in Fig. 62. As can be seen, $I(Q)$ develops more structure as we move away from the Θ point and, in addition, the peak moves to lower values of the scattering vector, pointing to a stiffening of the interaction as T grows and a subsequent increase in the mean distance between the particles, in full agreement with the experimental observations. Moreover, it can be seen that the solution develops quite strong ordering as we raise the temperature.

The theoretical investigations for the description of the scattering intensity curves of stars in the vicinity of the Θ point, revealed that the pair interaction which has to be employed is quite different from that for stars in a good solvent [315]. Indeed, application of the logarithmic-Yukawa potential of Eq. (5.57) to this case, would have led to the result that the solutions ought to be actually crystalline, i.e., that potential is too repulsive. This is expected, since the low quality of the solvent induces weaker repulsions between stars than a good solvent. Thus, although the Θ point is an unstable fixed point in the renormalization group-sense and therefore the universal properties of very long chains slightly away from the Θ-temperature are identical to those of chains in good solvents, we find that for nonuniversal quantities the vicinity of the Θ point matters. At this stage, it has been achieved to describe in a satisfactory way star solutions in good solvents on the one hand and in Θ-like solvents on the other, by employing different effective pairwise interactions for each case. Although the two interactions have some superficial similarities (e.g., the logarithmic term for close approaches), the arguments that lead to them are quite different for each case. Thus, the development of a unified theoretical approach which would apply for the whole range of solvent quality, i.e., going from Θ-like to a good solvent and which thus would bridge the gap between the two borderline cases, remains a problem for the future.

References

[1] V.F. Weisskopf, Trans. N.Y. Acad. Sci. 38 (1977) 2202.
[2] M. Gutzwiller, Phys. Today 48 (1995) 15.
[3] N.W. Ashcroft, Aust. J. Phys. 49 (1995) 3.
[4] J.-P. Hansen, I.R. McDonald, Theory of Simple Liquids, 2nd Edition, Academic Press, London, 1986.
[5] P.A. Egelstaff, An Introduction to the Liquid State, Clarendon Press, Oxford, 1994.
[6] J.S. Rowlinson, F.L. Swinton, Liquids and Liquid Mixtures, Butterworths Scientific, London, 1982.
[7] N.H. March, M.P. Tosi, Atomic Dynamics in Liquids, Dover Publications, New York, 1976.
[8] G.A. Martynov, Fundamental Theory of Liquids, Adam Hilger, Bristol, 1992.
[9] C.G. Gray, K. Gubbins, Theory of Molecular Fluids, Clarendon Press, Oxford, 1984.
[10] M.P. Allen, D.J. Tildesley, Computer Simulation of Liquids, Clarendon Press, Oxford, 1987.
[11] D. Frenkel, B. Smit, Understanding Molecular Simulation, Academic Press, San Diego, 1996.
[12] R.J. Hunter, Foundations of Colloid Science, Vol. I, Clarendon Press, Oxford, 1986.
[13] S.A. Safran, N.A. Clark (Eds.), Physics of Complex and Supermolecular Fluids, Wiley Interscience, New York, 1987.
[14] W.B. Russel, D.A. Saville, W.R. Schowalter, Colloidal Dispersions, Cambridge University Press, Cambridge, 1989.
[15] N.W. Ashcroft, N.D. Mermin, Solid State Physics, Holt Saunders, Philadelphia, 1976.
[16] C.F. Tejero, A. Daanoun, H.N.W. Lekkerkerker, M. Baus, Phys. Rev. E 51 (1995) 558.
[17] T.A. Witten, Rev. Mod. Phys. 71 (1999) S367.
[18] H. Löwen, Phys. Rep. 237 (1994) 249.
[19] A.P. Gast, W.B. Russel, Phys. Today 51 (1998) 24.
[20] H. Löwen, M. Watzlawek, C.N. Likos, M. Schmidt, A. Jusufi, A.R. Denton, J. Phys.: Condens. Matter 12 (2000) A465.
[21] P.N. Pusey, R.J.A. Tough, in: R. Pecora (Ed.), Dynamic Light Scattering with Applications to Chemistry and Biology, Plenum Press, New York, 1985.
[22] P.N. Pusey, in: J.-P. Hansen, D. Levesque, J. Zinn-Justin (Eds.), Les Houches, Session LI, Liquids, Freezing and Glass Transition, North-Holland, Amsterdam, 1991.
[23] J. Dhont, An Introduction to Dynamics of Colloids, Elsevier, Amsterdam, 1996.
[24] W.K. Kegel, A. van Blaaderen, Science 287 (2000) 290.
[25] C.A. Murray, D.G. Grier, Annu. Rev. Phys. Chem. 47 (1996) 421.
[26] J.C. Crocker, D.G. Grier, J. Colloid Interface Sci. 179 (1996) 298.
[27] M.P.B. van Bruggen, H.N.W. Lekkerkerker, G. Maret, J.K.G. Dhont, Phys. Rev. E 58 (1998) 7668.
[28] J.S. Higgins, H.C. Benoît, Polymers and Neutron Scattering, Clarendon Press, Oxford, 1994.
[29] P.G. de Gennes, Scaling Concepts in Polymer Physics, Cornell University Press, Ithaca, 1979.
[30] B.V.R. Tata, A.K. Arora, J. Phys.: Condens. Matter 7 (1995) 3817.
[31] P.G. Bolhuis, D.A. Kofke, Phys. Rev. E 54 (1996) 634.
[32] P.G. Bolhuis, D.A. Kofke, J. Phys.: Condens. Matter 8 (1996) 9627.
[33] D.A. Kofke, P.G. Bolhuis, Phys. Rev. E 59 (1999) 618.
[34] M. Kardar, R. Golestanian, Rev. Mod. Phys. 71 (1999) 1233.
[35] J.N. Israelachvili, J. Chem. Soc. Faraday Trans. II 69 (1973) 1729.
[36] J.-P. Hansen, H. Löwen, Ann. Rev. Phys. Chem. 51 (2000) 209.
[37] E. Allahyarov, H. Löwen, Influence of solvent granularity on the effective interaction between charged colloidal suspensions, preprint, cond-mat/0008391, Phys. Rev. E (2000), submitted.
[38] S.H. Chen, Annu. Rev. Phys. Chem. 37 (1986) 351.
[39] W. Härtl, H. Versmold, U. Wittig, Langmuir 8 (1992) 2885.
[40] N. Lutterbach, H. Versmold, V. Reus, L. Belloni, Langmuir 15 (1999) 337.
[41] N. Lutterbach, H. Versmold, V. Reus, L. Belloni, Langmuir 15 (1999) 345.
[42] S. Alexander, P.M. Chaikin, P. Grant, G.J. Morales, P. Pincus, D. Hone, J. Chem. Phys. 80 (1984) 5776.
[43] R.D. Groot, J. Chem. Phys. 95 (1991) 9191.
[44] M.J. Stevens, M.L. Falk, M.O. Robbins, J. Chem. Phys. 104 (1996) 5209.

[45] B.V. Derjaguin, L.D. Landau, Acta Physicochim. USSR 14 (1941) 633.
[46] E.J.W. Verwey, J.T. Overbeek, Theory of the Stability of Lyophobic Colloids, Elsevier, Amsterdam, 1948.
[47] H. Löwen, P.A. Madden, J.-P. Hansen, Phys. Rev. Lett. 68 (1992) 1081.
[48] H. Löwen, P.A. Madden, J.-P. Hansen, J. Chem. Phys. 98 (1993) 3275.
[49] M. Medina-Noyola, D.A. McQuarrie, J. Chem. Phys. 73 (1980) 6279.
[50] L. Belloni, J. Chem. Phys. 85 (1986) 519.
[51] S. Khan, T.L. Morton, D. Ronis, Phys. Rev. A 35 (1987) 4295.
[52] R. van Roij, J.-P. Hansen, Phys. Rev. Lett. 79 (1997) 3082.
[53] R. van Roij, M. Dijkstra, J.-P. Hansen, Phys. Rev. E 59 (1999) 2010.
[54] A.R. Denton, J. Phys.: Condens. Matter 11 (1999) 10 061.
[55] F. Wang, J. Hayter, L.J. Wilson, Acta Crystallogr. D 52 (1996) 901.
[56] D.H. Napper, J. Colloid Interface Sci. 32 (1970) 106.
[57] R. Evans, J.B. Davison, D.H. Napper, J. Polym. Sci. B10 (1972) 449.
[58] R. Evans, D.H. Napper, J. Colloid Interface Sci. 52 (1975) 260.
[59] M.D. Croucher, M.L. Hair, J. Colloid Interface Sci. 81 (1981) 257.
[60] A.J. Ward, A. Courts, The Science and Technology of Gelatin, Academic Press, London, 1977.
[61] P. Pincus, Macromolecules 24 (1991) 2912.
[62] Y. Kamiyama, J. Israelachvili, Macromolecules 25 (1992) 5081.
[63] N.W. Ashcroft, in: E.W. Montroll, J.L. Lebowitz (Eds.), The Liquid State of Matter: Fluids, Simple and Complex, North-Holland, Amsterdam, 1982.
[64] M. Dijkstra, R. van Roij, R. Evans, Phys. Rev. Lett. 81 (1998) 2268.
[65] M. Dijkstra, R. van Roij, R. Evans, Phys. Rev. Lett. 82 (1999) 117.
[66] M. Dijkstra, R. van Roij, R. Evans, Phys. Rev. E 59 (1999) 5744.
[67] M. Dijkstra, J.M. Brader, R. Evans, J. Phys.: Condens. Matter 11 (1999) 10 079.
[68] H. Löwen, G. Kramposthuber, Europhys. Lett. 23 (1993) 673.
[69] N. Kawanishi, H.K. Christenson, B.W. Ninham, J. Phys. Chem. 94 (1990) 4611.
[70] P. Richetti, P. Kekicheff, Phys. Rev. Lett. 68 (1992) 1951.
[71] A. Milling, S. Biggs, J. Colloid Interface Sci. 170 (1995) 604.
[72] D.C. Prieve, F. Luo, F. Lanni, Faraday Discuss. Chem. Soc. 83 (1987) 297.
[73] D.C. Prieve, J.Y. Walz, Appl. Opt. 32 (1993) 1629.
[74] A. Sharma, S.N. Tan, J.Y. Walz, J. Colloid Interface Sci. 191 (1997) 236.
[75] D.C. Prieve, Adv. Colloid Interface Sci. 82 (1999) 93.
[76] D. Rudhardt, C. Bechinger, P. Leiderer, Phys. Rev. Lett. 81 (1998) 1330.
[77] M. Watzlawek, Phase Behavior of Star Polymers, Shaker-Verlag, Aachen, 2000.
[78] A. Jusufi, M. Watzlawek, H. Löwen, Macromolecules 32 (1999) 4470.
[79] R. Evans, Adv. Phys. 28 (1979) 143.
[80] Y. Rosenfeld, N.W. Ashcroft, Phys. Rev. A 20 (1979) 1208.
[81] F.A. Rogers, D.A. Young, Phys. Rev. A 30 (1984) 999.
[82] P. Hutchinson, W.R. Conkie, Mol. Phys. 24 (1972) 567.
[83] D.S. Hall, W.R. Conkie, Mol. Phys. 40 (1980) 907.
[84] L. Verlet, Mol. Phys. 42 (1981) 1291.
[85] F.A. Lindemann, Phys. Z. 11 (1910) 609.
[86] H.R. Glyde, G.H. Keech, Ann. Phys. 127 (1980) 330.
[87] N.W. Ashcroft, in: E.K.U. Gross, R.M. Dreizler (Eds.), Density Functional Theory, NATO ASI Series, Plenum Press, New York, 1995.
[88] J.G. Kirkwood, J. Chem. Phys. 18 (1950) 380.
[89] W.W. Wood, J. Chem. Phys. 20 (1952) 1334.
[90] A. Bonissent, P. Pieranski, P. Pieranski, Philos. Mag. A 50 (1984) 57.
[91] K.W. Wojciechowski, Phys. Lett. A 122 (1987) 377.
[92] T.V. Ramakrishnan, M. Yussouff, Phys. Rev. B 19 (1979) 2775.
[93] A.R. Denton, N.W. Ashcroft, Phys. Rev. A 39 (1989) 4701.
[94] C.N. Likos, N.W. Ashcroft, Phys. Rev. Lett. 69 (1992) 316.

[95] A.D.J. Haymet, in: D. Henderson (Ed.), Fundamentals of Inhomogeneous Liquids, Marcel Dekker, New York, 1992.
[96] Y. Singh, Phys. Rep. 207 (1991) 351.
[97] D. Oxtoby, in: J.-P. Hansen, D. Levesque, J. Zinn-Justin (Eds.), Les Houches, Session LI, Liquids, Freezing and Glass Transition, North-Holland, Amsterdam, 1991.
[98] Y. Rosenfeld, M. Schmidt, H. Löwen, P. Tarazona, J. Phys.: Condens. Matter 8 (1996) L577.
[99] Y. Rosenfeld, M. Schmidt, H. Löwen, P. Tarazona, Phys. Rev. E 55 (1997) 4245.
[100] J.A. Cuesta, Y. Martínez-Ratón, Phys. Rev. Lett. 78 (1997) 3681.
[101] J.A. Cuesta, Y. Martínez-Ratón, J. Chem. Phys. 107 (1997) 6379.
[102] A. Khein, N.W. Ashcroft, Phys. Rev. Lett. 78 (1997) 3346.
[103] A. Khein, N.W. Ashcroft, Phys. Rev. E 60 (1999) 2875.
[104] D. Chandler, Introduction to Modern Statistical Mechanics, Oxford University Press, New York, 1987.
[105] A.R. Denton, Phys. Rev. E 62 (2000) 3855.
[106] H. Graf, H. Löwen, Phys. Rev. E 57 (1998) 5744.
[107] J.S. Rowlinson, Mol. Phys. 52 (1984) 567.
[108] E. Canessa, M.J. Grimson, M. Silbert, Mol. Phys. 64 (1988) 1195.
[109] M.J. Grimson, M. Silbert, Mol. Phys. 74 (1991) 397.
[110] G.C. Barker, M.J. Grimson, M. Silbert, Mol. Phys. 84 (1995) 211.
[111] N.W. Ashcroft, D. Stroud, Solid State Phys. 33 (1978) 1.
[112] A.R. Denton, H. Löwen, Phys. Rev. Lett. 81 (1998) 469.
[113] P.M. Chaikin, T.C. Lubensky, Principles of Condensed Matter Physics, Cambridge University Press, Cambridge, 1995.
[114] D.J. Amit, Field Theory, the Renormalization Group, and Critical Phenomena, 2nd Edition, World Scientific, Singapore, 1984.
[115] G. Gompper, M. Schick, in: C. Domb, J. Lebowitz (Eds.), Phase Transitions and Critical Phenomena, Vol. 16, Academic Press, London, 1994.
[116] W. Helfrich, Z. Naturforsch. Teil C 28 (1973) 693.
[117] C.N. Likos, K.R. Mecke, H. Wagner, J. Chem. Phys. 102 (1995) 9350.
[118] M. Doi, Introduction to Polymer Physics, Clarendon Press, Oxford, 1996.
[119] J. des Cloizeaux, G. Jannink, Polymers in Solution, Clarendon Press, Oxford, 1990.
[120] M. Doi, S.F. Edwards, The Theory of Polymer Dynamics, Clarendon Press, Oxford, 1986.
[121] B. Zimm, W.H. Stockmayer, M. Fixman, J. Chem. Phys. 21 (1953) 1716.
[122] W.H. Stockmayer, Macromol. Chem. 35 (1960) 54.
[123] P.J. Flory, J. Chem. Phys. 17 (1949) 303.
[124] P.J. Flory, Principles of Polymer Chemistry, Cornell University Press, Ithaca, 1953.
[125] J. Zinn-Justin, Phys. Rep. 70 (1981) 101.
[126] P. Grassberger, R. Hegger, L. Schäfer, J. Phys. A: Math. Gen. 27 (1994) 7265.
[127] L. Schäfer, Excluded Volume Effects in Polymer Solutions, Springer, Berlin, 1999.
[128] T.A. Witten, Rev. Mod. Phys. 70 (1998) 1531.
[129] S.T. Sun, I. Nishio, G. Swislow T. Tanaka, J. Chem. Phys. 73 (1980) 5971.
[130] P.J. Flory, J. Chem. Phys. 10 (1942) 51.
[131] M.L. Huggins, J. Phys. Chem. 46 (1942) 151.
[132] M.L. Huggins, J. Am. Chem. Soc. 64 (1942) 1712.
[133] T. Dobashi, M. Nakata, M. Kaneko, J. Chem. Phys. 72 (1980) 6692.
[134] T.A. Vilgis, Phys. Rep. 336 (2000) 167.
[135] S.F. Edwards, J. Phys. A8 (1975) 1670.
[136] S.F. Edwards, E.F. Jeffers, J. Chem. Soc. Faraday Trans. II 75 (1979) 1020.
[137] R.W. Richards, A. Maconnachie, G. Allen, Polymer 19 (1978) 266.
[138] I. Noda, N. Kato, T. Kitano, M. Ngasawa, Macromolecules 14 (1981) 668.
[139] M. Daoud, J.P. Cotton, B. Farnoux, G. Jannink, G. Sarma, H.C. Benoît, R. Duplessix, C. Picot, P.G. de Gennes, Macromolecules 8 (1975) 804.

[140] B. Krüger, L. Schäfer, A. Baumgärtner, J. Phys. (Paris) 50 (1989) 3191.
[141] G.S. Grest, K. Kremer, Phys. Rev. A 33 (1986) 3628.
[142] O.F. Olaj, K.H. Pelinka, Makromol. Chem. 177 (1976) 3413.
[143] O.F. Olaj, Makromol. Chem. 177 (1976) 3427.
[144] O.F. Olaj, W. Lantschbauer, Ber. Bunsen-Ges. Physik. Chem. 81 (1977) 985.
[145] O.F. Olaj, W. Lantschbauer, K.H. Pelinka, Macromolecules 13 (1980) 299.
[146] O.F. Olaj, G. Zifferer, H. Rhemann, Monatsh. Chem. 116 (1985) 1395.
[147] A.Y. Grosberg, P.G. Khalatur, A.R. Khokhlov, Makromol. Chem. Rapid Commun. 3 (1982) 709.
[148] L. Schäfer, A. Baumgärtner, J. Phys. (Paris) 47 (1986) 1431.
[149] J. Dautenhahn, C.K. Hall, Macromolecules 27 (1994) 5933.
[150] R. Czech, C.K. Hall, Macromolecules 24 (1991) 1535.
[151] A.A. Louis, P.G. Bolhuis, J.-P. Hansen, E.J. Meier, Phys. Rev. Lett. 85 (2000) 2522.
[152] P.G. Bolhuis, A.A. Louis, J.-P. Hansen, E.J. Meier, Accurate effective pair potentials for polymer solutions, preprint, cond-mat/0009093, J. Chem. Phys. 114 (2001) 4296.
[153] A.A. Louis, R. Finken, J.-P. Hansen, Europhys. Lett. 46 (1999) 741.
[154] P.J. Flory, W.R. Krigbaum, J. Chem. Phys. 18 (1950) 1086.
[155] F.H. Stillinger, J. Chem. Phys. 65 (1976) 3968.
[156] F.H. Stillinger, T.A. Weber, J. Chem. Phys. 68 (1978) 3837.
[157] F.H. Stillinger, T.A. Weber, Phys. Rev. B 22 (1980) 3790.
[158] F.H. Stillinger, J. Chem. Phys. 70 (1979) 4067.
[159] F.H. Stillinger, Phys. Rev. B 20 (1979) 299.
[160] A. Lang, C.N. Likos, M. Watzlawek, H. Löwen, J. Phys.: Condens. Matter 24 (2000) 5087.
[161] F.H. Stillinger, D.K. Stillinger, Physica A 244 (1997) 358.
[162] B.J. Alder, T.E. Wainwright, J. Chem. Phys. 27 (1957) 1208.
[163] W.W. Wood, J.D. Jacobson, J. Chem. Phys. 27 (1957) 1207.
[164] B.J. Alder, W.G. Hoover, D.A. Young, J. Chem. Phys. 49 (1968) 3688.
[165] W.G. Hoover, F.H. Ree, J. Chem. Phys. 49 (1968) 3609.
[166] A.D.J. Haymet, D. Oxtoby, J. Chem. Phys. 84 (1986) 1769.
[167] C.N. Likos, M. Watzlawek, H. Löwen, Phys. Rev. E 58 (1998) 3135.
[168] C.N. Likos, A. Lang, M. Watzlawek, H. Löwen, Criterion for determining clustering vs. reentrant melting behavior for bounded interaction potentials, preprint, cond-mat/0007089, Phys. Rev. E (2001), in press.
[169] A.A. Louis, P.G. Bolhuis, J.-P. Hansen, Mean field fluid behavior of the Gaussian core model, preprint, cond-mat/0007062, Phys. Rev. E 62 (2000) 7961.
[170] J.-P. Hansen, L. Verlet, Phys. Rev. 184 (1969) 151.
[171] J.-P. Hansen, D. Schiff, Mol. Phys. 25 (1973) 1281.
[172] L.L. Lee, K.S. Shing, J. Chem. Phys. 91 (1989) 477.
[173] L.L. Lee, J. Chem. Phys. 97 (1992) 8606.
[174] L.L. Lee, J. Chem. Phys. 103 (1995) 9388.
[175] L.L. Lee, D. Ghonasgi, E. Lomba, J. Chem. Phys. 104 (1996) 8058.
[176] L. Verlet, Mol. Phys. 41 (1980) 183.
[177] M.J. Fernaud, E. Lomba, L.L. Lee, J. Chem. Phys. 112 (2000) 810.
[178] J. Lebowitz, J.K. Percus, Phys. Rev. 144 (1966) 251.
[179] D. Frenkel, Phys. Rev. Lett. 56 (1986) 858.
[180] M. Schmidt, J. Phys.: Condens. Matter 11 (1999) 10 163.
[181] P. Bolhuis, D. Frenkel, S.C. Mau, D.A. Huse, Nature 388 (1997) 235.
[182] D. Frenkel, Phys. World 6 (1993) 24.
[183] L. Onsager, Proc. N.Y. Acad. Sci. 51 (1949) 627.
[184] V. Degiorgio, R. Piazza, M. Corti, J. Stavans, J. Chem. Soc. Faraday Trans. 87 (1991) 431.
[185] J.C. Crocker, D.G. Grier, Phys. Rev. Lett. 73 (1994) 352.
[186] J.C. Crocker, D.G. Grier, Phys. Rev. Lett. 77 (1996) 1897.
[187] R. Piazza, T. Bellini, V. Degiorgio, Phys. Rev. Lett. 71 (1993) 4267.

[188] P.N. Pusey, W. van Megen, Nature 320 (1986) 340.
[189] P.N. Pusey, W. van Megen, in: S.A. Safran, N.A. Clark (Eds.), Physics of Complex and Supermolecular Fluids, Wiley Interscience, New York, 1987.
[190] S. Asakura, F. Oosawa, J. Polym. Sci. 33 (1958) 183.
[191] A. Vrij, Pure Appl. Chem. 48 (1976) 471.
[192] S. Asakura, F. Oosawa, J. Chem. Phys. 22 (1954) 1255.
[193] R. Verma, J.C. Crocker, T.C. Lubensky, A.G. Yodh, Phys. Rev. Lett. 81 (1998) 4004.
[194] Y.N. Ohshima, H. Sakagami, K. Okumoto, A. Tokoyada, T. Igarashi, K.B. Shintaku, S. Toride, H. Sekino, K. Kabuto, I. Nishio, Phys. Rev. Lett. 78 (1997) 3963.
[195] C. Bechinger, D. Rudhardt, P. Leiderer, R. Roth, S. Dietrich, Phys. Rev. Lett. 83 (1999) 3960.
[196] D. Rudhardt, C. Bechinger, P. Leiderer, J. Phys.: Condens. Matter 11 (1999) 10 073.
[197] A.P. Chatterjee, K.S. Schweizer, J. Chem. Phys. 109 (1998) 10 464.
[198] A.P. Chatterjee, K.S. Schweizer, J. Chem. Phys. 109 (1998) 10 477.
[199] P.G. de Gennes, C.R. Acad. Sci. (Paris) 288B (1979) 359.
[200] J.F. Joanny, L. Leibler, P.G. de Gennes, J. Polym. Sci. Polym. Phys. Ed. 17 (1979) 1073.
[201] R. Lipowski, Europhys. Lett. 30 (1995) 197.
[202] T. Odijk, Macromolecules 29 (1996) 1842.
[203] T. Odijk, J. Chem. Phys. 106 (1996) 3402.
[204] E. Eisenriegler, A. Hanke, S. Dietrich, Phys. Rev. E 54 (1996) 1134.
[205] E. Eisenriegler, Phys. Rev. E 55 (1997) 3116.
[206] A. Hanke, E. Eisenriegler, S. Dietrich, Phys. Rev. E 59 (1999) 6853.
[207] A. Bringer, E. Eisenriegler, F. Schlesener, A. Hanke, Eur. Phys. J. B 11 (1999) 101.
[208] E.J. Meijer, D. Frenkel, J. Chem. Phys. 100 (1994) 6873.
[209] A. Milchev, K. Binder, Eur. Phys. J. B 3 (1998) 477.
[210] C.N. Likos, C.L. Henley, Philos. Mag. B 68 (1993) 85.
[211] A. Moussaïd, W.C.K. Poon, P.N. Pusey, M.F. Soliva, Phys. Rev. Lett. 82 (1999) 225.
[212] M. Fuchs, K.S. Schweizer, Europhys. Lett. 51 (2000) 621.
[213] J. Dzubiella, A. Jusufi, C.N. Likos, C. von Ferber, H. Löwen, J. Stellbrink, J. Allgaier, A.B. Schofield, P.A. Smith, W.C.K. Poon, P.N. Pusey, Phase separation in star polymer–colloid mixtures, preprint, cond-mat/0010176, Phys. Rev. Lett. (2000), submitted.
[214] A. Jusufi, J. Dzubiella, C.N. Likos, C. von Ferber, H. Löwen, Effective interactions between star polymers and colloidal particles, preprint, cond-mat/0012384, Phys. Rev. E (2000), submitted.
[215] H.N.W. Lekkerkerker, B. Widom, Physica A 285 (2000) 483.
[216] P. Attard, J. Chem. Phys. 91 (1989) 3083.
[217] P. Attard, G.N. Patey, J. Chem. Phys. 92 (1990) 4970.
[218] R. Dickman, P. Attard, V. Simonian, J. Chem. Phys. 107 (1997) 205.
[219] B. Götzelmann, R. Evans, S. Dietrich, Phys. Rev. E 57 (1998) 6785.
[220] B. Götzelmann, R. Roth, S. Dietrich, M. Dijkstra, R. Evans, Europhys. Lett. 47 (1999) 398.
[221] R. Roth, Depletion forces in hard sphere mixtures, Ph.D. Thesis, Bergische Universität Gesamthochschule Wuppertal, 1999, unpublished.
[222] R. Roth, R. Evans, S. Dietrich, Phys. Rev. E 62 (2000) 5360.
[223] R. Roth, B. Götzelmann, S. Dietrich, Phys. Rev. Lett. 83 (1999) 448.
[224] J.C. Crocker, J.A. Matteo, A.D. Dinsmore, A.G. Yodh, Phys. Rev. Lett. 82 (1999) 4352.
[225] J.M. Méndez-Alcaraz, R. Klein, Phys. Rev. E 61 (2000) 4095.
[226] A. König, Symmetry of quasicrystals – structure of liquids, Ph.D. Thesis, Cornell University, 2000, unpublished.
[227] J.S. McCarley, N.W. Ashcroft, Phys. Rev. B 49 (1994) 15 600.
[228] S. Andelman, J. Chem. Phys 64 (1976) 724.
[229] Y. Heno, C. Regnaut, J. Chem. Phys. 95 (1991) 9204.
[230] J.A. Cuesta, Y. Martínez-Ratón, J. Phys.: Condens. Matter 11 (1999) 10 107.
[231] H.H. von Grünberg, R. Klein, J. Chem. Phys. 110 (1999) 5421.
[232] Y. Mao, M.E. Cates, H.N.W. Lekkerkerker, Phys. Rev. Lett. 75 (1995) 4548.

[233] Y. Mao, M.E. Cates, H.N.W. Lekkerkerker, J. Chem. Phys. 106 (1997) 3721.
[234] Y. Mao, P. Bladon, H.N.W. Lekkerkerker, M.E. Cates, Mol. Phys. 92 (1997) 151.
[235] K. Yaman, C. Jeppesen, C.M. Marques, Europhys. Lett. 42 (1998) 221.
[236] J.S. Rowlinson, in: J.L. Lebowitz (Ed.), Studies in Statistical Mechanics, Vol. XIV, North-Holland, Amsterdam, 1988.
[237] A.P. Gast, C.K. Hall, W.B. Russel, J. Colloid Intererface Sci. 96 (1983) 251.
[238] E. Canessa, M.J. Grimson, M. Silbert, Mol. Phys. 67 (1989) 1153.
[239] M.M. Santore, W.B. Russel, R.K. Prud'homme, Macromolecules 22 (1989) 1317.
[240] H.N.W. Lekkerkerker, Colloid Surf. 51 (1990) 419.
[241] H.N.W. Lekkerkerker, W.C.K. Poon, P.N. Pusey, A. Stroobants, P.B. Warren, Europhys. Lett. 20 (1992) 559.
[242] S.M. Ilett, A. Orrock, W.C.K. Poon, P.N. Pusey, Phys. Rev. E 51 (1995) 1344.
[243] J.-T. Lee, M. Robert, Phys. Rev. E 60 (1999) 7198.
[244] E. Velasco, G. Navascués, L. Mederos, Phys. Rev. E 60 (1999) 3158.
[245] M.H.J. Hagen, D. Frenkel, J. Chem. Phys. 101 (1994) 4093.
[246] L. Mederos, G. Navascués, J. Chem. Phys. 101 (1994) 9841.
[247] M. Hasegawa, J. Chem. Phys. 108 (1998) 208.
[248] A. Daanoun, C.F. Tejero, M. Baus, Phys. Rev. E 50 (1994) 2913.
[249] T. Coussaert, M. Baus, Phys. Rev. E 52 (1995) 862.
[250] C.F. Tejero, A. Daanoun, H.N.W. Lekkerkerker, M. Baus, Phys. Rev. Lett. 73 (1994) 752.
[251] P.R. ten Wolde, D. Frenkel, Science 277 (1997) 1975.
[252] D. Frenkel, Physica A 263 (1999) 26.
[253] A. Cheng, M.L. Klein, C. Caccamo, Phys. Rev. Lett. 71 (1993) 1200.
[254] L. Mederos, G. Navascués, Phys. Rev. B 50 (1994) 1301.
[255] M. Hasegawa, K. Ohno, Phys. Rev. E 54 (1996) 3928.
[256] M. Hasegawa, K. Ohno, J. Phys.: Condens. Matter 9 (1997) 3361.
[257] C. Caccamo, D. Costa, A. Fucile, J. Chem. Phys. 106 (1997) 255.
[258] M.C. Abramo, C. Caccamo, J. Chem. Phys. 106 (1997) 6475.
[259] M. Hasegawa, K. Ohno, J. Chem. Phys. 111 (1999) 5955.
[260] L.A. Girifalco, J. Phys. Chem. 96 (1992) 858.
[261] A. Cheng, M.L. Klein, C. Caccamo, Phys. Rev. Lett. 71 (1993) 1200.
[262] M.H.J. Hagen, D. Frenkel, Nature 356 (1993) 425.
[263] P. Bolhuis, D. Frenkel, Phys. Rev. Lett. 72 (1994) 2211.
[264] P. Bolhuis, M. Hagen, D. Frenkel, Phys. Rev. E 50 (1994) 4880.
[265] D.A. Young, B.J. Alder, J. Chem. Phys. 73 (1980) 2430.
[266] C.N. Likos, Z.T. Németh, H. Löwen, J. Phys.: Condens. Matter 6 (1994) 10 965.
[267] N.F. Carnahan, K.E. Starling, J. Chem. Phys. 51 (1969) 635.
[268] C.N. Likos, G. Senatore, J. Phys.: Condens. Matter 7 (1995) 6797.
[269] C. Rascón, G. Navascués, L. Mederos, J. Phys.: Condens. Matter 7 (1995) 8211.
[270] C.N. Likos, Z.T. Németh, H. Löwen, J. Phys.: Condens. Matter 7 (1995) 8215.
[271] C. Rascón, G. Navascués, L. Mederos, Phys. Rev. B 51 (1995) 14 899.
[272] L. Mederos, G. Navascués, P. Tarazona, E. Chacón, Phys. Rev. E 47 (1993) 4284.
[273] L. Mederos, G. Navascués, P. Tarazona, Phys. Rev. E 49 (1994) 2161.
[274] C. Rascón, L. Mederos, G. Navascués, Phys. Rev. Lett. 77 (1996) 2249.
[275] I. Nezbeda, Czech. J. Phys. B 27 (1977) 247.
[276] T. Chu, D.R. Nelson, Phys. Rev. E 53 (1996) 2560.
[277] Z.T. Németh C.N. Likos, J. Phys.: Condens. Matter 7 (1995) L537.
[278] L. Verlet, J.-J. Weiss, Phys. Rev. A 45 (1972) 939.
[279] C. Rascón, L. Mederos, G. Navascués, J. Chem. Phys. 103 (1995) 9795.
[280] P. Bladon, D. Frenkel, Phys. Rev. Lett. 74 (1995) 2519.
[281] J.M. Kincaid, G. Stell, E. Goldmark, J. Chem. Phys. 17 (1976) 1073.
[282] P. Bolhuis, D. Frenkel, J. Phys.: Condens. Matter 9 (1997) 381.

[283] A.R. Denton, H. Löwen, J. Phys.: Condens. Matter 9 (1997) L1.
[284] A. Lang, G. Kahl, C.N. Likos, H. Löwen, M. Watzlawek, J. Phys.: Condens. Matter 11 (1999) 10 143.
[285] H.C. Andersen, D. Chandler, J.D. Weeks, Adv. Chem. Phys. 34 (1976) 105.
[286] C. Rascón, E. Velasco, L. Mederos, G. Navascués, J. Chem. Phys. 106 (1997) 6689.
[287] A.R. Denton, H. Löwen, J. Phys.: Condens. Matter 9 (1997) 8907.
[288] A.P. Gast, Langmuir 12 (1996) 4060.
[289] A.P. Gast, Curr. Opinion Colloid Interface Sci. 2 (1997) 258.
[290] G.S. Grest, L.J. Fetters, J.S. Huang, D. Richter, Adv. Chem. Phys. XCIV (1996) 67.
[291] W. Burchard, Adv. Polym. Sci. 143 (1999) 113.
[292] J.J. Freire, J. Pla, A. Rey, R. Prats, Macromolecules 19 (1986) 452.
[293] L.-L. Zhou, J. Roovers, Macromolecules 26 (1993) 963.
[294] J. Roovers, L.-L. Zhou, P.M. Toporowski, M. van der Zwan, H. Iatrou, N. Hadjichristidis, Macromolecules 26 (1993) 4324.
[295] W.D. Dozier, J.S. Huang, L.J. Fetters, Macromolecules 24 (1991) 2810.
[296] F. Mezei, in: F. Mezei (Ed.), Neutron Spin Echo, Springer, Berlin, 1979.
[297] K. Solc, W.H. Stockmayer, J. Chem. Phys. 54 (1971) 2756.
[298] K. Solc, J. Chem. Phys. 55 (1971) 2335.
[299] G. Tanaka, W.L. Mattice, Macromol. Theory Simul. 5 (1996) 499.
[300] K. Solc, Macromolecules 6 (1973) 378.
[301] K. Solc, Macromolecules 13 (1980) 506.
[302] J. Batoulis, K. Kremer, Macromolecules 22 (1989) 4277.
[303] G. Zifferer, J. Chem. Phys. 102 (1995) 3720.
[304] G. Zifferer, Macromol. Theory Simul. 6 (1997) 381.
[305] G. Zifferer, J. Chem. Phys. 110 (1999) 4668.
[306] A. Forni, F. Ganazzoli, M. Vacatello, Macromolecules 30 (1997) 4737.
[307] A. Sikorski, P. Romiszowski, J. Chem. Phys. 109 (1998) 6169.
[308] T.A. Witten, P.A. Pincus, M.E. Cates, Europhys. Lett. 2 (1986) 137.
[309] T.A. Witten, P.A. Pincus, Macromolecules 19 (1986) 2509.
[310] D. Richter, O. Jucknischke, L. Willner, L.J. Fetters, M. Lin, J.S. Huang, J. Roovers, C. Toporowski, L.L. Zhou, J. Phy. IV 3(Suppl.) (1993) 3.
[311] J. Roovers, Macromol. Symp. 121 (1997) 89.
[312] M. Adam, L.J. Fetters, W.W. Graessley, T.A. Witten, Macromolecules 25 (1991) 2434.
[313] L. Willner, O. Jucknischke, D. Richter, B. Farago, L.J. Fetters, J.S. Huang, Europhys. Lett. 19 (1992) 297.
[314] L. Willner, O. Jucknischke, D. Richter, J. Roovers, L.-L. Zhou, P.M. Toporowski, L.J. Fetters, J.S. Huang, M.Y. Lin, N. Hadjichristidis, Macromolecules 27 (1994) 3821.
[315] C.N. Likos, H. Löwen, M. Watzlawek, B. Abbas, O. Jucknischke, J. Allgaier, D. Richter, Phys. Rev. Lett. 80 (1998) 4450.
[316] C.N. Likos, H. Löwen, A. Poppe, L. Willner, J. Roovers, B. Cubitt, D. Richter, Phys. Rev. E 58 (1998) 6299.
[317] M. Watzlawek, H. Löwen, C.N. Likos, J. Phys.: Condens. Matter 10 (1998) 8189.
[318] J. Stellbrink, B. Abbas, J. Allgaier, M. Monkenbusch, D. Richter, C.N. Likos, H. Löwen, M. Watzlawek, Prog. Colloid Polym. Sci. 110 (1998) 25.
[319] M. Watzlawek, C.N. Likos, H. Löwen, Phys. Rev. Lett. 82 (1999) 5289.
[320] J. Roovers, Macromolecules 27 (1994) 5359.
[321] R. Seghrouchni, G. Petekidis, D. Vlassopoulos, G. Fytas, A.N. Semenov, J. Roovers, G. Fleischer, Europhys. Lett. 42 (1998) 271.
[322] J. Stellbrink, J. Allgaier, D. Richter, Phys. Rev. E 56 (1997) R3772.
[323] D. Vlassopoulos, T. Pakula, G. Fytas, J. Roovers, K. Karatasos, N. Hadjichristidis, Europhys. Lett. 39 (1997) 617.
[324] P.A. Nommensen, M.H.G. Duits, J.S. Lopulissa, D. van den Ende, J. Mellema, Prog. Colloid Polym. Sci. 110 (1998) 144.
[325] G. Fleischer, G. Fytas, D. Vlassopoulos, J. Roovers, N. Hadjichristidis, Physica A 280 (2000) 266.
[326] A.N. Semenov, D. Vlassopoulos, G. Fytas, G. Vlachos, G. Fleischer, J. Roovers, Langmuir 15 (1999) 358.

[327] D. Vlassopoulos, G. Fytas, J. Roovers, T. Pakula, G. Fleischer, Faraday Discuss. 112 (1999) 225.
[328] M. Kapnistos, A.N. Semenov, D. Vlassopoulos, J. Roovers, J. Chem. Phys. 111 (1989) 1753.
[329] D. Vlassopoulos, T. Pakula, G. Fytas, M. Pitsikalis, N. Hadjichristidis, J. Chem. Phys. 111 (1999) 1760.
[330] G.S. Grest, K. Kremer, T.A. Witten, Macromolecules 20 (1987) 1376.
[331] A. Jusufi, Diploma Thesis, Heinrich-Heine-Universität Düsseldorf, 1998.
[332] B.H. Zimm, W.H. Stockmayer, J. Chem. Phys. 17 (1949) 1301.
[333] M. Daoud, J.P. Cotton, J. Phys. 43 (531) 1982.
[334] O.V. Borisov, E.B. Zhulina, Eur. Phys. J. B 4 (1998) 205.
[335] S. Alexander, J. Phys. (Paris) 38 (1977) 983.
[336] P.G. de Gennes, Macromolecules 13 (1980) 1069.
[337] J. Batoulis, K. Kremer, Europhys. Lett. 7 (1988) 683.
[338] G.S. Grest, Macromolecules 27 (1994) 3493.
[339] K. Shida, K. Ohno, M. Kimura, Y. Kawazoe, Y. Nakamura, Macromolecules 31 (1998) 2343.
[340] L.A. Molina, J.J. Freire, Macromolecules 32 (1999) 499.
[341] G.S. Grest, M. Murat, in: K. Binder (Ed.), Monte Carlo and Molecular Dynamics Simulations in Polymer Science, Oxford University Press, New York, 1995.
[342] A. Forni, F. Ganazzoli, M. Vacatello, Macromolecules 29 (1996) 2994.
[343] A.M. Rubio, J.J. Freire, Macromolecules 29 (1996) 6946.
[344] S.-J. Su, M.S. Denny, J. Kovac, Macromolecules 24 (1991) 917.
[345] S.-J. Su, J. Kovac, J. Chem. Phys. 96 (1992) 3931.
[346] R. Toral, A. Chakrabarti, Phys. Rev. E 47 (1993) 4240.
[347] A.J. Barrett, D.L. Tremain, Macromolecules 20 (1987) 1687.
[348] A. Rey, J.J. Freire, J.G. de la Torre, Macromolecules 20 (1987) 342.
[349] O. Gratter, O. Kratky, Small Angle X-Ray Scattering, Academic Press, New York, 1982.
[350] A. Poppe, L. Willner, J. Allgaier, J. Stellbrink, D. Richter, Macromolecules 30 (1997) 7462.
[351] J.L. Alessandrini, M.A. Carignano, Macromolecules 25 (1992) 1157.
[352] G. Beaucage, J. Appl. Crystallogr. 28 (1995) 717.
[353] G. Beaucage, J. Appl. Crystallogr. 29 (1996) 134.
[354] O. Jucknischke, Untersuchung der Struktur von Sternpolymeren in Lösung mit Neutronenkleinwinkelstreuung, Ph.D. Thesis, Westfälische Wilhelms-Universität Münster, 1995.
[355] G.A. McConnell, A.P. Gast, J.S. Huang, S.D. Smith, Phys. Rev. Lett. 71 (1993) 2102.
[356] G.A. McConnell, E.K. Lin, A.P. Gast, J.S. Huang, M.Y. Lin, S.D. Smith, Faraday Discuss. Chem. Soc. 98 (1994) 121.
[357] G.A. McConnell, A.P. Gast, Phys. Rev. E 54 (1996) 5447.
[358] G.A. McConnell, A.P. Gast, Macromolecules 30 (1997) 435.
[359] K. Ishizu, T. Ono, S. Uchida, J. Colloid Interface Sci. 192 (1997) 189.
[360] K. Ishizu, S. Uchida, J. Colloid Interface Sci. 175 (1995) 293.
[361] S. Uchida, A. Ichimura, K. Ishizu, J. Colloid Interface Sci. 203 (1998) 153.
[362] S. Uchida, H. Takeda, K. Ishizu, J. Colloid Interface Sci. 213 (1999) 62.
[363] K. Ishizu, Prog. Polym. Sci. 23 (1998) 1383.
[364] J. des Cloizeaux, J. Phys. (Paris) 41 (1980) 223.
[365] C. von Ferber, Y. Holovatch, Theor. Math. Phys. 109 (1996) 34.
[366] C. von Ferber, Y. Holovatch, Europhys. Lett. 39 (1997) 31.
[367] C. von Ferber, Y. Holovatch, Phys. Rev. E 56 (1997) 6370.
[368] C. von Ferber, Y. Holovatch, A. Jusufi, C.N. Likos, H. Löwen, M. Watzlawek, J. Mol. Liquids, in press.
[369] J. Buitenhuis, S. Förster, J. Chem. Phys. 107 (1997) 262.
[370] B. Abbas, Diploma Thesis, Westfälische-Wilhelms Universität Münster, 1996.
[371] J. Stellbrink, J. Allgaier, M. Monkenbusch, D. Richter, A. Lang, C.N. Likos, M. Watzlawek, H. Löwen, G. Ehlers, P. Schleger, Prog. Colloid Polym. Sci. 115 (2000) 88.
[372] G. Nägele, Phys. Rep. 272 (1996) 215.
[373] W.Y. Shih, I.A. Aksay, R. Kikuchi, J. Chem. Phys. 86 (1987) 5127.

[374] Y. Monovoukas, A.P. Gast, J. Colloid Interface Sci. 128 (1989) 533.
[375] E.B. Sirota, H.D. Ou-Yang, S.K. Sinha, P.M. Chaikin, Phys. Rev. Lett. 62 (1989) 1524.
[376] J. Medeiros e Silva, B.J. Mokross, Phys. Rev. B 21 (1980) 2972.
[377] D. Hone, S. Alexander, P.M. Chaikin, P. Pincus, J. Chem. Phys. 79 (1983) 1474.
[378] K. Kremer, M.O. Robbins, G.S. Grest, Phys. Rev. Lett. 57 (1986) 2694.
[379] M.O. Robbins, K. Kremer, G.S. Grest, J. Chem. Phys. 88 (1988) 3286.
[380] M.J. Stevens, M.O. Robbins, J. Chem. Phys. 98 (1993) 2319.
[381] H.S. Kang, C.S. Lee, T. Ree, F.H. Ree, J. Chem. Phys. 82 (1985) 414.
[382] J.F. Lutsko, M. Baus, J. Phys.: Condens. Matt. 3 (1991) 6547.
[383] J.A. Barker, D. Henderson, J. Chem. Phys. 47 (1967) 4714.
[384] J.D. Weeks, D. Chandler, H.C. Anderson, J. Chem. Phys. 54 (1971) 5237.
[385] M. Watzlawek, C.N. Likos, H. Löwen, The phase behavior of star polymer solutions, in preparation.
[386] F.H. Stillinger, T.A. Weber, Phys. Rev. B 31 (1985) 5262.
[387] J. Tersoff, Phys. Rev. Lett. 56 (1986) 632.
[388] R. Biswas, D.R. Hamann, Phys. Rev. Lett. 55 (1985) 2001.
[389] R.S. Phillpot, J.F. Lutsko, D. Wolf, S. Yip, Phys. Rev. B 40 (1989) 2831.
[390] C.N. Likos, N.W. Ashcroft, Phys. Rev. E 52 (1995) 5714.
[391] J.Q. Broughton, X.P. Li, Phys. Rev. B 35 (1987) 9120.
[392] C. von Ferber, A. Jusufi, C.N. Likos, H. Löwen, M. Watzlawek, Eur. Phys. J. E 2 (2000) 311.
[393] C. von Ferber, A. Jusufi, M. Watzlawek, C.N. Likos, H. Löwen, Phys. Rev. E 62 (2000) 6949.
[394] K. Ohno, Phys. Rev. A 40 (1989) 1524.
[395] T. Bickel, C.M. Marques, C. Jeppesen, Phys. Rev. E 62 (2000) 1124.
[396] T. Bickel, C. Jeppesen, C.M. Marques, Local entropic effects of polymers grafted to soft interfaces, preprint, cond-mat/0006082.
[397] E. Eisenriegler, private communication.
[398] A.B. Bhatia, D.E. Thornton, Phys. Rev. B 2 (1970) 3004.
[399] P. Guenoun, F. Muller, M. Deslanti, L. Auvray, Y.J. Chen, J.W. Mays, M. Tirrell, Phys. Rev. Lett. 81 (1998) 3872.
[400] A. Jusufi, C.N. Likos, H. Löwen, Conformations of polyelectrolyte stars, in preparation.
[401] C.N. Likos, A. Jusufi, H. Löwen, W. Groenewegen, J.R.C. van der Maarel, Scattering from solutions of polyelectrolyte stars: theory, simulations, and experiment, in preparation.
[402] K.C.E. Mees, The Theory of Photographic Process, Macmillan, New York, 1966.
[403] G.M. Brown, G.A. Hope, J. Electroanal. Chem. 397 (1995) 293.
[404] G.J.C. Braithwaite, P.F. Luckham, A.M. Howe, J. Colloid Interface Sci. 213 (1999) 525.
[405] P.G. deGennes, C.R. Acad. Sci. Ser. II, Fascicule B Mech. Phys. Chim. Astron. 300 (1985) 839.
[406] K.A. Vaynberg, N.J. Wagner, J. Ahrens, C.A. Helm, Langmuir 15 (1999) 4685.
[407] A.M. Howe, A. Clarke, T.H.M. Whitesides, Langmuir 13 (1997) 2617.
[408] K.A. Vaynberg, N.J. Wagner, R. Sharma, P. Martic, J. Colloid Interface Sci. 205 (1998) 131.
[409] T. Cosgrove, J.H.E. Hone, A.M. Howe, R.K. Heenan, Langmuir 14 (1998) 5376.
[410] C.N. Likos, K.A. Vaynberg, H. Löwen, N.J. Wagner, Langmuir 16 (2000) 4100.
[411] A.A. Kornyshev, S. Leikin, J. Chem. Phys. 107 (1997) 3656, erratum, ibid. 108 (1998) 7035.
[412] E. Allahyarov, H. Löwen, Phys. Rev. E 62 (2000) 5542.
[413] H.M. Harreis, G. Suttman, C.N. Likos, H. Löwen, A.A. Kornyshev, Orientational order in DNA crystals, in preparation.
[414] C. Marquest, T.A. Witten, J. Phys. Paris 50 (1989) 1267.
[415] S. Katsura, Y. Abe, J. Chem. Phys. 39 (1963) 2068.
[416] N. Grewe, W. Klein, J. Math. Phys. 64 (1977) 1729.
[417] N. Grewe, W. Klein, J. Math. Phys. 64 (1977) 1735.
[418] W. Klein, H. Gould, R.A. Ramos, I. Clejan, A.I. Mel'cuk, Physica A 205 (1994) 738.
[419] Y. Rosenfeld, M. Schmidt, M. Watzlawek, H. Löwen, Phys. Rev. E 62 (2000) 5006.
[420] M. Schmidt, H. Löwen, Phys. Rev. Lett. 76 (1996) 4552.
[421] D. Ruelle, Statistical Mechanics, W.A. Benjamin, New York, 1969.

[422] H.L. Frisch, N. Rivier, D. Wyler, Phys. Rev. Lett. 54 (1985) 2061.
[423] W. Klein, H.L. Frisch, J. Chem. Phys. 84 (1986) 968.
[424] H.L. Frisch, J.K. Percus, Phys. Rev. A 35 (1987) 4696.
[425] B. Bagchi, S.A. Rice, J. Chem. Phys. 88 (1988) 1177.
[426] W. Klein, N. Grewe, J. Chem. Phys. 72 (1980) 5456.
[427] W. Klein, A.C. Brown, J. Chem. Phys. 74 (1981) 6960.
[428] J.L. Lebowitz, J.S. Rowlinson, J. Chem. Phys. 41 (1964) 133.
[429] T. Biben, J.-P. Hansen, J. Phys.: Condens. Matter 3 (1991) F65.
[430] J.L. Lebowitz, Phys. Rev. 133 (1964) A895.
[431] N.W. Ashcroft, D. Langreth, Phys. Rev. 156 (1967) 685, erratum, ibid. 166 (1968) 934.
[432] R.J. Baxter, J. Chem. Phys. 52 (1970) 4559.
[433] S.T. Milner, T.A. Witten, M.E. Cates, Macromolecules 21 (1988) 2610.
[434] J. Mewis, W.J. Frith, T.A. Strivens, W.B. Russel, A.I.Ch.E.J. 35 (1989) 415.
[435] U. Genz, B. D'Aguanno, J. Mewis, R. Klein, Langmuir 10 (1994) 2206.
[436] L. Belloni, J. Phys.: Cond. Matter 12 (2000) R549.